Probing zeolites by vibrational spectroscopies

UNIVERSITÀ DEGLI STUDI DI TORINO

S. Bordiga, C. Lamberti, F. Bonino, A. Travert, F. Thibault-Starzyk

"Probing zeolites by vibrational spectroscopies"

Chem. Soc. Rev., **44** (2015) 7262-7341

Doi: 10.1039/c5cs00396b

Probing zeolites by vibrational spectroscopies

Silvia Bordiga,[a] Carlo Lamberti,[*,b,c] Francesca Bonino,[a] Arnaud Travert,[d] and Frédéric Thibault-Starzyk[d]

[a] Department of Chemistry, NIS and INSTM Reference Centers, University of Torino, Via Quarello 15, I-10135 Torino, Torino, Italy
[b] Southern Federal University, Zorge Street 5, 344090 Rostov-on-Don, Russia
[c] Department of Chemistry, CrisDi Centre for Crystallography, University of Torino, Via Giuria 7, I-10125 Torino, Torino, Italy
[d] Laboratoire Catalyse et Spectrochimie, ENSICAEN - Université de Caen - CNRS, 6 Boulevard du Maréchal Juin, 14050 Caen Cedex, France

Abstract
This review faces the most relevant aspects of vibrational spectroscopies (IR, Raman and INS) applied to zeolites and zeotype materials. Surface Brønsted and Lewis acidity and surface basicity are treated in detail. The role of probe molecules and the relevance to tune both the proton affinity and the steric hindrance of the probe to fully understand and map the complex site population present inside microporous materials is critically discussed. A detailed description of the methods needed to precisely determine the IR adsorption coefficients is given allowing to make IR a quantitative technique. The thermodynamic parameters of the adsorption process that can be extracted from a variable temperature IR study are described. Finally, cutting edge space and time resolved experiments are reviewed. All aspects are discussed by reporting relevant examples. When available, the theoretical literature related to the reviewed experimental results is reported in order to support the interpretation of the vibrational spectra on an atomistic level.

[*] Corresponding author tel. +390116707841, e-mail: carlo.lamberti@unito.it

4.1. Basicity: general definition and applicability to zeolite basic centers

4.2. Probe molecules for characterization of zeolites basicity

4.2.1. X-H acids as probe

4.2.2. Lewis acids as probe

4.2.3. In-situ generated probe: NO^+.

5. Identification and location of sites in the framework of zeolites by the size of probe molecules

5.1. Influence of the pores and confinement on the spectrum and acid strength of OH groups. The H-USY zeolite as a key study.

5.2. Non-hierarchical zeolites. Are OH accessible or not? The influence of structure defects

5.3. Substituted pyridines: distinguishing internal and external silanol groups

5.4. Different probes for studying pore systems

5.4.1. Py and CO co-adsorption in mordenite

5.4.2. Acetonitrile and substituted acetonitrile

5.4.3. H-bonding: decrease of the interaction by steric hindrance

5.5. Hierarchical zeolites: the Accessibility Index ACI

6. Determination of the absorption coefficients of the IR modes: combined IR and microgravimetric experiments

6.1. Basic definitions

6.2. Selected examples

7. Determination of the adsorption enthalpies and entropies: variable temperature IR experiments

7.1. VTIR: Theory

7.2. VTIR: Examples

7.2.1. Adsorption of Ar, H_2, O_2, N_2 and CO on H-Na-Y zeolite

7.2.2. Discrimination between two different adsorption sites for CO on Na-ferierite zeolite

7.2.3. Linkage isomerism of simple molecules adsorbed zeolites: determination of the difference in ΔH^0 for the two isomers by VTIR

8. Space resolved experiments: IR microscopes, IR beamlines at synchrotron facilities and stimulated Raman scattering (SRS) microscopy

8.1. Development of microspectroscopic techniques to study heterogeneous catalysts

8.2. Styrene oligomerization in H-ZSM-5

8.3. Stimulated Raman scattering microscopy revealing the 3D acid site distribution in acid zeolite catalysts

9. Time resolved experiments

9.1. *In situ* IR studies on reactivity in zeolites

9.1.1. Reactivity of CO with Cp_2Cr encapsulated inside Na-Y zeolite

9.1.2. O_2-activation of H-Cu-SSZ-13 catalyst: *in situ* independent IR and XANES studies

9.1.3. NH_3-SCR reaction followed *in situ* on Cu-SSZ-13 catalyst

9.2. *Operando* experiments on zeolite catalysts

9.2.1. *Operando* for characterizing the active Brønsted acidic sites in hydrocarbon conversion reactions

9.2.2. *Operando* studies on ion-exchanged zeolites

1. Introduction

Vibrational spectroscopies have played a great role in the characterization of zeolites and zeotypes materials.[1-34] The insertion of heteroatoms (Ti, Ge, Sn, Zr, Fe, Ga, In, etc…), isomorphically substituting T centers, perturbs the [TO_4] framework modes and can be directly detected by IR and Raman, while, dealing with mesoporous materials, the approach of probe molecules, has given to vibrational spectroscopies a great potentiality. The heterogeneity of the different probes (CO, NO, CO_2, N_2, H_2, O_2, NH_3, Py, benzenes, substituted benzenes etc…) provides a large interval of chemical reactivity and steric hindrance making very high the number of potential experiment that can be performed on a microporous materials.

As is the case of all catalysts, also zeolites require special *in situ* and *operando*[35] conditions to be properly characterized, consequently several specific catalytic cells have been developed to allow IR and Raman experiments under relevant conditions.[14, 36-44]

In the characterization of zeolite and zeotype materials, among the different vibrational techniques infrared (IR), Raman, inelastic neutron scattering (INS) and electron energy loss spectroscopy (EELS) by far the most used is IR, followed by Raman spectroscopy INS and EELS. There is however one and two order of magnitude between the number of papers published with IR and those published with Raman and INS, respectively, see Table 1. For this reason the large majority of the examples reviewed in this work refer to IR studies. Few concern Raman studies and one INS, while EELS has been overlooked also owing to its need to operate under ultra-high vacuum conditions that are far away from the catalysts operation medium.

Table 1. Bibliometric data reporting the number of papers published in the 1996- May 2015 time interval combining as the keywords (zeolite OR zeolites OR zeotype OR zeotypes) with (IR OR FTIR OR Infrared OR "infra-red") or (Raman) or (INS OR "inelastic neutron scattering") or (EEL OR EELS OR "electron energy loss"). ISI web of science database.

Technique	N. of papers
Infrared	10133
Raman	1396
INS	129
EELS[(a)]	43

[(a)] The number of 43 papers obtained from this bibliographic research is actually overestimated, as several deal with electron energy loss in the 0.1-2 keV range obtained inside TEM instruments and providing XANES-like spectra.

The relative low number of papers published with INS is obviously justified by the relative high difficulty of access to neutron facilities. On the other hand, Raman spectroscopy has to face several severe experimental difficulties such as: (i) the low quantum efficiency of the Raman phenomenon that is a photon in-photon out process; (ii) the risk of radiation damage effects due to the relatively high power delivered per sample unit area by the laser sources; (iii) the high fluorescence background usually emitted by zeolites after thermal activation; (iv) the high blackbody radiation background emitted by the sample when performing high temperature experiments under *in situ* or *operando* conditions. Although severe, all these difficulties can be, at least partially, overcome by appropriate instrumental conditions as detailed here below and high quality results can be obtained by Raman spectroscopy.

The intrinsic low intensity of Raman spectra can be in part overcame by use of more powerful lasers sources; however is not always a viable solution because of the collateral risk of radiation damage effects. More efficient is the use of Fourier Transform Raman spectrometers working with

a near-IR (NIR) laser source or the use of a multichannel strip detectors in dispersive geometries allowing to collect simultaneously a significant fraction of the spectrum. Obviously FT-Raman cannot be used *operando* condition at high temperatures because of the huge background in the NIR coming from the blackbody radiation. Alternatively, enhancement phenomena could be exploited. This is the case of resonant Raman[20, 30, 31, 45-49] where the use of a laser with an appropriate λ, able matching a peculiar charge transfer transition, allows to enhance by some order of magnitude the Raman modes related to the species subjected to that CT (see Subsection 3.3.2). The availability of several Raman sources of different λ, or of a tunable laser is required to cover the larger number of cases possible. Alternatively, when dealing with metal nanoparticles embedded in the zeolite cages,[50-53] it is possible to perform surface-enhanced Raman spectroscopy (SERS) experiments.[49, 54, 55] SERS is a surface-sensitive technique that enhances Raman scattering by molecules adsorbed on metal surfaces. The enhancement factor can be as much as 10^{10}, which means the technique may potentially detect down to single molecules.[56] The drawback of SERS is that it requires a very peculiar class of materials. The last two methods allowing to enhance the intensity of the Raman spectra have the additional advantage to provide a microscopic resolution to the experiment (see Section 8). This is the case of stimulated Raman scattering microscopy SRS (see Subsection 8.3). SRS allows to increase the sensitivity of Raman by several orders of magnitude by combining two picosecond-lasers (Stokes and pump lasers) for obtaining non linear spectroscopy,[57-59] reaching a spatial resolution better than 1 μm.[60] SRS overcomes the speed limitation of confocal Raman microscopy while avoiding the nonresonant background problem of coherent anti-Stokes Raman scattering (CARS) microscopy.[59, 61, 62] Finally, tip-enhanced Raman spectroscopy (TERS)[49, 55, 63, 64] is a promising scanning probe microscopy technique that combines chemical/structural characterization capability of Raman spectroscopy with the spatial resolution of an atomic force microscopy (AFM). It is one of the few techniques that provide chemical and structural information at ambient condition at high spatial resolution, down to 30 nm. To the best of our knowledge TERS has been not applied to the investigation of zeolitic materials so far.

The risk of radiation damage by the laser beam can be overcame by the use of appropriate *operando* experimental cell mimicking a fluidize-bed reactor where the catalyst particles move continuously inside the beam,[38, 44] see Subsection 9.2.5. Finally, the problems related to the background generated by fluorescence centers or by blackbody radiation in high-temperature experiments can be overcame by the use of UV and far-UV lasers.[20, 30, 31, 65]

On the other hand, Raman spectroscopy exhibits some relevant advantages with respect to IR that makes it the vibrational technique of choice in some specific applications relevant to the zeolite class of materials. This is the case of *in situ* or *operando* experiments performed in the liquid phase using water as solvent. The huge IR absorbtion coefficient of H-bonded water molecules in the liquid phase obscures the infrared spectrum in the 4000-1000 cm^{-1} region while the Raman spectra are almost unaffected by the presence of the liquid phase, being the H_2O molecule a very poor Raman scatterer. Raman spectroscopy is better suited to investigate the zeolite framework stretching region 1200-700 cm^{-1}, that is only partially inaccessible to IR spectroscopy owing to the fact that the 1200-1000 cm^{-1} interval is obscured by the asymmetric stretching of the [TO_4] units, see Subsection 3.3. Finally Raman spectroscopy is more appropriate to investigate the zeolite deactivation processes due to coke formation insides the pores (see Subsection 9.2.5) as the black nature of such carbonaceous species totally absorb the mid-IR radiation. All these aspects have been treated along the text by some relevant examples.

Summarizing, this complex analysis of the advantages and disadvantages of the three main vibrational techniques (IR, Raman and INS) well explains the important difference in terms of published papers emerging form Table 1.

Coming to the content of this review, we start discussing in great detail how vibrational spectroscopies have shed light on the aspects of solid acidity and basicity of zeolites. Brønsted and Lewis acidities are treated in Sections 2 and 3, respectively, while Section 4 is devoted to basicity, where we underline how distinguishing between surface Lewis and Brønsted bases is misleading and should be avoided. Section 5 illustrates how IR spectroscopy, using probe molecules of different hindrance, can discriminate among different sites hosted in crystalline nanoporous materials. The relevant problem of making IR technique a quantitative technique is faced in Section 6, where the accurate determination of the molar absorption coefficients ε is discussed. In Section 7 we review IR experiment performed at variable temperature, showing how it is possible to extract thermodynamic entities such as the entropy and enthalpy of adsorption that are site-specific and not averaged values as those obtained with the standard calorimetric approaches. Finally, in sections 8 and 9 we face the cutting edge topics of space and time resolved experiments down to the μm and the μs resolution, respectively.

It is worth stressing that this review is focoused on the experimental aspects of vibrational spectroscopies applied to zeolites. This choice reflects the competencies of the authors the fact that this themed issue of the journal has already an authoritative review focused in highlighting the advances in theory and their application within the field of zeolite chemistry.[66] Notwithstanding this limitation, we are fully aware that the contribution of theoretical calculations to the field is tremendeous and that in several cases it has been essential to the correct interpretation of the experimental results. For this reason, any time the specific reviewed experimental example was complemented by parallel *ab initio* calculation, the corresponding study was mentioned and quoted. Indeed the quoted literature well reports several contributions from the higly reputed theoretical colleagues as e.g.: Bagus, Catlow, Civalleri, Damin, Doll, Ferrari, Garrone, Nachtigall, Nachtigallova, Pacchioni, Pelmenschikov, Ranghino, Ricchiardi, Sauer, Ugliengo, Valenzano, van Santen, etc...

The review has been written in a modular way, so that each section is self-consistent and independent and can be read separately from the remaining text. However several cross links among the different sections have been done in order to obtain a homogeneous text that is aimed to go beyond the topic of each single section.

2. Brønsted acidity in zeolites

2.1. General considerations

The protonic form of the zeolites are active catalyst in a large variety of reactions,[67-69] like hydrocarbon cracking,[70-73] alkylation of aromatic hydrocarbon,[74-76] alkane hydroisomerization,[77-80] conversions of methanol to hydrocarbons,[81-91] to olefins,[82, 88, 92-97] or to gasoline.[88, 98, 99] and of other oxygen compounds [100] To optimize such reactions, an accurate determination of the acidic strength of the Brønsted sites is required.

Besides theoretical approaches,[66, 101-113] several experimental methods have been developed to measure the acidic strength in solids in general and zeolites in particular. Among them we mention: titration methods,[114-116] calorimetric measurements,[115, 117-119] temperature programmed desorption (TPD) of basic molecules (like ammonia),[120] and, on the spectroscopic side, ^{1}H[107, 110, 113, 121-129] and ^{17}O[130, 131] solid state NMR and IR.[18, 99, 120, 123, 125-128, 132-163]

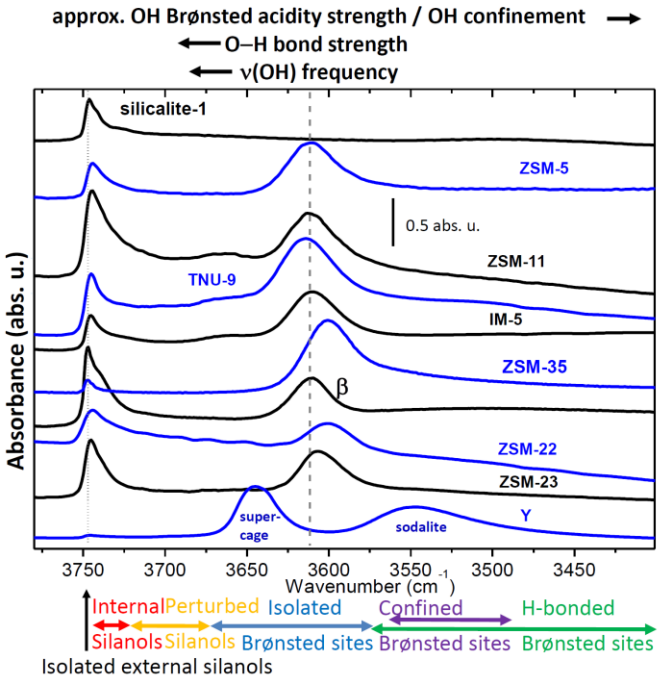

Figure 1. IR spectra activated protonic zeolites. From top to bottom: Al-free silicalite-1 (MFI, ∞), ZSM-5 (MFI, 18), ZSM-11 (MEL, 20), TNU-9 (TUN, 20), IM-5 (IMF, 16), ZSM-35 (FER, 15), β (BEA, 18), ZSM-22 (TON, 30), ZSM-23 (MTT, 23), Y (FAU, 3). In parenthesis the zeolite topology[164, 165] and the Si/Al ratio. All spectra have been obtained after thermal activation of the zeolites in vacuo to remove all molecules (mainly water) adsorbed in the zeolitic channels that otherwise would perturb the O–H stretching. The spectral regions concerning isolated, internal and perturbed silanols and concerning isolated, H-bonded and confined Brønsted sites are roughly defined in the bottom using colored arrows. The intervals of regions are only qualitative. Dotted and dashed vertical lines represent the position of isolated silanols and of the Brønsted sites in H-ZSM-5 zeolite. Previously unpublished figure.

IR spectroscopy allows to evaluate the strength of the O–H bond by the direct measurement the ν(OH) stretching frequency: the higher is ν(OH), the stronger is the O–H bond, the less prone is the Al–O–H zeolitic site to release H^+ to an adsorbed base B, and consequently the lower is the Brønsted acidic strength of the site. This simple concept is clearly shown in Figure 1, where the IR spectra of several activated zeolites are reported in the O–H stretching region. Thermal activation in vacuo at high temperature is a mandatory pre-treatment to remove all molecules (mainly water) adsorbed in the zeolitic channels that otherwise would perturb the O–H stretching, as deeply discussed in the following. At higher frequency, all zeolites exhibit a peak that has a sharp maximum in a very narrow interval (3747-3744 cm^{-1}) independently on the zeolite topology and on the Si/Al ratio. This band is differently tailed in the low-frequency side depending on the different materials and reflects the presence of internal silanol generated by one (or more) Si vacancies.[46, 166-171] In the Al-free silicalite-1 (top spectrum in Figure 1) the silanol band is the only spectroscopic feature in the whole ν(OH) stretching region owing to the absence of Brønsted sites. Also in this case, the low frequency tail reflects the presence of internal silano nests. The high frequency of the silanol bands reflects an almost negligible acidic strength of the silanols. Moving to lower frequency, the 3650-3600 cm^{-1} interval is the region of the isolate (unperturbed) Brønsted sites. The ν(OH) mode of Brønsted sites hosted in the supercage of the Y zeolite occurs at 3645 cm^{-1} (the literature often refers to this band as the high-frequency (HF) band of Y zeolite). Stronger are the Brønsted sites of all other zeolites reported in Figure 1, falling in the 3615-3600 cm^{-1} interval. Unfortunately, in this case, the absolute value of the ν(OH) mode cannot be used to

establish a reliable Brønsted acidity strength scale, indeed the fine position of the band is slight perturbed by very weak Si–O–H···O adducts with adjacent oxygen atoms of the framework. This fact is evident in the case of the Brønsted sites hosted in the sodalite cage of the Y zeolite, absorbing at 3545 cm^{-1} (the literature often refers to this band as the low-frequency (LF) band of Y zeolite) where, owing to the small size of the sodalite cage, the hydrogen bond with the framework oxygen is quite strong. See Section 5.1 for a more detailed description of the IR spectrum of H-Y zeolite and, in particular, Figure 20 for a scheme reporting the structure of Y zeolite. HF and LF bands are also present in H-mordenite, although characterized by a much smaller difference in the corresponding $\tilde{\nu}$(OH), see below Sections 5.4.1 and 6.2, together with Figure 22 and Figure 26. For these reason, a reliable infrared acidity strength scale can be obtained only with the use of probe molecules by carefully monitoring all perturbation of the vibrational featured induced by the adsorption of the probe on the Brønsted site, as detailed in the next section.

It is finally worth noticing that the relative ratio between the intensities of the IR bands associated to Brønsted site and external silanols is related to two factors: the Si/Al ratio of the zeolite and the average crystal size. When two different families of Brønsted sites are present, such as the HF and LF components in H-Y or H-mordenite zeolites mentioned above, the relative intensity of the two bands does not immediately reflect the relative population of the two sites because the molar absorption coefficient ε of the ν(OH) mode is strongly enhanced in vase of H-bonding, occurring in the Brønsted groups confined in the sodalite cage of Y or in the side-pocket om mordenite zeolites. These aspects will be deeply discussed further on in Section 6.

2.2. Brønsted acidity in zeolites investigated by probe molecules of different proton affinity: spectroscopic scale of acidity

Vibrational spectroscopy has definitely played the major role in elucidating the interaction mechanisms and the structure of the formed species. The classical IR spectroscopic way to study the acidity of Brønsted sites in zeolites is to measure the perturbation of vibrational modes of OH sites upon interaction with bases. The method is based on the experimental observation that the formation of ZH···B adducts between a Brønsted acid ZH of the zeolitic framework and a base B via the acid-base reaction (see Eq. (1) and Scheme 1) is accompanied by a downward shift of the ν(OH) stretching frequency which is proportional to the reaction enthalpy.

$$ZH + B \rightarrow ZH\cdots B \qquad (1)$$

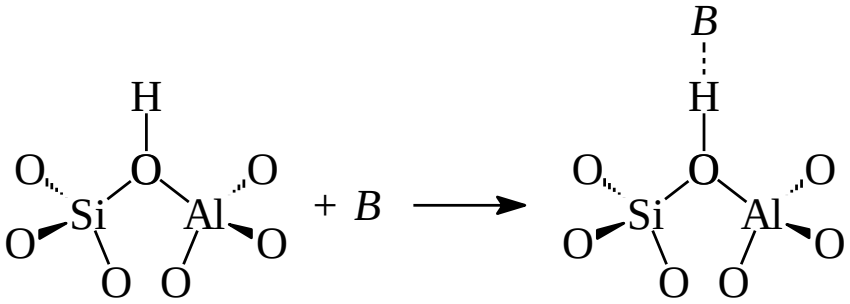

Scheme 1. Formation of ZH···B adducts between a Brønsted acid ZH hosted inside a zeolite channel, Z ≡ [(–O)$_3$–Si] –O–[Al–(O–)$_3$] and a base B via a classical acid-base reaction. Previously unpublished scheme.

This perturbative effect is not only documented for number of hydrogen bonded compounds in the crystalline state[172] and for homogeneous systems in solutions[173] but also for the heterogeneous ones like those encountered in zeolite channels[137, 145, 174] and at the surface of oxides.[175, 176] In particular, one of the key questions associated with the activity of the Brønsted groups present in the zeolite channels is related to the estimation of their acid strength and to the comparison with that of the most common mineral acids and superacids.[136] To illustrate in a systematic way the results obtained by the application of vibrational spectroscopy, we have chosen zeolite β zeolite as a prototype system and we will follow with IR spectroscopy the perturbation induced on the ν(OH) stretching frequency by B molecules characterized by a proton affinity (PA) ranging in a very broad interval: N_2 (PA = 118.2 kcal mol^{-1}), CO (PA = 141.9 kcal mol^{-1}), C_2H_4 (PA = 162.6 kcal mol^{-1}), C_3H_6 (PA = 179.5 kcal mol^{-1}), H_2O (PA = 166.5 kcal mol^{-1}), CH_3CN (PA = 188.6 kcal mol^{-1}), CH_3OH (PA = 181.9 kcal mol^{-1}), $(CH_3)_2O$ (PA = 192.1 kcal mol^{-1}), tetrahydrofuran (THF, PA = 196 kcal mol^{-1}) and pyridine (Py, PA = 204 kcal mol^{-1}).[145, 151] All these molecules have a basic character increasing along the sequence, and when appropriate temperature and pressure conditions are adopted, they can form hydrogen bonded adducts with the Brønsted groups, as shown in Scheme 1.

The spectroscopy of the homogeneous ZH···B systems comprising an acid ZH and a base B can be outlined by briefly describing six representative situations: i) ZH isolated; ii) ZH interacting with B through a weak H-bond; iii) ZH interacting with B through a H-bond of medium-strong strength; iv) ZH interacting with B through a strong H-bond; v) ZH interacting with B through a very strong H-bond; vi) $Z^-\cdots H{-}B^+$ hydrogen bonded ionic pairs, corresponding to the proton transfer.

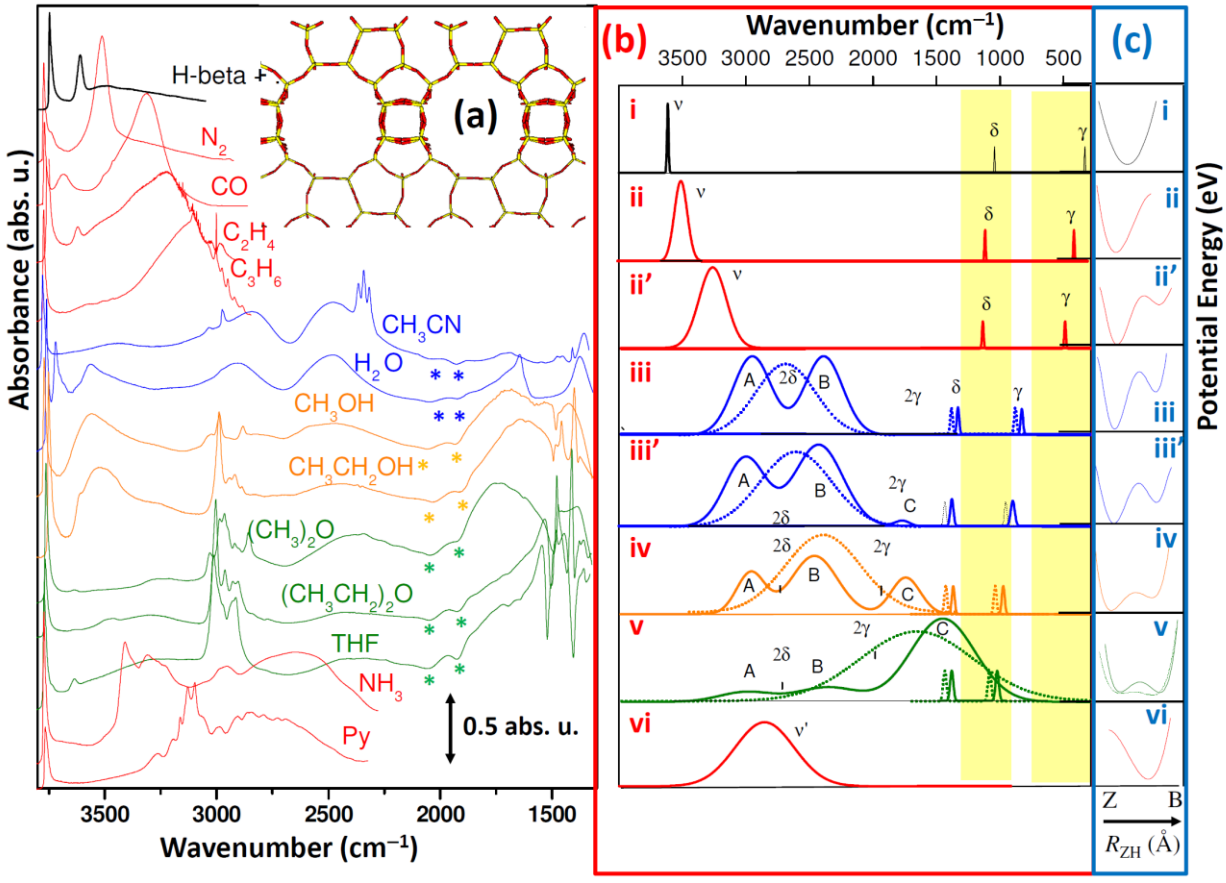

Figure 2. Part (a): experimental IR spectra of unperturbed H-β (black top curve) and of H-β/B 1:1. B bases have been reported from top to bottom according to the increasing proton affinity and classified in classes identified by the line color: N_2, CO, C_2H_4, C_3H_6 (top red spectra), CH_3CN, H_2O (blue spectra), CH_3OH, CH_3CH_2OH (orange spectra), $(CH_3)_2O$, $(CH_3CH_2)_2O$, THF (green spectra) and NH_3 and Py (bottom red spectra). The asterisks indicate the "false" bands due to the effects of bases adsorption on the zeolite skeletal modes as discussed in [177]. The top right corner report a sticks representation of the β zeolite (BEA topology[165]) viewed from the [010] direction, Si or Al (yellow), O (red). Part (b), frames (i-vi): qualitative representation of the IR spectra of unperturbed and of weak, medium, and strong A-H···B or $A^-\cdots H\text{-}B^+$ H-bonded complexes. The half-width of the bending modes is assumed somewhat arbitrarily to slightly increase upon increasing the hydrogen bond strength. The yellow areas correspond to regions obscured by the skeletal modes of the zeolite framework. Part (c), frames (i-vi): schematic representation of the correlated evolution of the proton potential energy as function of the Z-H distance in Z-H···B or $Z^-\cdots H\text{-}B^+$, following [178]. The separation barrier in (v) and (vi) can be very low, and a potential curve characterized by an asymmetric single flat minimum could be used in place. Adapted and implemented by permission of the American Chemical Society (copyright 1997) from Ref. [145].

The complex spectral features reported Figure 1 are described in the following in the order of increasing proton affinity of the adsorbed base B. As Z is not a single atom but represents a zeolitic framework, see Scheme 1, the unperturbed ZH oscillator is characterized by three vibrational modes, the stretching ν, and the bending modes δ and γ (in and out of the plane), see Figure 2(b)i. The proton potential energy of the unperturbed AH is that typical of anharmonic oscillator, the shape of the function being that of a curve with a single minimum, see Figure 2(c)i.

Upon interaction with a weak B base, the ν(AH) stretching undergoes a negative shift ($\Delta\tilde{\nu}$) comprised in the 0-400 cm^{-1} interval and a proportional increase of the integrated intensity (*I*) and of the Full Width Half Maximum FWHM (*FWHM*). At the same time, the bending modes δ and γ shift to higher frequencies. This is schematically represented in Figure 2(b)ii and (b)ii', top red spectra in Figure 2(a)ii and (a)ii'. It can be easily verified that, in first approximation *FWHM* is empirically proportional to the red shift of the band $|\Delta\tilde{\nu}\,(OH)|$ with a proportionality factor close to three quarters:

$$FWHM \sim -3/4\ \Delta\tilde{\nu}\,(OH) \qquad (2)$$

$\Delta\tilde{\nu}\,(OH)$, *I* and *FWHM* are proportional to the enthalpy of formation of the H-bond.[173] The increase of the integrated intensity and of Δ_{FWHM} is due to anharmonic coupling between the ν(OH) mode and the low frequency external mode ν(Z···B) (in turn coupled with the thermal bath fluctuations.[179] Because of this anharmonic coupling, the ν(ZH···B) mode can be better described as a continuum. Upon formation of a weak hydrogen bond, the proton potential becomes more anharmonic and the equilibrium R_{ZH} distance increases, as represented in Figure 2(c)ii and (c)ii'.

Upon formation of AH···B adducts characterized by hydrogen bonds of medium strength, the $|\Delta\tilde{\nu}|$ gradually increases up to 1000 cm^{-1}, with parallel increase of *I* and *FWHM*, as represented by the dotted curves in Figure 2(b)iii, (b)iii'. However the spectroscopy of H-bonded systems of medium strength is not so simple as illustrated by the dotted curves, because the shape of the bands is deeply modified by Fermi resonance effects with 2δ and 2γ overtones.[180-182] As well known, Fermi resonance occurs between two very close vibrational levels of proper symmetry: as consequence the two original modes mix together and originate two different bands, each of them being a mixture of the original modes.[145, 183] According to a simplified approach,[184] the Fermi resonance between the ν(ZH···B) and the 2δ and 2γ modes of the ZH···B adduct in medium strength hydrogen-bonded systems modifies the profile of the ν(OH) mode with appearance of up to three components named A, B, C in Figure 2(b)iii, (b)iii', (b)iv and (b)v. The simplest case is verified

when the maximum of the band of the ν(ZH···B) coincides with the 2δ, being the 2γ band outside the unperturbed envelope of the ν(OH) mode (dotted curves in Figure 2(b)), as represented in Figure 2(b)iii. In this case the observed ν(ZH···B) band is split into two bands of equal intensity (A, B), while the C is not observed. By increasing the hydrogen-bond strength, the 2δ frequency becomes higher than the maximum of the ν(ZH···B) band (that progressively redshifts) and the 2γ frequency falls in its low frequency tail. Here both 2δ and 2γ overtones become internal to the further broadened ν(ZH···B) continuum. As a consequence, the C band starts appearing on the extreme low frequency flank with very low (Figure 2(b)iii') or low (Figure 2(b)iv) intensity. The relative intensity of the A, B and C observed bands changes gradually from $I_A \cong I_B >> I_C$ to $I_A < I_B \cong I_C$ with the increase of the strength of the hydrogen bond (from medium to strong) and the increase of the R_{ZH} (decrease of the R_{HB} distance) in the ZH···B complex. The corresponding potential energy profiles are represented in Figure 2(c)iii' and (c)iv. Bands of this type are well-known in the literature and are usually considered to correspond to proton potential functions consisting of an asymmetric double minimum, with a gap of energy between the two minima, decreasing as the strength of the H-bond increases,[185]. The present description is only qualitative, since the real shape of the potential for hydrogen bonds corresponding to shifts $\Delta\nu(OH) = -1000$ cm^{-1} is not really well established.[186] Parallel to the hydrogen bond strength increase, the tunneling probability increases too, and a clear localization of the proton becomes increasingly difficult, due to its fast fluctuation among the two limit structures under the effect of external perturbations: the system consequently evolves progressively towards more polar forms.

For very strong H-bonds the interaction energy between ZH and B reaches its maximum value, and correspondingly Δν(OH) reaches its maximum (from –2000 to –2500 cm^{-1}) while the R_{ZB} distance reaches its minimum, see Figure 2(c)v. Under these circumstances the potential function of the proton is characterized by a symmetric double minimum curve, with a very low gap of energy between the two minima, or by a single broad and flat minimum,[185] see Figure 2(c)v, where A and B components undergoes a nearly complete disappearance and only the C component is remaining as the dominating feature. This C band (also "D" by some authors), is a very intense, broad, band, extending towards low frequencies, see Figure 2(b)v. This absorption is generally modulated by a large variety of narrow Evans windows caused by direct resonant interaction with the δ (and perhaps γ) mode and with the internal mode of the A and B moieties.

When the proton affinity of B approaches 200 Kcal mol^{-1} (as for NH_3 and Py), the H-bond interaction between ZH and B can be followed by a proton transfer reaction leading to the formation of the anion Z^- and the protonated HB^+ hydrogen bonded pair. The probability that protonation can really occur does not depend only on the strength of the H-bond (and so, on the proton affinity of the reactants), but also on the stabilization of the ionic pairs: this stabilization is due, in homogeneous conditions, to solvent effects[118, 119] and, in heterogeneous conditions, to the interaction with the surfaces.[145, 148] Remembering the elementary concept that the stronger is the base B, the weaker is hydrogen bond in the $A^-\cdots HB^+$ pair, the IR spectroscopy of the pair becomes similar again to that of the hydrogen bonded systems of medium strength, Figure 2(b)vi. The frequency of the ν($BH^+\cdots Z^-$) band increases while the $\Delta\tilde{\nu}$ (OH), *I* and *FWHM* decrease. In Figure 2(b)vi, no attempt is made to localize the δ and γ modes, since they are heavily mixed with internal modes of BH^+ (ring modes in the case of PyH^+).[138]

After this general introduction we will discuss in some detail the cases of N_2, CO and CD_3CN probes, see parts (a), (b) and (c) of Figure 3, respectively. By starting from the molecules with lower PA, parts (a) and (b) of Figure 3 report the modifications induced by the hydrogen bonding perturbation on the ν(OH) stretching mode of the Brønsted groups of β zeolite as function of the

pressure of N_2 and CO respectively (the same probes were send by Wakabayashi et al. on H-ZSM-5[187]). From the spectra it is clearly emerging that upon dosage of the base B the ν(OH) mode of unperturbed groups (band at 3614 cm^{-1}) is gradually consumed while that of the ν(OH···B) vibration (shifted to lower frequency) simultaneously shows up. The clear isosbestic points observed in both spectra ensure that the 1:1 process illustrated in Scheme 1 is really occurring in a stoichiometric way. Other important observations are: (i) the negative shift $\Delta\tilde{\nu}$ (OH) increases on passing from N_2 ($\Delta\tilde{\nu}$ = –126 cm^{-1}) to CO ($\Delta\tilde{\nu}$ = –319 cm^{-1}), *i.e.* with the proton affinity of the base; (ii) the full width at half maximum (FWHM) of the ν(OH) mode increases on passing from the unperturbed Brønsted groups (*FWHM* ≈ 20 cm^{-1}) to the N_2 (*FWHM* ≈ 85 cm^{-1}) and CO (*FWHM* ≈ 220 cm^{-1}) adducts, in fair agreement with the empirical correlation reported in eq. (2). The results illustrated in Figure 3a,b are the typical ones expected for the presence of linear hydrogen bonds[173, 188] and represent further and clear demonstration of the formation of 1:1 adducts. Following the immense literature on the IR spectroscopy of the hydrogen-bonded systems, the shift to lower frequency and the increase of the bandwidth are due to the decrease of the force constant induced by the polarization of the O-H bond and by coupling of the ν(OH) with the ν(O···B) modes of the adducts, which consequently can be better expressed as ν(OH···B) ± ν(O···B).[151]

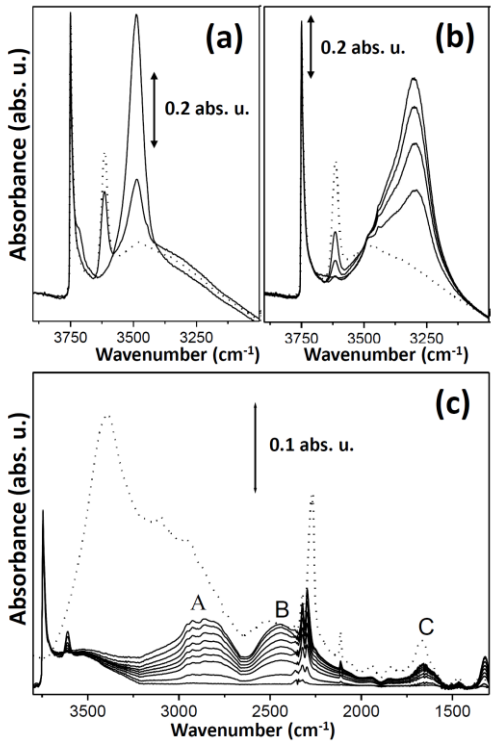

Figure 3. Part (a): IR spectra in the O-H stretching region of increasing equilibrium pressures (up to 133 Pa) of N_2 (PA = 118.2 kcal mol^{-1}) adsorbed at liquid nitrogen temperature on activated H-β zeolite. Part (b): as part (a) for CO dosage (up to 1o00 Pa, PA = 141.9 kcal mol^{-1}). In parts (a) and (b) the dotted line spectrum is that recorded before gas dosage. Part (c): IR spectra of increasing equilibrium pressures of CD_3CN adsorbed on H-β zeolite. Solid line spectra 1-9 refer to CD_3CN equilibrium pressures in the 0-10^{-1} Torr interval (1 Torr = 133.3 Pa), while the dotted line one refers to a much higher pressure (30 Torr). Labels A, B and C denote the three components due to Fermi resonance effects (see text). Parts (a), (b) adapted by permission of the American Chemical Society (copyright 1997) from Ref.[145] Part (c) adapted by permission of Elsevier (copyright 2002) from Ref. [151].

The formation of the hydrogen bonded adducts is accompanied also by a perturbation of the internal modes of the base, resulting in $\Delta\tilde{\nu}$ (NN) = +6 cm^{-1} and $\Delta\tilde{\nu}$ (CO) = +34 cm^{-1}, for N_2 and

CO probes, respectively, see the original paper for more details.[145] At highest filling conditions (not reported in Figure 3b), also the silanols located on the external surfaces of the microcrystals or at internal defects form hydrogen bonded adducts with CO.[145] The shift induced on the ν(OH) stretching frequency of the silanols is definitely smaller ($\Delta\tilde{\nu}$ (OH) = –90 cm^{-1}) than that observed for the Brønsted sites: this is simply the consequence of the fact the shift of the ν(OH) mode of the acid centers caused by the interaction with a given base is related to the acid strength of the group itself. In other words this different response simply reflect the fact that the OH groups of the structural Brønsted sites are much stronger acid than the OH groups of the silanols. This observation can be supported by a large amount of experimental observations obtained with different bases and different zeolites (see Figure 4), so proving its general validity. This general correlation, which is the extension to heterogeneous systems of the well-known Bellamy-Hallam-Williams (BHW) relation extensively documented in homogeneous phase,[189-195] will form the basis of the spectroscopic method for the acid strength evaluation of the surface acidic sites on oxides[196] and of Brønsted groups of zeolitic systems.[145, 148, 197]

In this review article it not possible to continue in the same detailed way the description of the spectra obtained with molecules like ethene, propene, acethylene, etc. which come immediately after N_2 and CO in the PA scale (Figure 2). We move to acetonitrile (PA = 188.6 kcal mol^{-1}). The reasons of this choice are twice: i) the acetonitrile probe (CH_3CN and CD_3CN) has been studied extensively over a great variety of zeolites;[137, 146, 151, 177, 186, 197-202] ii) the acetonitrile-zeolite complex is characterized by a complex spectroscopy generated by Fermi resonance effects.[145, 186] As these effects are dominant in the spectra of the adducts of structural Brønsted sites with bases of medium-strong PA, their detailed illustration for the acetonitrile complexes can be useful for the comprehension of a great variety of experiments involving different and stronger bases. The spectra of increasing doses of deuterated acetonotrile adsorbed on β-zeolite[201] are illustrated in Figure 3c, where we observe the progressive erosion of the structural Brønsted groups because of the formation of hydrogen bonded adducts (full line spectra in Figure 3c); at the highest filling conditions also the band due the silanol groups is eroded (dotted line spectrum). While upon interaction with the nitrile molecule the silanol band originates a broad peak shifted at lower frequency (in $\Delta\tilde{\nu}$ (OH) = –345 cm^{-1}; *FWHM* = 260 cm^{-1}), two absorptions with apparent maxima at 2856 and at 2452 cm^{-1} (previously named A and B) originate from the structural Brønsted peak (instead of the single one expected on the basis of the previous results). Other relevant features of the spectra illustrated in Figure 2 are: i) the ν(CN) modes of the structural Brønsted groups and of the weaker silanols are found at 2297 and 2275 cm^{-1} respectively (*i.e.* at frequencies higher than those of the free molecule); ii) a novel band at 1325 cm^{-1} shows up with coverage which is ascribed to the δ mode of the Brønsted-acetonitrile group. The last result demonstrates that the interaction has become sufficiently strong to shift the δ mode in a frequency range not dominated by the framework vibrations (a fact which makes it observable). The observation of the precise position of the δ mode gives us the key for the explanation of the presence of A-B doublet. In fact as the minimum separating the A and B partners is observed at a frequency corresponding to the twice of the δ mode, it can be readily inferred that it corresponds to the Evans window generated by Fermi resonance effect between the ν(OH···B) ± ν(O···B) mode centered at 2680 cm^{-1} (*FWHM* = 750 cm^{-1}) and the 2δ overtone. In Figure 3c also a band at 1680 cm^{-1} (labeled with the symbol C) is clearly evident. A similar band is observed for acetonitrile on H-ZSM-5 and H-MOR.[177] The assignment of this peak will be given in the following after a general introduction to the Fermi resonance effects in hydrogen bonded systems.

Once the strong Brønsted groups have been fully consumed, further dosage of B leads to the progressive consumption of the silanols (which, as discussed above, are Brønsted sites of weaker acidity) and also to the formation of liquid-like species in the channels. From the previous consideration it is evident that by investigating the whole spectroscopic isotherms, it is possible to verify the effect of the same base on two Brønsted sites of different strength present in the same solid and characterized by a very similar environment. This is true not only for the simplest bases like N_2 and CO, but also for other bases like C_2H_2, C_2H_4, C_3H_6, H_2O, CH_3CN, CH_3OH, CH_3CH_2OH, $(CH_3)_2O$, $(CH_3CH_2)_2O$ and THF. The shifts $\Delta\tilde{\nu}$ (OH) obtained by interaction of these bases with the silanols of the external surfaces of the β zeolite are identical to those found on silica and on silicalite upon interaction with the same bases.[133, 139, 178, 183, 184, 196, 203, 204] The $\Delta\tilde{\nu}$ (OH) values of the stretching band of the strong Brønsted groups are reported vs. the analogous shift observed on silanols in the BHW plot of Figure 4.

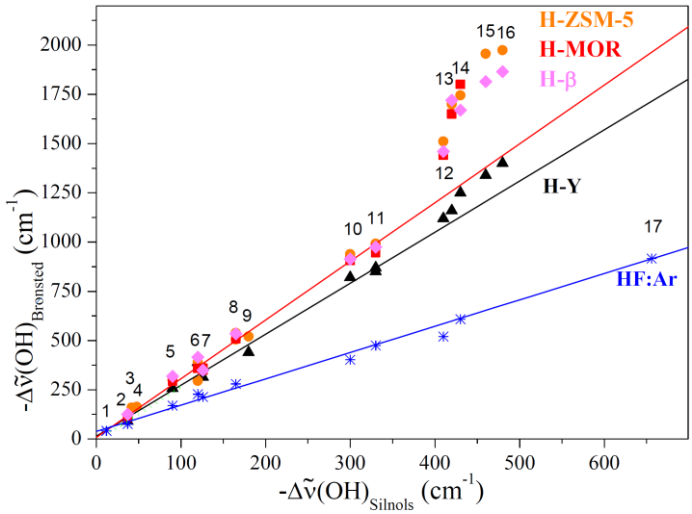

Figure 4. BHW plot of the $\Delta\tilde{\nu}_{\text{Brønsted}}$(OH) observed for the Brønsted sites inside H-ZSM-5 (orange • symbol),[179] H-MOR (red ■ symbol),[179] H-β (pink ♦ symbol),[145] and H-Y (black ▲ symbol)[179] zeolites upon formation of 1:1 hydrogen bonded complexes, with different basis *vs*. the $\Delta\tilde{\nu}_{\text{Silanols}}$(OH) of the silanols groups in 1:1 hydrogen complexes with the same bases. The different bases can be recognized as labelled with numbers: (1) O_2; (2) N_2; (3) N_2O; (4) CO_2; (5) CO; (6) C_4H_4S, C_2H_2; (7) C_2H_4, C_6H_6, C_4H_6 ; (8) C_4H_4O, C_3H_6; (9) HC_2CH_3; (10) H_2O; (11) CH_3CN, CH_3CO; (12) CH_3OH; (13) CH_3CH_2OH; (14) $(CH_3)_2O$; (15) $(CH_3CH_2)_2O$; (16) THF; (17) NH_3. The two green ■ symbols represent the experimental data of H-β/H_2O in interaction with N_2 and CO;[145] the blue * symbols represent the experimental data of HF in cryogenic Ar matrices.[205-210] For each family of data, the straight line with the sane color represents the best linear fit of the experimental points in the $\Delta\tilde{\nu}_{\text{Brønsted}}$(OH) < 1000 cm^{-1} interval.[145, 179] The data for H-ZSM-5, H-MOR and H-β have been fitted with an unique line, being virtually indistinguishable within the experimental errors. See Table 2 for the quantitative results of the fits. Adapted by permission of the American Chemical Society (copyright 1997) from Ref.[145].

This kind of plot is suggested by the well-known fact that, in solution it is possible to study the properties of an acid solute X–H, by directly comparing the $\Delta\tilde{\nu}$ (XH) caused by the formation of 1:1 XH···B adduct with the frequency shift caused by the same base on a second different solute X'–H (for instance, pyrrole used as a standard). This has been verified in a variety of solvents.[189-193, 195] For each solute and for hydrogen bonds of weak-medium strength, linear relationships are constantly observed, and the relative slopes of the straight lines obtained for different X–H systems have been correlated with the pKa values of the solutes in aqueous solutions. From Figure 4 it is clearly emerging that a linear relationship exists between the $\Delta\tilde{\nu}_{\text{Brønsted}}$(OH) shifts of the stretching mode of the strong Brønsted sites of H-β (pink ♦ symbol), H-ZSM-5 (orange • symbol), H-MOR

(red ■ symbol), and H-Y (black ▲ symbol) zeolites and the $\Delta\tilde{\nu}_{\text{Silanols}}$(OH) of silanols (used as standards)[139, 145, 151] and that the slope of the straight line is a characteristic parameter of each zeolite, see Table 2. The universal validity of this correlation is proved also by the fact that the shifts $\Delta\tilde{\nu}_{\text{Silanols}}$(OH) of the silanols stretching correlate linearly also with the shifts obtained for HF interacting with the same bases in an argon matrix,[205-210] (blue * symbols in Figure 4), which is not obvious because of the different "solvents" (zeolite framework and argon).

It is worth noticing that the linear correlation illustrated in Figure 4 holds only for $\Delta\tilde{\nu}_{\text{Brønsted}}$(OH) of strong Brønsted sites stretching not greater than 1000 cm^{-1}. For $\Delta\tilde{\nu}_{\text{Brønsted}}$(OH) > 1000 cm^{-1}, the linear correlation is lost because we are comparing strong hydrogen bonds (associated with proton potentials characterized by two minima separated by a low or negligible energy barrier, see bottom parts of Figure 2) with medium strength hydrogen bonds in SiOH···B adducts (where the potentials still retain a single minimum). There is actually another potential case where the linear correlation foreseen by the BHW relationship will fail in zeolites, or in microporous materials in general. Indeed the BHW holds only if the base B is free to optimize its orientation in order to maximize the hydrogen bond interaction with the acidic site. This may not be fully possible if the molecule B is quite large and if the zeolite pores are quite narrow, as documented by the work of Onida et al.[211] and reviewed in detail in Section 5.4.3.

From the data summarized in Figure 3 and Table 2 it emerges that the shifts $\Delta\tilde{\nu}_{\text{Brønsted}}$(OH) are practically identical for H-MORD, H-β and H-ZSM-5: this means that the slope of the straight lines corresponding to these zeolites is identical (within the experimental error) and hence that the acidic character of the Brønsted sites of all of these zeolites is nearly equal. This is the reason why Pazé et al.[145] decided to report only an unique linear fit for the three datasets joint together (2.93 ± 0.05, see fourth row in Table 2). Conversely, the acidity of these three solids is appreciably greater than that of H-Y (2.59 ± 0.12 in Table 2) as far as H-ZSM-5 and H-MORD and much greater than HF in Ar matrix (1.30 ± 0.04). Worth of note is the fact that in the intercept value is always very small (in an ordinate scale that goes up to 2000 cm^{-1}) approaching the ideal 0 cm^{-1} theoretically expected for a null perturbation.

Table 2. Summary of the best linear fits performed on the $\Delta\tilde{\nu}_{\text{Brønsted}}$(OH) vs. $\Delta\tilde{\nu}_{\text{Silanols}}$(OH) data reported in Figure 4 for the different zeolites. As the slope of H-ZSM-5, H-MOR and H-β zeolites are, within the incertitude comparable, the best linear fit has been repeated also for the three datasets joint together (fourth row). Previously unpublished Table analyzing data reported in refs.[145, 179, 205-210]

System	slope	intercept (cm^{-1})	R^2
H-ZSM-5	2.98 ± 0.09	8 ± 16	0.9887
H-MOR	2.91 ± 0.07	8 ± 13	0.9959
H-β	2.89 ± 0.12	36 ± 23	0.9897
<H-ZSM-5, H-MOR, H-β>	2.93 ± 0.05	15 ± 10	0.9908
H-Y	2.59 ± 0.12	14 ± 26	0.9849
HF : Ar	1.30 ± 0.04	39 ± 11	0.9904

It has been established that, in heterogeneous systems, the ratio of frequency shift of the strong Brønsted groups and that of the SiOH groups (used as standard) measured in the same conditions is correlated with the proton affinities by the empirical relation:[145, 151, 174, 177, 197]

$$PA_{Bronsted} = PA_{Silanols} - A\log\left[\frac{\Delta\tilde{\nu}_{Bronsted}}{\Delta\tilde{\nu}_{Silanols}}\right] \quad (3)$$

where PA_{Silanols} = 1390 kJ mol^{-1} and where A = 442.5 kJ mol^{-1}. It is evident that this equation affords a means for measuring the proton affinity of the Brønsted sites of any zeolite. The most important conclusion which can be derived is that the $\Delta\tilde{\nu}_{\text{Brønsted}}(\text{OH})/\Delta\tilde{\nu}_{\text{Silanols}}(\text{OH})$ ratio is independent of the base B used to probe the zeolite

2.3. From H-bond to the protonation of acetonitrile: exploring superacidity

Zeolites have often been described as solid solvents. They can stabilize dissociated ionic species, and play the same solvating role as water. This aspect of zeolites opens the way to a new part of the acidity scale. Acidity in a mixture is limited by the dissociation of the solvent in which the reaction is observed. This is what defines the scale of pH in water. It was thus proposed that, in the absence of water, zeolites could allow the use of stronger acids, without the usual limit in strength imposed by water. A strongly acidic zeolite could even contain so-called superacidic sites in itself, and it has long been an important issue to detect and measure such sites. It should be noted that superacidity, by definition, disappears in the presence of water (the system would then fall back in the pH scale between 1 and 14, as defined in water). The Hammett acidity scale H_0 is used to monitor acidity out of the pH scale, and the scale is this way extended to negative values. For an acid BH which will dissociate into B^- and H^+, with an equilibrium constant K_a, the Hammett acidity function H_0 is defined as:

$$H_0 = pK_a + log\left(\frac{[B^-]}{[BH]}\right) \quad (4)$$

Concentrated anhydrous sulphuric acid has been defined as the limit of superacidity, with a Hammet constant of H_0 = −12. Adding SO_3 to concentrated sulphuric acid yields a superacid solution, known as oleum. A [SO_3-H_2SO_4] pair is formed (at higher SO_3 concentration, poly sulphuric acids are obtained: $H_2S_3O_{10}$, $H_2S_4O_{13}$…]. SO_3 is a strong Lewis acid that enhances H_2SO_4 Brønsted acid by withdrawing its electrons. The same happens in "magic acid" HSO_3F-SbF_5 or in some hydrotreated or steamed zeolites. The least trace of water dissociates the complex and destroys superacidity (quantitatively), and any superacidity can only be studied in perfectly anhydrous conditions (which is very hard to reach on zeolites). Superacidity can be measured by protonation of very weakly basic probe molecules, as for example some nitriles.

Anquetil at al.[212] have shown that acetonitrile is protonated in solution at H_0= −10.6, see Figure 4. When the acid strength of the solution increases, the ν(CN) vibration band at 2300 cm^{-1} (for H-bonds in moderately acid solutions) shifts towards higher frequencies, and suddenly disappears when protonation takes place. A new ν(CN) vibration band appears at 2324 cm^{-1}. This very specific spectroscopic feature is a good way to detect protonation, and to measure the strength of an acidic medium.

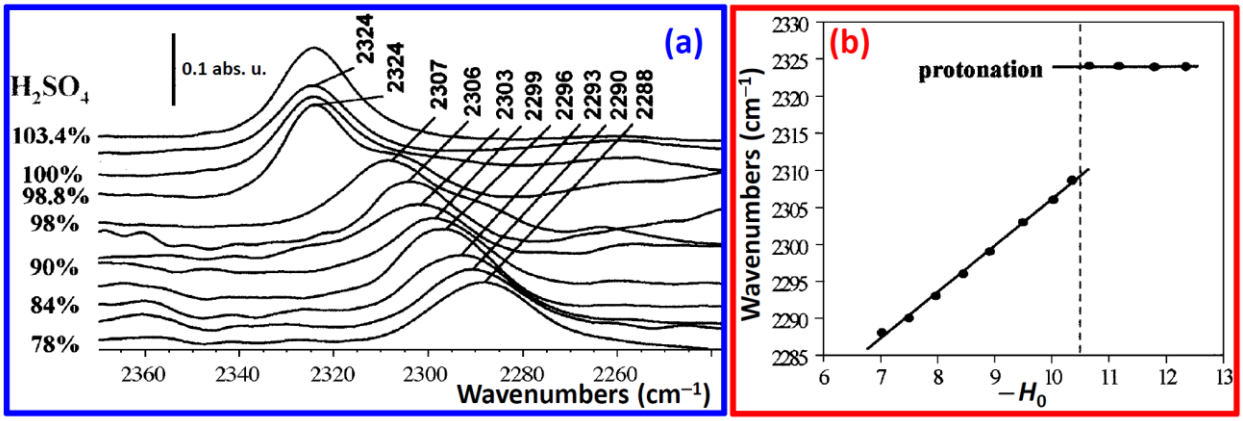

Figure 5. Part (a): ν(C≡N) frequency of CD_3CN in various H_2SO_4 concentration solutions. Part (b): variation of ν(C≡N) of the spectra reported in part (a) with H_0. Adapted by permission of the Royal Society of Chemistry (copyright 1999) from Ref.[212].

The acid strength at which the nitrile is protonated can be tuned by halogen substitution. Halogenated acetonitrile is less basic, and the threshold for protonation shifts to stronger acids. Chloro-acetonitrile is protonated at H_0= −12.4, bromo-acetonitrile at −12.6, and dichloro-acetonitrile is only protonated at H_0= −13.2, leading to a powerful scale for measuring superacidity in solids. These authors have applied this technique to zeolites (which actually did not reach the level of superacidity) and to sulphated zirconia, for which protonation was measured at H_0= −13, and thus revealed itself as superacid.[212]

This shows that although some zeolites are very strong acids, those tested in that study (including the so-called "super-acidic" steamed Y zeolite) did not reach the limit of superacidity. Only some solids like sulfated zirconia[213-216] and the the perfluorosulfonic membrane Nafion[136, 138, 139, 177, 217, 218]were measured as superacidic.

2.4. INS and ab initio (MP2) study of the possible protonation of H_2O in H-ZSM-5

The group of Jobic and Sauer have investigated with combined inelastic neutron scattering (INS) and DFT the adsorption of water, at different concentrations, in H-ZSM-5.[219] The study was aimed to determine whether the acidic sites in H-ZSM-5 are sufficiently strong to protonate water or not.

$$Z^-OH^+ + H_2O \rightarrow Z^-OH^+\cdots H_2O \rightleftharpoons ZO^-\cdots H_3O^+ \qquad (5)$$

As deeply discussed in Section 2.2, the relevance of evaluating the correct acidity strength of a given site hosted in the internal or external surfaces of a mesoporous material is of high relevance. It is consequently important to determine whether reaction (5) is fully displaced to the right or not. Section 2.2 and Figure 2 have shown how elegant, but complex, is the IR spectroscopy of strong and very strong H-bonded complexes in zeolites. INS represents an interesting alternative method to face this problem. This technique is particularly sensitive to vibrational modes involving hydrogen motions because of the large incoherent cross section and the low mass of the proton.[220, 221] Indeed, the incoherent cross sections of the most abundant nucleai present in zeolitic frameworks are Si (0.004 barn, 1 barn = 1×10^{-24} cm^2), Al (0.0082 barn), O (0.0008 barn), P (0.005 barn), B (1.7 barn), Ti (2.87 barn), Fe (0.4 barn), Ga (0.16 barn), Ge (0.18 barn), Sn (0.022 barn), to be compared to that of hydrogen (82.02 barn). Furthermore, vibrational frequencies below

800 cm^{-1} are easier observed with INS than with IR. Another important feature is that the INS intensities are directly related to atomic displacements which can be computed from empirical force fields or from ab initio quantum chemical methods.[219, 221] Excellent agreement can be obtained between experimental INS spectra and simulated spectra using theoretical frequencies and atomic displacements as inputs.[222] Since atomic displacements of water molecules adsorbed on Brønsted sites in zeolites were calculated for the two possible water structures by Krossner and Sauer,[223]in a successive work in collaboration with Jobic, the INS spectra of water in interaction with an acid site were simulated and compared with the experimental data, see Figure 6.

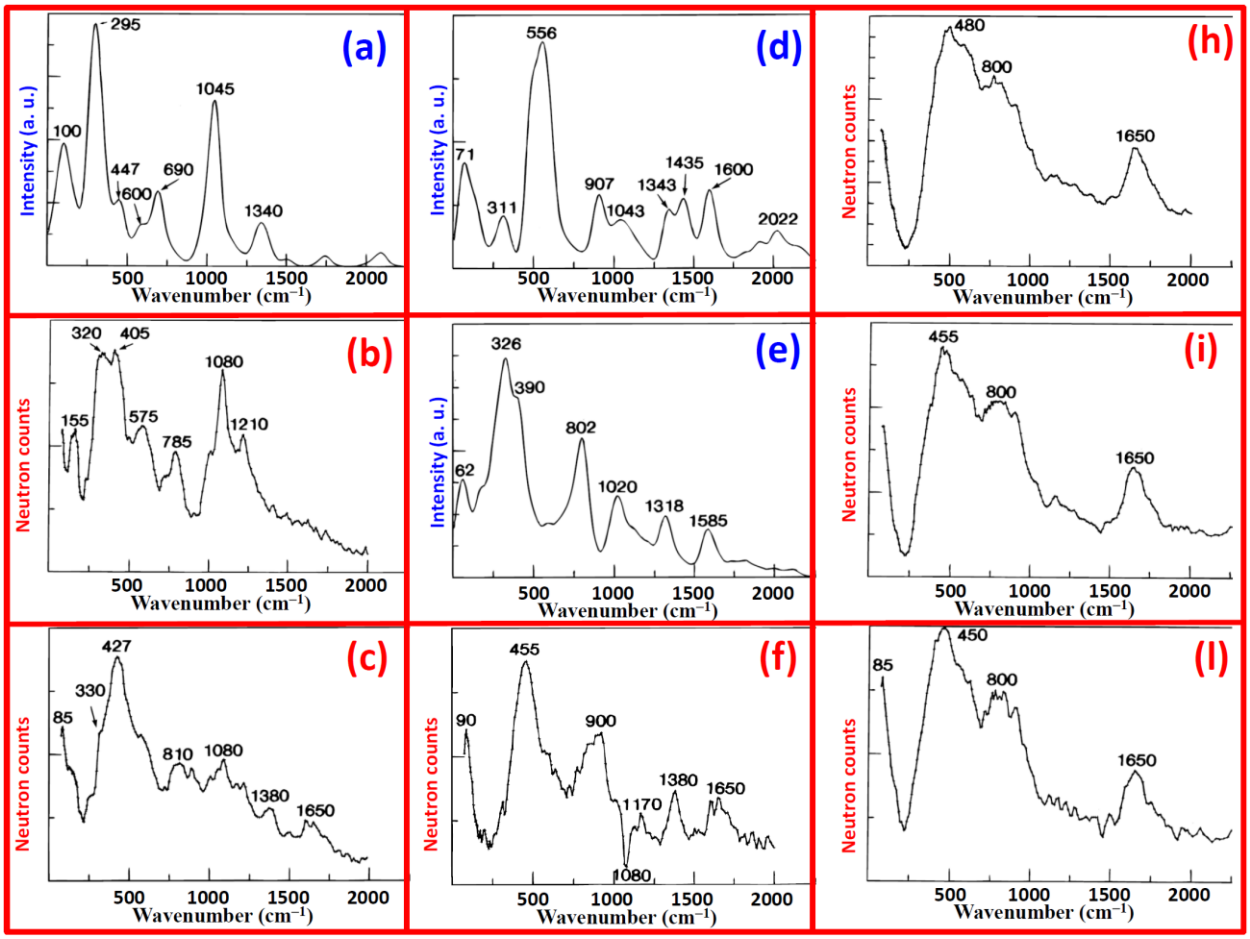

Figure 6. Part (a): calculated INS spectrum of dehydrated H-ZSM-5. Part (b): experimental INS spectrum of dehydrated H-ZSM-5. Part (c): INS of H2O adsorbed on H-ZSM-5 (loading θ_1: 3.5 molecules per unit cell). Part (d): simulated INS spectrum for a hydroxonium ion (H_3O^+). Part (e): simulated INS spectrum for a water molecule hydrogen-bonded to a bridging hydroxyl group. Part (f): difference spectrum between the experimental INS spectra reported in parts (c) and (b). Parts (g) (h) (i): Experimental INS spectra of water adsorbed at 35, 10.2 and 6.2 molecules per unit cell. Adapted by permission of the American Chemical Society (copyright 1996) from Ref.[219]

Authors were able to conclude that simulations of INS spectra based on ab initio MP2 calculations show that a water molecule is attached to an acid site via two hydrogen bonds. And that protonated species are not observed, so that in H-ZSM-5 the reaction (5) stops at the mid term.

3. Lewis acidity in zeolites investigated by probe molecules

Lewis acid centers (i.e. electron acceptor centers) in zeolites can be of three main types: (i) charge balancing extraframework cations,[204, 224-231] discussed in Section 3.1; (ii) extraframework aluminum species Al^{3+},[113, 204, 232-244] reviewed in Section 3.2; and (iii) heteroatoms substituted in framework T positions,[21, 22, 245-257] detailed in Section 3.3. Sections 3.1, 3.2 and 3.3 are devoted to discuss how IR spectroscopy is able to characterize charge balancing cations, extraframework aluminum species and heteroatom in zeolitic frameworks, respectively.

3.1. Charge balancing extraframework cations

3.1.1 Alkaline and alkaline-earth cations

CO molecule has been the most widely probe used to characterize cationic sites in zeolites. In case of adsorption on alkaline and alkaline-earth cations the interaction is of pure electrostatic origin as, the absence of metal *d*-electrons prevents the presence of σ- (M^{n+}←CO) and π- (M^{n+}→CO) components. The electric field created by the positive charge of the non-*d* cation, partially compensated by the first-shell negatively charged oxygen atoms, causes a polarization of the CO molecule which depends on the local electric field strength of the site, i.e. on the charge density of the cation mainly, modulated by the neighbor anions.[29, 226, 228-230, 258-260] The spectroscopic evidence of the polarization of the CO molecule is an upwards shift (blue-shift) of the stretching frequency of the C-O bond with respect to the $\tilde{\nu}_0$(CO) of the gas (2143 cm^{-1}),[261] owing to the increase of the force constant of the C-O bond, and the decrease of the bond length.[29, 262-266]

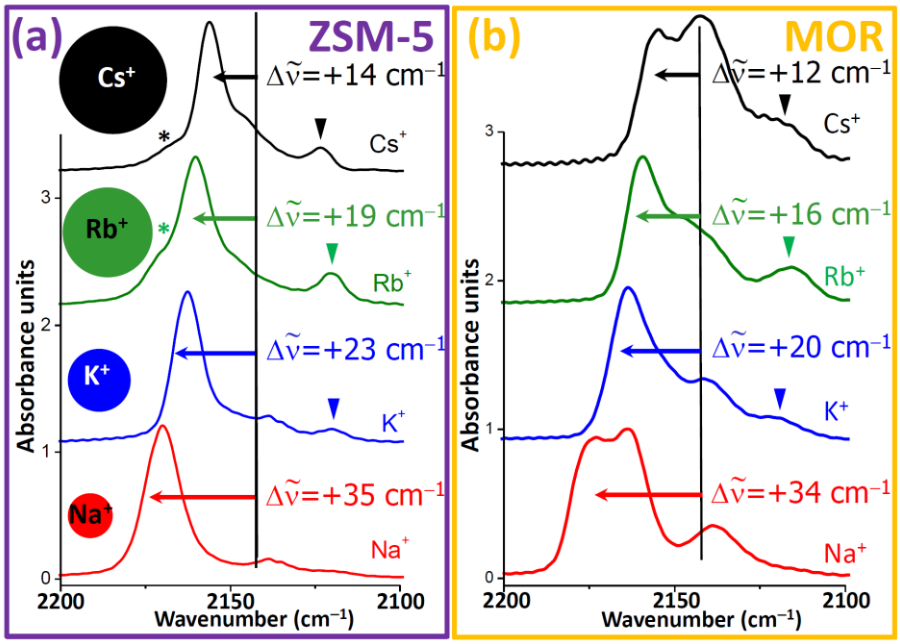

Figure 7. Part (a): IR spectra of CO adsorbed M^+-ZSM-5 at 77 K at an equilibrium pressure of ca. 102 Pa (M = Cs, Rb, K. Na). The main band is due to $M^+\cdots$CO adducts. The shoulder present in the left side of the main band of Rb and Cs (evidenced with *) is due to a small fraction of sodium still present after the ion-exchange procedure.[228] On the left side the different cation sizes are schematically represented. Part (b): as part (a) for M^+-MOR. All spectra are background subtracted. On both parts the vertical black line represents the C-O stretching frequency of the unperturbed molecule in the gas phase $\tilde{\nu}_0$(CO) = 2143 cm^{-1}, while the horizontal arrows gives a qualitative idea of the blue shift $\Delta\tilde{\nu}$ (CO) undergone by the CO molecule upon adsorption on the cationic sites. The broad band around 2138 cm^{-1} is due to liquid-like CO physisorbed in the cannels,[226, 227, 267, 268] while the band at lower wavenumbers, evidenced with a triangle in the Cs, Rb and K cases (not visible in the Na one) is due to minioritary to $M^+\cdots$OC adducts. Previously unpublished figure reporting spectra published data in Refs.[228, 229]

The close shell configuration of all alkali metal cations M^+ makes them ideal probing sites for a pure electrostatic interaction. In such a case, the perturbation of the C-O stretching frequency (Figure 7), $\Delta\tilde{\nu}$ (CO), is proportional to the local electric field strength ($\|\boldsymbol{E}\|$) according to the Stark effect:[230]

$$\Delta\tilde{\nu}\,(\mathrm{CO}) \propto \|\boldsymbol{E}\| = (1/4\pi\varepsilon_0)\,(q_{\mathrm{site}}/d^2_{\mathrm{M\text{-}CO}}) - \|\boldsymbol{E}_z\| \qquad (6)$$

where ε_0 is the vacuum permittivity ($\varepsilon_0 = 8.854 \times 10^{-12}$ C^2 m^{-2} N^{-1}) i.e. $1/4\pi\varepsilon_0 = 8.9876 \times 10^9$ N m^2 C^{-2}), q_{site} is the formal M^+ site charge (lower than $|e|$ because of the contribution of the negatively charged framework oxygen atoms, see inset in Figure 8a), $-\|\boldsymbol{E}_z\|$ is the contribution of the zeolitic environment and where $d_{\mathrm{M\text{-}CO}}$ is the distance between the cation nucleus and the CO baricenter ($d_{\mathrm{M\text{-}CO}} = R_{\mathrm{M}} + R_{\mathrm{CO}}$, being R_{M} the cationic radius[269] and R_{CO} the CO semi-axis along the C-O direction (R_{CO} = 2.1 Å),[270]) see inset in Figure 8a). This fact is clearly evident in the spectra reported in Figure 7, reporting the IR spectra collected at liquid nitrogen temperature on M-ZSM-5, part (a), and on M-MOR, part (b), (M = Cs, Rb, K and Na) where the $\Delta\tilde{\nu}$ (CO) of the main band follow the order Na > K > Rb > Cs. On a quantitative ground, a linear correlation between $\Delta\tilde{\nu}$ (CO) and $d^{-2}_{\mathrm{M\text{-}CO}}$ is clearly appreciable from the data reported as full symbols in Figure 8. Part (a) refers to the M-ZSM-5 and M-MOR spectra reported in Figure 7 while part (b) other zeolitic frameworks (ferrierite, β, and Y).

The model reported in Eq. (6) was derived by Lamberti et al.,[230] who used the experimental $\Delta\tilde{\nu}$ (CO) values measured by FTIR on Na^+-, K^+-, Rb^+- and Cs^+-exchanged ZSM-5 and MOR zeolites to determine, the local positive electric field strength at the cation site $\|\boldsymbol{E}\|$ (2-6 V nm^{-1}), the effective charge on the cationic site (q_{site} = +0.65-0.75 |e|) and the negative contribution from the negatively charged zeolitic framework $-\|\boldsymbol{E}_z\|$ (-4.2 and –4.7 V nm^{-1} ZSM-5 and MOR, respectively). From model (6), the slope of the line resulting from the best linear fit of the points obtained on the different cationic forms of a given zeolitic framework is directly proportional to q_{site}, i.e. on the average charge of the first shell oxygen atoms. This means that the slope of the lines reported in Figure 8 is an indirect measure of the basicity of the zeolitic framework (see Section 4). From the data reported in Figure 8 it emerges the following framework basicity scale: Y >> MOR ~ ZSM-5 ~ FER ~ β. Figure 8a also contains the data collected on Li-ZSM-5 and Li-MOR, where the local electric field is as high as 8.2 V nm^{-1}. Please note the remarkable values of the local electric field probed by CO, as 1 V nm^{-1} = 10^9 V m^{-1}. The existence of a simple electrostatic interaction was observed already in the late seventies by Hauge et al., who monitored the $\Delta\tilde{\nu}$ (CO) of carbon monoxide in interaction with different alkali-metal fluoride molecules isolated in cryogenic argon matrices.[271] They found that the positive $\Delta\tilde{\nu}$ (CO) was roughly increasing upon decreasing the cationic radius (R_{M}), a clear evidence that the $M^+\cdots$CO interaction is of pure electrostatic origin.

The simple electrostatic model here summarized[230] has successively been significantly improved by the more sophisticated *ab initio* approach, on naked cations[272] and on fragments mimicking the zeolite sites,[273] by Ferrari et al.. These two successive studies confirmed the electrostatic nature of the interaction. In this regard, also the theoretical works of Larin et al.[259, 260] are worth to be mentioned together with the successive and more refined works of Nachtigall at al.[274-281]

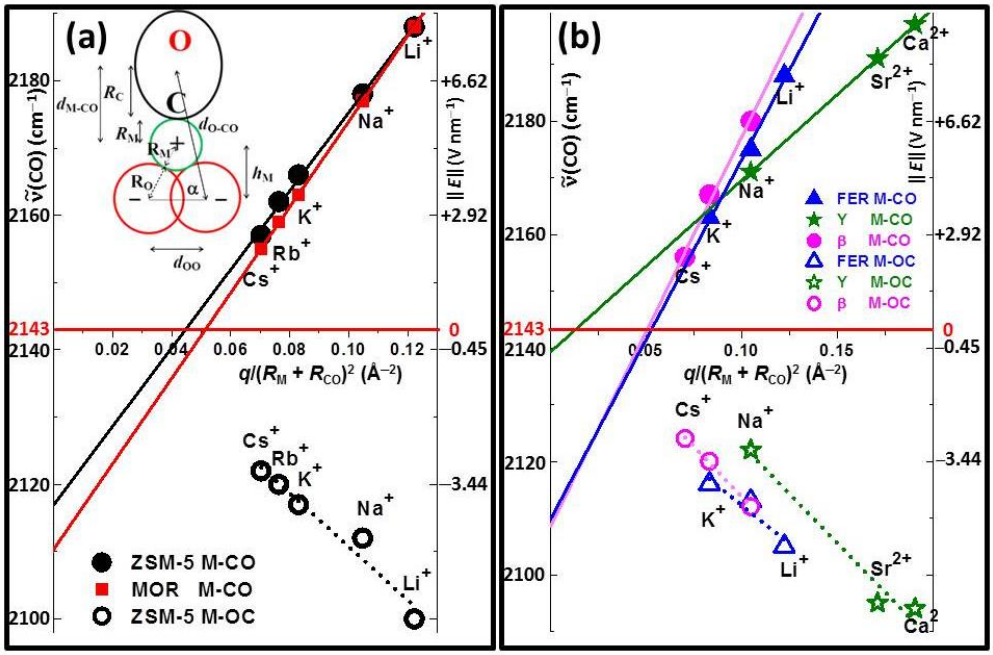

Figure 8. Part (a): Left ordinate axis: $\tilde{\nu}$ (CO) stretching frequency (left axis:) of the *vs.* $d^{-2}_{M\text{-}CO} = (R_M + R_{CO})^{-2}$ for alkali-metal exchanged ZSM-5 (black circles, corresponding to the spectra reported in Figure 7a) and mordenite (red squares, corresponding to the spectra reported in Figure 7b). Full symbols refer to $M^+\cdots CO$ adducts (blue shifted main IR band); open symbols refer to $M^+\cdots OC$ adducts (red shifted minor IR band). The abscissa axis has been located at $\tilde{\nu}(CO) = 2143$ cm^{-1}, corresponding to $\Delta\tilde{\nu}(CO) = 0$ cm^{-1} and $||\boldsymbol{E}|| = 0$ V nm^{-1}. Right axis evaluation of the local electric field strength probed by CO, from $\Delta\tilde{\nu}(CO)$ according to the Stark effect quantified by Pacchioni et al.[282] Dotted and dashed curves reports the best linear fits of the two datasets; corresponding interception with the ordinate axis ($R_M \rightarrow +\infty$ limit) provides the magnitude of the negative electric field E_z generated by the negatively charged zeolite cavities, see Eq. (6). The inset report a scheme the cation site geometry showing the relationships among the geometrical quantities used in Eq. (6). Part (b): as part (a) for ferrierite (blue triangles), Y (green stars) and β (pink circles) zeolites. Parts (a) and (b) have been plotted with different scales, so that a direct comparison between the line slopes of the two parts is not possible. The inset in part (a) has been adapted with permission from Ref.[230], copyright American Institute of Physics 1995. The remaining parts are previously unpublished graphical material summarizing data from Refs.[228, 229, 283-287]

Other minor spectroscopic features are present in the spectra reported in Figure 7. The broad band around 2138 cm^{-1}, just below the vertical black line of the unperturbed CO molecule the gas phase ($\tilde{\nu}_0(CO) = 2143$ cm^{-1}), is due to liquid-like CO molecules inside the zeolitic channels.[226, 227, 267, 268] while the band at lower wavenumbers observed in the Cs- Rb- and Na-forms of both ZSM-5 and MOR frameworks is due to a minority $M^+\cdots OC$ adducts[288] that will be discussed in deep detail below in Section 7.2.3 referred to variable temperature IR experiments. In particular see below Figure 32 and Table 9. This band is not observed at 77 K on Na-exchanged zeolites and is formed only at higher temperatures. Also for $M^+\cdots OC$ adducts the interaction is of electrostatic origin and is governed by Eq. (6), the only difference with respect to the dominant $M^+\cdots CO$ adducts is that, being the dipole of the CO molecule inverted, the Stark effect generated by the local electric field at the cationic site has the opposite effect and results in a weakening of the C-O bond with a consequent red-shift of the ν(CO) mode. Again, the entity of the perturbation (and so of the red-shift) is proportional to the local electric field, so that a linear correlation between $\Delta\tilde{\nu}$ (CO) and $(d_{M\text{-}CO})^{-2}$ is observed also for this family of bands, that has however a negative slope, compare continuous lines with dotted segments in Figure 8.

3.1.2. Transition metal cations: the copper case

Cation-exchanged zeolites with transition metal cations represent a large class of materials that played an important role in catalysis. Vibrational spectroscopies, in particular IR, have been very informative in determining the coordination and oxidation state of the extraframework cations. In the following we will use copper-exchanged zeolites as case study to discuss in detail the potentialities of IR spectroscopy, while the other relevant charge-balancing transition-metal cation are here just briefly mentioned: chromium,[289] manganese,[290-293] iron,[21, 249-251, 294-305] cobalt,[293, 306-313] nikel,[293, 314] zinc,[315-323] molybdenum,[324, 325] palladium,[326-331] silver,[53, 266, 332-339] iridium,[340] cadmium,[289] platinum,[341-343] and gold.[344-351] In the cases of tri- and tertra-valent cations (Fe, Co, Zn, and Mo) IR spectroscopy was determinant to discriminate between framework insertions (isomorphycally substituting T sites, see Subsection 3.3) and extraframework charge balancing cationic positions. In the cases of noble metals (Pd, Ag, Ir, Pt and Au) IR spectroscopy was of great help in discriminating between isolated charged couterions and clustered reduced nanoparticle and in following their evolution along different thermal, reductive, oxidative treatments. In the quoted works from the groups of Gates and Lamberti the IR characterization was complemented by a parallel EXAFS and XANES study. The remaining part of this subsection is devoted to Cu-exchanged zeolites. This choice has been dictated by the huge experimental and theoretical work done in the last decades on Cu-exchanged zeolites,[23, 29, 161, 162, 266, 352-365] mainly because of their use as efficient catalyst for NO_x selective catalytic reduction (SCR) by ammonia (NH_3-SCR),[364, 366-374] vide infra Subsection 9.1.3.

In this context, we want to stress that the choice of the appropriate probe molecule is a crucial point in FTIR spectroscopy. Different probe molecules may be able to reveal different aspects of the investigated surface, and often the combined use of markedly different probes is the key to reach a comprehensive understanding of the surface.[23, 29] In this section we will show how the combined use of CO, N_2, and NO probes to characterize Cu-exchanged and zeolites ZSM-5, MOR, β, Y, SSZ-13, has been largely informative.[161, 375-386] The use of a weakly interacting probe such as N_2 allows to minimize the perturbation induced by the probe and so to better discriminate among similar adsorption sites. The use of CO allows selectively towards Cu^+ sites, while NO can probe both Cu^+ and Cu^{2+} sites. Experiments performed at liquid nitrogen temperature allow to detect the surface sites characterized by a weak interaction with the probe (not visible in RT experiments). This is relevant for N_2 while a low-temperature experimental set-up is essential for NO that is reactive at RT and therefore does not act solely as a probe.[378, 385, 386]

In the presence of an acceptor of electron pairs, such as a transition metal cation possessing empty orbitals of suitable energy (and thus acting as Lewis acidic center) the C-end lone pair of CO is transferred to the metal cation giving rise to a σ-coordination ($M^{n+}\leftarrow$CO). In this case too, the interaction between CO and the metal cation causes the $\Delta\tilde{\nu}$ (CO) stretching frequency to shift towards a value higher than that of the gas, as was the case for the electrostatic interaction discussed in Section 3.2.1. It is generally accepted that the higher is the blue-shift, the stronger is the interaction, according to the Lewis acidic strength of the metal site.[29, 262-266, 387] Moreover, in the case of transition metal cations possessing partially filled *d* orbitals, a significant $M^{n+}\rightarrow$CO π-donation can occur from the orbitals of the *d*-block metal back to the orbitals of the CO molecule. The increase of the electronic density in the anti-bonding orbitals of the CO molecule causes the force constant of the C-O bond to decrease, the C-O bond length to increase and thus the $\Delta\tilde{\nu}$ (CO) to be red-shifted with respect that of the gas. The strength of the bond between CO and the *d*-block metal cations, and the $\Delta\tilde{\nu}_{CO}$ stretching frequency, are not expected in such a case to be simply correlated. In fact, as far as the strength of the carbonyl bond increases, as a consequence of the

synergistic effect of the σ- ($M^{n+}\leftarrow CO$) and π- ($M^{n+}\rightarrow CO$) components, the resulting $\Delta\tilde{\nu}$ (CO) is located in a spectral position which is a compromise of a blue- and a red-shifts,[29, 262-266, 337, 388-392]

Cu-exchanged zeolites are usually prepared through a liquid phase exchange from cupric salts, resulting in the introduction of divalent cations in the framework.[393] Since the late eighties they have been widely investigated because of their catalytic activity in the NO direct decomposition.[369, 393-400] Upon thermal activation cupric ions are reduced to cuprous species, resulting in Cu^+-zeolites.[363, 383, 384, 386, 401-403]

The CO probe has been used to testify the high coordinative unsaturation of the Cu^+ cations hosted in zeolites. Indeed, depending on CO equilibrium pressure (P_{CO}) and temperature, carbonyl complexes of high structural and spectroscopic quality have been formed on Cu^+ sites. At room temperature relatively stable adducts such as the mono- $[Cu(CO)]^+$ and dicarbonyl $[Cu(CO)_2]^+$ complexes are observed,[266, 375, 376, 378-386, 388, 404-406] (see Figure 9ab) which evolve to tricarbonyl $[Cu(CO)_3]^+$ species when the system is cooled down to liquid nitrogen temperature,[266, 376, 378-386, 404, 405] see Figure 9c. The occurrence of a $Cu^+\cdots(CO)\rightarrow Cu^+\cdots(CO)_2$ transformation has been proved using two-dimensional correlation spectroscopy (2D-COS)[266] and by Cu K-edge EXAFS spectroscopy.[407] Please note that 2D-COS is a mathematical method to analyze a series of spectra collected on a system subjected to a perturbation (such as a gradient in pressure or temperature). It is used to assess statistic relationships between the different spectroscopic features that are changing along the dynamic series, in order to extract valuable information that can be otherwise difficult to obtain.[408-417]

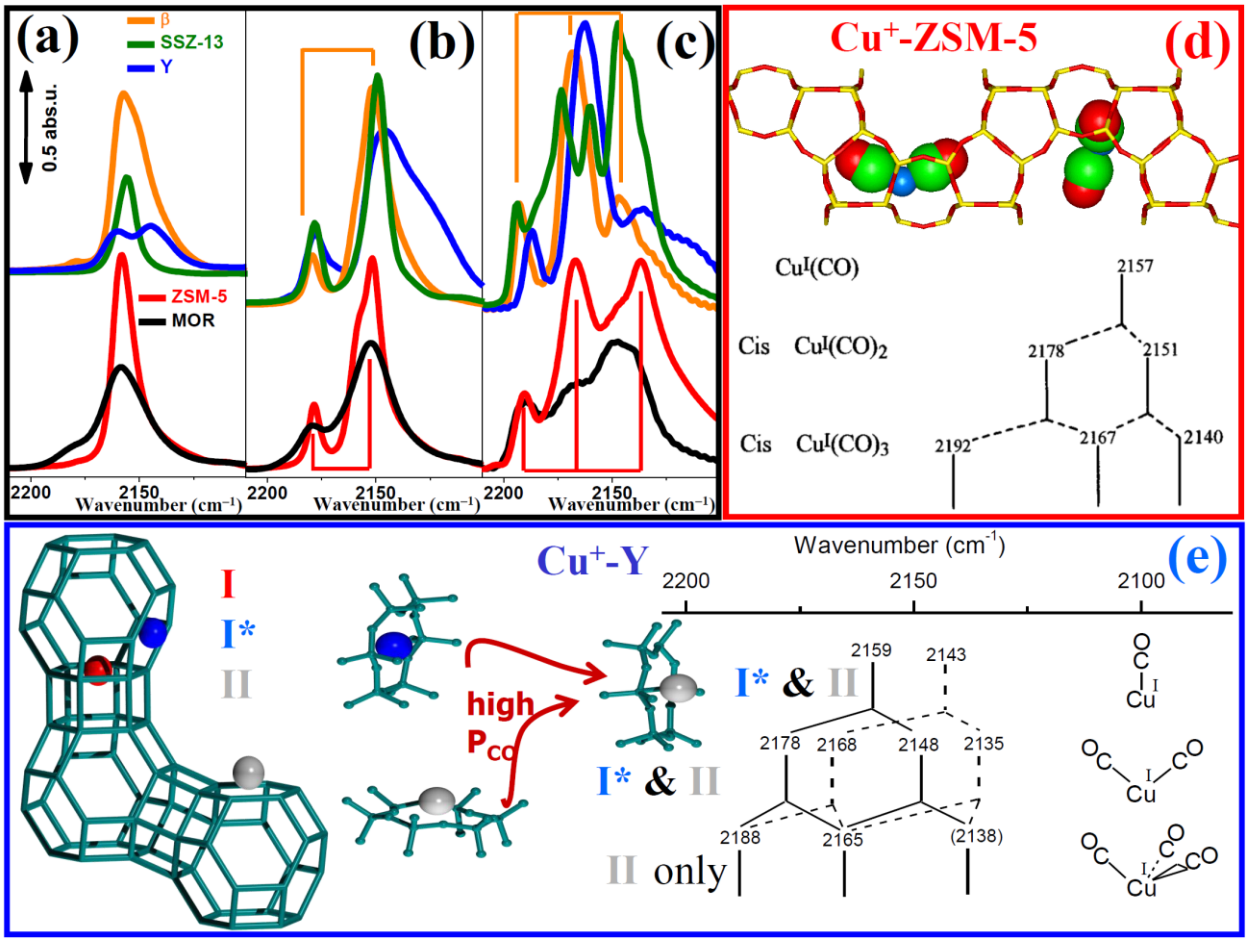

Figure 9. IR spectra of CO dosed, at liquid nitrogen temperature, on Cu^+-β (orange curves), H^+-Cu^+-SSZ-13 (green curves), Cu^+-Y (blue curves) Cu^+-ZSM-5 (red curves), and Cu^+-MOR (black curves), zeolites. Parts (a), (b) and (c) reports low, medium and high P_{CO} spectra, respectively, approximately corresponding to mono-, di- and tri-carbonyl complexes. Part (d): schematic representation of a fraction of the ZSM-5 framework with two equivalent Cu^+ sites forming a di-carbonyl complex (top, corresponding to the situation monitored by the red spectrum in part b) and evolution of the C-O stretching frequencies along the $Cu^+\cdots(CO) \rightarrow Cu^+\cdots(CO)_2 \rightarrow Cu^+\cdots(CO)_3$ driven by P_{CO} increase. Part (e): schematic representation of a fraction of the Y framework with three un-equivalent Cu^+ sites (**I**, **I*** and **II**, left) as determined by XRPD.[384] an of the P_{CO}-induced **I*** → **II** migration (center), and of the evolution of the C-O stretching frequencies along the $Cu^+\cdots(CO) \rightarrow Cu^+\cdots(CO)_2 \rightarrow Cu^+\cdots(CO)_3$ driven by P_{CO} increase. Site **I** is not accessible by CO. See Table 3 for the exact frequencies of mono-, di- and tri-carbonyls components. Previously unpublished figure reporting spectra published in Refs.[161, 378, 379, 384] (parts a-c) and adapting schemes published in Ref.[29, 407] (part d) and Refs.[29, 384] (part e).

IR spectroscopy of CO dosed at increasing P_{CO} on Cu^+-zeolites is reported in Figure 9a,b,c for β, SSZ-13, Y, ZSM-5, and mordenite hosting frameworks. At low P_{CO} (Figure 9a), a single band is observed for the monocarbonylic complex in ZSM-5, β SSZ-13 and mordenite zeolites. Conversely in Y zeolite two different $Cu^+\cdots CO$ adducts are observed characterized by $\tilde{\nu}$ (CO) = 2160 and 2144 cm^{-1}, which are formed on two different cationic sites, labeled as **II** and **II*** respectively (see Figure 9e).[384] This IR evidence is supported by Rietveld refinement of XRPD data collected at the ESRF synchrotron, where two different cationic sites have been determined in the supercage.[384] By increasing P_{CO} (Figure 9b), the formation of $Cu^+\cdots(CO)_2$ adducts is observed for all samples, as proved by the splitting of the monocarbonyl band into two bands due to the $\nu_{asym}(CO)_2$ and $\nu_{sym}(CO)_2$ modes of the complex.[161, 378, 379, 384, 404, 407] The fact that both bands are IR active indicates that the intrazeolitic $Cu^+\cdots(CO)_2$ adducts have C_{2v} symmetry (or lower), while the homogeneous counterparts are linear ($D_{\infty h}$).[418] A further increase of P_{CO} (Figure 9c) causes for ZSM-5, β and Y zeolites a nearly total $Cu^+\cdots(CO)_2 \rightarrow Cu^+\cdots(CO)_3$ transformation as indicated by the appearance of a new triplet of IR active bands. This means that we are dealing with a complex of symmetry rather smaller than C_{3v}, unlike homogeneous counterparts which form planar adducts of D_{3h} symmetry.[418] In Cu^+-SSZ-13 a significant fraction of $Cu^+\cdots(CO)_2$ complexes is still present.[161]

As far as mordenite is concerned, the presence of cations in the less accessible side pocket sites implies the co-presence of mono-, di- and tri-carbonyl adducts even at the higher P_{CO},[379] resulting in a broader and rather unresolved IR spectrum (black curve in Figure 9c). For Y zeolite, it is worth noticing that, in spite of the presence of two cationic sites in the supercage, the IR spectrum obtained at high P_{CO} indicates the presence of one only family of $Cu^+\cdots(CO)_3$ adducts. This relevant fact is explained in terms of the high solvatation power of the CO molecules, which are able to extract the Cu^+ cations in the more shielded position (site **II***) as proved by both EXAFS and XRPD,[384] see Figure 9e. The set of spectra collected on Cu^+-Y represents a clear example of adsorption-induced effects cation displacement. A similar solvatation effect, promoted by CO adsorption, has been observed for Cu^+-ZSM-5,[404, 407] for Ni^{2+}/SiO_2,[419, 420] and for Cr^{2+}/SiO_2.[421] The experiments reported in Figure 9abc indicates that ZSM-5 and β zeolites are more suitable for the formation of well defined, $Cu^+\cdots(CO)_n$ (n = 1, 2, 3) complexes, than Y or MOR zeolite and are exemplificative on how IR spectroscopy of adsorbed probe molecules is able to discriminate among different surface sites. The case of H^+-Cu^+-SSZ-13 (green curves in Figure 9c),[161] the situation is more complex because at high P_{CO} also $ZOH^+\cdots CO$ adducts are observed both on Brønsted sites (2173 cm^{-1}) and on external silanols (2160 cm^{-1}), together with the liquid-like component (2138 cm^{-1}).[226, 227, 267, 268]

The exact frequencies of mono-, di- and tri-carbonyls components reported formed inside Cu-exchanged zeolites reported in Figure 9a, and discussed here above, and inside other is given in Table 3.

Table 3 C-O, $\nu_a(CO)_m$ (m = 1, 2, 3), stretching frequencies of carbonyl adducts in Cu^+-zeolites and supported Cu_2O. When needed, label "a" (a = l, m, h) refers to low, medium and high frequency components of the adduct. For Cu_2O/SiO_2 and bulk Cu_2O samples, an interval of frequencies has been reported for $\nu(CO)$, $\nu_l(CO)_2$ and $\nu_h(CO)_2$ since the frequency position of the band was pressure dependent.[422] sh = shoulder; N. F. = not formed; N.D. = not detected (because experiments were performed at RT). New table, updating tables previously published in Refs.,[161, 423] and reporting data published in the references quoted in the last column.

Sample	$\tilde{\nu}$(CO) (cm^{-1})	$\tilde{\nu}_l(CO)_2$ (cm^{-1})	$\tilde{\nu}_h(CO)_2$ (cm^{-1})	$\tilde{\nu}_l(CO)_3$ (cm^{-1})	$\tilde{\nu}_m(CO)_3$ (cm^{-1})	$\tilde{\nu}_h(CO)_3$ (cm^{-1})	Reference
H-Cu-SSZ-13 [a]	2155	2150	2178	2134 (sh)	2169 (sh)	2194	[161]
Cu-ZSM-5 [a]	2158	2150	2178	2134 (sh)	2166 (sh)	2192	[161]
Cu-β [a]	2158, 2153	2152	2180	2134 (sh)	2168 (sh)	2193	[161]
Cu-ZSM-5 [b]	2157	2151	2178	2138	2167	2192	[378]
Cu-β [b]	2157	2152	2180	2146	2167	2193	[424]
Cu-SSZ-13	2154	2151	2178	N.D.	N.D.	N.D.	[425]
Cu-MOR [b]	2159	2152	2180	2146	2167	2193	[379]
Cu-FER [b]	2157	2149	2178	2135 (sh)	2170	2191	[426]
Cu-Y [b] Site II	2159	2148	2178	2138	2165	2188	[384]
Site II*	2143	2135	2168				
Na-Cu-ETS-10(B)	≅ 2155	≅ 2150	≅ 2180	≅ 2135	2162	2191	[423]
Cu^+-MCM-41	2159	2152	2180	2138	2171	2194	[427]
Cu_2O/SiO_2	2132-2127	2127-2120	2162-2154	N.F.	N.F.	N.F.	[422]
Cu_2O unsupported	2127-2121	2121-2113	2158-2145	N.F.	N.F.	N.F.	[422]

[a] Cu-zeolites prepared via standard liquid phase cation exchange with cupric salts and subjected to reduction by thermal activation in vacuo.

[b] Cu-zeolites prepared via stoichiometric gas-phase exchange with CuCl, resulting in the atomic ratio Cu/Al = 1.

N_2 molecule interacts with cuprous ions inside zeolites gives a ν(NN) band in the 2300-2290 cm^{-1} region,[377, 378, 428] *i.e.* significantly downward shifted with respect to the (Raman active) gas-phase value of 2321 cm^{-1}. The bathocromic shift could be explained in terms of chemical interaction involving molecular orbitals (MO) of the probe molecule and suitable d orbital of the metal cation.[29] For dinitrogen, the corresponding MOs are $3\sigma_g$ which acts as an electron donor, and the empty $1\pi_g$ which is the electron acceptor. Both the σ-donor and the π-acceptor interactions weaken the N≡N bond, thus explaining the observed bathocromic shift in the $Cu^+\cdots N_2$ adducts.[29] Interaction of N_2 with Cu^{2+} and with H^+ is much weaker.

The IR spectra of N_2 adsorbed on *vacuum* activated Cu-SSZ-13 is reported in Figure 10a. A predominant band, centered at 2293 cm^{-1}, is observed starting from low coverages. This component increases in intensity upon increasing coverage without shifting, while a second component centered around 2300 cm^{-1}, progressively develops. Both components are assigned to $Cu^+\cdots N_2$ stable complexes.[161, 377, 378, 428] The presence of two components in the spectrum of Cu-SSZ-13 implies the presence of two significantly different (in terms of the cation local environment) Cu^+ sites, supporting the conclusions raised by Dedecek *et al.*[429] and by Szanyi et al.[425, 430] As expected, involved Cu^+ sites behaves as isolated adsorbing sites for N_2, because of the invariance of the corresponding IR band upon pressure changes.

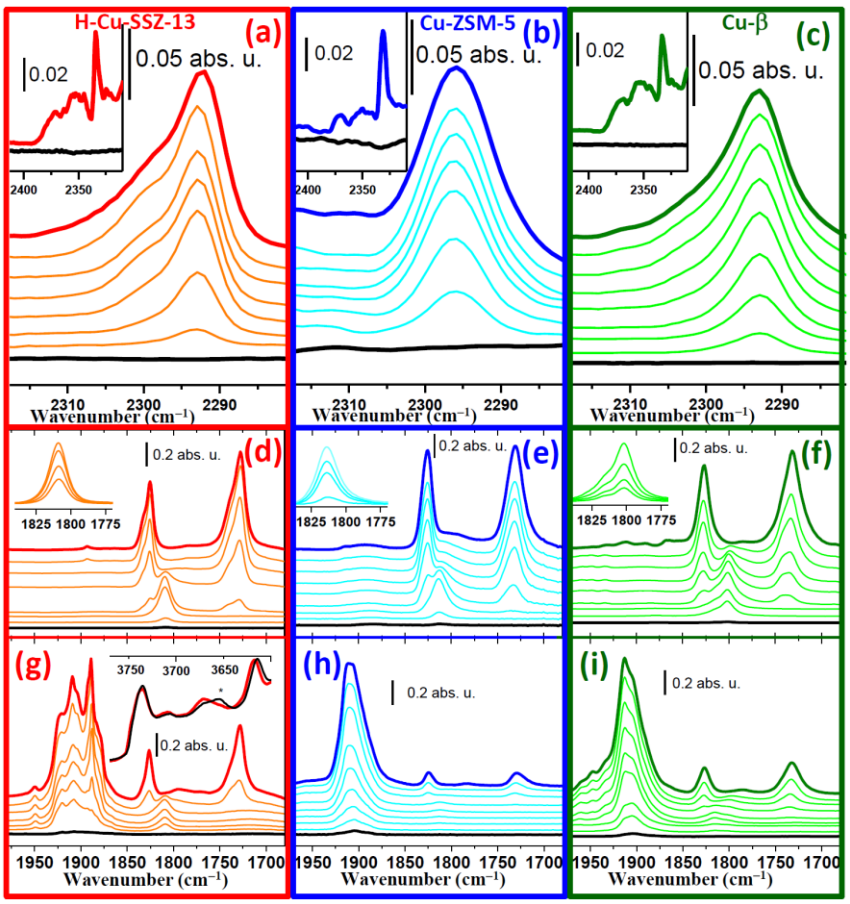

Figure 10. Part (a): IR spectra of N_2 dosed at liquid nitrogen temperature (~100 K) on *vacuum* activated H-Cu-SSZ-13 zeolite. The bold black spectrum is the background collected before N_2 dosage, orange spectra represent increasing equilibrium N_2 pressures, from 10^{-2} up to 5 Torr (bold red curve). The main part refers to the ν(N-N) stretching region of $Cu^+\cdots N_2$ adducts, while inset reports the region related to adducts formed on Brønsted sites ($ZOH^+\cdots N_2$) and extraframework species ($Al^{3+}\cdots N_2$). Part (b): as Part (a) for Cu-ZSM-5 zeolite. Part (c): as Part (a) for Cu-β zeolite. Part (d): IR spectra of NO dosed at liquid nitrogen temperature (~100 K) on *vacuum* activated H-Cu-SSZ-13 zeolite at increasing equilibrium pressure (from 7 *x* 10^{-2} to 7 *x* 10^{-1} Torr, red bold curve).The spectra in the main part show the $Cu^+\cdots NO \rightarrow Cu^+\cdots(NO)_2$ evolution; the inset reports low coverage spectra corresponding to $Cu^+\cdots$ NO complexes. Part (e): as Part (d) for Cu-ZSM-5 zeolite. Part (f): as Part (d) for Cu-β zeolite. Part (g) as part (a) for the O_2 activated zeolites showing $Cu^{2+}\cdots NO$ and residual $Cu^+\cdots(NO)_2$ adducts. Inset in part (g) reports the corresponding bands in the ν(OH) region, testifying the erosion of the 3650 cm^{-1} band (see *) upon formation of NO adducts with dehydrated $[Cu–OH]^+$ species. Previously unpublished figure adapting spectra published in Ref.[161]

A single and symmetric band centered at 2296 cm^{-1} is observed on *vacuum* activated Cu-ZSM-5 (Figure 10b). Also in this case the frequency of the band is coverage independent. This frequency is almost equivalent to that found on a Cu^+-ZSM-5 prepared by gas phase exchange with CuCl,[378] see also Table 4. This implies that, if present, different Cu^+ cationic sites in ZSM-5 are characterized by a very similar local environment that cannot be discriminated by N_2 adsorption. The spectra of N_2 adsorbed on Cu-β (Figure 10c) are dominated by a coverage independent component at 2293 cm^{-1}. A second component, less intense and resolved than in the Cu-SSZ-13 case, develops at the higher coverages around 2300 cm^{-1}.

The fact that the bathochromic shift of the main component is larger in Cu-SSZ-13 and Cu-β than in Cu-ZSM-5 implies that the dominant Cu^+ sites in SSZ-13 and β are able to perform a more efficient σ-donation and π-back-donation process with the MO of the N_2 molecule. This

could be associated to a larger space in the cation vicinity, and or to a more effective iconicity of the cation in case of Cu-SSZ-13 and Cu-β.[161]

In both Cu-SSZ-13 and Cu-β samples, the less abundant Cu^+ sites, responsible of the shoulder around 2300 cm^{-1}, interacts with N_2 in a similar way that the Cu^+ cations hosted in the MOR framework,[428] see Table 4. The absence of any adsorption around 2283 cm^{-1} testifies that no undesired Cu_2O extra-phase[423] is present in the three samples.

Table 4 $\tilde{\nu}$(NN), stretching frequencies of dinitrogen adducts formed on Cu^+ sites in Cu-exchanged zeolites and zeotypes, and on supported Cu_2O. sh = shoulder. New table, updating tables previously published in Refs.,[161, 423] and reporting data published in the references quoted in the last column.

Sample	$\tilde{\nu}$(NN) (cm^{-1})	Reference
Cu-SSZ-13 [a]	2293, 2300 (sh)	161
Cu-ZSM-5 [a]	2296	161
Cu-β [a]	2293, 2300 (sh)	161
Na-Cu-ETS-10 [a]	2281	423
Na-Cu-ETS-10 [a,c]	2285	423
Cu-MOR [a]	2299	428
Cu-ZSM-5 [b]	2295	378
Cu_2O/SiO_2	2283	423

[a] Cu-zeolites prepared via standard liquid phase cation exchange with cupric salts and subjected to reduction by thermal activation in vacuo.

[b] Cu-zeolites prepared via stoichiometric gas-phase exchange with CuCl, resulting in the atomic ratio Cu/Al = 1.

[c] Sample obtained after a second ion exchange process.[423]

We will conclude this section discussing the interaction of NO with both Cu^+ and Cu^{2+} sites in zeolites. The main difference between CO and NO is that the additional electron in NO occupies the π*-orbital. This causes a greater NO sensitivity to the electronic state of the cation during formation of the M···NO bond than for CO, since even slight alterations in electron density in this orbital noticeably change the frequency of the NO stretching vibration, $\tilde{\nu}$ (NO). Contextually, NO is traditionally used to probe the oxidation state of copper cations in zeolites, due to its ability to form nitrosyl stable adducts with both Cu^{2+} and Cu^+ cations.[29, 161, 375, 376, 378, 385, 386, 431]

At room temperature coordination of NO to the Cu^+ sites and formation of nitrosyls, is combined with decomposition reaction, with initial formation of N_2O and $Cu^{2+}(NO)(NO_2)$ adducts.[376, 378, 385] For this reason, in order to suppress NO decomposition, NO must be dosed at liquid nitrogen temperature in order to be used as a probe molecule on copper sites.

Figure 10 reports NO adsorption experiments on *vacuum* (parts d, e and f) and O_2 activated (parts g, h and i) samples. Starting from low NO coverages, *vacuum* activated Cu-SSZ-13 (Figure 10d) shows a band centered at 1810 cm^{-1} due to the interaction between NO and isolated Cu^+ leading to the formation of Cu^+···NO mononitrosyl complexes;[29, 161, 376, 378, 385, 386] First NO dosages on the sample are reported in the inset of the figure, and clearly show a symmetric and well defined band. By increasing NO coverage, the 1810 cm^{-1} band evolves in two main components at 1826 (with a shoulder at 1833 cm^{-1}) and 1728 cm^{-1} (with a shoulder at 1742 cm^{-1}) ascribed as symmetric and asymmetric stretching of $Cu^+(NO)_2$ dinitrosyl complexes, respectively.[29, 161, 376, 378, 385, 386] A single NO molecule is able to form similar Cu^+···NO adducts on two slightly different Cu^+ sites (already detected by N_2 adsorption, see Figure 10a) but, when a second NO molecule is inserted, the Cu^+···$(NO)_2$ complexes are able to probe a larger space around the Cu^+ sites and so to better discriminate among them. The absence of any significant band in the 1950-1870 cm^{-1} range, where

Cu^{2+}···(NO) complexes are expected, implies that nearly all cupric ions in accessible positions have been reduced to cuprous ions during the thermal activation. This is in line with what already observed for other Cu^{2+}-exchanged zeolitic systems.[383, 386] *Vacuum* activated Cu-ZSM-5 (Figure 10e) and Cu-β (Figure 10f) show approximately the same trend as Cu-SSZ-13, and corresponding mono- and dinitrosyl complexes frequencies are reported in Table 5. In Cu-ZSM-5 the shape of mononitrosyl band at 1813 cm^{-1} is significantly tailed on the low frequency side suggesting some site heterogeneity, while for Cu-β where two components are observed at 1802 cm^{-1} and 1815 cm^{-1} (shoulder). In both cases, we observe a total conversion of mono-nitrosyl into di-nitrosyl complexes upon increasing the P_{NO}. The exact frequencies of the observed nitrosyl complexes are reported in Table 5, together with literature data reported for comparison.

Despite the presence of oxygen during the thermal treatment, a not negligible amount of Cu^{+} is monitored on the O_2 activated samples (Figure 10 parts g, h and i). Both shape and position of Cu^{+}···$(NO)_n$ (n=1,2) complexes bands in O_2 activated sample are approximately equal to those observed on *vacuum* activated samples implying that the Cu^{+} location and distribution are not affected by the presence of oxygen during the thermal treatment. The complexity of the absorption features of Cu^{2+}(NO) adducts (particularly relevant for Cu-SSZ-13) clearly suggests the presence of different Cu^{2+} cationic sites.

Table 5 ν(N-O), stretching frequencies of mono- and di-nitrosyl adducts in Cu^{+} sites in zeolites and in supported Cu_2O. Table reproduced with permission from Ref.,[161] copyright Royal Society of Chemistry.

Sample (site)	$\tilde{\nu}$(NO) (cm^{-1})	$\tilde{\nu}_{sym}(NO)_2$ (cm^{-1})	$\tilde{\nu}_{asym}(NO)_2$ (cm^{-1})	Reference
Cu-SSZ-13 (A)	1809	1826	1728	161
Cu-SSZ-13 (B)	1809	1833 (sh)	1742 (sh)	161
Cu-SSZ-13[a]	1810, 1785 (sh)	N.O.	N.O.	425
Cu-ZSM-5	1813	1730	1825	161
Cu-ZSM-5 [b]	1812	1734	1827	378
Cu-β	1802, 1815 (sh)	1828	1734, 1743 (sh)	161
Cu-β [a]	1810	N.O.	N.O.	432
Cu-β [b]	1811	1730	1826	424
Cu-MOR [b](main channel)	1813	1730	1828	23
Cu-MOR [b] (side pocket)	1813	1785	1870	23
Cu-Y [b] (II)	1814	1728	1824	384
Cu-Y [b] site (II*)	1788	N.O.	N.O.	384
Cu_2O/SiO_2	1775	1709	1811	423

[a] Experiment performed at RT, thus under NO decomposition conditions.
[b] Cu-zeolites prepared via stoichiometric gas-phase exchange with CuCl, resulting in the atomic ratio Cu/Al = 1.

Table 6 ν(N-O) stretching frequencies of mono-nitrosyl adducts in Cu^{2+} sites in zeolites and in supported CuO. w = weak; m = medium; s = strong; sh = shoulder. Table reproduced with permission from Ref.,[161] copyright Royal Society of Chemistry.

Sample(site)	$\tilde{\nu}$(NO) (cm^{-1})	Reference
Cu-SSZ-13	1950^{w}, 1921^{m}, 1909^{m}, 1904^{m}, 1890^{s}	161
Cu-SSZ-13 [a] (I)	1920-1880	425
Cu-SSZ-13 [a] (II)	1948,1930	425
Cu-ZSM-5	1912, 1905, 1895 (sh)	161
Cu-ZSM-5 [a]	1921, 1912, 1906, 1895	433
Cu-ZSM-5 [b]	1890	378
Cu-β	1912, 1903, 1895 (sh)	161
Cu-β [a]	1896	432
Cu-MOR [a]	1960, 1938, 1921, 1909^{s}, 1895	433
Cu-Y [b] (II)	1955	384

Cu-Y [b] (II*)	1923	[384]
CuO	1865, 1855	[434]

[a] Experiment performed at RT, thus under NO decomposition conditions.
[b] Cu-zeolites prepared via stoichiometric gas-phase exchange with CuCl, resulting in an atomic ratio Cu/Al = 1.

This section was devoted to the use of probe molecule to characterize by IR Cu sites in Cu-exchanged zeolites. As detailed hereafter in Subsections 9.1.2, 9.1.3 and 9.3.1, IR played also a relevant role in determining the reactivity of Cu-zeolites.[162, 363, 364, 378, 385, 386, 435, 436]

3.1.3. Post-transition metal and lantanides cations

Besides the standard cation exchange procedure, directly leading post-transition metal cations into extraframework cationic positions inside the zeolite pores, several post-transition metals have been successfully introduced into the zeolitic framework via isomorphic substitution on tetrahedral Si sites, see Subsection 3.3. As was the case for iron,[21, 249-251, 294-305] severe thermal treatments can generate the migration of a fraction of post-transition metal from framework into extraframework positions, similar to those occupied via the conventional cation exchange. For both gallium,[437-445] and indium,[439, 440] IR spectroscopy has been the technique of choice to discriminate framework M(III) species, leading to Brønsted acidity, to extraframework M(III) species, leading to Lewis acidity and to monitor their relative evolution along different activation/reaction treatments. IR spectroscopy was also informative in the characterization of the cationic exchange with lead(II),[289] and of post-synthesis modification with tin precursors.[446, 447]

We finish this brief excursus on the periodic table of the elements by considering lanthanide cations. Their insertion as charge balancing cations inside zeolitic frameworks, besides some catalytic applications,[448-454] results in remarkable luminescence properties.[455-464] Again, the local environment, the accessibility and the reactivity of lanthanide charge balancing cation has been widely investigated by vibrational spectroscopies. Without entering into the details, we report some relevant bibliography for the different cations: lanthanum,[448-453, 465-472] cerium,[449, 454, 472-477] praseodymium,[449, 472] neodymium,[449, 465, 467, 468, 470, 472, 478] samarium,[449, 467, 468, 472, 475, 476, 479] europium,[449, 458, 472, 480-484] gadolinium,[449, 467, 468, 481, 484] terbium,[458, 481, 483, 485] dysprosium,[467, 468] holmium,[476] erbium,[486] and ytterbium.[465, 470, 487]

3.1.4. Correlation among different probes and different cationic sites

As clearly shown in Section 3.1.2, the use of different probes such as CO (Figure 9), N_2 (Figure 10a-c) and NO (Figure 10d-i) allows reaching a deep understanding on the nature and coordination of adsorbing sites.

We start this comparison considering H_2 and CO probes. For electrostatic-type interactions, when comparison is made with the spectroscopic data concerning adsorption on the same sites, it is found that the shifts of the $\Delta\tilde{\nu}$(CO) and $\Delta\tilde{\nu}$(HH) frequencies are linearly correlated and that the bathochromic shift of the ν(HH) mode is basically twice the hypsochromic shift of ν(HH):[29, 304]

$$\Delta\tilde{\nu}(\mathrm{CO}) \approx -2\,\Delta\tilde{\nu}(\mathrm{HH}) \qquad (7)$$

The validity of the empirical relationship (7) can be appreciated from the data reported in Figure 11a. This is mainly due to the fact that the $\Delta\tilde{\nu}$(HH) of the single H-H bond is more sensitive than the $\Delta\tilde{\nu}$(CO) of the triple C≡O bond to local effects (like structure, number of ligands in the coordination sphere, etc.) possibly influencing the physicochemical properties of the adsorbing centers.[18] The data reported in Figure 11a clearly show that the relationship is verified for a number

of systems including SiO_2, acidic and exchanged zeolites, oxides, etc. The region delimited by the grayed region corresponds to H_2 and CO interaction mechanisms prevalently dominated by electrostatic forces. It is on the contrary noteworthy the relevant scatter of the points corresponding to Cr^{2+} species grafted on Silica,[488] a system where covalent contributions play a certain role in both the Cr^{2+}/CO and Cr^{2+}/H_2 interaction.[489]

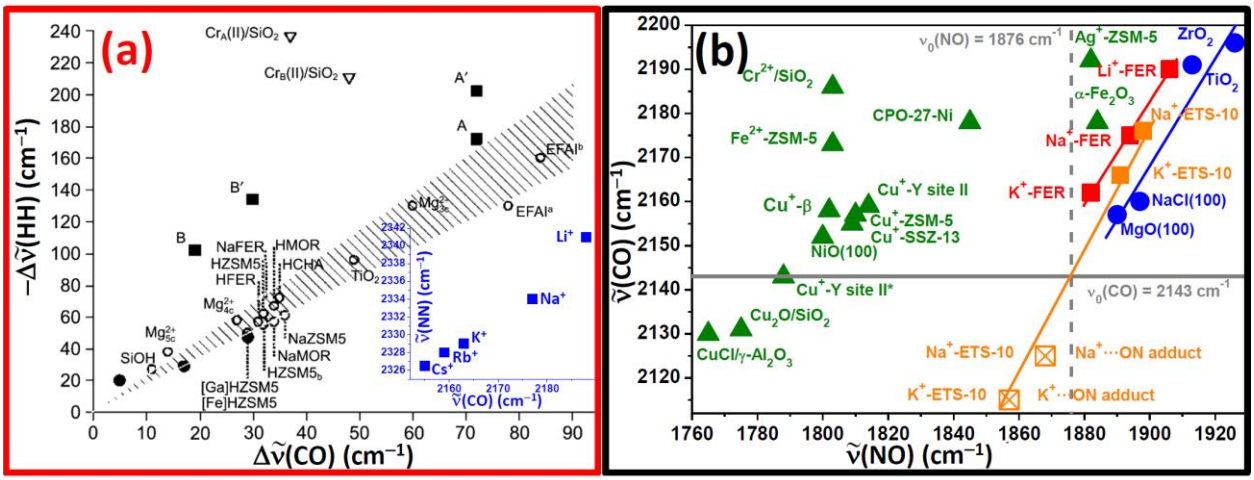

Figure 11. General comparison between different probes used to characterize the same sites. Part (a): Plot of the shifts $-\Delta\tilde{\nu}$(HH) for H_2 adsorbed on the Lewis or Brønsted acid sites of zeolitic and oxidic materials *vs.* the corresponding shifts observed for CO: $\Delta\tilde{\nu}$(CO). Circled data are taken from Zecchina *et al.*[18] Triangles refer to the Cr^{2+}/SiO_2 system (Phillips catalyst). [489] The data concerning the Fe-Sil Lewis acid sites are represented by flied squares ($\Delta\tilde{\nu}$(HH) values taken from Berlier *et al.*;[304] $\Delta\tilde{\nu}$(CO) values taken from Berlier *et al.*[249]: A and A' refer to Fe^{3+} centres, B and B' to Fe^{2+}); those concerning the Brønsted sites by filled circles. The region delimited by the grayed region corresponds to H_2 and CO interaction mechanisms prevalently dominated by electrostatic forces. Adapted with permission from Ref.,[249] copyright Elsevier 2006. The blue inset reports the correlation between $\tilde{\nu}$(NN) and $\tilde{\nu}$(CO) observed in alkali-metal exchanged MOR; previously unpublished graphic reporting data from Refs.[204, 229] Part (b): $\tilde{\nu}$(CO) vs. $\tilde{\nu}$ (NO) of monomeric CO and NO complexes formed on Li^+-, Na^+-, K^+-ferrierite (red squares); Na^+-, K^+-ETS-10 (orange squares); TiO_2, ZrO_2, NaCl and MgO (blue circles) and α-Fe_2O_3, NiO, Cu^+-ZSM-5, Ag^+-ZSM-5, CPO-27-Ni, CuO_2/SiO_2, CuCl/γ-Al_2O_3, and Cr^{2+}/SiO_2 and Fe^{2+}-ZSM-5 (green triangles). In the Cr^{2+}/SiO_2, Fe^{2+}-ZSM-5 and γ-CuCl/Al_2O_3 cases, where only dinitrosyl adducts have been observed, the baricenter frequency has been reported. For systems undergoing a coverage dependent shift the frequency of the $\theta\rightarrow 0$ limit has been reported. The data concerning MgO and NaCl are inferred from the published data by assuming that the $\tilde{\nu}$(NO) frequencies of the monomers are coinciding with the highest frequency mode of the adsorbed dimers. Adapted an implemented with permission from Ref.,[29] copyright Royal Society of Chemistry, 2010.

The comparison between CO and NO probes used on the same sites is reported in Figure 11b. Investigated systems are: Li^+-, Na^+- and K^+-FER,[490] Na^+- and K^+-ETS-10,[382] Cu^+-ZSM-5,[378, 385] Cu^+-Y,[384] Cu^+-β,[161] Cu^+-SSZ-13,[161] Ag^+-ZSM-5,[334, 335] and Fe^{2+}-ZSM-5,[249] and, for comparison, TiO_2,[491] ZrO_2,[491] MgO,[39] NiO,[492] α-Fe_2O_3,[21] Cu_2O/SiO_2,[423] NaCl,[493] CuCl/γ-Al_2O_3,[431] Cr^{2+}/SiO_2,[488] and CPO-27-Ni.[494, 495]

A linear dependence of has been obtained for the $\tilde{\nu}$ (CO) vs. $\tilde{\nu}$ (NO) data collected on alkali-metal exchanged ferrierite (red squares in Figure 11b), where the interaction is of pure electrostatic origin and where the anionic environment is exactly the same for the three investigated cations (see the discussion in Section 3.1.1). For the same reason, the same holds for the Na^+- and K^+-exchanged ETS-10 ($M^+\cdots$NO and $M^+\cdots$ON linkage isomers, full and open orange squares, respectively in Figure 11b) and for the $\tilde{\nu}$ (NN) vs. $\tilde{\nu}$ (CO) relation obtained on Li^+- Na^+- K^+- Rb^+- and Cs^+-exchanged mordenite,[204, 229] see inset in in Figure 11a.

An acceptable linear dependence between $\tilde{\nu}$(CO) and $\tilde{\nu}$(NO) has also been obtained for non-*d* and d^0 systems (blue circles in Figure 11b); the less accuracy of the linear fit is due to the different anionic environments of the investigated samples. Anyhow, it is evident that the overall red, orange and blue set of data are well correlated, proving that all these interactions are mainly dominated by the electrostatic interaction and that that the two molecules are responding in the same way to the Stark effect induced by the same cation sites.

When *d*-metals are considered (green triangles), any attempt to rationalize $\tilde{\nu}$(CO) vs. $\tilde{\nu}$(NO) fails, proving that the extent of the π-back donation is significantly different for the CO and NO probes.[29] It is in particular worth noticing that, with the only exceptions of Cu_2O/SiO_2 and γ-$CuCl/Al_2O_3$, for all the remaining investigated *d*-systems, the $\tilde{\nu}$(CO) is blue shifted, indicating a dominance of electrostatic and σ-donation interactions, while the $\tilde{\nu}$(NO) are significantly red shifted (only Ag^+-ZSM-5 and α-Fe_2O_3 making exception), revealing the major role played by the π-back donation interaction.

3.2. Extraframework Al^{3+} species

Extraframework Al^{3+} species are usually formed upon thermal activation of zeolites.[496-498] In some cases, like the ultra-stable Y zeolites (H-USY) one, the partial dealumination process is done on purpose activating the zeolite under steam conditions,[240, 499-501] see below section 5.1.

The absence of *d*-electron implies that the interaction of extraframework Al^{3+} species with probes is of electrostatic nature and the high charge/radius implies that we are dealing with strong Lewis centers. CO molecule probes extraframework Al^{3+} species forming $Al^{3+}\cdots CO$ adducts characterized by a very high $\tilde{\nu}$(CO) stretching frequency.[502, 503] Figure 12a shows the interaction, at liquid nitrogen temperature, of CO on H-MOR exhibiting a fraction of extraframework Al^{3+} species. The weak band at 2225 cm^{-1}, is due to $Al^{3+}\cdots CO$ adducts, the main band at 2173 cm^{-1} is due to the interaction with Brønsted sites ($ZOH^+\cdots CO$ adducts)[229] while the band developing at 2138 cm^{-1} at the high P_{CO} only is due to liquid-like CO formed inside the zeolite channels.[226, 227, 267, 268] The high polarizing power of extraframework aluminum makes $Al^{3+}\cdots CO$ adducts stable at 77 K upon prolonged outgassing down to 1.0×10^{-2} Torr.

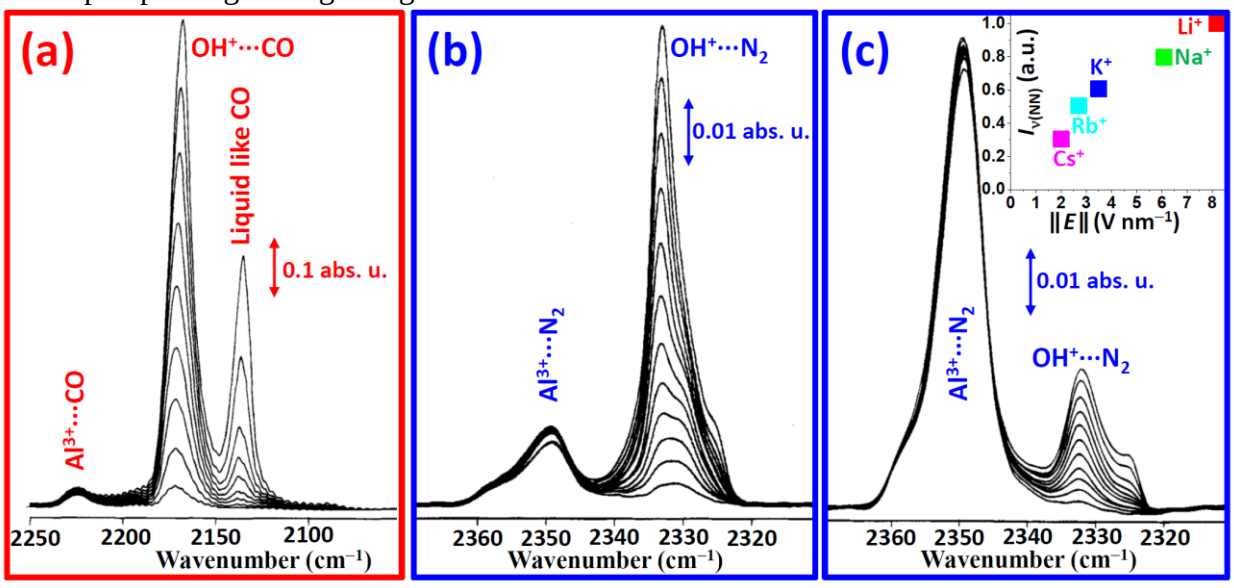

Figure 12. Part (a): IR spectra of CO adsorbed, at 77 K and increasing CO equilibrium pressures (from 1.0×10^{-2} to 20 Torr), on H-MOR previously activated in vacuo at 673 K. Part (b): IR spectra of N_2 adsorbed at 77 K and increasing

N_2 equilibrium pressures (from 1.0×10^{-2} to 50 Torr), on H- MOR previously activated in vacuo at 673 K. Part (c): as Part (b) for H-MOR previously activated in vacuo at 973 K. All spectra were background subtracted using as background the spectrum collected before probe dosage. The inset reports, for different alkali-metal exchanged mordenites the relative integrated area of the ν(NN) band versus the local electric field intensity $\|\boldsymbol{E}\|$ intensity generated at the cationic site and measured using CO probe, see Section 3.1.1 and Eq. (6). Part (a) has been adapted with permission from Ref.,[229] copyright American Chemical Society 1995; parts (b) and (c) have been adapted with permission from Ref.,[204] copyright American Chemical Society 1995.

Being IR-inactive in its unperturbed form, N_2 probe is more suitable than CO to detect small fraction highly polarizing Lewis centers like extraframework Al^{3+}.[204] This fact is clearly visible in Figure 12b, showing the IR spectra of the same H-MOR sample probed by N_2. The relative intensity of the $Al^{3+}\cdots N_2$ adducts around 2350 cm^{-1}, with respect to that of the more abundant $ZOH^+\cdots CO$ adducts (band at 2334 cm^{-1}), is much higher than in the case of the CO probe Figure 12a. Indeed, the molar absorption coefficient $\varepsilon(\tilde{\nu}_{NN})$ increases by increasing the local electric field strength generated at the adsorption site, see the empirical data reported in the inset of Figure 12c. Moreover, N_2 probe is able to distinguish between two families of extraframework Al^{3+} species (band at 2349 cm^{-1}, and shoulder around 2357 cm^{-1}) while an almost uniform and featureless band was observed using CO as probe (Figure 12a).

Increasing the activation temperature from 673 to 973 K the fraction of extraframework Al^{3+} species increases, to the detriment of the Brønsted sites, compare part (c) and (d) of Figure 12. Again, because of the much higher $\varepsilon(\tilde{\nu}_{NN})$, the integrated area of the band due to $Al^{3+}\cdots N_2$ adducts gain much more intensity than the intensity loss of the band due to $ZOH^+\cdots N_2$.

The insets of Figure 10a-c reports the ν(NN) region of strong Lewis sites for the vacuum activated Cu-SSZ13, Cu-ZSM-5 and Cu-β zeolites, respectively.[161] Also in these examples N_2 was more efficient than CO in the detection of a very small fraction of extra-framework Al^{3+} species thanks to the dramatic increase of the absorption coefficient of the ν(NN) mode when the molecule is adsorbed on an high polarizing Lewis center, able to cause a stronger induced dipole on the molecule.[161]

Pyridine (Py) probe has been widely used to probe the progressive migration of Al^{3+} species form framework into extraframework position along progressive dealumination processes.[496, 497, 504-511] Indeed, its ability to detect both Brønsted and Lewis acidic centers allows to follow the increase of the $Al^{3+}\cdots Py$ adducts around 2350 cm^{-1}, to the detriment of the $ZOH^+\cdots Py$ or $ZO\cdots PyH^+$ complexes (see Section 2.2).

3.3. Heteroatoms substituted in framework T positions

Microporous crystalline silica frameworks may incorporate hetero-atoms, of which aluminum is the most common, leading to zeolites, as largely discussed in this review. Other examples of isomorphous substitution of framework silicon atoms are iron, titanium, gallium, germanium, boron, vanadium and tin.[31, 159, 163, 247, 447, 512-531]

Framework trivalent heteroatoms (Al, Fe, Ga, In B) are responsible for Brønsted activity (see Section 2) of different strength.[156, 437, 441, 532, 533] In the as synthesized materials, heteroatoms occupy tetrahedral T-sites, substituting silicon; however, depending on the heteroatom valence state, on the presence/absence of charge balancing cations and on their nature (template cation, alkali-metal cation, NH_4^+, H^+ Brønsted site, etc…) the local environment of the heteroatom at framework position will exhibit different symmetry such as T_d, and distorted-T_d, etc…, see Figure 13. Moreover, depending on the heteroatom nature and on the zeolite framework structure, heteroatoms have different stability and the simple template burning process or more severe post-

synthesis treatments may cause the migration of a fraction of heteroatoms from framework into extra-framework positions. IR spectroscopy of adsorbed probes has been a powerful technique to discriminate between framework and extra-framework species[140, 249, 250, 298, 303, 438, 442, 443, 445]

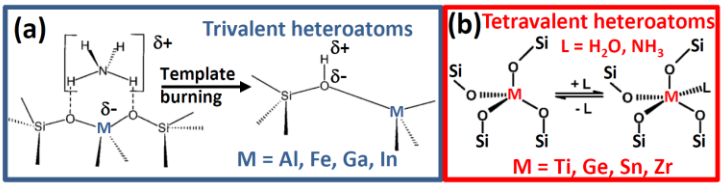

Figure 13. Possible local environments of heteroatoms hosted in zeolitic frameworks. Part (a): M^{3+} heteroatoms induces a negative charge to the framework and experience a T_d-like environment when the framework charge is balanced by NH_4 ion, by the template molecule or an alkali-metal cation (left part). When the charge is balanced by a proton (Brønsted site) then the symmetry is distorted (right part). Part (b): M^{4+} heteroatoms do not induce any charge to the framework, they doesn't imply the presence of a charge balancing cation or Brønsted site and in vacuum-activated materials experience a T_d-like environment. Upon interaction with ligands (L = H_2O or NH_3) M modifies its local environment coordinating one ligand molecule in its first coordination sphere. Adapted with permission from Ref.,[257] copyright Elsevier 2014.

Depending on the activation and reaction conditions, the local structure, the accessibility, the reactivity and the nuclearity of heteroatoms may significantly deviates from the initially synthesized ones. As the hetero-atoms location in zeolitic frameworks defines their unique catalytic behavior, it is very relevant to shed light on this matter. Among the most useful characterization technique to reach this goal we mention X-ray absorption spectroscopies (both XANES and EXAFS)[257] and vibrational spectroscopies (mainly IR and Raman).[22] In Subsection 3.3.1 we will show how the insertion in the MFI framework of Ti, Fe, B, Al, as well as Si vacancies, is affecting the zeolite skeleton vibrational modes, while in Subsection 3.3.2 we will show how resonant Raman spectroscopy was able to shed light on the Ti-peroxo complex formed in TS-1 upon contact with H_2O/H_2O_2 solution, that is the active site for several selective oxidation reactions relevant for fine chemistry.[247, 528]

3.3.1. Modification of the framework modes

Zeolites and Al-free silicalites are characterized by strong framework modes associated to the Si-O, or more generally to the T-O (T= Si or Al), stretching modes.[46, 224, 534-537] The fundamental framework modes fall in the 1300-750 cm^{-1} region. These modes can be described both using as building unit, the [SiO_4] tetrahedron that is interconnected with other units through the corner oxygen atoms or, even in a simpler way, by considering that the smallest building-block is represented by [Si–O–Si] group (with a Si–O–Si angle of 140–160 °). The vibrational features of the framework can be derived from those of these species.[46] The stretching modes of the [SiO_4] unit are the asymmetric $\nu[SiO_4]_{asym}$ modes (triply degenerated in the perfect T_d symmetry), observed in the range 1300-1000 cm^{-1} and the total-symmetric $\nu[SiO_4]_{sym}$ observed in the 850-750 cm^{-1} range. The first one is strongly IR active and the second one weakly IR active, while in Raman it is observed the opposite, see Figure 14a, bottom curves. The spectra region in the 1000-850 cm^{-1} window is known as the relative-transparency window of zeolites, where it is possible to measure the perturbation induced to the [SiO_4] by: (i) isomprphous heteroatom insertion;[22, 45, 46, 156, 245, 246, 532, 536-545] (ii) extraframework cations strongly interacting with the framework;[381, 404, 436] and (iii) even Si vacancies generating internal silanol nests.[168, 169, 539]

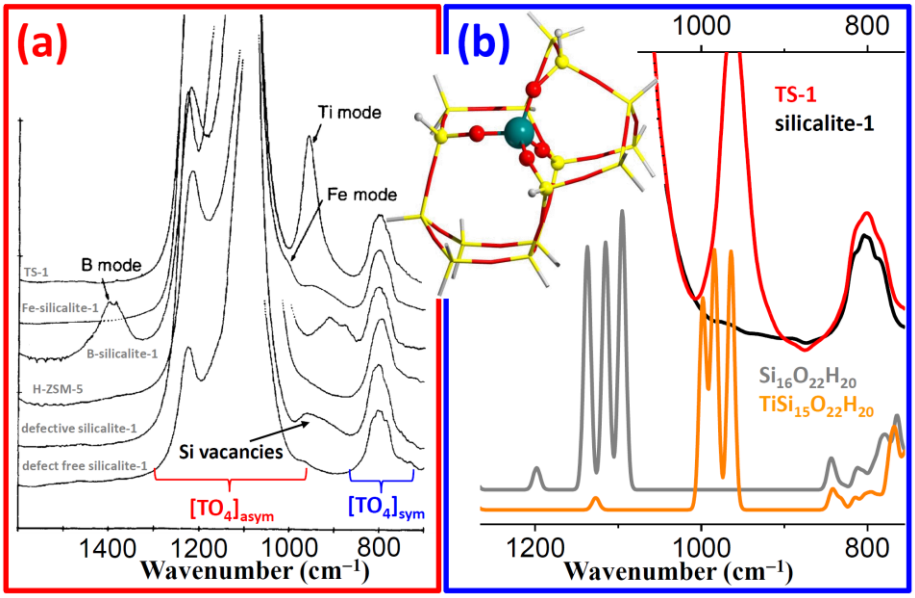

Figure 14. Part (a): diffuse reflectance IR spectra, in the framework skeleton stretching region, of pure and substituted silicalites-1 (diluted in KBr) activated at room temperature. From bottom to top: defect-free silicalite-1; defective silicalite-1 (with a high concentration of Si vacancies); H-ZSM-5 (Al-silicalite-1); B-silicalite-1; Fe-silicalite-1; Ti silicalite-1 (TS-1). Part (b): effect on the vibrational properties of diluted Ti insertion in of MFI framework; comparison between experimental (dehydrated TS-1, red curve and defect free silicalite-1, black curve) and computational ($TiSi_{15}O_{22}H_{20}$ and $Si_{16}O_{22}H_{20}$ clusters) approaches. The inset shows the cluster, extracted from the MFi framework, and used in the DFT calculations Si (yellow), Ti (olive), O (red), H (hydrogen). Part (a) has been adapted with permission from Ref.,[539] copyright Royal Society of Chemical 1992; part (b) has been adapted with permission from Ref.,[536] copyright American Chemical Society 2002.

Insertion of heteroatoms affects the vibrational spectra of the zeolites mostly in the framework mode region, even if some changes are also expected in the OH stretching region due to a change in the acidity strength, expected when a Si species has been replaced by another elements, such as a Fe(III) or a Ti(IV) sites. Among these vibrations it is expected that the presence of heteroatoms in substitutional position such as B(III), Fe(III) or Ti(IV) cause the appearance of new IR and Raman bands that are considered diagnostic of the presence of these guest atoms in the framework and are used to monitor the abundance of these species, as their intensity is proportional to the concentration of the heteroatoms. Isomorphous insertion heteroatoms results in the appearance of a band around 960 cm^{-1}, for Ti(IV), 1010 cm^{-1} for Fe(III) two components around 1380 and 920-890 cm^{-1}, see Figure 14a, top curves.[539] A broad band, covering almost the whole transparency window (990-920 cm^{-1},), is observed on defective silicalite-1.

In this regard, the computational DFT study, performed with the ONIOM scheme, of Damin et al.[536, 537] is very explicative, see Figure 14b. Extracting from the MFI framework a cluster with 16 T-centers ($Si_{16}O_{22}H_{20}$) and optimizing its structure at the DFT level of theory, authors were able to reproduce the spectrum of the fully siliceous silicalite-1 material, compare the theoretical spectrum (gray curve) with the experimental one (black curve). Substituting in the cluster the central Si atom by Ti, Damin et al.[536, 537] obtained the ($TiSi_{15}O_{22}H_{20}$ cluster, see inset in Figure 14b), which vibrational spectrum (orange curve) is able to reproduce the Ti-specific band at 960 cm^{-1} observed in Ti-silicalite-1 (TS-1, red spectrum in Figure 14b).[22, 46, 245, 246, 536-539, 544, 545]

In case of Raman spectroscopy, a further instrument to monitor the presence into the zeolitic lattice, even of a very low amount of heteroatoms, comes to the possibility to exploit Resonance effects.[45, 46] Figure 15b report a series of Raman spectra collected on the same TS-1

material with different excitation lines. For sake of comparison, part (a) of the figure reports the UV-Vis DRS spectrum of dehydrated TS-1. The band at 208 nm (48000 cm^{-1}) is the ligand to metal charge transfer (LMCT) which occurs from the four nearly equivalent oxygen atoms to the Ti(IV) centre in the quasi-tetrahedral [TiO_4] unit, leading to the symmetric expansion of the tetrahedral unit.[46] In the same figure, also the four laser lines are indicated with arrows. It is evident that by progressively increasing the energy of the exciting source we enter into the Ti-specific LMCT band and thus we expect to observe a strong enhancement of the Ti-specific vibrational modes that fulfil the resonance Raman selection rules. In particular we expect resonance, when Raman spectroscopy is performed upon using a wavelength close to an electronic adsorption of the sample most likely associated to a LMCT transition. This condition guarantees a high transfer of energy to the sample. If the electronic absorption is due to a localized centre, such as a transition from the ligand to the metal atom, the excitation is also partially localized and the vibrational features of the immediate vicinity of the absorbing atom can be enhanced by several orders of magnitude, if they meet the appropriate enhancement selection rules. Two types of vibrations are enhanced: (a) totally symmetric vibrations with respect to the absorbing centre, and (b) vibrations along modes which cause the same molecular deformation induced by the electronic excitation.[46] Figure 15b shows the Raman spectra collected on the dehydrated TS-1 using the four different lasers. Beside the typical modes of the siliceous MFI framework at 800 and 370 cm^{-1}, two Ti-specific bands at 960 and 1125 cm^{-1} are observed. It is evident that only the latter mode is enhanced by tuning the exciting laser source within the Ti-specific LMCT band.[46, 48, 546] The ratio between the intensities of the two Ti-specific modes increases progressively by moving from the near-IR to the far-UV source: specifically $I(1125)/I(960)$ = 0.25, 0.48, 0.65 and 12.50 using the 1064, 442, 325 and 244 nm lasers, respectively (Figure 15b). Similar enhancements have been observed in the Raman studies of Ti-STT[545] and Ti-CHA[544] frameworks.

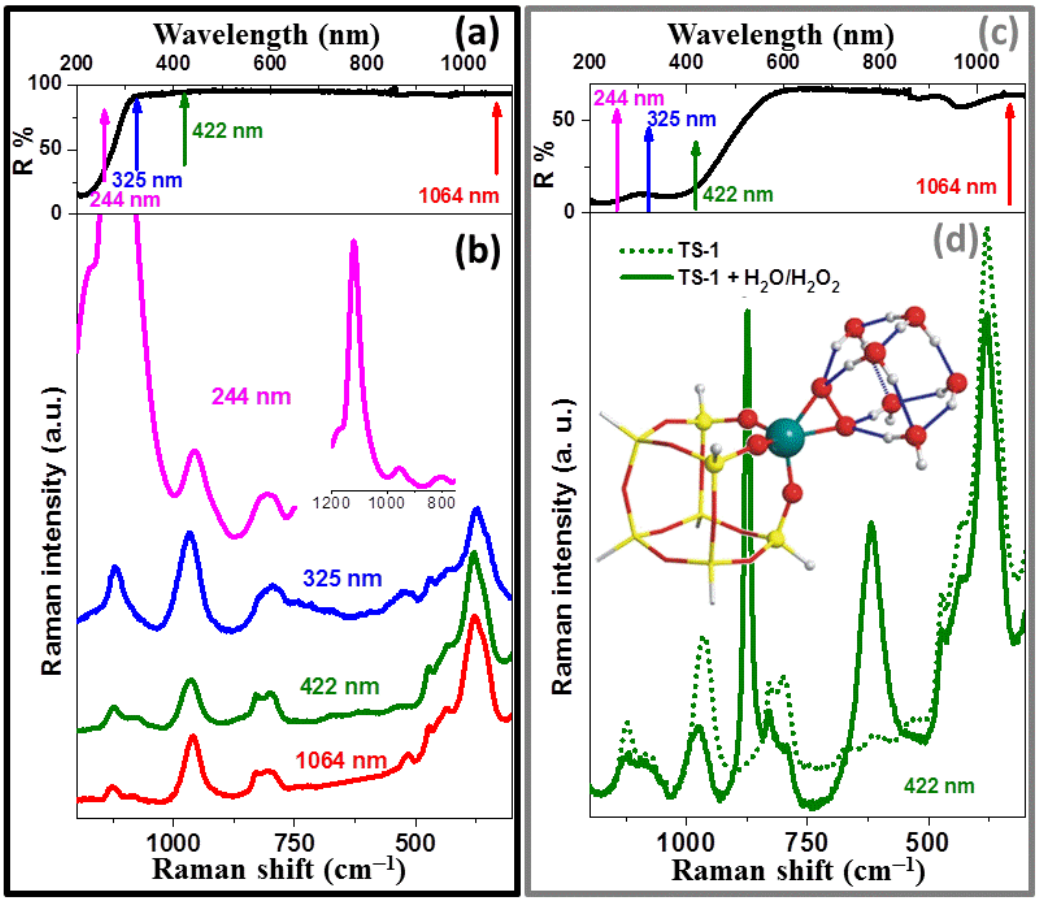

Figure 15. Part (a): UV-Vis DRS spectra of dehydrated TS-1 catalyst reporting the typical 208 nm (48.000 cm^{-1}) LMCT band; also reported are the four excitation laser lines used in this Raman study: Near-IR (red), visible (green), near-UV (blue) and far-UV (violet). Part (b): Raman spectra of dehydrated TS-1 obtained with four different lasers emitting at λ = 1064, 422, 325 and 244 nm (red, green, blue and violet lines respectively). Raman spectra have been vertically shifted for clarity. Although the intensity of each spectrum depends upon different factors, the evolution of the *I*(1125)/*I*(960) ratio by changing the laser source is remarkable. The inset reports the Raman spectrum collected with the 244 nm laser in its full scale, in order to appreciate the intensity of the 1125 cm^{-1} enhanced mode. Part (c): UV-Vis DRS spectra of TS-1 catalyst in contact with the H_2O_2/H_2O solution reporting the typical 385 nm (26.000 cm^{-1}) LMCT band of the Ti-peroxo complex; also reported are the four excitation laser lines used in this Raman study: Near-IR (red), visible (green), near-UV (blue) and far-UV (violet). Part (d): Raman spectra, collected with the 442 nm laser, of TS-1 before and after interaction with H_2O_2/H_2O solution (doted and full line respectively). The inset reports the optimized anhydrous [$^{=}O_2$-Ti$(OSi)_3$ + 5 H_2O + H_3O^+] cluster adopted for the calculation (B3-LYP/6-311+G(d,p) level). The sticks and balls vs. the sticks notation discriminates the model zone (treated at high level) from the complementary part of the cluster treated at low level only. Colour coded: green Ti; red O; yellow Si; white H; blue lines represents H-bonds. The main parts have been adapted with permission from Ref.[48], copyright Royal Society of Chemical 2003; The inset in part (d) has been reproduced with permission from Ref.,[22] copyright Royal Society of Chemical 2007.

In the case of Ti-Silicalite, where the Ti–O and Si–O bonds have different polarity and a different force constant, the ν_{asym}(X–O–Si) mode can be considered as a ν(Si–O) mode perturbed by an adjacent Ti_4C centre. Moreover, the total-symmetric $\nu[SiO_4]_{sym}$ mode, where the four (Si–O) bonds expand and contract in phase (and the Ti–O distances simultaneously contract and expand in phase, should be IR inactive and only weakly Raman active. Indeed, a peak at 1125 cm^{-1} is present in the Raman spectrum (Figure 15b). This peak is not observed with silicalite-1, as

expected. DFT calculations[46] have shown that the 1125 cm^{-1} Raman peak is associated with the expansion and contraction of the coordination sphere constituted by the four equivalent oxygen atoms surrounding the Ti center is further confirmed by the Raman resonance obtained using a 244 nm excitation line, i.e. a frequency where the characteristic oxygen to titanium charge transfer absorption of tetrahedral Ti in Ti-Silicalite occurs. In fact the peak at 1125 cm^{-1} is enhanced by a factor between 10^1 and 10^2, as expected for a resonance enhanced mode where the UV excitation causes the simultaneous and symmetric elongation of *all* the four Ti-O distances. The remaining three modes (non-symmetric $\nu[SiO_4]_{asym}$ modes) are responsible for the 960 cm^{-1} band (see orange spectrum in Figure 14b) which is the fingerprint IR-band of Ti-silicalite (red spectrum in Figure 14b). From the point of view of the [Si-O-Ti] groups these modes have mixed ν_{sym} and ν_{asym} character. It is evident that these considerations are highly qualitative: a better description could be given on the basis of the stretching vibrations of the cluster shown in the inset of Figure 15b or on the basis of the analysis of the elementary cell modes.

Following these considerations, the insertion of a lighter atom in the structure, like for instance B, would be associated with a ν(B-O-Si) mode falling at frequencies higher than those typical of silicalite and M-ZSM-5 (M = H, Na). Indeed, the spectrum of H-B-Silicalite shows a strong peak at 1380 cm^{-1}, which confirm this simple model (Figure 14a).[539] However, since it disappears upon dosing with NH_3 (i.e. upon formation of NH_4^+), it has been assigned to a local mode of the planar $[BO_3]$ structure, which is transformed into the tetrahedral structure upon NH_3 contact. From this result it is inferred that the nasym of genuine ν(B–O–Si) groups of regular framework B falls at frequencies not substantially different from those of (Al–O–Si) and (Si–O–Si) units. Vibrational, B K-edge XANES and DFT studies on B-CHA have successively confirmed this interpretation.[156, 532, 533]

3.3.2. Reactivity of Ti centers in TS-1

TS-1 is an industrial catalyst used for several partial selective oxidation reactions using H_2O_2 as oxidizing agent.[247, 547-550] Due to the presence of H_2O in the reaction medium (which precludes an extended use of IR spectroscopy) the vibrational features of the active Ti-peroxo complex have been clearly observed only in 2002 (i.e. more than 20 years after the catalyst patent) with a resonant Raman study.[47]

A previous Raman study from the same group[551], exploiting a 1064 nm exciting source, was only able to measure the O-O stretching of peroxo complexes formed on Ti sites upon contacting TS-1 with $H_2O_2/NH_3/H_2O$ (840 cm^{-1}) and $H_2O_2/NaOH/H_2O$ (843 cm^{-1}) basic solutions, Note that the O-O stretching frequency of the H_2O_2 molecules in aqueous solution occurs at 875 cm^{-1}. The reason of the partial success is probably due to the fact that, in basic solutions, the peroxo species are more stable and hence they are not readily destroyed by the laser beam. The same experiment on H_2O_2/H_2O solution was not successful because of the labile nature of the complex. On this basis it becomes clear thus that the only route that can be followed to improve the quality of the Raman spectra is to operate in resonance conditions.

Of course, as the peroxo species are absorbing in the visible, an exciting source in the same spectral region must be used, because in this way the vibration associated to the Ti-peroxo species can undergo a Raman enhancement phenomenon, if the selection rules are fulfilled. Among the four laser lines available, the most suitable one to stimulate the resonance enhanced response is the 442 nm (22625 cm^{-1}) source which, lying on the low energy tail of the LMCT band around 385 nm typical of TS-1/H_2O_2/H_2O system (see Figure 15c). Figure 15d reports the Raman spectra, collected with the 442 nm laser, of TS-1 before and after interaction with H_2O_2/H_2O solution (dashed and full line respectively). Interaction with H_2O_2 causes: (i) a decrease in intensity and the

blue shift of the 960 cm^{-1} mode, now at 976 cm^{-1}, (ii) the quenching of the 1125 cm^{-1} mode, due to a rupture of the T_d-like symmetry, see section 3.3.1; (iii) the appearance of the strong and sharp (O-O) stretching mode at 875 cm^{-1}, due to H_2O_2/H_2O solution physisorbed into the zeolite channels, and (iv) the appearance of a strong and complex new feature centered at 618 cm^{-1}. Features (i-iii) are also observed when the same experiment is performed with a 1064 nm laser source.[551] Conversely the 618 cm^{-1} was not observed neither on the TS-1/H_2O_2/H_2O system using a 1064 nm source nor on the Ti-free silicalite-1 molecular sieve upon interaction with H_2O_2/H_2O solution with 442 nm exciting source, and was so ascribed to a Raman enhanced vibration mode of the Ti-peroxo complex.[47, 48]

The similarity between the spectroscopic features, both UV-Vis and Raman, of $(NH_4^+)_3(TiF_5O_2)^{3-}$ and TS-1/H_2O_2/H_2O systems, allowed Bordiga et al.[47, 48] to conclude definitively that the species responsible for the band at 26000 cm^{-1} of the TS-1/H_2O_2/H_2O system is a "side on" Ti-peroxo species characterized by a Raman mode at 618 cm^{-1} which is resonance enhanced upon using by an exciting laser line falling in the LMCT transition. This vibrational assignment was successively supported by EXAFS[552, 553] and DFT[22] data.

4. Basicity in zeolites

The basic properties of zeolites have been generally much less studied than their acidic properties: an extended bibliographic search on zeolites basicity typically yields ten times less entries than an equivalent query bearing on acidity. This might partly reflects the fact that industrial heterogeneous catalytic processes using basic or amphoteric catalysts are much less developed than acid-catalyzed processes, and that to the best of our knowledge, none of them uses basic zeolites.[554-556] Further, even though basic zeolites are largely used in other relevant industrial processes such as drying, separation or ion exchange,[557, 558] fundamental studies specifically dealing with the characterization of the basicity of these materials are scarce. As will be seen in more details below, this reflects the fundamental difficulty in specifically probing zeolite basic sites (usually framework oxygen atoms) without the involvement of neighboring acidic centers (usually metal cations), while the symmetric situation (probing Lewis acidic centers while strongly limiting the interactions of the probe with framework oxygen atoms) is usually easier to realize (see Section 3 above). While challenging, the characterization of basic properties of zeolites is worthwhile to carry out, allowing establishing structure-activity or structure-selectivity relationships for current (acid-)base catalyzed reactions or separation processes, or for emerging applications, such as the development of processes based on biomass for the production of fuels and chemicals which often require basic functionalities. A number of comprehensive reviews on the structure and properties of basic zeolites,[555, 559-561] or on the characterization of surface basic properties by IR spectroscopy,[4, 562] have been published. In the following, generalities on surface basicity of zeolites and its characterization by probe molecules monitored by IR spectroscopy will be given. Then, this overview will focus on recent advances made in the characterization of zeolite basic centers by IR spectroscopy. Examples of recent infrared *operando* studies carried out on basic zeolites will be described in Section 9, below.

4.1 Basicity: general definition and applicability to zeolite basic centers

While many definitions of basicity have been proposed,[563] only two of them are commonly used in surface chemistry, namely the Brønsted-Lowry definition, stating that a base B^-, hosted in zeolite Z, accepts a proton from an acid HA :

$$ZB^- + HA \rightarrow ZB\text{-}H + A^- \quad (8)$$

and the Lewis definition, stating that a base ZB: donates a lone pair to the acid A, resulting in the formation of the adduct ZB:A :

$$ZB: + A \rightarrow ZB:A \quad (9)$$

It is worth noticing that in this section the situation is reversed with respect to that faced in Section 2 where we reported on the characterization of Brønsted acidity in zeolites: here the base is on the solid ZB and the acid HA is a molecule from the gas or liquid phase, in Section 2, the base B was in the gas phase and the acid was on the internal surfaces of the solid ZH, see Eq. (1).

Any acid compound, or acid function in a complex compound, or acidic center on a surface can generally be classified as Lewis or Brønsted without ambiguity or reference to a given base. For instance, as detailed in the preceding sections, zeolite extra framework cations are Lewis acid centers, while bridged OH groups are Brønsted acid sites. For basic centers, however, no such an a priori classification can be made in so far as lone electron pair donors (Lewis bases) are also proton acceptors. With this respect, the class of a basic center, Lewis or Brønsted, is essentially context-dependent and given by the class of the acid interacting with it, be it a probe molecule used to characterize the basicity, a reactant involved in a base-catalyzed reaction, or an adsorbate to trap or to separate from a mixture. Therefore, distinguishing between surface Lewis and Brønsted bases is misleading and should be avoided.

The most important class of basic zeolites is by far the family of aprotic, ion-exchanged zeolites, in particular FAU zeolites (X or Y type, see below Figure 20 for a view of the structure) which may regarded as archetypical of basic zeolites. In these materials, the charge defect induced by framework Al^{3+} cations, is compensated by extra-framework mono- or multivalent cations M^{n+} (for a detailed review on the position and the distribution of these cations in FAU zeolites with respect to their type and composition, we refer the reader to the work of Frising and Leflaive[564]). In such materials, the negative charge borne by oxygen framework atoms primarily depends on the structure and chemical composition of the zeolite. A simple but powerful concept allowing assessing the average negative charge of framework oxygen atoms vs. composition is the electronegativity equalization principle of Sanderson,[565, 566] which was applied to zeolites by Mortier.[224] Within this paradigm, the average partial charge of the framework oxygen atoms δ_O is proportional to the difference between the intermediate electronegativity of the zeolite atoms, S_{int} with the oxygen electronegativity (S_O = 5.21):

$$\delta_O \propto S_{int} - S_O \quad (10)$$

where S_{int} is the geometric mean of the electronegativities of the component atoms of the zeolite. In other words, the lower the electronegativities of the cations, the lower the intermediate electronegativity, the more negative the oxygen framework atoms. Hence, the oxygen charge increases with the amount of Al in the framework (S_{Al} = 2.22 vs. S_{Si} = 2.84), or when the electronegativity of the extra-framework counter-cations is low (for instance for alkaline-exchanged zeolites, the oxygen charge increases from Li to Cs-exchanged zeolites: S_{Li} = 0.74, S_{Cs} = 0.28).

Besides, while framework oxygen atoms have been by far the most investigated in the literature, other basic centers can be encountered in zeolites, such as for instance hydroxy groups

resulting from water dissociation of hydrated extra framework cations, [567] basic oxygen atoms or hydroxy groups of oxide clusters,[568] or basic NH groups obtained by nitridation.[569]

The characterization of the basicity of a zeolite involves determining the number and the strength of these basic centers. IR spectroscopy being sensitive to chemical bonds, it generally does not allow for detecting the basic sites themselves, with the notable exception of basic extra-framework OH groups,[567, 570] and NH groups of nitrided zeolites.[571, 572] Hence, the general approach to characterize zeolite basicity involves the use of acidic probe molecules that, ideally, would react with the basic centers according to reactions (8) or (9) above. It must be noted, however, that while such equilibria may be investigated in dilute solutions, the surface density of basic sites and the proximity of acidic centers often prevent observing selectively reactions (8) or (9) in zeolites. This is virtually always the case for the Brønsted equilibrium (8), where the conjugated base of the acid (A^-) forms a complex with Lewis acid centers (M^{n+}) in the vicinity of the basic center:

$$Z[B^-, M^{n+}] + HA \rightarrow Z[B\text{-}H + M^{n+}\text{-}A^-] \qquad (11)$$

Thus, within basic zeolites, for a given acid HA, the realization of the Brønsted equilibrium (11) is simultaneously driven by the strength of vicinal basic and acidic centers, which does not allow to conclude on basicity alone. The characterization of basic centers using protic probe molecules is thus generally carried out in conditions allowing preventing the dissociation (8) and restricting the acid-base interactions to the formation of hydrogen bonds between the acidic protons and the basic centers:

$$ZB^- + HA \rightarrow ZB^- \cdot\cdot HA \qquad (12)$$

While seemingly paradoxical (the reaction defining basicity is avoided), such a situation allows one to selectively probe the basic sites. With respect to the Brønsted definition, the hydrogen bonding interactions can be viewed as incipient proton-transfer reactions, i.e. a frozen stage of reaction (8) in which a partial bond $ZB^{-}\cdots H$ is formed while the HA bond is weakened.[573] Within this approach, the (Brønsted) strength of the basic site is heuristically approximated by the strength of the hydrogen bond, which have been indeed shown generally strongly correlated in the case of gas phase or liquid phase complexes.[105] Alternatively, the formation of hydrogen bonded complexes (12) can also be considered in some extent as a particular case of the Lewis definition (9), since it generally involves a small charge transfer from the proton acceptor (base) to the proton donor (acid), of the order of 0.01 to 0.03 electrons.[105] Deviations from the ideal case of the Lewis (9) or hydrogen bond formation equilibria (12), are however generally encountered because the acid probe can usually interact with a vicinal acid center via a basic moieties b:

$$Z[B^-, M^{n+}] + HAb \rightarrow Z[B^- \cdot\cdot HAb: M^{n+}] \qquad (13)$$

$$Z[B: M^{n+}] + Ab \rightarrow Z[B:Ab:M^{n+}] \qquad (14)$$

While the very same complication can also occur when probing the acidic centers (Section 3 above), it is virtually always present for basicity characterization, where the probe, for obvious geometrical reasons, is often located ‘in between’ the basic center and the acid site. In other cases, the basic probe molecule may even undergo dissociation, leading to *in situ* generation of an acid A^+ interacting with the basic center:

$$Z[B: , M^{n+}] + Ab: \rightarrow Z[B:A^{+}, b^{-}: M^{n+}] \quad (15)$$

Once these limitations are taken into consideration, i.e. providing a suitable probe interacting as selectively as possible with the basic centers has been found, the basic strength is often assessed by the spectrum of the acid base-complex. Ideally, the stretching vibration between the acid and the base (ZB···A or ZB···HA) would be the most direct spectroscopic indicator of such interactions, but these bands are in the far infrared region, which generally prevent their observation, particularly in condensed phase. Also, while in gas or liquid phase the base often presents group vibrations that are selectively affected by the formation of a Lewis or hydrogen bond complex, zeolite Al-O and Si-O bond vibrations are strongly coupled and the perturbation of the resulting framework modes induced by adsorption cannot be directly related to the strength of the adsorption (see section 8 below). Hence, the only spectroscopic indicators available for the characterization of zeolite basicity are generally the vibration modes of the acidic probe molecule which are perturbed by the nature and the strength of the acid-base interaction. The following part briefly describes the most important probe molecules used for this purpose with illustrations by recent findings in this field.

4.2 Probe molecules for characterization of zeolites basicity

4.2.1. X-H acids as probe

The largest and most used class of probe molecules for the characterization of zeolite basicity consist in acidic, non-reacting molecules, containing an acid X-H functional group (X = C, N, O) which forms a hydrogen bond with basic centers according to reaction (12) or most often (13) above. The formation of these complexes is generally evidenced by a significant downward shift and broadening of the ν(X-H) stretching band which extent, usually quantified by the frequency shift $\Delta\tilde{\nu}$ (X-H) with respect to that observed in gas phase or dilute solution, is indicative of the hydrogen bond strength, hence the basic strength of the oxygen center. While generally straightforward to evidence, however, hydrogen bonding always complicate the spectra by broad and poorly resolved features, often impairing conclusions as to the heterogeneity of these sites. Moreover, also the intensity of these bands increase with the strength of the hydrogen bond, hence preventing quantification to be made. See the parallel discussion done in Section 2.2 for the Brønsted acidity.

Pyrrole (C_4H_4NH) has been one of the earliest employed probe molecule for this purpose.[574] On alkali-exchanged X zeolites, its ν(N-H) is shifted by ~ –200 cm^{-1} for Li-X to ~ –300 cm^{-1} for Cs-X with respect to dilute solution: $\tilde{\nu}_0$(N-H) = (3497 cm^{-1}).[4, 575-5781-31-3] Such shifts are indicative of relatively weak hydrogen bonds (relative frequency shift lower than 10%),[573] and no dissociation or surface transformation of pyrrole over basic zeolites is generally reported when the adsorption is carried out at room temperature. This contrasts with even weakly basic metal oxides such as γ-Al_2O_3 on which formation of pyrrolate species has been evidenced.[4] Moreover, for a given zeolite structure, the observed shifts are strongly correlated to the negative charge of the oxygen framework derived from the electronegativity equalization principle.[4, 575, 576, 579] Pyrrole thus appears as an excellent probe for the study of zeolites basicity. While early works mostly considered the global maximum of the ν(N-H) band as a descriptor of average basicity, more recent studies have generally attempted to decompose the broad ν(N-H) band into several components in order to get more insight in the heterogeneity of basic sites. Individual components were assigned to framework basic oxygen sites differing by the nature of the extra-framework cation in case of

partially exchanged zeolites,[576] to the position of the cation,[580] or from the number of aluminum atoms in the rings of the site where the cation is located.[576, 580, 581] Kučera et al. have investigated zeolite basic sites heterogeneity with a combined experimental and theoretical study of pyrrole adsorption on alkali-exchanged MFI zeolites.[581] Figure 16a shows the spectra obtained after pyrrole adsorption followed by desorption at increasing temperatures on two K-MFI zeolites differing by their Si/Al ratio. The ν(N-H) band clearly presents two main components, I and II, at high and low frequency, respectively, which both increase with the concentration of framework aluminum, hence with zeolite basicity. Interestingly, the low frequency component, corresponding to stronger sites (lower $\tilde{\nu}$(NH), higher $|\Delta\tilde{\nu}$(NH)| and higher thermal stability), is the most increased. In parallel, modeling of pyrrole adsorption in these systems using hybrid DFT/molecular mechanics calculations indicated that the extent of the $\Delta\tilde{\nu}$(N-H) frequency shift is primarily governed by the nature of the T atoms binding the framework oxygen atom: H-bonded complexes, via the N atom, with [≡Si-O-Si≡] centers such as structure I (Figure 16b) present moderate frequency shifts ($\Delta\tilde{\nu}$(N-H) from -50 to -100 cm^{-1}), while those formed with [≡Al-O-Si≡] centers (Figure 16c, structure II) lead to much larger shifts: $\Delta\tilde{\nu}$(N-H) < -150 cm^{-1}. The Al content and distribution in the ring was also found to have a significant impact on the $\tilde{\nu}$(NH) frequency. For instance, when Al pairs are separated by two vs. three SiO_4 tetraedra, N-H stretching frequencies can be lowered by ~ 50-100 cm^{-1}, thus confirming the large impact of Al distribution put forward by previous studies.[575-577, 582, 5831, 41, 4]

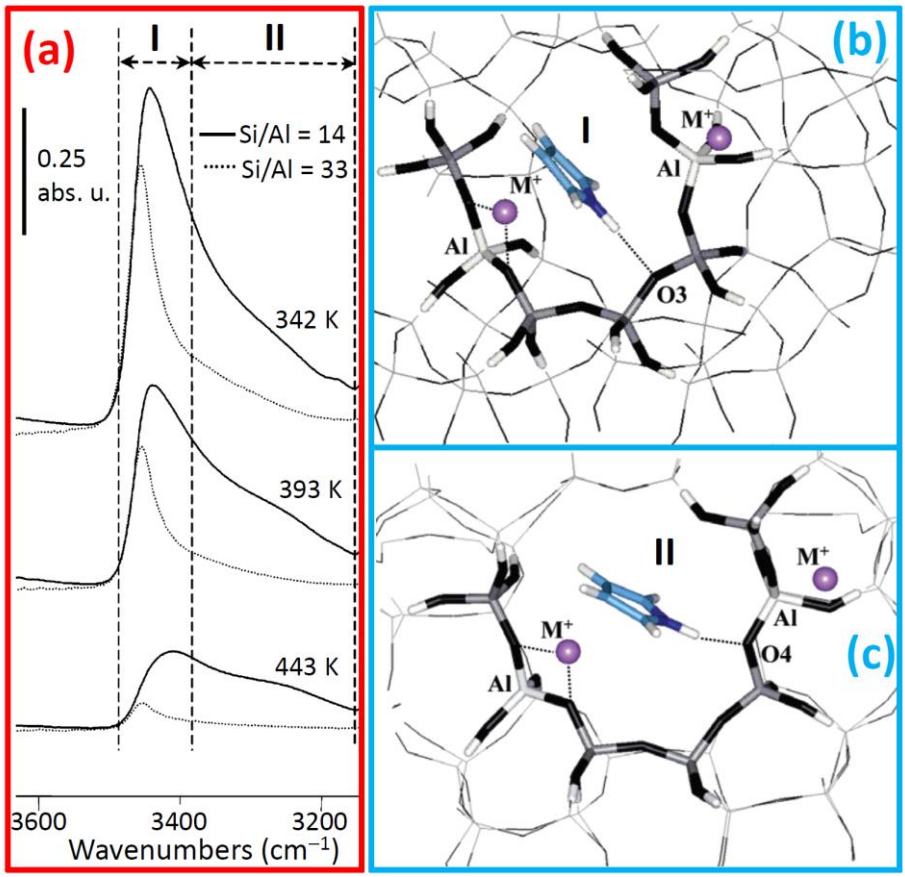

Figure 16. Part (a): FTIR spectra of pyrrole adsorbed on K-MFI with Si/Al ratios 14 and 33 (full and dotted curves, respectively) after pyrrole desorption at 343, 393, and 443 K (top, middle and bottom curves, respectively). Part (b): pyrrole adsorption complexes with (I) Si-O-Si centers (I), as computed with a hybrid quantum mechanics/interatomic

potential function approach. Part (c): as part (b) for pyrrole adsorption on Al-O-Si centers (II). Adapted with permission from Ref. [581], Copyright American Chemical Society, 2004.

While the ν(N-H) frequency shifts are dominated by the framework oxygen basicity, these theoretical calculations also show that the cation–π-ring interaction, clearly seen in the complexes shown in Figure 16b,c, plays an important role in the stabilization of these complexes, which is in line with previous theoretical works on alkaline-exchanged FAU zeolites.[584, 585] Such interactions, which can be evidenced by a significant upward shift of the ν(C-H) out-of-plane deformation modes,[584] can be strong enough to displace the extra-framework cations within the FAU structure. Hence, pyrrole adsorption on basic zeolites essentially proceeds according to reaction (13) above and is governed by basic *and* acidic centers.[580] With this respect, pyrrole adsorption energetics – as assessed by, e.g., conventional TPD experiments, should *not* be considered as an indicator of framework basicity unless validated by parallel IR experiments.

Halocarbons, in particular chloroform (CCl_3H) are also classically used of basicity characterization. Choroform, while having the same deprotonation energy as pyrrole (1500 kJ mol^{-1}),[586] generally presents much lower frequency shifts when adsorbed on basic zeolites: from ~ –20 cm^{-1} for Li-X to –100 cm^{-1} for Cs-X zeolites, but still strongly correlated with the oxygen negative charge.[587] Such low frequency shifts are due to significant interactions of the halogen atoms with extra-framework cations.[588] Besides, C-Cl bonds having a ionic character, chloroform can also react, in particular when traces of water are present,[587] and, on top of the recommendations given for pyrrole, extra-precautions should be used when using this probe on zeolites. Fluoroform (CF_3H) having stronger carbon-halogen bonds is more stable than chloroform. However, when adsorbed on a basic zeolite, the ν(C-H) band can be shifted toward *higher* frequencies with respect to the free molecule. This behavior was initially interpreted as resulting from strong interactions of fluorine with extra-framework cations, preventing the formation of hydrogen bonded complexes.[562, 588] Recently, however, the use this probe has been reinvestigated by Tsyganenko and co-workers on metal oxides and basic zeolites.[589, 590] They showed that the modifications of the ν(C-H) band frequency and intensity upon adsorption actually follow the trends expected for the so called blue-shifting or improper H-bonds, that have attracted a lot of attention since the early 2000's.[591-594]

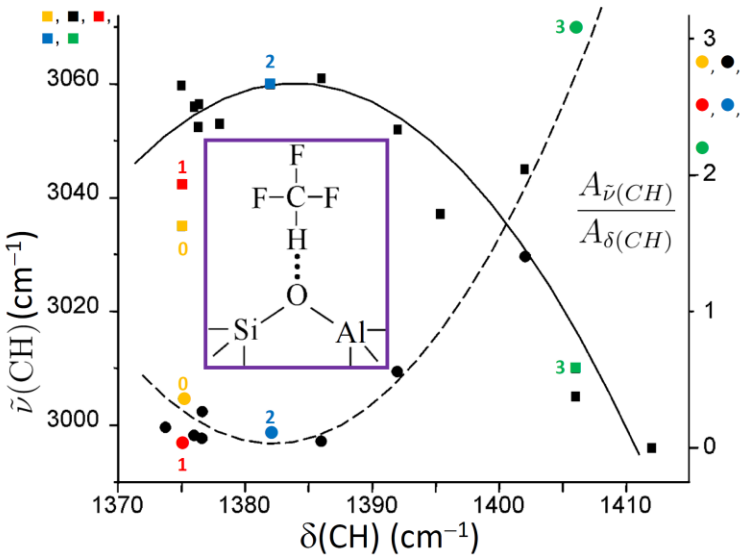

Figure 17. Positions of ν(CH) band (squares, left scale) and the ratio of integrated intensities of the stretching and bending CH vibrations $A_{\tilde{\nu}(CH)} / A_{\delta(CH)}$ (circles, right scale) of H-bonded fluoroform plotted against δ(CH) values over metal oxides and zeolites. For this review the more relevant set of data are those marked with colored symbols: 0 – free molecule; 1 – Al-free silicalite; 2 – Na-Y; 3 – Na-X. The central inset reports the scheme of an H-bonded fluoroform with a basic framework oxygen atom of a zeolitic framework. Adapted with permission from Ref. [590], Copyright Elsevier, 2014.

Such a behavior occurs when the isolated H-bond donor has a negative dipole moment derivative (i.e. corresponding to a bond dipole directed in the sense $C^{\delta+}$-$H^{\delta-}$). In such a case, weak hydrogen bond interactions first lead to upward frequency shift (i.e. blue shifting H-bond) and to an intensity decrease, while for sufficiently strong hydrogen bonds, the 'normal' downward shift and intensity the increase of the intensity of the ν(C-H) band is observed. This is illustrated in Figure 17 which shows the evolution of the frequency of the ν(C-H) mode (squares, left ordinate axis) and its intensity normalized to that of the δ(C-H) mode (circles, right ordinate axis) of adsorbed fluoroform. Framework oxygen centers having a very weak or intermediate basicity such as those of Al-free silicalite-1 or Na-Y zeolite give rise to improper, blue shifting hydrogen bonds (red and blue squares in Figure 17), while the stronger basic centers of Na-X zeolite lead normal, red shifting hydrogen bonds (green square). Finally, the upward shift of the δ(C-H) mode appears roughly correlated with the basic strength of the oxides investigated in this study, and the authors suggested that it could be used as an approximate measure of surface basicity, as for 'normal' H-bonds. The non-monotonic behavior of the ν(C-H) band with the basic strength, however, makes the analysis of the spectra not strightforwars, preventing the use of this probe for routine analysis of surface basicity. Sánchez-Sánchez et al. have investigated the use of a chloro-fluorocarbon probe molecule, CCl_2FH, on alkali exchanged zeolites and found that the correlation between the ν(C-H) frequency shift and the oxygen negative charge is generally worse than those obtained for chloroform, which they ascribed to the influence of fluorine-cation interactions, evidenced by NMR.[595] It should also be noted that later this molecule was also found to form blue-shifting hydrogen bonds,[596] which could thus contribute worsening such correlations.

The other class of C-H acids used for basicity characterization is the family of acetylenic compounds. Acetylene (C_2H_2), first proposed by Uvarova et al.,[597] presents ν(C-H) frequency shifts sensitive to the strength of basic sites of alkali exchanged zeolites of ~ –80 and –115 cm^{-1} for Na-Y and Na-X zeolites, respectively. More recently, the use of this probe has been extended to the study of a large series for metal oxides, confirming its interest for the study of basicity.[598] It should be noted however, that the C-H stretching mode of acetylenic compounds is generally coupled with the C≡C stretching vibration, and, in the case of acetylene, with the second C-H vibration, leading to symmetric and antisymmetric ν(C-H) modes. In order to limit the latter coupling, heavier alk-1-ynes such as propyne or but-1-yne could be used. Although not reported with much details, propyne was also used by Uvarova et al. and Knözinger and Huber on alkali exchanged FAU zeolites, showing ν(C-H) frequency shifts consistent with oxygen framework basicity.[9, 597]Finally, Lavalley et al. have proposed the use of but-1-yne (CH_3CH_2CCH) and have shown that this probe could be used for zeolites presenting a moderate basicity such as Na-Y or Na-X zeolites and could be more sensitive to the heterogeneity of basic sites than pyrrole.[599] On more basic zeolites such as Cs exchange FAU, however, but-1-yne undergo isomerization reactions, preventing its use over such solids.

4.2.2. Lewis acids as probe

Carbon dioxide (CO_2) is certainly the most employed probe used for the characterization of surface basicity. On basic zeolites, however, the most striking adsorption mode of CO_2 is generally the formation of linear complexes with extra-framework cations, leading to intense bands around 2360 cm^{-1} due to the asymmetric stretching vibration ν_3 that shifts toward high wavenumber as the polarizing power of the cation increases[600, 601] (for more details, see Sections 3.1 and 7.2). In addition to the bands of linearly adsorbed CO_2, the formation of carbonate species, characterized by ν(COO) bands in the 1300-1700 cm^{-1}, range is generally evidenced on zeolites presenting medium to strong basic strength, such as Na- or heavier alkaline ions exchanged X zeolites,[4, 568] K, or Cs-exchanged zeolites,[602, 603] while no such species are detected on zeolites having weaker sites (e.g. Li-X, Li-Y or Na-Y).[602] Carbonate species formed are characterized by two ν(CO) bands resulting from a symmetry lowering as compared to the free CO_3^{2-} ion. On alkali exchanged zeolites, these bands, assigned to symmetric and asymmetric COO vibrations, generally appear at ~ 1650–1700 cm^{-1} and ~ 1300–1400 cm^{-1}, which, by analogy with metal oxides,[39] are indicative of bridged carbonate species formed with the basic framework atoms (Figure 18a). Yet, contrarily to the case of other probe molecules, no systematic trend between the position of these bands and the expected basic strength of the zeolite have been reported to our knowledge. Generally, these species are irreversibly adsorbed at room temperature and are thus much more strongly adsorbed than CO_2 complexes, but represent a minority species. By comparing successive CO_2 adsorption isotherms on K-Y and Cs-Y zeolites, Pirngruber et al. have estimated an amount of carbonate species of ~ 5 per unit cell (UC), to be compared with a total CO_2 capacity of ~ 70-90 molecules per UC.[602] This result is in line with the much earlier estimate of ~ 3 irreversibly adsorbed CO_2 species per UC in Na-X zeolites by Jacobs et al.[604] Although many recent theoretical studies have been devoted to CO_2 adsorption on alkali-exchanged zeolites, none of them have modeled the structure or the formation of such species. On the basis of DFT calculations carried out on linear ion-CO_2 complexes, however, Pirngruber et al. have discussed the formation of such species by noting that on basic zeolites such as K-Y or Cs-Y zeolites, the carbon atom of CO_2 adsorbed in 12-ring windows (supercage) do interact with the zeolite framework oxygen atoms, leading to a slight bending of the O=C=O angle (< 3°), and can be considered as precursors of bridged carbonate species (Figure 18b).[602] The impossibility to form carbonate species on light-alkali exchanged zeolites such as Li- or Na-Y is explained, within this qualitative model by (i) the lower basicity of framework oxygen atoms and (ii) the position of these small cations, close to the hexagonal window and leading to short $M^+\cdots OCO$ distances (Figure 18c), preventing the interaction of the carbon atom with the framework oxygen atoms. Finally, it is worth noticing that CO_2 can probe other basic sites than framework oxygen atoms. It is the case, for instance, of extra-framework aluminic species of acidic BEA zeolites, that are slightly basic can lead to carbonate or hydrogen carbonate species (Figure 17a),[603, 605] basic hydroxy groups resulting from water dissociation of hydrated extra framework cations, leading to hydrogen carbonate species,[567] and metal oxide clusters, leading to (hydrogen)carbonate species similar to those formed on amorphous oxides.[568, 603]

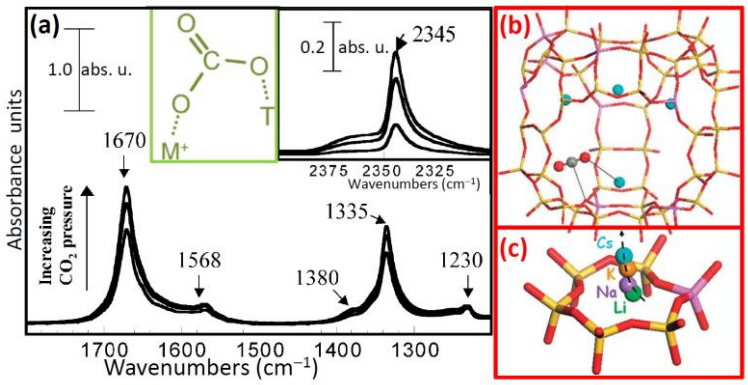

Figure 18. Part (a): IR spectra of CO_2 adsorption on K-X zeolite at 373 K showing the formation of carbonate and hydrogen carbonate species. Black inset: linearly adsorbed CO_2 species. Green inset: Schematic structure of bridged carbonate species in alkali zeolite (T = Si or Al). Part (b): sticks (zeolite framework) and balls (CO_2 and extraframework cations) representation of the CO_2 molecule (carbonate precursor) adsorbed in the 12 member ring window of Cs-Y zeolite (supercage). The shortest C···Oz and O···Cs^+ are represented by the dashed lines. The O=C=O angle is 177.7 °. Part (c): Structure of the hexagonal window separating the supercage and the sodalite (see below the inset in Figure 20 for a larger view of the Y structure) cages with the optimized position of (Li, Na, K, Cs) cations in site II. Color code of partd (b) and(c): Si atoms, purple sticks: Al atoms, red sticks: oxygen atoms, red balls: O, green balls: gray ball: C, Li, violet ball: Na, orange ball: K, blue ball: CsPart (a): Adapted with permission from Ref.,[567] Copyright American Chemical Society 2003; parts (b) and (c): Adapted with permission from Ref.,[602] Copyright Royal Society of Chemistry 2010.

For completeness, it should be noted that boric acid trimethyl ester ($B(OCH_3)_3$) was proposed as a Lewis acid probe molecule by Li et al. for the characterization of basic properties of metal oxides,[546] and zeolites.[606] The formation of Lewis complexes with framework oxygen anions changes the planar symmetry of this molecule into a pyramidal one, leading to the splitting of a degenerate vibration involving the B-O bonds (1360 cm^{-1}). However the position and splitting of these bands was not sensitive to the strength of basic centers, and this probe has not been used much since these early studies.

4.2.3. In-situ generated probe: NO^+

Recently, the disproportionation reaction of NO_2, leading to a nitrate anion and a NO^+ cation (nitrosonium) has been used to characterize the basicity of alkali exchanged FAU zeolites:[607, 608]

$$[ZO^-, M^+] + 2NO_2 \rightarrow [ZO^-{:}NO^+ , M^+{:}NO_3^-] \qquad (16)$$

In this reaction, formally equivalent to (15) above, nitrate ions are stabilized by extra-framework cations while NO^+ directly interacts with framework oxygen atoms. The $\nu(NO^+)$ stretching frequency, was found to be strongly sensitive to the electron density of the oxygen atom, decreasing from 2110 cm^{-1} to 1970 cm^{-1} from Li-Y to Rb-Y zeolites, and 1976 to 1903 cm^{-1} from Li-X to Rb-X zeolites. These species were studied with periodic DFT calculations which confirmed such a trend (e.g. decrease of the $\nu(NO^+)$ frequency with increasing size of the alkali cation on the one hand, and from Y- to X-zeolites, on the other hand.[609, 610]

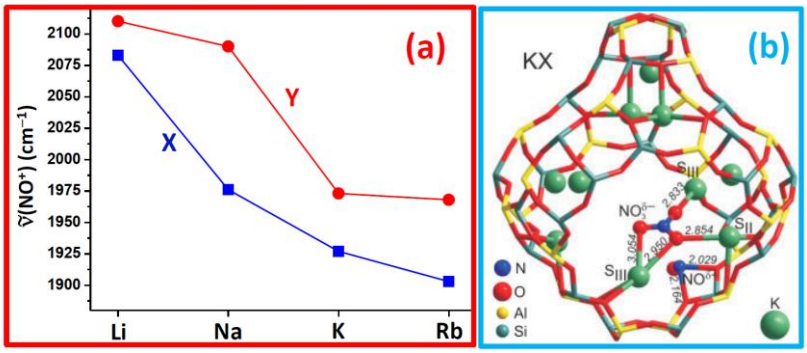

Figure 19. Part (a): positions of ν(NO^+) bands on alkali-exchanged X- and Y-zeolites. Previously unpublished figure summarizing data reported in Refs.[607, 608] Part (b): Stabilization of the NO^+/NO_3^- ion pair formed by N_2O_4 disproportionation in site III of K-X zeolite (D_{2h} symmetry), see also inset in Figure 20. Selected interatomic distances (Å) are shown in italic. Adapted with permission from Ref.[610], Copyright Wiley 2010.

5. Identification and location of sites in the framework of zeolites by the size of probe molecules

Pores are the main feature of zeolites. Molecular sieving can influence reactants and probe molecules. Catalytic activity and selectivity of zeolites can only be understood by knowing the location of sites and by knowing how easily these sites can be reached by reactants. The question is also valid for all sites, not only catalytically active. Silanol groups and simple adsorption sites, Brønsted and Lewis sites (vide supra sections 2 and 3, respectively), all can be accessible or not, subjected to diffusion limitation, to confinement, etc. Infrared spectroscopy is a major tool for evidencing and studying these effects.

The difference (behaviour, catalytic activity, silanols and lattice OH groups) between internal and external sites in zeolites has long been a matter of study.[168, 169, 611-616] In recent years, hierarchical materials have provided a method for overcoming diffusion limitations in zeolites.[89-91, 97, 617-654] The question of the accessibility of catalytic sites in these materials has raised a new interest in the use of infrared spectroscopy of probe molecules.[90, 91, 97, 629-634, 636, 637, 641, 653]

This section is divided into five subsections. The first one is devoted to IR investigation of the influence of the pores and confinement on the acid strength of OH groups in the supercage and sodalite cage of H-USY zeolite. Subsection 5.2 discusses the accessibility of Brønsted sites in defect-free and in defective zeolites. Subsections 5.3 shows how the use of different methyl-substitutes Py allows to discriminate between internal and external OH groups in H-ZSM-5 zeolite. The methodology of using a set of different probes, with increasing hindrance, to investigate the accessibility of zeolitic pore systems is discussed in Subsection 5.4 with several examples. Subsection 5.5 present IR characterizations of hierarchical zeolites. Finally, the use of two nitriles probes of different size, CH_3CN and benzonitrile (PhCN), to characterize the accessibility of Brønsted sites in progressively dealuminated mordenites, potentially pertinent to this section, is reviewed in Subsection 8.3 of Section 8 (devoted to space resolved experiments) because based on the stimulated Raman scattering (SRS) microscopy.[655]

5.1. Influence of the pores and confinement on the spectrum and acid strength of OH groups. The H-USY zeolite as a key study.

The protonic form of ultra-stable Y zeolites (H-USY) is obtained by a prolonged steaming at high temperature an H-Y zeolite. The process is aimed at removing the more unstable Al^{3+} species from

the zeolitic framework resulting in a loss of the corresponding Brønsted sites and the appearance of extraframework Al^{3+} Lewis sites (see above Section 3.2). This benefits catalytic application of the material in industrial plants as it guarantees a more stable activity of the catalyst with time.[240, 499-501] Among all the catalytic applications of USY, on the industrial ground, the most important is fluid catalytic cracking (FCC) of the high-boiling hydrocarbon fraction of petroleum crude oil, which is converted to more valuable gasoline, olefinic gases, and other products.[71, 72, 582, 656-660] Furthermore, the mesopore network, formed during steaming, improves the transport properties of the catalyst and, thus, its overall efficiency.[72, 661]

As already discussed in Section 2.1, in first approximation, the frequency of ν(OH) groups depends on the electron density on the OH bond. Silanols groups, non acidic and with a fairly strong O-H bond, appear in the IR spectrum as a sharp band in the 3750-3740 cm^{-1} range, while acidic bridged OH groups have much less electron density in their weaker O-H bond, and that bond vibrates around 3600 cm^{-1}, see Figure 1.

As already briefly mentioned in Section 2.1, any interaction between the OH group and an electron donor (zeolite wall or extraframework phase) will shift the ν(OH) vibration band towards lower frequency. This is particularly clear in H-USY zeolites, see Figure 20. Bridged OH groups located in the large supercage of the FAU structure appear at 3630 cm^{-1}, while they appear at 3565 cm^{-1} when located in sodalite units (these ν(OH) bands are thus often denoted as high and low frequency, HF and LF, respectively). The IR spectrum of H-USY reported in Figure 20 differs significantly from that or H-Y reported in Figure 1 (bottom curve). The relative intensity of the silanols band with respect to those of Brønsted sites reflects the much smaller crystal size of the H-USY sample, while the steaming process results in structured bands for both HF and LF components.

The redshift of the LF component is due to interaction of the OH group with the neighbouring walls of the sodalite cage (H-bonding with adjacent framework oxygen atoms, scheme in Figure 20). As we will see later, this has no influence on the acid strength of the bridged OH group. The main difference for any catalytic activity is that access to OH groups in sodalite cages is highly hindered, and no reactant can usually interact with LF OH groups. Interaction can also be between the OH group and some neighbouring extraframework phase. In acidic USY zeolite, the extraframework phase pulls out electrons from the O-H bond. This results in increased acidity for the bridged OH groups, and in a further red-shift of the ν(OH) vibration bands, indeed the maximum of the HF band occurs at 3645 cm^{-1} H-Y (bottom curve in Figure 1) and at 3630 cm^{-1}, in H-USY (Figure 20). Depending on the type and location of the interacting extraframework phase, four different ν(OH) vibrations bands were identified, with two different types and two different locations of extraframework phase for each HF and LF OH group.[662]

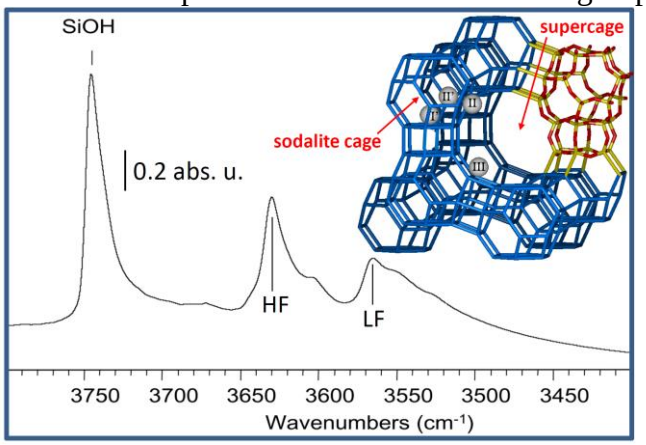

Figure 20. Main part: IR spectrum of H-USY in the region of ν(OH) vibration bands. The HF and LF bridged OH groups in supercages and sodalite units are visible together with their red-shifted part due to interaction with extraframework phase. The top right corner hosts a stick representation of Y zeolite (FAU topology[165]) showing a supercage and several sodalite cages. Also reported are the location of the Brønsted sites in the supercage (site II) and in the sodalite cages (sites I' and II'). Site III, also located in the supercage, is occupied only for X zeolites, showing a lower Si/Al ratio. Main part: adapted with permission from Ref. [662], Copyright Elsevier, 2007.

5.2. Non-hierarchical zeolites. Are OH accessible or not? The influence of structure defects

In zeolites without defects, the perfect crystalline structure will present the expected pore channels, and a fairly simple reasoning will be able to predict and understand accessibility of sites. Silanol groups will only be external, with no silanol nests, and access to Brønsted sites (see Section 2) will be geometrically restricted by the pore windows. There will be in the general case no Lewis sites (no defects, and no extra-framework phase, see Section 3). The absence of Lewis sites can be checked after the measurement by cleaning the surface of the solid under vacuum and adsorbing pyridine as the last probe molecule. If pyridine detects Lewis sites, this is an indication of framework damage, either before or during the experiment. Framework damage can ease transport of the probe molecule to adsorption sites, by creating defects in the pore system. It can also have the opposite effect: too fast a calcination of a sensitive zeolite (e.g. mordenite) can completely block the pore system and pyridine will detect only a fraction of the Brønsted sites (but might detect unexpected Lewis sites due to extra-framework aluminium phase).

The general case is that of a zeolite containing defects. Steamed or stabilized zeolites, thermally treated zeolites with a fast heating ramp, all contain a significant amount of defects, Lewis sites, etc. Some sites that would not be accessible in a perfect crystal now become within reach to many probe molecules. Many studies about accessibility to some peculiar sites in zeolites (like side pockets in mordenites) are seriously questionable about the thermal history of the zeolite and the presence of defects. Such fragile zeolites should be activated heting very slowely, sometime 1 K min^{-1}, but always by less than 3 K min^{-1}. Access to hindered sites has been claimed in zeolites where the structure was in fact damaged and where the structure of the pore around the adsorption site was not what it was supposed to be (which would have been detected by checking the absence of Lewis sites at the end of the experiment).

It has long been said that probe molecules must be small, so that they can probe all of the sites in zeolites. However, playing with the probe size is a useful tool for understanding the relationship between acidity and activity. In the perfect or in the defect-containing zeolite, exploring the pores can be done using probe molecules with various sizes. The interaction of the probe molecule with the site for that purpose can be manifold: protonation, H-bonding, deuterium exchange and so on …

5.3. Substituted pyridines: distinguishing internal and external silanol groups

Py is a common probe for characterising acid sites in zeolites. It penetrates in most catalytically significant pores. Methyl substituted pyridines, like 2,4,6-collidine (2,4,6-trimethyl pyridine), are larger molecules, and their access to some micropores is limited. In H-MFI, collidine was used to distinguish OH groups located inside or outside the pore system, schematically represented as blue and red spheres in Figure 21c, respectively. The acidic Brønsted SiOHAl groups, located inside the micropores, are out of reach of collidine. T atom vacancies result in internal silanols nest,[168-170] consisting in internal Si-OH groups located inside the micropores (not represented in Figure 21c), and they vibrate at a slightly lower frequency than the usual external silanol groups, see the

spectral region labelled as "internal silanols" in Figure 1 and Figure 20. Sending 2,4,6-collidine to H-ZSM-5 results in the consumption of the silanol bands at 3745 cm^{-1}, while the band around 3610 cm^{-1}, due to internal Brønsted sites is left unperturbed, compare full and dashed spectra in Figure 21a. Actually a minor fraction of the silanol band is still present in the dashed spectrum; this persistent component centred and tailed toward lower frequencies with respect to the band of the external silanols. The spectra reported in Figure 21a are the direct spectroscopic proofs of the existence of internal silanols in ZSM-5, not reachable by 2,4,6-collidine probe. Interestingly, the internal silanols in H-MFI disappear by interaction with traces of coke generated during xylene isomerisation (Figure 21b). Coke traces can only be formed in the additional space in structure defects, and this is where these internal silanols are present.[414]

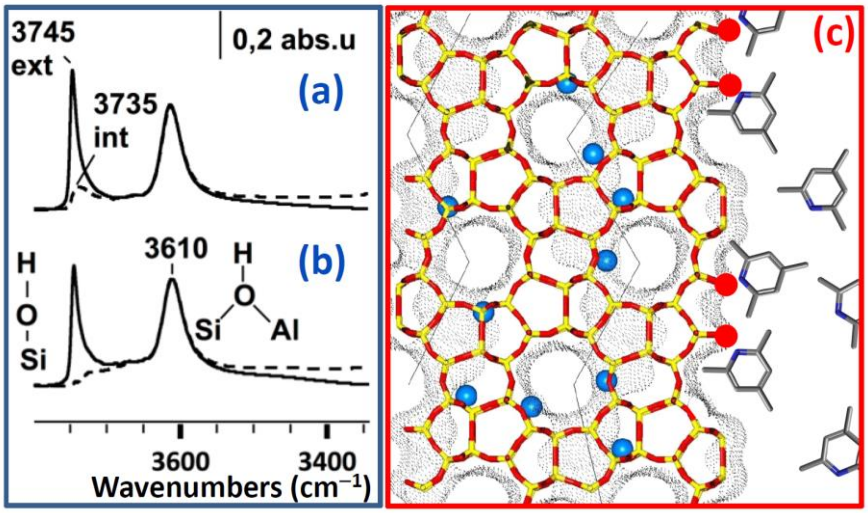

Figure 21. Part (a): IR spectra in the ν(OH) stretching region of H-ZSM-5 before (full line) and after (dashed line) adsorption of collidine. As 2,4,6-collidine does not enter the micropores of ZSM-5, only the OH groups located on the external faces of the zeolite crystals are consumed, leaving internal Brønsted sites untouched and evidencing the band due to internal silanols. Part (b): as part (a) for H-ZSM-5 that was subjected to a coke formation process after xylene isomerisation. On the coked sample, internal silanols have disappeared. Part (c) sticks representation of ZSM-5 zeolite (MFI topology[165]) fragment viewed along the [010] direction of the straight channels; sinusoidal channels, running along the perpendicular [100] direction, are evidenced by black segments. Also the crystal surface is represented where 2,4,6-colodine (sticks representation) have been dosed in excess. Red and blue spheres represent possible location of external (silanols) and internal (Brønsted sites) OH groups, respectively, while the sticks code is as follows: Si or Al (yellow), O (red), N (blue), C (grey). Dots outline the Connolly surface[663] obtained with a probe molecule 2.8 Å in diameter. This scheme represents an ideal, defect free crystal, where internal silanols are absent. Part (c): previously unpublished; parts (a) and (b): adapted with permission from Ref.[414], Copyright Elsevier, 2001.

5.4. Different probes for studying pore systems

5.4.1. Py and CO co-adsorption in mordenite

The size difference between probe molecules is a very sensitive tool for exploring pores. Combining probe molecules by adsorbing them together is a way to obtain information from both probes in accessibility and strength of the sites.[664] In this regard, the mordenite framework provides a clear example. As was the case for H-Y (see above Figure 1 and Figure 20 and related discussions) also H-mordenite, exhibits two different types of Brønsted sites characterized by ν(OH) mode absorbing around 3612 and 3585 cm^{-1},[133, 204, 229, 665-667] also defined as HF and LF components, respectively (Figure 22a). Compared to H-Y by a much smaller difference in the corresponding $\tilde{\nu}$(OH) characterizes the HF and LF components in H-mordenite and a careful

deconvolution process was needed to single them out.[666, 667] The HF component is due to Brønsted sites hosted in the main channels (a straight 12-membered ring channel running along the [001] direction and characterized by an elliptical cross section of 0.65 nm x 0.70 nm in diameter).[165] These channels have side pockets, in the perpendicular [0l0] direction, circumscribed by 8-membered rings which are accessible through windows with a free diameter of ca. 0.39 nm and that hosts the Brønsted sites responsible to the LF component. See Figure 22b for a view of the mordenite structure along the main channel direction. Py probe has access to the Brønsted sites located in the main channels, but not to those hosted in the smaller side pockets. This can be seen on the spectra of the ν(OH) vibration band (main part in Figure 22a). After adsorption of Py, only the HF of the band for acidic lattice OH groups is perturbed and disappears: this corresponds to the 2/3 of the lattice OH groups located in the main channels. The lower frequency part of the band (spectrum n in Figure 22a) can thus be assigned to the OH groups in the side pockets of mordenite.

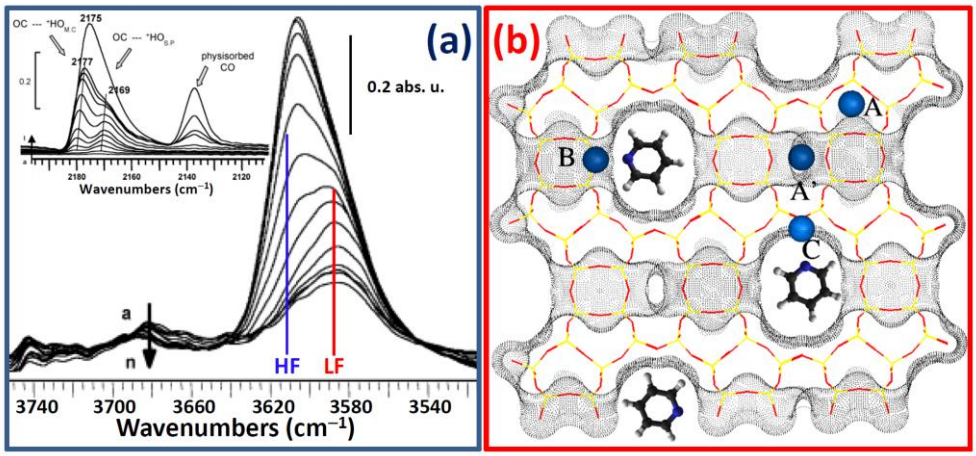

Figure 22. Part (a) IR spectra in the ν(OH) stretching region of thermally activated H-mordenite before (curve a) and along adsorption of increasing amounts of Py (curves b to n). Inset: IR spectra in the ν(CO) stretching region of thermally activated H-mordenite before (curve a) and along adsorption of increasing amounts of CO (curves b to l). Vertical colored lines highlight the position of the partially overlapped HF and LF components. $^{+}HO_{MC}$ and $^{+}HO_{SP}$ represent the Brønsted sites in the main channel and in side pockets, respectively. Adapted with permission from Ref.,[664] Copyright American Chemical Society, 2004. Part (b): sticks representation the mordenite structure (MOR topology[165]) projected along the [001] direction, showing possible location of internal Brønsted sites. Sites B and C are located in the 12-memebered-ring main channel and are accessible to Py molecules (also drawn in sticks and balls representation), while sites A and A' are located inside the side pocket and cannot be perturbed by Py. The colour code is as follows: Si or Al (yellow), O (red), N (blue), C (dark grey), H (white). Dots outline the Connolly surface obtained with a probe molecule 2.8 Å in diameter. Adapted with permission from Ref.,[386] Copyright American Chemical Society, 2003.

CO is small probe molecule interacting with all acidic sites, wherever they are located in the pore system of mordenite.[379, 664] As discussed in section 2, the strength of the interaction of CO with the acidic sites gives information on the acidic strength. When CO is adsorbed on the clean and empty zeolite, all of the sites are measured together (inset in Figure 22a). When CO is adsorbed on mordenite with preadsorbed pyridine, CO only measures the strength of H-bonding in small side pockets where pyridine cannot enter. The acidic strength of the OH groups in the main channels can be obtained by difference. Thus, by co-adsorbing Py and CO, the steric hindrance of pyridine allows differentiating location of sites and measuring the strength of OH in various locations by CO. In particular, CO molecules interacting with Brønsted sites in the main channel gives rise to the IR band that, upon increasing the CO equilibrium pressure, moves from 2180 to

2175 cm^{-1} while those probing Brønsted sites in the side pockets are characterized by a ν(CO) that goes from 2171 to 2169 cm^{-1}.[664] A more recent and more detailed analysis of mordenite was even capable to identify and measure the third possible location for OH groups in the window between the main channels and side pockets.[664]

5.4.2. Acetonitrile and substituted acetonitrile

(Deuterated) acetonitrile is a small and versatile probe molecule. It can detect Lewis and Brønsted sites,[4, 136, 137, 146, 177, 198, 202, 317, 668-673] and is able to see sites in small pores, even side pockets of mordenite,[212, 674] see Figure 22b. The size of the probe molecule can be increased and tuned by introducing methyl or larger substituents on the methyl group of acetonitrile. An accessibility scale was thus introduced by Busca by first using pivalonitrile (2,2-dimethyl-propionitrile)[675, 676] and then propionitrile, isobutyronitrile (2-methyl-propionitrile), 2,2-diphenyl-propionitrile, benzonitrile, and ortho-toluonitrile.[677] The Genoa group used that first accessibility scale to probe external vs. internal sites in many different zeolite structures. They showed that bridged acidic OH only form inside the pore system, and not on the external surface, whereas aluminium atoms on the external surface cannot form bridging OH Brønsted sites, and are at the origin of strong external Lewis acidity.

5.4.3. H-bonding: decrease of the interaction by steric hindrance

Onida et al.[211] have shown that large molecules are limited in their H-bonding inside zeolites. The larger the molecule, the larger the deviation from the strength expected. With a series of weak bases with increasing size steric hindrance to the interaction of a probe molecule with an acidic site is a possible measure of the accessibility in a zeolite. The following molecules have been employed in this study: N_2 (0.31 nm), CO (0.34 nm), ethylene (C_2H_4, 0.48 nm), propene (C_3H_6, 0.65 nm), benzene (C_6H_6, 0.72 nm), toluene (C_7H_8, 0.82 nm) and 1,3,5-trimethylbenzene (TMB, 0.88 nm), the parenthesis reports the corresponding molecular cross section and, when needed, the chemical formula or the acronym used to plot the data in Figure 23.

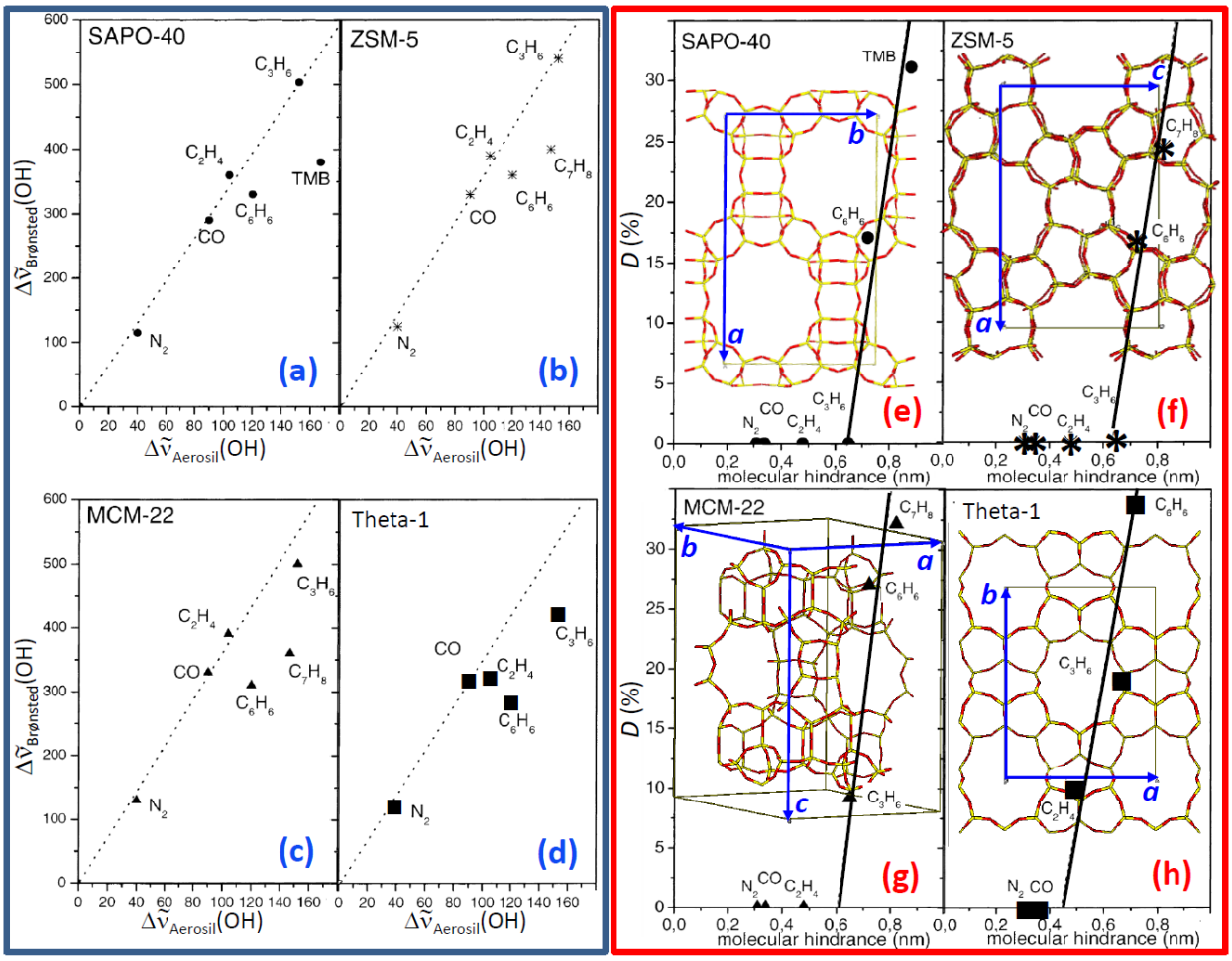

Figure 23. Parts (a-d): BHW plots (see above Figure 4 and related discussion) referred to SAPO-40, ZSM-5, MCM-22, and Theta-1 zeolites, respectively, obtained taking as reference the values for the isolated silanol at the surface of Aerosil (amorphous, high surface area SiO_2). Dotted lines represent the best linear fits performed on the fraction of data that obey the BHW linear correlation. Parts (e-h): Correlation between the deviation from the BHW model, defined according to Eq. (17), and the molecular hindrance defined as the largest transverse molecular diameter of probe molecule for SAPO-40 (AFR topology), ZSM-5 (MFI topology), MCM-22 (MWW topology), and Theta-1 (TON topology).[165]. Also reported in parts (e-h) are a graphical sticks representation of the corresponding zeolite structure with the corresponding unit cell and crystallographic *a*, *b* and *c* axis (when not along the view direction). Si or Al atoms (yellow), O atoms (red). The zeolite structures are new graphical materials, while all the remaining items have been adapted with permission from Ref.,[211] Copyright American Chemical Society, 2002.

As deeply discussed in Section 2.2 (see Figure 4), the strength of the H-bonding between an acidic solid and probe molecules is usually measured by a procedure similar to BHW plots,[189-193, 195] comparing the shift in the ν(OH) caused by adsorption of the probe on the solid, $\Delta\tilde{\nu}_{\text{Brønsted}}(\text{OH})$, with the shift that would be observed on a reference material such as silica (open surface, $\Delta\tilde{\nu}_{\text{Silica}}(\text{OH})$). On zeolites, large molecules deviate from the expected linear plot on an open surface. Indeed the BHW holds only if the base B is free to optimize its orientation in order to maximize the hydrogen bond interaction with the acidic site. For a given zeolite topology, this request starts to be no longer valid when molecular hindrance (defined as the largest transverse molecular diameter) exceeds a given value related to the zeolite pore dimensions. This is clearly shown in Figure 23a-d. As an example, Figure 23a shows that in SAPO-40, exhibiting large 12-memebred rings along the [001] direction (6.7 Å x 6.9 Å),[165] only benzene and TMB deviate from the BHW

linearity. Analogously, for a given base B, probing different zeolitic frameworks, the hydrogen bond interaction can be optimized in large pore zeolites while it may not be the case in small pores zeolites. This is the case of propene, which spectroscopic data lies on the BHW line (dotted lines in Figure 23a-d) for SAPO-40 and ZSM-5 frameworks (parts a,b), while it deviates slightly for MCM-22 (part c) and significantly for Theta-1 frameworks (part d). This observation agrees with the topologies of the investigated zeolites, which frameworks are reported in sticks representation in Figure 23e-h. ZSM-5 exhibits a couple of interconnected 10-membered rings-pores running along [100] (5.1 Å x 5.5 Å, sinusoidal) and [010] (5.3 Å x 5.6 Å, linear) directions; MCM-22 possess a complex, two-dimensional, pore structure with sinusoidal 10-membered ring channels with an elliptical ring cross section of (4.1 Å x 5.1 Å) and (4.0 Å x 5.1 Å); Theta-1 has 1-dimensional linear channels formed by 10-membered rings with an elliptical cross section of (4.6 Å x 5.7 Å).[165]

Onida et al.[678] defined for each molecule B, and for each zeolite, the percentage deviation (*D*) as:

$$D = 100\ \frac{[\Delta\nu_{\text{Brønsted(OH)}}]_{BHW} - [\Delta\nu_{\text{Brønsted(OH)}}]_{Exp}}{[\Delta\nu_{\text{Brønsted(OH)}}]_{BHW}}, \qquad (17)$$

where, $[\Delta\tilde{\nu}_{\text{Brønsted}}(\text{OH})]_{Exp}$ is the experimental shift (ordinate of the scattered data in Figure 23a-d) and $[\Delta\tilde{\nu}_{\text{Brønsted}}(\text{OH})]_{BHW}$ is the expected shift in case of absence of hindrance. The latter is obtained as ordinate at the corresponding $\Delta\tilde{\nu}_{\text{Silica}}(\text{OH})$ abscissa value, of the linear fit performed on the fraction of data (see dotted lines in Figure 23a-d and Table 7 for quantitative values). *D* values computed for all IR experiments, and reported against the molecular hindrance, resulted in the plots of Figure 23e-h.

Table 7. Summary of the best linear fits performed on the fraction of $\Delta\tilde{\nu}_{\text{Brønsted}}(\text{OH})$ vs. $\Delta\tilde{\nu}_{\text{Aerosil}}(\text{OH})$ data reported in Figure 23a-d that, for the different zeolites, lies on the BHW line. Due to the low number of available couples of experimental frequency shifts (4 for SAPO-40 and ZSM-5, 3 for MCM-2 and only 2 for Theta-1), the datum of the unperturbed systems ($\Delta\tilde{\nu}_{\text{Brønsted}}(\text{OH})$ 0 cm^{-1}; $\Delta\tilde{\nu}_{\text{Aerosil}}(\text{OH})$ = 0 cm^{-1}) has been added to all fits. Previously unpublished Table analyzing data reported in ref.[211] These data cannot be directly compared with those reported in Table 2 because the reference shift has been taken from different materials: high surface area amorphous Aerosil in the present case, and the external silanols of the same zeolite in the study of Pazè et al.[145]

System	slope	intercept (cm^{-1})	R^2
H-SAPO-40	3.37 ± 0.11	–7 ± 10	0.9956
H-ZSM-5	3.65 ± 0.13	–5 ± 12	0.9953
H-MCM-22	3.77 ± 0.14	–8 ± 10	0.9959
H-Theta-1	3.53 ± 0.26	–8 ± 15	0.9891

This study evidenced that on more constrained acid sites, the deviation from the BHW linearity is more important.[678] The validity of the measurement of acidity with large probe molecules is thus shown to be biased, but an interesting scale of "hindrance to the acid site" between zeolites have been established (opposite to accessibility): SAPO-40 ≈ ZSM-5 < MCM-22 < Theta-1. This is clearly evidenced in the plots reported in Figure 23e-h. Moreover, if care is made to calculate the BHW acidity slope only on the fraction of data that are not subjected by hindrance problems, then a spectroscopic determination of the acidic strength can still be obtained, see dotted lines in Figure 23a-d and Table 7 for quantitative values. From such data it emerges the following acidic scale: SAPO-40 < ZSM-5, ≈ MCM-22. Unfortunately no conclusive estimation can be done for Theta-1, because the slope of the BHW line has been obtained using only two

couples of experimental data and resulted in too large a relative error to make a conclusive comparison with the remaining three zeolitic systems. Nevertheless, a quantitative result can in principle be obtained selecting other small molecules with different proton affinities.

5.5. Hierarchical zeolites: the Accessibility Index ACI

Hierarchical zeolites are now one of the main interests for industrial applications of zeolites,[89-91, 97, 617-654] especially in the field of oil refining and processing. The main interesting feature in hierarchical zeolites is their increased accessibility to the active site and reduction of diffusion limitations. Therefore, the availability of a reliable tool for comparing and quantifying accessibility in hierarchical zeolite became a key issue.

Py can be branched with methyl groups to produce a family of probe molecules that are often used to study the location of sites in or out of the zeolite pores: pyridine (Py, ~6 Å, entering 10-MR, but not 8-MR), lutidine (Lu, 2,6-dimethylpyridine, ~7 Å), collidine (Coll, 2,4,6-trimethylpyridine, 7-8 Å, entering 12-MR) and di-tert-butylpyridine (DTBPy, 2,4- di-tertiobutyl-pyridine, not entering 12-MR openings). By increasing the size of the probe molecules, it is possible to tune the size of the pores under exploration. The fairly small Py does not penetrate the small side-pockets of mordenite, but will reach any other larger pore system, while larger molecules, Coll[99] or DTBPy[652] will only explore the external surface of many hierarchical zeolites.

Co-adsorption of carbon monoxide and a series of substituted pyridines was used to measure accessibility in progressively dealuminated mordenites.[679, 680] The largest probe molecule (DTBPy) was adsorbed first, followed by the others in decreasing size order, to finish with CO, one of the smallest possible probe molecule. On the parent sample, only Py and CO entered the pore system, with two third of the sites for Py and one third only accessible to CO, as expected in the main channels to side pockets ratio for lattice OH groups (see Figure 22b for a view of the mordenite structure). In the progressive dealumination process, mesopores were created and accessibility was progressively increased. Thus, larger probes like Coll, Lu or even DTBPy could make their way to the acid sites in the pores, leaving less and less adsorption sites for CO only (Figure 24). Quantities can be determined using the molar absorption coefficients for Brønsted or Lewis sites. The authors used here: $\varepsilon_{Brønsted}$ (1545) = 1.02 cm/μmol and ε_{Lewis}(1454) = 0.89 cm/μmol for Py; for Coll $\varepsilon_{Brønsted}$ (1632–1648) = 10.1 cm/μmol as determined in dealuminated mordenites,[679, 680] or for Lu: ε_{Lewis}(1609-1617) = 4.4 cm/μmol, $\varepsilon_{Brønsted}$(1643-1655+1627-1630) = 6.8cm/μmol as determined on various solids.[681] It should be noted that the values for the various ε can differ from one experimental system to the other, as will be explained in Section 6 and the values used here seems reasonable in view of the rest of the literature.

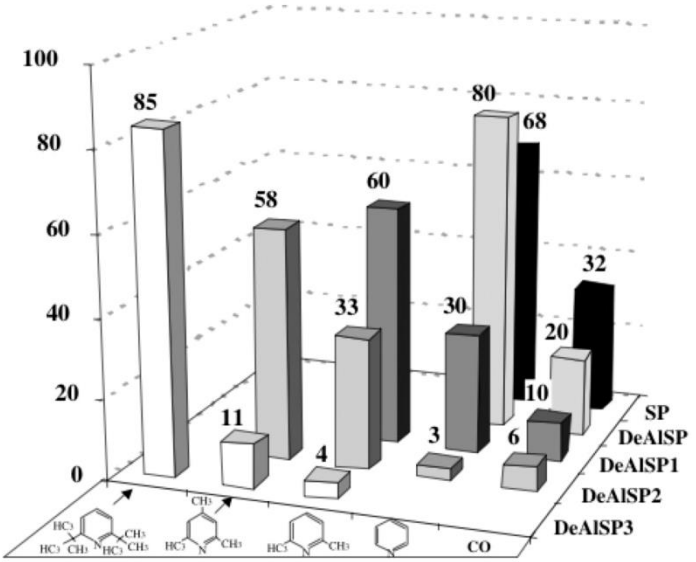

Figure 24. Co-adsorption of a series of substituted pyridines and CO on increasingly dealuminated mordenites. On the parent zeolite (denoted as SP), 2/3 of acid sites are accessible to Py, and 1/3 remain for CO. On the first dealuminated mordenite, DeAlSP, the accessibility to Py increases to 80%, leaving only 20% for CO. During progressive dealumination, up to sample DeAlSP3, the accessibility increases for larger probes such as Lu, Coll and DTBPy, to eventually reach 85% accessibility to DTBPy, leaving 11% to Coll, 4% to Lu, and nothing for smaller molecules. Reproduced with permission from Ref.,[680] Copyright Elsevier, 2006.

Substituted pyridines were adsorbed and co-adsorbed with CO to evidence the extreme accessibility of bridged acid sites in delaminated MFI zeolites.[89] All acidic sites were shown to be in close neighborhood to the external surface, or located in pore-mouths. A careful and detailed analysis of benzene and cyclohexane adsorption and transport in various hierarchical ZSM-5 based materials confirmed that strong Brønsted sites are only located in micropores, and showed that the structure and acidity in micropores were preserved during the creation of the mesopores.[636]

A reliable tool for comparing and quantifying accessibility in hierarchical zeolite was made available with the Accessibility Index (ACI). The Accessibility Index for a given probe molecule is the number of sites detected by that particular probe, divided by the total number of sites.[630] The total number of sites can be the number expected theoretically (based on chemical analysis of Al, for example) or measured with a probe reaching all possible sites, like CO or pyridine, depending on the type of sample. The first series of probe molecules for measuring ACI was the substituted alkylpyridines with different sizes (Py, Lu and Coll). It was applied to hierarchical ZSM-5 crystals, prepared by selective silicon extraction of a parent commercial sample in alkaline medium (desilication). The samples contained different degrees of intracrystalline mesoporosity. The Accessibility Index for pyridine, ACI(Py), did not change in the series containing increasing amounts of mesopores, and was above 0.9 already in the parent sample, as expected. The increase in ACI(Lu) was noticed upon introduction of mesopores, and went from ca. 0.5 on the parent sample to nearly 1 on the highly mesoporous sample. The evolution of ACI(Coll) also evolved noticeably, from nearly 0 on the parent sample, and progressively increasing to ~0.4 on the final sample. The ACI is a powerful tool to standardize acid site accessibility in zeolites and can be used to rank the effectiveness of synthetic strategies towards hierarchical zeolites (mesoporous crystals, nanocrystals, and composites).

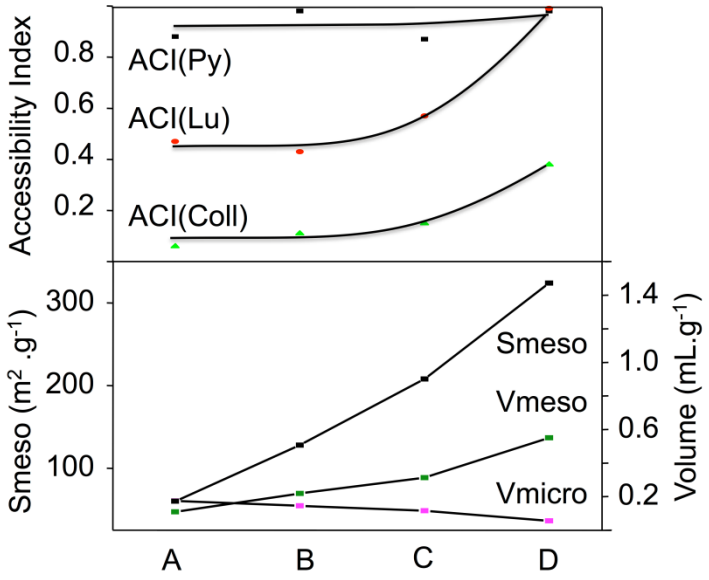

Figure 25. Changes in ACI for Py, Lu and Coll in a series of progressively desilicated H-ZSM-5 (from A to D). Upon desilication, the mesoporous surface and volume in the samples increase, and the microporous volume decreases. At the same time, changes in ACI for bulky molecules (Lu and Coll) show the increased accessibility in the samples. Previously unpublished figure summarizing data reported in Ref.[630]

Other probe molecules were used for measuring ACI depending on the type of sites measured, as for example substituted nitriles for a quantification of accessible Lewis sites.[641]

6. Determination of the absorption coefficients of the IR modes: combined IR and microgravimetric experiments

6.1. Basic definitions

Infrared spectroscopy is a quantitative tool in homogeneous systems, and the Beer-Lambert law[682, 683] is used to measure the amount of species under study in liquids and gases. The same is very often assumed to be true in transmission spectroscopy on a pellet (wafer), and IR is commonly used to determine the number of surface species on powders. This allows the determination of the amount of probe molecules on the surface and thus of the amount of adsorption sites: acidic or basic sites, accessible metallic sites…

The Beer-Lambert's law describes the attenuation of light through a sample:

$$T(\tilde{\nu}) = \frac{I(\tilde{\nu})}{I_0(\tilde{\nu})} = e^{-\kappa(\tilde{\nu})cd} \quad , \qquad (18)$$

where $T(\tilde{\nu})$ is the transmittance, $I(\tilde{\nu})$ is the intensity of transmitted light, $I_0(\tilde{\nu})$ is the intensity of incident light on the sample, d is the sample's (wafer's) thickness (in cm), c is the concentration of absorbing species (in mol dm^{-3}), and $\kappa(\tilde{\nu})$ is the molar absorption coefficient (in mol^{-1}·dm^3·cm^{-1}), at a given frequency ($\tilde{\nu}$). This law can also be written with optical density ($A(\tilde{\nu})$ or absorbance):

$$A(\tilde{\nu}) = \varepsilon'(\tilde{\nu})\, cd \, , \qquad (19)$$

Where, $\varepsilon'(\tilde{\nu})$ is then the molar absorption coefficient (also $mol^{-1}\cdot dm^3\cdot cm^{-1}$) and $\varepsilon'(\tilde{\nu}) = \kappa(\tilde{\nu})$ / 2.3. The amount of species interacting with the light beam is *cd*, and the following figure is used in the commonly used pellets:

$$cd = \frac{n}{s} \ , \qquad (20)$$

where *n* is the number of adsorbing species in the pellet (in μmol), and *S* the area of the pellet (in cm^2). From Eqs. (19) and (20) it follows:

$$A(\tilde{\nu}) = \varepsilon'(\tilde{\nu})\ [10^{-3}\ n/S] \rightarrow \varepsilon'(\tilde{\nu}) = A(\tilde{\nu})[10^{+3}\ S/n], \qquad . \qquad (21)$$

In the following we will refer to the molar absorption coefficient $\varepsilon'(\tilde{\nu}_0)$ of a given vibrational mode of a given adduct, that occurs at a given wavenumber $\tilde{\nu}_0$, so that when there is no risk of ambiguity, we shall refer to it simply as ε'. Depending on authors, and in order to simplify formulas, units for ε' can commonly be $mol^{-1}\ dm^3\ cm^{-1}$, or $mol^{-1}\cdot cm^2$ (1000 times difference). For quantitative evaluations, both the maximum absorbance and integrated area can be used for measuring a band. The latter is much more sensitive to baseline perturbations, but much less to differences in temperature, resolution, or to most other perturbations of the vibrator. The integrated area $I(\tilde{\nu}_0)$ of a given IR band absorbing at $\tilde{\nu}_0$ is expressed in cm^{-1}, and the integrated molar absorption coefficient $\mathcal{E}(\tilde{\nu}_0)$

$$\mathcal{E}(\tilde{\nu}_0) = I(\tilde{\nu}_0)\ [10^{+3}\ S/n], \qquad . \qquad (22)$$

will then be consequently expressed in cm $mol^{-1}\cdot$, or more commonly in $cm\cdot\mu mol^{-1}$.

6.2. Selected examples

The key to the quantitative measurements is thus the determination of $\mathcal{E}$, the (integrated) molar absorption coefficient for a given absorption band of a given (adsorbed) species. The simplest and oldest method for the determination of the integrated molar absorption coefficient is by introducing known amounts of the probe molecule inside the cell, and by following the progressive change of the band under study, assuming that all of the probe is chemisorbed on the sample, at least for the first doses introduced. Indeed, for the first few doses, there is a linear relationship between the amount introduced in the cell and the intensity change for bands of surface species on the solid. The integrated molar absorption coefficient is then the slope of the straight line obtained (see Figure 26a). When most of the adsorption sites are saturated, some of the adsorbed probe molecule is only physisorbed and a plateau is progressively observed.[667, 684-686] The data reported in Figure 26 refer to the dosage of progressive and carefully calibrated amount of Py to H-mordenite zeolite.[667] The first Py dosages affects only the HF ν(OH) component (Figure 26b). Py molecules interacting with the Brønsted sites in the main channel are protonated according to the reaction $Z_{MC}H\cdots Py \rightarrow Z_{MC}^{-}\cdots PyH^{+}$ (MC = main channel, see above Section 2.2), as revealed by the comparison of the typical PyH^+ component at 1545 cm^{-1}. From the data reported in Figure 26, Maache et al.[667] determined that the amount of Py necessary to completely erode the HF component was 5 μmol (point and spectrum C in parts (a) and (b) of Figure 26, respectively). Beyond this amount of dosed Py, the curve in Figure 26a indicates that a fraction of the additional Py is not protonated. This is due to the fact that additional Py molecules have to interact with the

Brønsted sites hosted in the side pockets where hindrance problems prevent the formation of a fully optimized H-bond (see Section 5.4.3). Indeed, as already discussed in Section 5.4.1 (see Figure 22), the small 8-membered rings windows (free diameter of ca. 0.39 nm), giving access to the side pockets, limits the strength of the H-bond interaction, resulting in just a coordination reaction: $Z_{SP}H\cdots Py \rightarrow Z_{SP}H\cdots Py$ (SP = side pocket). From the slope of the straight obtained when reporting the pyridinium band intensity versus the amount of pyridine introduced Maache et al.[667] deduced an integrated molar absorption coefficient for the PyH^+ band of $\mathcal{A}(1545) = 1.8$ cm μmol^{-1}. The same value was measured by Khabtou et al.[504] for the band resulting by the formation of $Z_{MC}^-\cdots PyH^+$ adducts in the supercage of Y zeolite.

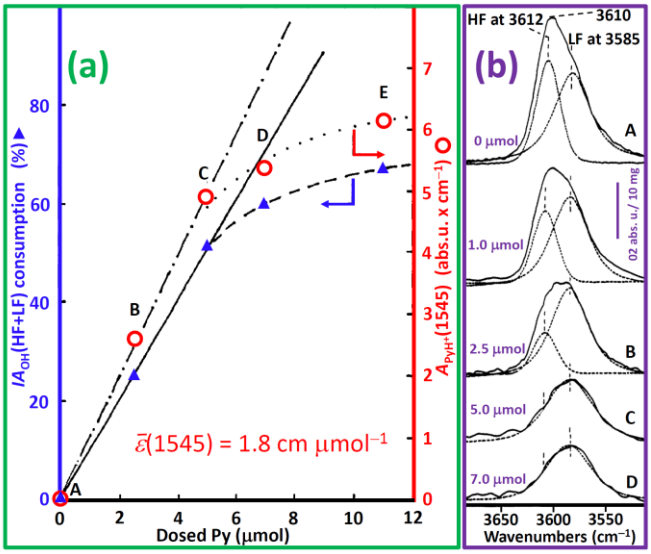

Figure 26. Part (a): variation, with the amount of Py introduced in H-mordenite (activated at 723 K), of the intensity of the pyridinium complex formed on the Brønsted sites hosted in the main channel (IR band at 1545 cm^{-1}, red open circles and right ordinate axis) and of the proportion of the correspondingly affected Brønsted ν(OH) (complex IR band initially at 3610 cm^{-1}, blue full triangles and left ordinate axis). The latter has been defined as 100 x [*I*(dose 0) – *I*(dose x)] / *I*(dose 0). Point C corresponds to the complete disappearance of the HF ν(OH) band due to Brønsted sites hosted in the main channel of mordenite (Figure 22). The slope of the dot dashed line implied $\mathcal{A}(1545) = 1.8$ cm μmol^{-1}. Part (b) selection of IR spectra showing the effect of increased amount of Py adsorption on the complex ν(OH) band of acidic Brønsted sites and the deconvolutions performed to quantitatively single out the HF and LF components. Adapted with permission from Ref.,[667] Copyright Elsevier, 1995.

It was known that on solids, calibration curves are necessary, and that Beer-Lambert's law is not always valid (especially with H-bonds). However, huge differences where observed between values reported by the different laboratories working in the domain. This was often assigned to a poor description of the experimental approach.[504] Morterra et al. questioned the whole approach, and made a thorough examination of methanol adsorption on various samples of silica. They reproduced an adsorption isotherm in a spectrometer (optical adsorption isotherm) and in a gas-volumetric apparatus connected to a heat-flow microcalorimeter.[687, 688] They showed that, although ε is in the same range on solids as in liquids, ε can greatly vary from one solid to the other for the same adsorbed species. The sample geometry and physical properties have a great influence: wafer thickness (5 mg/cm^2 is very different from 30 mg/cm^2) and pressure during the making, particle size, and all parameters influencing optical path and light diffraction and scattering in the sample (specific surface area, morphology of the particles…) will affect the apparent ε. It then became

clear that integrated molar absorption coefficients had to be measured for each sample and for each type and size of wafer.

The accuracy of the volumetric measurement in the infrared cell was also questioned, and the intensity of infrared bands for adsorbed species at saturation was compared with the amount of sites expected based on chemical analysis.[670] It is however by measuring the weight of probe species adsorbed on the solid and by plotting that versus the intensity of the corresponding infrared bands that the greatest accuracy was obtained. This was first achieved by reproducing the same adsorption and temperature programmed desorption experiments (under the same pressure and temperature conditions, with the same waiting time for diffusion) in a microbalance and in an infrared cell.[504, 680, 681] In a second step, and to be sure that conditions were rigorously the same, the experiment was performed in a combined experimental setup, by in-situ gravimetry with a MacBain balance inside the infrared spectrometer.[689]

In an improved setup developed in Caen, the sample inside the infrared cell was attached by a platinum wire to the beam of a microbalance, its weight (ca 20 mg) being measured with 1 µg accuracy during adsorption and desorption experiments.[42] With this set-up qualitative as well as quantitative information is obtained simultaneously by combining thermogravimetry and *operando* IR spectroscopy with on line mass spectrometry (see Figure 27a). The weight (and thus the number of adsorbed probe µmol) and IR spectra of a solid sample can be measured simultaneously in real time *operando* conditions, in a gas flow at temperature between room temperature and 773 K. Integrated molar absorbance coefficients ε can consequently be obtained directly. This approach was used to study the quantitative infrared response of adsorbed water and ammonium ions in a NH_4^+-Y zeolite during calcination. On line analysis of gases exiting the cell was done by mass spectrometry (MS), black curves (left ordinate axis) in Figure 27b. The desorption of water alone was observed first, during which the infrared spectrum of ammonium ions was deeply modified, moving from 1643 to 1455 cm^{-1} (Figure 27c), but not the corresponding integrated molar absorption coefficient for the whole band, that was found to be: ε(1643 - 1455) = 12 ± 1 cm μmol^{-1}. Conversely, due to the strong H-bonding between water molecules, the integrated molar absorption coefficient of the bending mode of water was water-coverage dependent, varying in the 1 to 4 cm μmol^{-1} interval.[42]

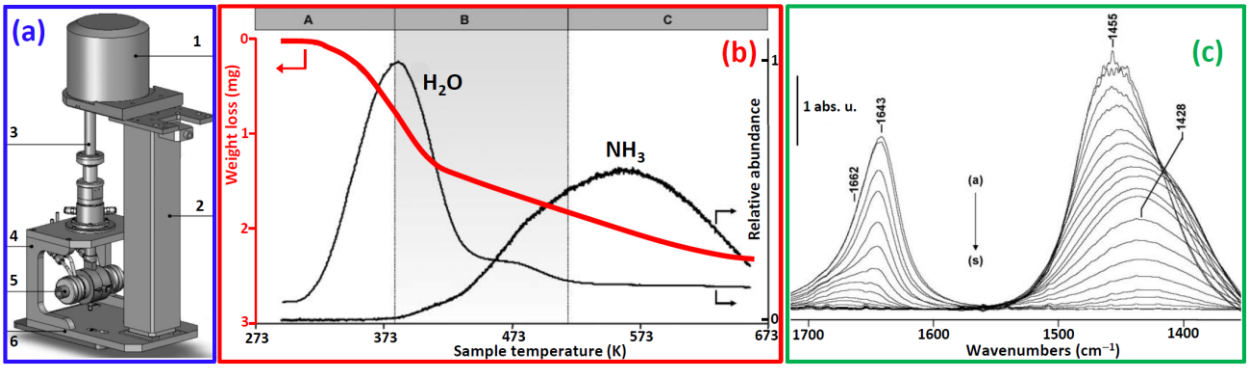

Figure 27. Part (a): general view of the integrated IR-microbalance system (AGIR setup), consisting in Setaram microbalance B Setsys (1); Telescopic column (2); IR cell-balance link (3); IR cell support (4); IR cell/*operando* reactor (5); support and spectrometer base-plate (6). Part (b): Data recorded vs. temperature during the calcination of NH_4-Y zeolite under a flow of Ar (heating ramp from 300 K to 660 K at 3 K min^{-1}). Black curves (right ordinate axis, MS data) report the relative intensity of the m/z=18 (water), (b) m/z=15 (ammonia, intensity x 100); the red curve (left ordinate axis, microbalance data) reports the weight loss of the sample (activated weight=20 mg). The experiment can be split in 3 steps: A: desorption of water alone, B: desorption of both water and ammonia, and C: desorption of ammonia alone. Part (c): IR spectra, in the bending region of water and ammonium, recorded during the experiment

shown in part (b), taken every 5 min. (from a to s): The bands of the δ(H_2O) and δ(NH) modes are visible at 1643 and 1455 cm^{-1}, respectively. The latter moves downward to 1428 cm^{-1} once water is totally desorbed, step C in part (b). Adapted with permission from Ref.,[42] Copyright the Royal Society of Chemistry, 2010.

Comparing the results obtained in this so-called AGIR setup (for Analysis by combined Gravimetry and IR) with those in the usual volumetric dosed glass cell, it was shown that, depending on the probe molecule vapor pressure and on its affinity for glass and gaskets, the results could be markedly different from one cell to the other. Phenol, for example, has a very low vapor pressure and adsorbs on the cell walls at the same time as it is chemisorbed on oxide samples. The measurement of its molar absorption coefficient was very difficult and unreliable with a conventional approach. When measured with the AGIR, it was two orders of magnitude greater than the one seemingly measured volumetrically in a glass cell.[690] Thus, not only are the physical optical properties of the solid influencing the absorption coefficient, but the results can also be greatly influenced by the geometry of the infrared cell employed, and simultaneous *in situ* gravimetric measurements must be used to calibrate quantitative infrared experiments with adsorbed species on oxides and zeolites.

This experimental setup works in vacuo or (preferentially) under gas flow, and can thus be used to measure the weight of a catalytic sample together with its infrared spectrum under reaction conditions, and is thus perfectly adapted to *operando* studies.

7. Determination of the adsorption enthalpies and entropies: variable temperature IR experiments

In the last decade, infrared spectroscopy has been widely used to extract thermodynamic values of the process of molecular adsorption on surface sites inside zeolites, mainly by the groups of Tsyganenko (Saint Petersburg, Russia), Otero Arean (Palma de Mallorca, Spain), Garrone (Turin Polytechnic, Italy) and Zecchina (Turin University, Italy) on the experimental ground and by the group of Nachtigall (Prague, Czech Republic) on the computational side.[17, 154, 274-281, 283-285, 288, 691-721] In few words, the technique is based on the displacement of the equilibrium between the molecules in the gas phase and those adsorbed on a given type of surface site performed by changing the temperature T of the system, see Figure 28a for CO adsorbed on cromocene (Cp_2Cr) hosted inside polystyrene (PS) porous polymeric matrix.

$$\text{Surface\_site} + (\text{Molecule})_{gas} \rightleftharpoons \text{Surface\_site\_}(\text{Molecule})_{adsorbed} \qquad (23)$$

$\theta(T)$ is defined as the fractional occupation of a given surface site:

$$\theta(T) = N_{occ}(T)/N_{tot} \propto \exp(-\Delta H^0/K_B T) \ , \qquad (24)$$

where N_{tot} is the total number of surface sites, where $N_{occ}(T)$ is the number of sites engaged by the molecule and where its dependence form T is driven by the third hand proportionality, being $-\Delta H^0$ the adsorption enthalpy, i.e. the variation of enthalpy undergone along the adsorption process from the gas phase to the formation of the surface molecular adduct (23), and being K_B the Boltzman constant ($K_B = 1.38 \times 10^{-23}$ J K^{-1}). From Eq. (24) it emerges that $\theta(T)$ will increase upon decreasing T and *vice versa*.

Once absorbed on the surface, the molecule provides a peculiar IR band that reflects the perturbation induced by the surface site. More peculiar bands are obtained in case the probe

molecule is more complex than a simply diatomic molecule. The integrated area of such band, $I(T)$, provides a direct measurement of the number of engaged surface sites, at the given temperature T, that can be measured quantitatively as fraction of total surface sites once a data collection has been performed at sufficiently low temperature to reach to total engagement ($\theta = 1$) of the surface site. Experimentally speaking, $\theta = 1$ is reached once a further decrease of T will not result in an increase of $I(T)$, such area is defined as I_M. In such a way, the surface coverage at any temperature is simply obtained as $\theta(T) = I(T)/I_M$. A detailed description of the thermodynamic relations related to VTIR spectroscopy allowing to extract accurate ΔH^0 and ΔS^0 values of the adsorption process is reported in section 7.1, while in this introduction section only qualitative aspects will be discussed.

Usually the adsorption enthalpy is measured by the isosteric method[717, 722-725] or by microcalorimetry,[168, 170, 266, 336, 405, 537, 600, 716, 722, 726-733] both diffusely employed in the investigation of molecular adsorption in zeolites.

The isosteric method is applied to at least two isotherms at different temperatures, which must not be too far apart (typically $\Delta T \sim 10$ K). Whenever possible, more than two isotherms should be measured and the plot of $\ln(P)$ versus $1/T$ checked for linearity. The isosteric method is very sensitive to any error in the measurement of the equilibrium pressure and particular care must be adopted when applying the isosteric method at surface coverage $\theta < 0.5$. In spite of these limitations, the accuracy of the method improves as the pressure is increased; this is unlike calorimetry, which tends to become less accurate at higher pressures.[722]

Microcalorimetry requires that a carefully weighted amount of activated sample is loaded in a calorimeter which temperature is kept fixed along the experiment. A small amount of probe is dosed on the sample and the number of adsorbed mmol (Δn_{ads}) is obtained by an accurate measurement of the equilibrium pressure (P_e) and from an accurate knowledge of the expansion volume (V) according to the equation:

$$\Delta n_{ads} = \Delta n_{dosed} - (P_e\ V)/(k_B\ T)\ , \qquad (25)$$

where ($k_B = 1.3806\times10^{-23}$ J K^{-1} $= 8.617\ 3\times10^{-5}$ eV K^{-1}) is the Boltzman gas constant and where Δn_{ads} is the number of mmol dosed on the sample, known from the experiment.[168, 170, 266, 336, 405, 537, 600, 729, 730] The calorimeter measures the energy release ΔQ by the adsorption of Δn_{ads} mmol of gas, so that the absorption enthalpy is obtained by:

$$-\Delta H^0 \equiv q_{diff} = \Delta Q\ /\ \Delta n_{ads}\ . \qquad (26)$$

When the heat signal from the calorimeter goes to zero and the pressure is constant the equilibrium is reached and a new dose Δn_{dosed} can be sent to the sample. Note that depending on the system, the time needed to reach the equilibrium may span from minutes to hours. Figure 28d reports the primary and the secondary isotherms while volumetric isotherms for CO adsorbed on Cp_2Cr/PS, showing the integrated number of adsorbed mmol ($\Delta n_{ads} = \Sigma\Delta n_{ads}$) as a function of the equilibrium pressure P_e. The equivalence of the two isotherms reflects the absence of irreversible absorption on this system. Figure 28e reports the calorimetric isotherm showing the differential heat of adsorption as a function of the coverage. The example reported by Groppo and coworkers[734] is quite relevant as it is one of the few study where both the standard microcalrimetric and the spectroscopic VTIR methods were applied simultaneously on the same system, allowing to appreciate the equivalence of the two approaches. Besides the first point, always related to some defective more energetic sites, all remaining points of the primary and secondary calorimetric

isotherms lies between 54.1 and 46.5 kJ mol^{-1}, see Figure 28e, values that are in excellent agreement with the value of 48.4 obtained by VTIR, see Figure 28c.

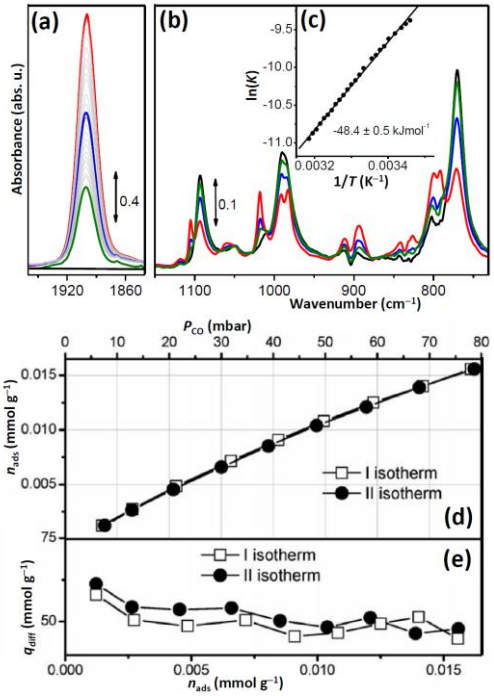

Figure 28. Example of adsorption enthalpy determined on the same system by VTIR, parts (a-c) and by standard microcalorimetry, parts (d,e). FTIR spectra in the ν(CO) region (part a) and in the region of Cp modes (part b) of $Cp_2Cr\cdots CO$/PS system as a function of the CO coverage, tuned acting on the sample temperature. Green, blue and red curves indicate the spectra collected at T = 315, 300 and 288 K, respectively. The black curve refers to the spectrum collected before CO dosage. All spectra are background subtracted. Part (c): dependence of $\ln(K) = \ln\{I(T)/[(I_M - I(T))(p/p_0)]\}$, as a function of $(1/T)$ for CO adsorption on the $CrCp_2$/PS system, see below Eq. (30), (31). The enthalpy of $Cp_2Cr\cdots CO$ complex formation is also reported with the statistic error associated with the linear fit. Part (d): primary (open squares) and secondary (solid circles) absolute volumetric isotherms obtained for CO adsorption on $CrCp_2$/PS at 303 K as a function of the equilibrium pressure P_e. Part (e): dependence of the differential molar adsorption heat q_{diff} on CO coverage. Adapted by permission of the Royal Society of Chemical (copyright 2009) from Ref.[734]

The VTIR approach has two main advantages with respect to the standard calorimetry methods such as for example the isosteric method and microcalorimetry described above: VTIR is in fact site-specific (the value obtained is not averaged on different adsorption sites, as with most of the calorimetry methods) and also allows for determination of the enthalpy of adsorption for molecules with a very low interaction energy for which cryogenic temperatures are necessary to be used. For this reason, VTIR has been particularly relevant to investigate weakly bonded adducts in zeolites such as those formed adsorbing H_2, Ar, O_2, and N_2 probes. Section 7.1 deals with a concise, but rigorous approach to the thermodynamic that is behind the VTIR approach, while section 7.2 is devoted to the description of few selected examples.

Obviously, VTIR technique has required the development of specific IR cells allowing the activation of the zeolite, the dosage of the desired probe molecule and the accurate tuning of both the equilibrium pressure and the sample temperature. This is the case of the cell developed by Tsyganenko et al.[694] in Saint Petersburg, allowing a precise control of the sample temperature down to liquid nitrogen temperature, and of that developed by Spoto et al. in Turin (University), working down to liquid helium temperature.[39]

7.1. VTIR: Theory

At any given temperature T, the integrated intensity, $I(T)$, of the IR absorption band of a molecule adsorbed on a surface site is proportional to surface coverage, θ, thus giving information on the activity (in the thermodynamic sense) of both the adsorbed species and the empty adsorbing sites. Simultaneously, the equilibrium pressure (p) does the same for the gas phase. Hence, the corresponding adsorption equilibrium constant, K, can be determined. The variation of K with temperature leads to the corresponding values of adsorption enthalpy and entropy. Assuming Langmuir-type adsorption, we have:[17, 39, 735, 736]

$$\theta(T) = I(T)/I_M = K(T)\,(p/p_0) / [1 + K(T)\,(p/p_0)] \qquad (27)$$

where I_M stands for the integrated intensity corresponding to full coverage ($\theta = 1$), p_0 is the reference pressure (usually taken as 1 Torr or 1 mbar, while in few cases some authors have chosen 1 bar, vide infra). Inverting eqn (27), the equilibrium constant $K(T)$ can be obtained as:

$$K(T) = \frac{A(T)}{[A_M - A(T)](p/p_0)} \qquad (28)$$

Combination of eqn. (28) with the well-known van't Hoff equation (29)

$$K(T) = \exp(-\Delta H^0/RT)\,\exp(\Delta S^0/R) \qquad (29)$$

leads to eqn. (30):[17, 39, 736]

$$\ln\left[\frac{A(T)}{[A_M - A(T)](p/p_0)}\right] = (-\Delta H^0/RT) + (\Delta S^0/R), \qquad (30)$$

where R is the gas constant (8.314 J K^{-1} mol^{-1}), $-\Delta H^0$ and ΔS^0 are the variation of enthalpy and entropy, undergone along the adsorption process from the gas phase to the formation of the surface molecular adduct, see Eq. (23). Defining $Y = \ln\{I(T)/[(I_M - I(T))\,(p/p_0)]\}$, Eq. (30) becomes:

$$Y = (-\Delta H^0/R)\,T^{-1} + (\Delta S^0/R)\,. \qquad (31)$$

Eqn. (31) is the equation of a line in the (Y, T^{-1}) plane, so that different couples of (Y_i, T_i^{-1}) values obtained by VTIR experiments at different temperatures will allow to derive both ΔH^0 and ΔS^0 values through a standard linear fit procedure, with ΔH^0 related to the slope of the line Y and ΔS^0 related to its intercept with the ordinate axis, see e.g. Figure 28c. Obviously, this approach assumes a temperature independence of both ΔH^0 and ΔS^0.

It is now worth spending few words on the role that a different choice of p_0 has on the ΔH^0 and ΔS^0 values derived from this method. Note that ΔH^0 and ΔS^0 are the differences of the two thermodynamic functions (H and S) between two states: the adsorbed state where the molecule is adsorbed on the surface and the reference state where the molecule is in the gas phase. From Eq. (30) it emerges that changing from p_0 to p_0' the first hand member of Eq. (30) will change by a constant value of $\ln(p_0/p_0')$. This change will not affect the slope of the Y line, so the arbitrary choice of p_0 is not affecting the ΔH^0 value extrapolated from the VTIR data. Conversely, it will change the intercept with the ordinate axis and so the extrapolated ΔS^0 by a factor $R\,\ln(p_0/p_0')$.[736, 737] This makes sense because, for an ideal gas, H is not depending on p, while S does. It is so

obvious that a change in the reference pressure p_0 will affect the entropy of the reference gas phase and so the ΔS^0 extrapolated value. As a consequence, when discussing ΔS^0 values reported in the literature from different authors, care must be made to the adopted p_0 reference value. Changing the reference pressure p_0 from 1 mbar to 1 Torr (1.32 mbar) will result in a change of ΔS^0 of R ln(1.32) = 2.28 J K^{-1} mol^{-1}, but changing from 1 Torr to 1 atm (760 Torr) will imply a change of R ln(760) = 55.15 J K^{-1} mol^{-1}.[736, 737] As the error associated to the determination of ΔS^0 with the VTIR method is about ± 10 J K^{-1} mol^{-1}, see below Table 8, literatures values obtained using p_0 = 1 mbar can be, in first approximation, directly compared with values obtained with p_0 = 1 Torr, while the 55.15 J K^{-1} mol^{-1} correction must be applied when comparison is made with values obtained with p_0 = 1 bar.[736, 737]

7.2. VTIR: Examples

7.2.1. Adsorption of Ar, H_2, O_2, N_2 and CO on H-Na-Y zeolite

Gribov et al.[154] investigated the adsorption of Ar, H_2, O_2, N_2 and CO on H-Na-Y zeolite (Si/Al = 2.9; H^+/Na^+ = 5) by means of VTIR in the (90–20 K) temperature and (0–40 mbar) pressure ranges. Two pressure regimes were singled out, characterized by: (a) specific interaction at low pressure of the probe molecules with the internal Brønsted and Lewis sites, and (b) multilayer adsorption at higher pressure. In this review we will focus on regime (a) only. When the probe molecule (B) is adsorbed on a Brønsted site hosted in a zeolitic framework, there are three independent ways to calculate the adsorption enthalpy from VTIR data. This is achieved by studying the dependence upon T of (i) the intensity of the ν(OH) band of free HF Brønsted groups in the supercage (Z-OH, decreasing upon θ increase, see Figure 29a); (ii) the intensity of the ν(OH) of perturbed HF Brønsted groups (Z-OH···B increasing upon θ increase, see section 2 and see Figure 29a.); (iii) the intensity of the stretching vibration band of adsorbed base (when possible, see Figure 29b). Eq. (31) has been used to plot the three set of experimental data (Figure 29c) and the ΔH^0 and ΔS^0 values extracted from the corresponding linear fits are equivalent, within the error bars. A significant difference in the slope (and thus in ΔH^0) is appreciable just by a simple inspection of the data referring to CO (open squares), N_2 (open squares), O_2 (crosses), Ar (open stars) and H_2 (open diamonds) molecules adsorbed in H-Na-Y, that are plotted in Figure 29d together with the corresponding best linear fits. Quantitative valued for $-\Delta H^0$) are, in kJ mol^{-1}: 11.4 (H_2), 14.8 (O_2), 15.2 (Ar), 22.2 (N_2), and 30.6 (CO),[154] see Table 8.

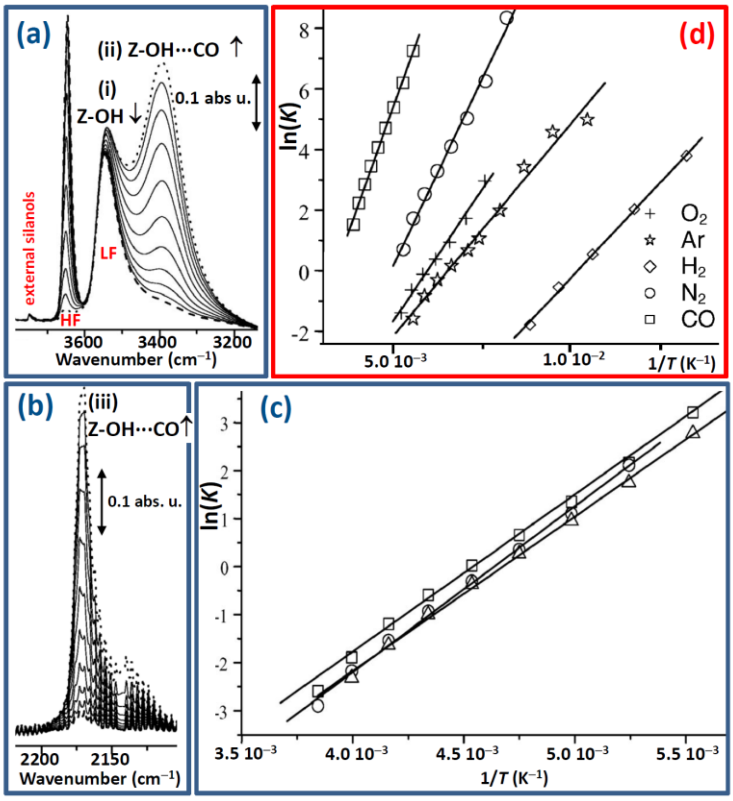

Figure 29. Part (a): VTIR spectra, in the ν(OH) stretching region, collected by dosing CO on H-NA-Y zeolite at constant *p*, changing *T* in the 280 K (dashed spectrum) – 170 K (dotted spectrum) interval. Part (b): as part (a) in the ν(CO) stretching region Part (c): $\ln(K) = \ln\{I(T)/[(I_M - I(T))\ (p/p_0)]\}$ vs. $1/T$ plots, Eqs. (30) and (31), obtained from the decrease of the band (i) in part (a), and from the from the increase of the bands (ii) or (iii) in parts (a) and (b), respectively. Part (d): $\ln(K)$ vs. $1/T$ plots for CO (averaged over the 3 datasets reported in part (c), open squares), N_2 (open squares), O_2 (crosses), Ar (open stars) and H_2 (open diamonds). The different slopes clearly reflect the different adsorption enthalpies of the different molecules. Adapted by permission of the Royal Society of Chemical (copyright 2006) from Ref.[154]

7.2.2. Discrimination between two different adsorption sites for CO on Na-ferierite zeolite

As anticipated above, the greatest advantage of the VTIR technique versus the standard microcalorimetry and isosteric heat of adsorption measurements consists in its site selectivity. A typical example where this advantage has been exploited is reported by the joint experimental and theoretical work of Arean and Nachtigall[719] Figure 30a reports the VTIR spectra of the adsorption of CO on Na-ferierite zeolite having a Si:Al ratio of 8:1. Two IR bands are clearly observed at 2175 and 2158 cm^{-1}, clearly due to the presence of two families of adsorption sites. The weak IR absorption band observed at 2113 cm^{-1} is due to a minority of CO molecules interacting through the oxygen atom with a single Na^+ cation.[288] This specie is no longer discussed in this section as Section 7.2.3 will be devoted to it.

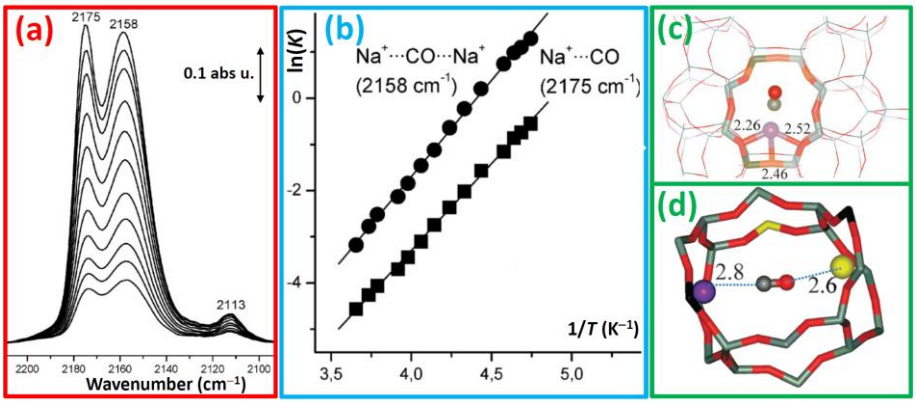

Figure 30. Part (a): VTIR spectra (zeolite blank subtracted) of CO adsorbed on Na-FER, Si:Al = 8:1. From top to bottom, temperature goes from 207 to 264 K and the equilibrium pressure moves from 0.19 to 1.17 mbar. Part (b): $\ln(K) = \ln\{I(T)/[(I_M - I(T))\,(p/p_0)]\}$ vs. $1/T$ plots, Eqs. (30) and (31), of the deconvoluted components of the 2175 and 2158 cm^{-1} bands reported in part (a). Part (c): optimized coordination of the Na^+ cation and the corresponding single site CO adsorption complex responsible of the 2175 cm^{-1} band. Framework Al, Si, and O atoms are depicted as black, grey, and red sticks, respectively; Na^+, C and O atoms of CO are shown as violet, grey and red balls, respectively. Distances are given in Å. Part (d): optimized CO adsorption complexes formed on dual cation sites responsible of the 2158 cm^{-1} band. The CO molecule interacts with the primary Na^+ cation (violet ball) through the C atom (grey ball) and with the secondary Na^+ cation (yellow ball) through the O atom (red ball). Framework Al, Si, and O atoms are depicted as black, grey and red sticks, respectively. Adapted by permission of the Royal Society of Chemical (copyright 2012) from Ref.[719]

Periodic DFT calculations allowed the authors to attribute the former to CO molecules interacting with a single Na^+ cation through the carbon end (see Figure 30c) and the later to CO molecules interacting with two adjacent Na^+ cations through both ends (see Figure 30d). An accurate band deconvolution was used to disentangle the integrated area of the two components in all the series of spectra reported in Figure 30a, allowing so the authors to use Eq. (31) for the two separated datasets and so to obtain $-\Delta H^0$ = 30 and 35 kJ mol^{-1} for the $Na^+\cdots CO$ and the $Na^+\cdots CO\cdots Na^+$ complexes, respectively. It is evident that the standard microcalorimetry and isosteric heat of adsorption measurements would have provided only averaged values in this case. Periodic DFT calculations further supported the energetic values extracted from VTIR: the computed $-\Delta H^0$ was found to be 29 and 32-35 kJ mol^{-1} for the $Na^+\cdots CO$ and the $Na^+\cdots CO\cdots Na^+$ complexes, respectively, see Table 8.

Table 8. Summary of some relevant adsorption enthalpies ($-\Delta H^0$), entropies ($-\Delta S^0$) and wavenumber of the measured IR band ($\tilde{\nu}$) for molecular adsorption on Brønsted and Lewis acidic sites in zeolitic frameworks as determined by VTIR. When provided by the original works, also the corresponding incertitude has been reported. For comparison also some results obtained adsorption by microcalorimetry (μCal), isosteric heat of adsorption (Qisost); chromatography pulse (CP) and periodic DFT (pDFT) techniques are also reported. NR = not reported; NM = not measurable. Some correlation among the values reported in this Table are reported in Figure 31. Previously unpublished Table analyzing data reported in the references quoted in the last column.

probe	Zeolite, site	method	$\tilde{\nu}$ (cm^{-1})	$-\Delta H^0$ (kJ mol^{-1})	$-\Delta S^0$ (J K^{-1} mol^{-1})	Ref.
H_2	H-Na-Y, Brønsted site in supercage	VTIR	4115	11.4	NR	[154]
H_2	Li-FER, Li^+ site	VTIR	4090	4.1 ± 0.8	57 ± 10	[704]
H_2	Li-ZSM-5, isolated Na^+ site	VTIR	4092	6.5 ± 0.5	90 ± 10	[275]
H_2	Na-FER, Na^+ site	VTIR	4100	6.0 ± 0.8	78 ± 10	[274]
H_2	Na-ZSM-5, isolated Na^+ site	VTIR	4101	10.3 ± 0.5	121 ± 10	[275]
H_2	Na-ZSM-5, isolated Na^+ site	VTIR	4100	11	NR	[702]

H_2	K-FER, K^+ site	VTIR	4111	3.5 ± 0.8	57 ± 10	274
H_2	K-ZSM-5, isolated Na^+ site	VTIR	4112	9.1 ± 0.5	124 ± 10	275
H_2	Mg-Na-Y, Mg^{2+} site in supercage	VTIR	4056	18.2 ± 0.8	136 ± 10	706
H_2	Mg-X, Mg^{2+} site in supercage	VTIR	4065	13 ± 0.8	114 ± 10	738
H_2	Ca-A, Ca^{2+} site	VTIR	4083	12 ± 1	121 ± 10	739
H_2	Ca-Na-Y, Ca^{2+} site in supercage	VTIR	4078	15 ± 1	127 ± 10	710
H_2	Ca-X, Ca^{2+} site in supercage	VTIR	4082	11 ± 1	118 ± 10	712
N_2	H-Y, Brønsted site in supercage	VTIR	2334	15.7 ± 0.8	121 ± 10	708
N_2	H-Na-Y, Brønsted site in supercage	VTIR	2336	20.2	NR	154
N_2	H-ZSM-5, Brønsted site	VTIR	2331[a]	19.7 ± 0.5	125± 5	697
N_2	H-FER, Brønsted site	VTIR	2331[a]	19.1 ± 1.0	131 ± 10	707
N_2	H-β, Brønsted site	VTIR	2333	19 ± 1.0	140 ± 10	715
N_2	H-MCM22, Brønsted site	VTIR	2332	14.5 ± 2.0	105 ± 10	721
O_2	H-Na-Y, Brønsted site in supercage	VTIR	1553	14.8	NR	154
Ar	H-Na-Y, Brønsted site in supercage	VTIR	3616[b]	15.2	NR	154
CO	H-ZSM-5, Brønsted site	VTIR	2173	29.4 ± 0.8	148 ± 10	708
CO	H-ZSM-5, averaging all sites	μCal	NM	27	NM	728
CO	H-Y, Brønsted site in supercage	VTIR	2173	25.6	161	693
CO	H-Na-Y, Brønsted site in supercage	VTIR	2162	30.6	NR	154
CO	H-FER, Brønsted site	VTIR	2172	28.4 ± 0.8	147 ± 10	708
CO	H-FER, Brønsted site	VTIR	2173	28.4 ± 1.0	145 ± 10	719
CO	H-β, Brønsted site	VTIR	2174	27 ± 1.0	150 ± 10	715
CO	H-MCM22, Brønsted site	VTIR	2174	23.5 ± 2.0	130 ± 10	721
CO	Na-β, isolated Na^+ site	VTIR	2180	29.3	NR	285
CO	Na-FER, isolated Na^+ site	VTIR	2175	30.5 ± 3.0	150 ± 10	278
CO	Na-FER, isolated Na^+ site	pDFT	2178	29	NR	719
CO	Na-FER, interaction with 2 Na^+ sites	VTIR	2158	34.5 ± 3.0	152 ± 10	278
CO	Na-FER, interaction with 2 Na^+ sites	pDFT	2153-2175	32-35	NR	719
CO	Na-Y, isolated Na^+ site	VTIR	2172	27 ± 2	NR	719
CO	Na-Y, isolated Na^+ site	pDFT	2172	24-26	NR	719
CO	Na-A, interaction with 2 Na^+ sites	VTIR	2163	27	NR	719
CO	Na-A, interaction with 2 Na^+ sites	pDFT	2160	30	NR	719
CO	K-β, isolated K^+ site	VTIR	2167	25.7	NR	285
CO	K-FER, K^+ isolated site	VTIR	2163	25 ± 2.0	NR	719
CO	K-FER, isolated K^+ site	pDFT	2164	18-20	NR	719
CO	Cs-X, basic framework O	VTIR	2124	25 ± 1.0	71 ± 5	705
CO	Ca-A, Ca^{2+} site S1	VTIR	2179	31.3 ± 2.0	176 ± 10	281
CO	Ca-A, Ca^{2+} site S2	VTIR	2188	45.6 ± 2.0	170 ± 10	281
CO	Ca-Y, site in supercage	VTIR	2197	47	NR	284
CO	Ca-Y, $Ca(CO) \rightarrow Ca(CO)_2$ equilibrium	VTIR	2191	36	NR	284
CO	Sr-Y, site in supercage	VTIR	2191	45.3	179	283
CO	Sr-Y, $Sr(CO) \rightarrow Sr(CO)_2$ equilibrium	VTIR	2187	30.2	138	283
CO_2	H-Y, Brønsted site in supercage	VTIR	2353	28.5 ± 1.0	129 ± 10	713
CO_2	H-Y, Brønsted site in supercage	Qisost	2360	27	NM	723
CO_2	H-ZSM-5, Brønsted site	VTIR	2345	31.2 ± 1.0	140 ± 10	711
CO_2	H-ZSM-5, Brønsted site	μCal	NM	30	NM	727
CO_2	H-ZSM-5, Brønsted site	Qisost	NM	28.8	NM	724
CO_2	H-ZSM-5, Brønsted site	Qisost	NM	28.7 ± 0.7	83	725
CO_2	H-ZSM-5, Brønsted site	CP	NM	33	83	740
CO_2	H-β, Brønsted site	VTIR	2348	33 ± 1.0	146 ± 10	715
CO_2	H-FER, Brønsted site	VTIR	2346	30.2 ± 1.0	125 ± 10	741
CO_2	Na-A, interaction with 2 Na^+ sites	VTIR	2360	42 ± 2.0	135 ± 10	717
CO_2	Na-A, interaction with 3 Na^+ sites	VTIR	2349	44 ± 2.0	140 ± 10	717

CO_2	Na-A, averaging Na^+ sites	Qisost	NM	47	NM	[717]
CO_2	K-FER, isolated K^+ site	VTIR	2346	40 ± 1.0	148 ± 10	[716]
CO_2	K-FER, interaction with 2 K^+ sites	VTIR	2355	43 ± 1.0	152 ± 10	[716]
CO_2	K-FER, average on all sites	μCal	2347	50-59 [c]	NM	[716]
NH_3	H-ZSM-5, Brønsted site, NH_4^+ formation	VTIR	1410	128 ± 5.0	184 ± 10	[714]

[a] The reported values refer to the average of the $-\Delta H^0$ and $-\Delta S^0$ values obtained applying the VTIR approach to both the ν(OH) band of the engaged Brønsted sites and to the ν(CO) or ν(NN) band of the adsorbed molecules.
[b] In this case the VTIR approach was applied to the perturbation of the HF band of Bronsted sites in the Y supercage which wavenumber moves downward from 3650 cm^{-1} to 3616 cm^{-1} upon formation of ZOH···Ar adducts, resulting in $\Delta\tilde{\nu}$ (OH) = 34 cm^{-1}, see Section 2.1.
[c] Depending on the Si/Al ratio.

Table 8 summarizes the adsorption enthalpies, entropies (when available) and the wavenumber of the measured IR band for some relevant examples of molecular adsorption on Brønsted and Lewis acidic sites in zeolitic frameworks as determined by VTIR that could not be discussed in detail for sake of brevity. When performed on the same system, few $-\Delta H^0$ values obtained with other experimental approaches (or DFT calculations) are also reported for comparison. Figure 31 summarizes some correlations among the $-\Delta H^0$, $-\Delta S^0$, $\tilde{\nu}$ (HH) and $\tilde{\nu}$ (CO) values obtained by VTIR experiments for the adsorption of molecules in zeolitic frameworks. The overall data do not show a commune simple trend (Figure 31), nevertheless, there is a rough positive correlation between enthalpy and entropy of adsorption:

$$-\Delta H^0 \ \alpha \ -\Delta S^0 \qquad (32)$$

and this correlation is better defined within the subsets of data referred to a single molecule. Besides molecular adsorption in zeolites,[735, 736, 742] such trend, already referred to as entropy–enthalpy compensation, was observed in the literature for a range of chemical processes involving weak interaction forces such as the formation of weakly associated molecular complexes,[743, 744] weak hydrogen bonding[745, 746] and Langmuir-type adsorption from solution.[746]

Correlation (32) is related to the fact that the stronger the interaction between the probe molecule and the adsorbing centre is, the greater will be the corresponding decrease of molecular motion freedom, which results in an increasing order of the system. Hence, referring to absolute values, a greater $-\Delta H^0$ will result in a correspondingly greater $-\Delta S^0$.[735, 736, 742]

Otero Arean and Garrone have recently showed that within zeolites and Cr-MIL MOFs the enthalpy–entropy correlation ($-\Delta H^0 \ \alpha \ -\Delta S^0$) does not follow a straight line, but a concave curve.[735, 742] This trend, clearly observed also in the whole set of data reported in Figure 31a is due to the fact that the adsorbed molecules cannot lose more than all of their degrees of freedom of motion, $-\Delta S^0$ has consequently an inherent limit, whereas (in principle) $-\Delta H^0$ has not. The $-\Delta S^0$ limit is not reached in the adsorption process, because some rotational and vibrational freedom (against the adsorption site) remains in the adsorbed state. The summary of the data obtained on zeolites (Figure 31a), representing a larger dataset with respect to that considered in the works of Otero Arean and Garrone, [735, 742] confirm their model as a steep increase in $-\Delta H^0$ is observed when $-\Delta S^0$ approaches values as high as 120 J mol^{-1} K^{-1}.

From Figure 31b (c) a rough negative (positive) correlation between enthalpy and the $\tilde{\nu}$ (HH) ($\tilde{\nu}$ (CO)) stretching frequency is clearly observed. This behaviour is due to the fact that a stronger absorption enthalpy results in a larger perturbation of the stretching mode of the molecule $|\Delta\tilde{\nu}|$, that is negative for H_2 ($\Delta\tilde{\nu}$ (HH) < 0) and positive for CO ($\Delta\tilde{\nu}$ (CO) > 0).[23, 29, 231]

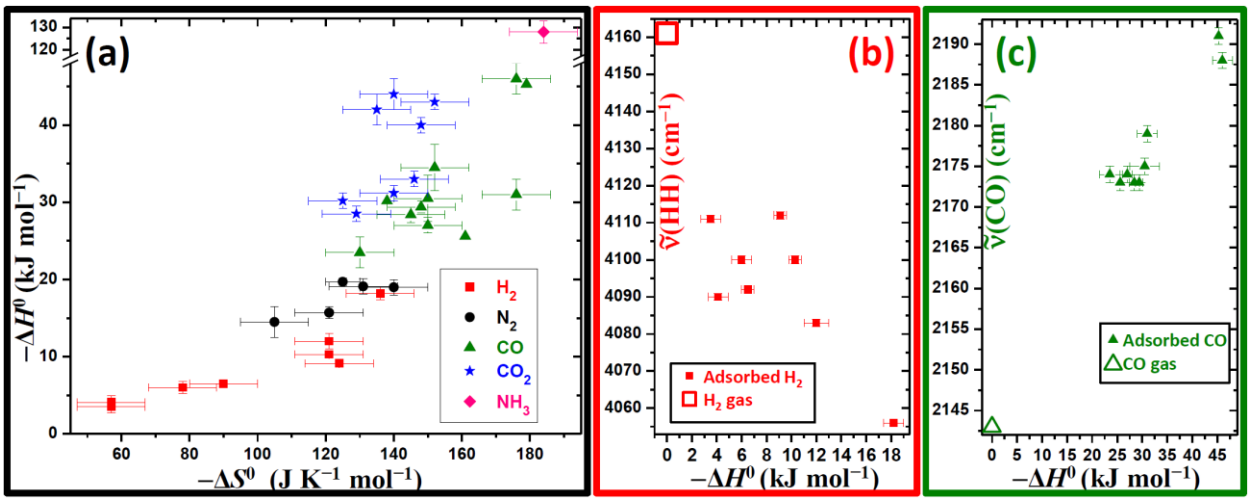

Figure 31. Part (a): Correlation between $-\Delta H^0$ and $-\Delta S^0$ values obtained by VTIR experiments for the adsorption of H_2 (red squares), N_2 (black circles) CO (black circles) CO_2 (blue stars) and NH_3 (pink rhomb) molecules in zeolitic frameworks. Part (b): Correlation between $\tilde{\nu}$ (HH) and $-\Delta H^0$ for H_2 molecule adsorbed in zeolites (full red squares); the open red squares represent the unperturbed H_2 molecule ($-\Delta H^0$ = 0 kJ mol^{-1}; $\tilde{\nu}$ (HH) = 4161 cm^{-1}). Part (c): Correlation between $\tilde{\nu}$ (CO) and $-\Delta H^0$ for CO molecule adsorbed in zeolites (full green triangles); the open green triangle represents the unperturbed CO molecule ($-\Delta H^0$ = 0 kJ mol^{-1}; $\tilde{\nu}$ (CO) = 2143 cm^{-1}). When reported in the original articles also the incertitude on $-\Delta H^0$ and $-\Delta S^0$ values have been plotted; for both $\tilde{\nu}$ (HH) and $\tilde{\nu}$ (CO) we assumed an error of ± 1 cm^{-1}, as most experiments have been performed with a resolution of 2 cm^{-1}. Previously unpublished figure analyzing data reported in the references quoted in the last column of Table 8.

7.2.3. Linkage isomerism of simple molecules adsorbed zeolites: determination of the difference in ΔH^0 for the two isomers by VTIR

Linkage isomerism is present when we have the co-presence of two (or more) coordination compounds having the same composition but differing with the connectivity of the metal (M) to a ligand (L). If the ligand is a diatomic molecule (L = AB) then only two linkage isomers are possible: M···AB and M···BA. The linkage isomeric complexes have different vibrational frequencies, and so can be identified by IR,[747, 748] if both energetically stable. The relative population of the two isomers will be determined by the relative difference in ΔH^0 and by the temperature of the experiment, so that a focused VTIR experiment will allow to determine the difference in the relative stability $\Delta[\Delta H^0]$ of the two complexes. The phenomenon of isomerism on adsorption has a relevant importance in catalysis, because the energetically less favorable state has different chemical properties and the excess of energy, which could be used to pass the activation barriers. It can thus be considered as an activated state and could play the role of intermediate in catalytic reactions.[748]

As deeply discussed in Section 3.1.1., CO forms, with alkaline metal cations hosted in zeolite channels and cavities, linear $M^+\cdots CO$ adducts through the carbon end, for which IR spectra are characterized by a main, blue-shifted cation specific, IR band appearing in the 2150-2180 cm^{-1} range (M = Li, Na, K, Rb, Cs). At lower frequency, a weak band always mirrors the main band (compare the trends of the full and open symbols in Figure 7), being red-shifted of about the same range as the blue shift undergone by the main band (see Table 9):[226-228] lower $|\Delta\tilde{\nu}|$ for Cs, larger for Li. Several different attributions were assigned to red-shifted band, among them also a coordination to the cation site via the oxygen end, forming linear $M^+\cdots OC$ linkage isomer. The

definitive proofs that this was the correct assignment comes some years later and was due to a VTIR experiment performed on Na-ZSM-5 by Arean et al.[288]

The IR spectra of that experiment are reported in Figure 32: part (a) reports the temperature range 83-203 K while part (b) refers to the 223-303 K interval. In part (a) the main band at 2178 cm^{-1}, due to the standard $Na^+\cdots CO$ adduct widely discussed in Section 3, behaves in an expected way, see Eq. (24) upon temperature increase decreasing its intensity (see blue arrow), but the small band at 2113 cm^{-1} behave in the opposite way, as it increases upon increasing T (see red arrow). In the temperature range covered by panel (b) both bands decreases upon increasing T (see corresponding arrows). This observation allowed Arean et al to definitively assign the 2113 cm^{-1} band to $Na^+\cdots OC$ adduct and to extract from the IR data the enthalpy needed to change form C-bonded adducts to O-bonded ones.

Indeed the two adducts are in thermodynamic equilibrium among the two linkage isomers:

$$ZM^+\cdots CO \rightleftharpoons ZM^+\cdots OC \qquad (33)$$

which is driven by temperature T and by the difference in the adsorption enthalpies between the two linkage isomers:

$$\Delta[\Delta H^0] = \Delta H^0(M^+\cdots OC) - \Delta H^0(M^+\cdots CO) \qquad (34)$$

A VTIR experiment, acting on the temperature, is able to displace this equilibrium. The constant K of the equilibrium (33) is given by:

$$K = \frac{\theta(T)_{M\cdots OC}}{\theta(T)_{M\cdots CO}} = \frac{I(T)_{M\cdots OC}}{I(T)_{M\cdots CO}} \frac{\varepsilon_{M\cdots CO}}{\varepsilon_{M\cdots OC}} \ , \qquad (35)$$

where $\theta(T)_{M\cdots OC}$ and $\theta(T)_{M\cdots CO}$ are the fractional coverages of the O- and C-bonded complexes (at the temperature T), respectively and where corresponding $I(T)$ and ε are the integrated IR band and the molar absorption coefficient. The third term of Eq. (35) holds because for both complexes $I(T) \propto \theta(T)\varepsilon$ with the same proportionality constant related to the sample thickness and the cation concentration in the sample. Combining Eq. (35) with the van't Hoff equation (29), once obtains:

$$\frac{I(T)_{M\cdots OC}}{I(T)_{M\cdots CO}} \frac{\varepsilon_{M\cdots CO}}{\varepsilon_{M\cdots OC}} = \exp(-\Delta[\Delta H^0]/RT) \exp(\Delta[\Delta S^0]/R) \qquad (36)$$

Taking the natural logarithm it is finally obtained:

$$ln\left[\frac{I(T)_{M\cdots OC}}{I(T)_{M\cdots CO}}\right] = -\frac{\Delta[\Delta H^0]}{RT} + \frac{\Delta[\Delta S^0]}{R} + ln\left[\frac{\varepsilon_{M\cdots CO}}{\varepsilon_{M\cdots OC}}\right] \ . \qquad (37)$$

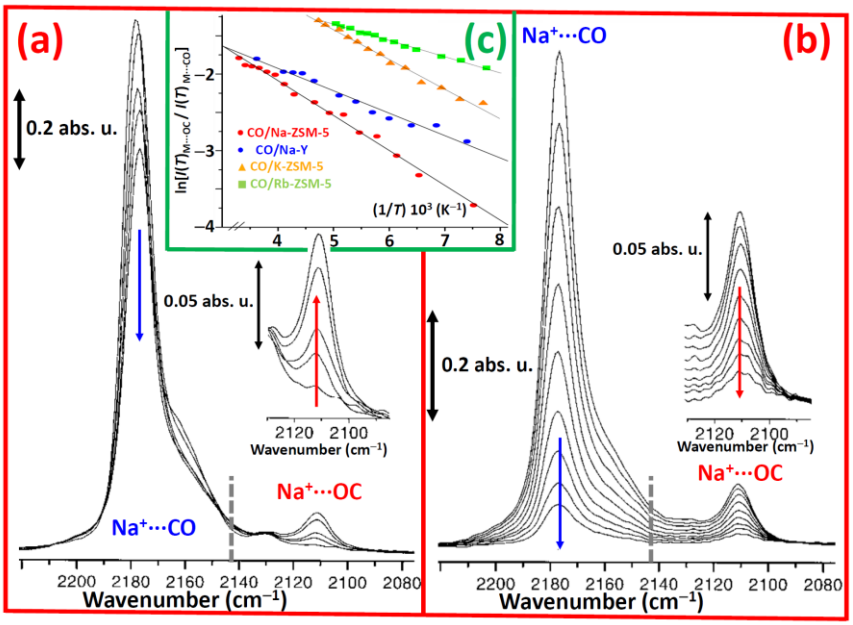

Figure 32. VTIR spectra of CO (ca. 0.8 Torr) adsorbed on Na-ZSM-5. Part (a) from top to bottom: 83, 133, 153, 183, and 203 K. Part b) from top to bottom: 223, 233, 243, 253, 263, 273, 283, 293, and 303 K. The two insets show an expanded view of the $ZNa^+\cdots OC$ band. The blue and red arrows indicates the evolution of the $ZNa^+\cdots CO$ and $ZNa^+\cdots OC$, respectively, in the temperature interval concerned by the two parts of the figure. The gray dashed lines indicate the position of the ν(CO) stretching frequency of the unperturbed molecule: $\tilde{\nu}_0(CO) = 2143\ cm^{-1}$. Part (c): $\ln[I(T)_{M\cdots OC}/I_{M\cdots CO}]$ vs. $1/T$ plots, Eq. (37), obtained from the spectra reported in parts (a) and (b) (red circles). Remaining data refers to similar experiments performed on other zeolites and reported in successive articles: Na-Y (blue circles),[691] K-ZSM-5 (orange triangles),[694] Rb-ZSM-5 (green squares).[698] The corresponding full lines represent the best linear fit of the experimental data. See Table 9 for the quantitative values of $\Delta[\Delta H^0]$ determined from the slopes of the best fit lines. Parts (a), (b) adapted by permission of Wiley-VCH (copyright 1998) from Ref.;[288] Part (c) adapted by permission of MDPI AG (copyright 2002) from Ref.[287]

According to Eq. (37), the measure of the integrated area of the IR bands of the two linkage isomers as a function of T allows extract $\Delta[\Delta H^0]$ as the slope of the best linear fit of the experimental data (Figure 32c red dots), obtaining $\Delta[\Delta H^0] = 3.8\ kJ\ mol^{-1}$. Unfortunately, in this case, $\Delta[\Delta S^0]$ can be obtained only if the two molar absorption coefficient of the two adducts have been carefully determined (see Section 6).

After this important experiment, several others followed on different zeolites, which results are summarized in Table 9, while for some of them, the corresponding van't Hoff's plots are reported in Figure 32c: Na-Y (blue circles),[691] K-ZSM-5 (orange triangles),[694] and Rb-ZSM-5 (green squares).[698] Note that in all cases the $\Delta[\Delta H^0]$, defined in Eq (34), are positive as the O-bonded complexes are always less stable than the corresponding C-bonded ones, so that the slopes of the van't Hoff's plots are negative, while in all the other examples reported in Section 7.2 they were positive, see Figure 28c, Figure 29c,d and Figure 30b and, the corresponding ΔH^0 values are negative, see Table 8.

Table 9. Summary of some relevant adsorption enthalpy differences $\Delta[\Delta H^0]$ for the $ZM^+\cdots CO \rightleftharpoons ZM^+\cdots OC$ equilibrium between the two linkage isomers in different zeolites and of the wavenumber of the corresponding C- and O-bonded adducts, as determined by VTIR. Previously unpublished Table analyzing data reported in the references quoted in the last column.

Zeolite	$\tilde{\nu}$ (CO) of $ZM^+\cdots CO$ (cm^{-1})	$\tilde{\nu}$ (CO) of $ZM^+\cdots OC$ (cm^{-1})	$\Delta[\Delta H^0]$	Ref.

			(kJ mol^{-1})	
H-ZSM-5	2174	2120	4.6	[698]
Li-ZSM-5	2195	2100	7.8 [a]	[696]
Li-ZSM-5 [b]	2188	2110	5.1[a]	[696]
Na-ZSM-5	2178	2113	3.8	[288]
K-ZSM-5	2166	2117	3.2	[694]
Rb-ZSM-5	2161	2120	1.8	[698]
Cs-ZSM-5	2157	2122	-	[284]
Silicalite-1	2160	2122	3.0	[700]
Na-β	2180	2112	5.8	[285]
K-β	2167	2120	5.6	[285]
Cs-β	2156	2124	-	[286]
Na-FER	2175	2113	4.0	[278]
H-Y	2173	2124	4.3	[692]
Na-Y	2171	2122	2.4	[691]
Ca-Y	2197	2094	11.0	[284]
Ca-Y [b]	2191	2094	8.0	[284]
Sr-Y	2191	2095	9.8	[283]
Sr-Y [b]	2187	2098	7.6	[283]
Na-ETS-10	2176	2115	-	[382]
K-ETS-10	2166	2125	-	[382]

[a] In this case a quantitative determination of $\Delta[\Delta H^0]$ was more complex because of the concomitant presence of di-carbonyl $Li^+(CO)_2$ and $Li^+(CO,OC)$ species, partially overlapped to the bands of $Li^+(CO)$ and $Li^+(OC)$ monocarbonyl species, complicating the equilibria present in the system and making more difficult the quantitative extraction of the $I(T)_{Na\cdots OC}$ and $I_{Na\cdots CO}$ integrated area.[695, 696]

[b] Values referring to the $ZM^{2+}\cdots(CO)_2 \rightleftharpoons ZM^{2+}\cdots(CO,OC)$ equilibrium between dicarbonyl species (M = Ca or Sr). In this case the presence of more than one equilibrium makes the extraction of the $\Delta[\Delta H^0]$ value has been more complex than the explained here in Eqs. (34)-(37) referring to the unique equilibrium (33) and the reader should refer to the original works for the complete set of equations.

CO molecule is not the only one able to form linkage isomers once adsorbed in zeolites. Tsyganenko et al.[748] observed the linkage isomerism phenomenon for the CN^- anion adsorbed on different alkali-metal exchanged X zeolites. Performing VTIR experiments they were able to obtain the adsorption enthalpy differences $\Delta[\Delta H^0]$ for the $ZM^+\cdots NC^- \rightleftharpoons ZM^+\cdots CN^-$ equilibrium, as summarized in the top part of Table 10. It is interesting to note that no linkage isomerism was found for CO adsorbed on M-X-zeolites (M = alkali metal cation). This is due to strong interaction of CO with the basic oxygen anions that have a higher negative charge for these systems.[705] For this reason CO interaction with the framework oxygen atoms of Cs-X zeolites is even stronger than with Cs^+ cations, and that results, for lowest coverages, in the band at 2124 cm^{-1}, corresponding to an ν(CO) mode that is red-shifted instead of blue-shifted, as always observed for $M^{n+}\cdots CO$ adducts on alkali- and alkali-hearth-cations, see Section 3.1, Figure 7, Figure 8, and Table 8. On these basis Tsyganenko et al. attributed this band to CO molecules, which form side-on $O^{\delta-}\cdots CO$ complexes with the most basic surface O anions.[705] This attribution is in agreement with the high basicity of Cs-X zeolites, see Section 4. The anionic nature of the CN^- molecule

(isoelectronic to CO) minimize the integration with the negatively charged framework oxygen atoms and makes the linkage isomerism possible.

Linkage isomers have also been reported by Zecchina et al.[382] for the NO molecule adsorbed on alkali-metal exchanged ETS-10 zeolites, see bottom part of Table 10. It is worth noticing that the $\tilde{\nu}$ (CO) and $\tilde{\nu}$ (NO) frequencies of the linkage isomers observed on Na-ETS-10 and K-ETS-10 exhibit a perfect linear correlation, see above full and open orange squares in Figure 11b.

Table 10. Top part: summary of the adsorption enthalpy differences $\Delta[\Delta H^0]$ for the $ZM^+\cdots NC^- \rightleftharpoons ZM^+\cdots CN^-$ equilibrium in different cation exchanged forms of X zeolite and of the wavenumber of the corresponding N- and C-bonded adducts, as determined by VTIR. Table reproduced with permission from Ref.[748], copyright Royal Society of Chemistry 2010. Bottom Part: as top part for the $ZM^+\cdots NO \rightleftharpoons ZM^+\cdots ON$ equilibrium in different cation exchanged forms of ETS-10 zeotype; unpublished table reporting data from Ref.[382]

Zeolite	$\tilde{\nu}$ (CN) of $ZM^+\cdots NC^-$ (cm^{-1})	$\tilde{\nu}$ (CN) of $ZM^+\cdots CN^-$ (cm^{-1})	$\Delta[\Delta H^0]$ (kJ mol^{-1})
Na-X	2195	2184	> 20
K-X	2157	2144	21 ± 5
Rb-X	2150	2138	17 ± 3
Cs-X	2149	2138	7.7 ± 1.0
Zeolite	$\tilde{\nu}$ (NO) of $ZM^+\cdots NO$ (cm^{-1})	$\tilde{\nu}$ (NO) of $ZM^+\cdots ON$ (cm^{-1})	$\Delta[\Delta H^0]$ (kJ mol^{-1})
Na-ETS-10	1898	1857	-
K-ETS-10	1891	1868	-

8. Space resolved experiments: IR microscopes, IR beamlines at synchrotron facilities and stimulated Raman scattering (SRS) microscopy

This Section is divided into three subsections. The first deals with a general overview on of microspectroscopic techniques applied to heterogeneous catalysts. Subsection 8.2 deals with a scanning IR microspectrometric study of the styrene oligomerization in H-ZSM-5 performed at the U10B beamline of the NSLS synchrotron. Finally, subsection 8.3 discusses how stimulated Raman scattering microscopy reveals the evolution of the accessibility and 3D distribution of Brønsted sites in mordenites subjected to a progressive dealumination treatment.

8.1. Development of microspectroscopic techniques to study heterogeneous catalysts

Besides the development of environmental TEM,[749-766] *in situ* diffraction setups,[767] several *in situ* microspectroscopic techniques have been recently developed to investigate, at the micrometric and sub-micrometric scale, catalytic reactions in heterogeneous catalysts: XAFS,[24, 768-775] fluorescence,[24, 655, 771, 776-797] UV-Vis,[798] Raman,[24, 26, 799-801] and IR,[24, 26, 40, 661, 770, 790, 802-819] particularly using synchrotron radiation IR sources. These spectroscopic methods have proven to be very successful in elucidating valuable structure-function relationships for catalytic reactions.

The greet advantage of combining vibrational spectroscopies with microspectroscopic methodology consists in providing at the μm scale a direct insight into the chemical nature of the reagent molecules, potential reaction intermediates, and reaction products. Coupling an IR spectrometer with an optical microscope allows to ensure that only a localized area of the catalyst sample is probed.[40] This innovative technique was particularly informative in the characterization of zeolitic and microporous materials. Published studies covered several aspects including the decomposition of the organic template,[802] the mapping of the boron distribution in B-ZSM-5,[782]

diffusion phenomena,[661, 790, 803, 805, 806, 808, 809, 814-816, 819] mass transport,[810-812] hydrogen and deuterium spillover in Y zeolite,[804] ethene oligomerization in H-ZSM-5,[799] and styrene oligomerization in H-ZSM-5.[40]

8.2. Styrene oligomerization in H-ZSM-5

Weckhuysen et al.[40] developed the scanning IR microspectrometer system working in reflection mode reported in Figure 33a and operating at the U10B beamline of the National Synchrotron Light Source (NSLS), Brookhaven National Laboratory (Upton, NY, USA). With this instrument the authors followed *in situ* the styrene oligomerization in H-ZSM-5 zeolite. A coffin-shaped H-ZSM-5 crystal (100 μm × 20 μm × 20 μm, see microphotograph in parts (d) and (e) of Figure 33) was exposed to 4-fluorostyrene and heated to 373 K for 10 min and the IR spectrum from the 5 μm × 5 μm region in the center of the crystal was recorded (top curve in Figure 33b). Two sharp features, at 1534 cm^{-1} (with the shoulder at 1521 cm^{-1}) and at 1510 cm^{-1} are due to the oligomeric products (structures **2** and **3** in Figure 33d) and to the reactant (structure **1** in Figure 33d and bottom IR spectrum in Figure 33b), respectively. Figure 33c reports spectra recorded *in situ* during the reaction at 373 K, showing the decrease of the reactant band and the increase of the product feature.

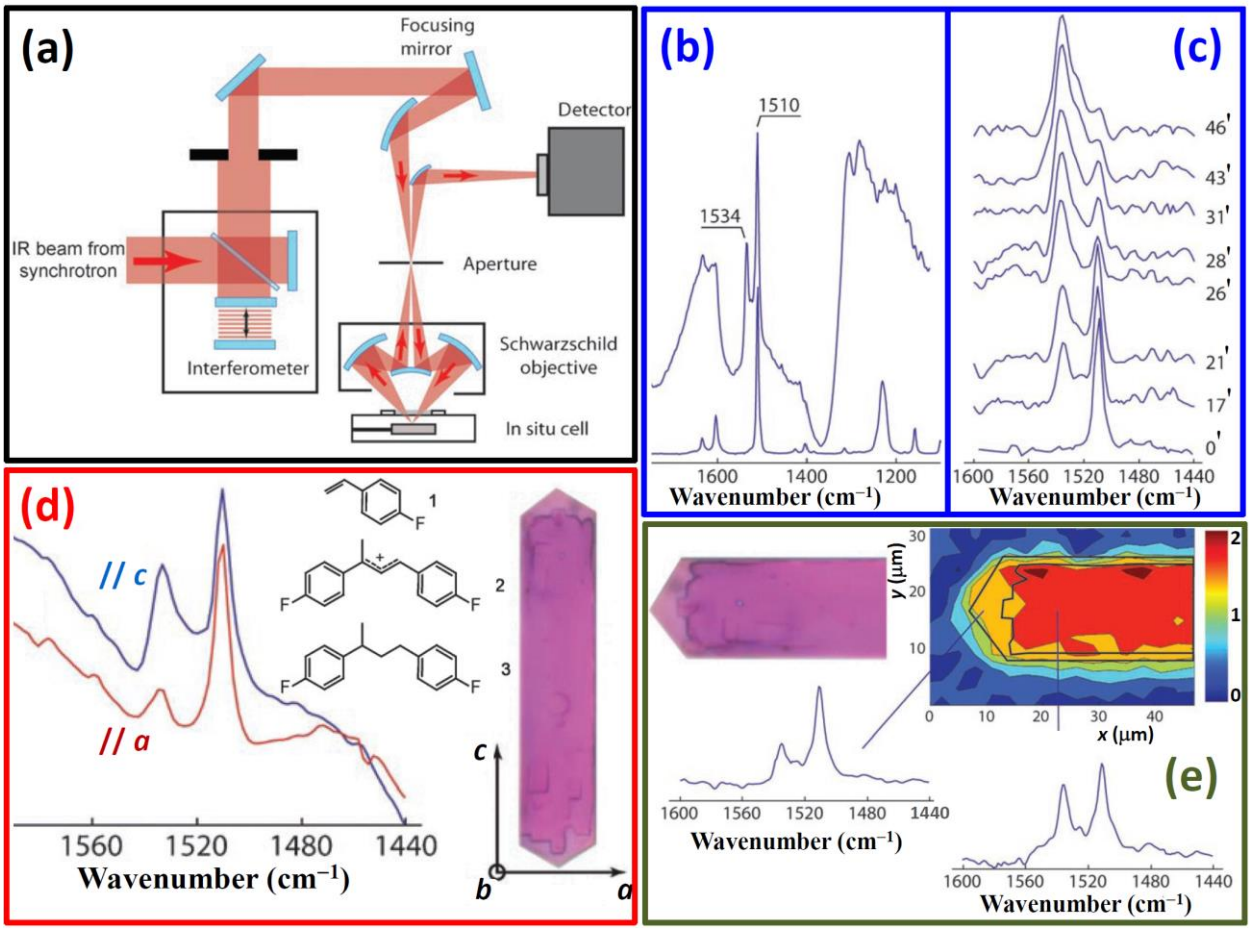

Figure 33. Part (a): Scheme of the scanning IR microspectrometer system working in reflection mode. The microscope uses a Schwarzschild-type objective. An area of the sample defined by the aperture is spectroscopically sampled by the instrument, and an image is built-up by raster scanning the specimen through the focused beam. Part (b): IR spectrum of an individual H-ZSM-5 crystal in contact with 4-fluorostyrene (top spectrum); IR spectrum of liquid 4-fluorostyrene (bottom spectrum). Part (c): time evolution (from bottom to top in minutes) of the background subtracted

IR spectra taken *in situ* during the oligomerization reaction of 4-fluorostyrene. Part (d): Optical microphotograph of the H-ZSM-5 crystal after reaction with 4-fluorostyrene showing the crystallographic directions *a*, *b* and *c* (right). *In situ* IR spectra recorded with two light polarizations parallel to the *a* (red curve) and *c* (blue curve) MFI axis (left). The central part reports the chemical structures of 4-fluorostyrene monomer **1** and of the two dimeric reaction products **2** and **3**. Part (e): fragment of optical microphotograph of the ZSM-5 crystal after reaction with 4-fluorostyrene (top left). Intensity of the IR band at 1534 cm^{-1} mapped over the crystal after reaction (top right. IR spectra taken from the edge (bottom left) and the body (bottm right) of the crystal, demonstrating the differences in the intensity ratio of the bands. Adapted by permission from Ref.[40], copyright Wiley-VCH (2008).

It is interesting to note that the intensity of the band at 1534 cm^{-1} strongly depends upon the relative orientation between the polarization vector of the synchrotron radiation IR light and the crystal axis (Figure 33d). Based on the light-polarization dependence of the optical absorption, only straight channels of ZSM-5 were found to host the oligomerization products.[780] In the spectra reported in Figure 33d the intensity of the IR band associated with the oligomeric products is higher with the light polarized along the *c* direction, implying that the transition moment associated with the vibrational mode is likely to be directed perpendicular to the long molecular axis of the dimeric carbocation.[40] It is interesting to notice that the electronic dipole moment associated with optical transitions coincides with the long molecular dimension,[780] i.e., orthogonal to the vibrational one.

In a second series of experiments reported in the same work, Weckhuysen et al.[40] mapped the distribution of the reaction products **2** and **3** over the H-ZSM-5 crystal by scanning the individual crystal under the IR microscope. The spatial map of the 1534 cm^{-1} band is shown in Figure 33e. In a previous work, UV/ Vis microspectroscopy results have shown that dimeric carbocations are exclusively formed in the case of 4-fluorostyrene,[779] with lower concentrations at the edges of the crystals compared to that in the center. The intergrowth structure of ZSM-5[820-822] entails that the two-dimensional channel network is oriented nonuniformly, i.e., at the edges of the crystal straight pores, open to the top surface of the crystal are accessible. On the contrary, in the center region of the crystals sinusoidal pores are accessible. A nonuniform product distribution was rationalized in terms of blockage of straight versus zigzag pores, as discussed in previous publications.[779, 780] The spatially resolved IR spectra here reviewed (see spectra in Figure 33e) are fully in line with the optical absorption results, with lower intensity of the 1534 cm^{-1} band at the edges as compared to the body of the crystal, further supporting the assignment.

8.3. Stimulated Raman scattering microscopy revealing the 3D acid site distribution in acid zeolite catalysts

3D nanoscale reactivity mapping of catalytic reactions in zeolite catalysts has become possible with visible light. Infrared microspectroscopy (see previous Sections) does not offer the required 3D spatial resolution, but Raman does, and it could lead to very interesting information on the location of catalytic sites in the pore system. Raman is however not so interesting as such because of the strongly interfering background fluorescence and because of the inherently weak signals. The sensitivity of Raman was increased recently by several orders of magnitude by combining two picosecond-lasers (Stokes and pump lasers) for obtaining non linear spectroscopy.[57-59] When the difference between the two lasers matches a vibrational frequency in the sample, a Raman peak is detected, (intensity increase in the Stokes and decrease in the Pump). This has been used to design a spectroscopic technique with a spatial resolution better than 1 μm,[60] widely applied to biological issues.[823-831] The technique is named stimulated Raman scattering (SRS) microscopy is a newly developed label-free chemical imaging technique that overcomes the speed limitation of confocal

Raman microscopy while avoiding the nonresonant background problem of coherent anti-Stokes Raman scattering (CARS) microscopy.[59, 61, 62]

SRS microscopy was recently applied by Roeffaers et al.[655] to nitriles probes (CH_3CN and benzonitrile, hereafter PhCN) in small-port mordenite crystals (5-10 µm large), see (Figure 34). They applied this sophisticated technique to shed light into an old open question in the zeolite community, related to the small-port (SP) and large-port (LP) transition in mordenites.[832-835] It is indeed known since decade that mordenite exists in two forms that differ in their adsorption behavior: SP-MOR and LP-MOR, having effective apertures of ca. 4 and ca. 7 Å, respectively. The effective aperture of LP-MOR is in accordance with the diameter of the large channels in the ideal crystal structure of mordenite,[165] see above Figure 22b. The SP to LP transition is achieved by a simple thermal treatment, where dealumination of the zeolite framework occurs, and is complete when about 20% of the tetrahedral framework aluminum is converted into octahedrally coordinated extra-framework species. According to Van Geem et al.,[834] the pore blocking in SP-MOR is caused by structural defects originating from differently oriented mordenite chains. The transition involves the removal of framework Al from the 4-membered rings forming the wall of the 8-membered ring side channels. Thereby, connections between segments of the main channel system are formed.

Roeffaers et al.,[655] by tuning the polarization of the laser beams, could show the specific orientation of deyterated acetonitrile in the side pockets and isolate the corresponding spectrum (Figure 34a-d). A uniaxial symmetry was observed with the signal about 2.3 times higher when the lasers are polarized in the crystallographic *b*-axis than in either the *a*- or *c*-axis, indicating that a fraction of nitriles is symmetrically oriented with respect to the crystallographic *b*-axis.

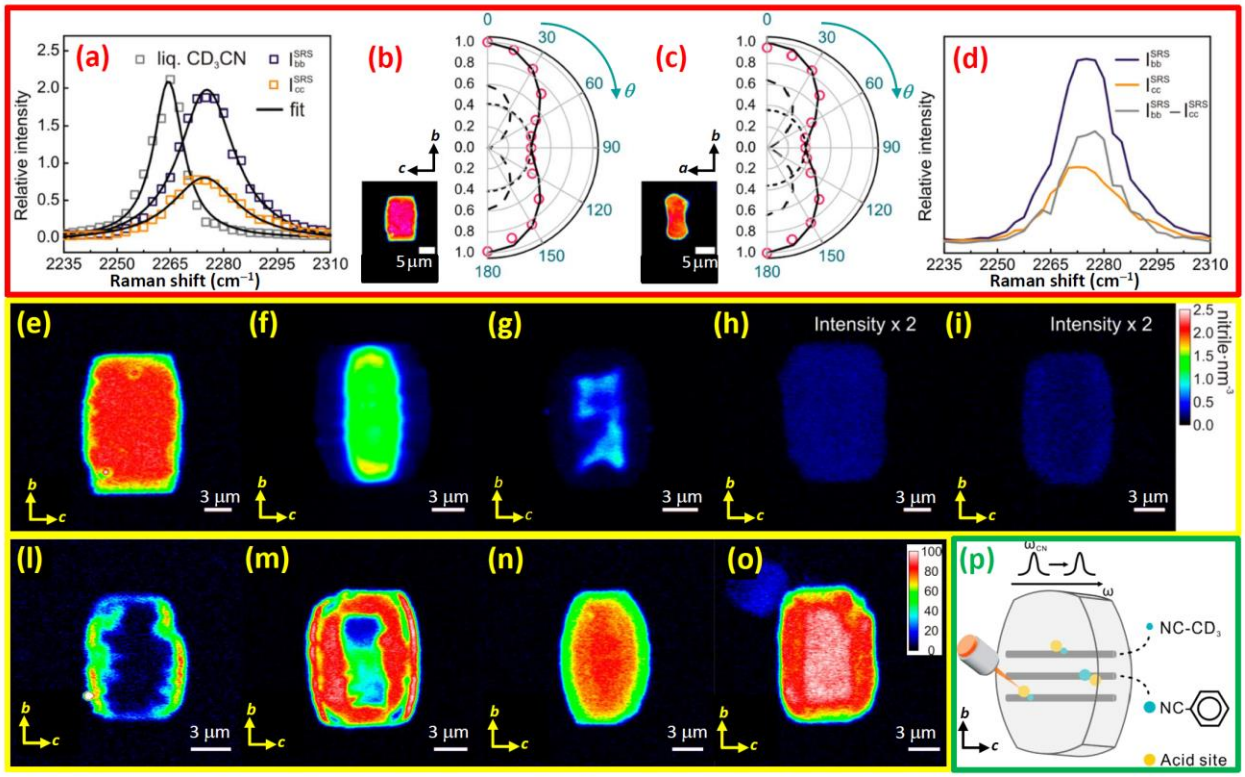

Figure 34. The top parts (a-d): SRS microspectroscopy and polarization dependence of CD_3CN adsorbed in the parent SP-MOR. Part (a): SRS response of the ν(C≡N) stretch region of liquid CD_3CN (×0.2, black data) and of CD_3CN adsorbed in the zeolite pores (averaged over a whole crystal) recorded with lasers polarized in crystallographic *b*- (violet data) and *c*-axes (orange data); the experimental spectra (scattered data) are fitted by a single Lorentzian curve

(solid line). Parts (b,c): polar plot for ν(C≡N) stretch (2275 cm^{-1}) in zeolite crystals with different crystal orientations shown in the insets as a function of θ (angle between laser polarization and crystallographic *b*-axis); the polar plots can be simulated by the sum (solid line) of a cos (2θ) function (anisotropic component, dashed line) and a circle (isotropic component, dotted line). Part (d): spectra for the anisotropic (violet curve) and the isotropic (orange curve) components in the ν(C≡N) stretch and of their difference (gray curve). Middle parts (e-i): chemical mapping of CD_3CN adsorbed in H-MORs at progressive stages of dealumination, from the parent SP-MOR (e) to strongly dealuminated on the right (i). False colour scale indicates the acid site density: from 0 to 2.5 nitrile/nm^3 for parts (e-g) and from 0 to 1.25 nitrile/nm^3 for parts (h,i). Crystal axes are indicated by arrows. Bottom parts (l-o): chemical mapping (2249 cm^{-1}) of PhCN adsorbed in H-MORs revealing the accessibility of acid sites; gradual enhancement of acid site availability in mildly dealuminated MOR from early (l), intermediate (m), and to late stages (n) of dealumination as well as severely dealuminated MOR (o). Images were recorded with lasers polarized along the crystallographic *c*-axis. False color scale indicates relative abundance of PhCN (from 0 to 100 a.u.). Crystal axes *b*, *c* are indicated by arrows. Part (p): cartoon representation of the SRD microscopy method. Adapted by permission from Ref.,[655] copyright American Chemical Society (2014).

They have mapped the concentration of the CD_3CN probe in the crystal, from 0 to 2.5 molecule/nm^3, which matched the framework aluminum atom density (Figure 34e-i). The authors followed the dealumination of the samples, and showed that it happened preferentially in the main channels, and leading to extraframework aluminum preferentially located in the side pockets, close to the remaining acid sites. Following the methodological scheme of using probes of increasing size (see Section 5), the increased accessibility of larger nitriles (PhCN) to the pores was also studied when increasing dealumination (Figure 34l-o). The influence on catalytic performance confirmed the observations, with increased accessibility but decreased acid sites density.[655]

9. Time resolved experiments

A full understanding of a catalytic reaction requires a thorough identification of precursor and intermediate species. Active species should be distinguished from spectators, often present on the surface of heterogeneous catalysts in general and inside zeolites pores in particular. In this regard spectroscopies in general and infrared (IR) spectroscopy, in particular, can play an important role. However, the spectroscopic identification of precursor and intermediate species is often difficult owing to their transient nature. The control of experimental parameters such as temperature, equilibrium pressure, reactants feed composition, and reactant-catalyst contact time allows experimentalists to alter the rates of dynamic processes and consequently to modify appreciably the relative concentrations of precursor, intermediate, and product species present under reaction conditions. In this context, time-resolved FTIR spectroscopy (with constant temperature and pressure during the experiment) and also temperature-time resolved (with both temperature and time changing simultaneously in a controlled way during the experiment) can be useful for kinetic investigations of several types of reactions.

The replacement of dispersive spectrometers by FTIR instruments in the 1980s drastically reduced the time scale for acquisition of an IR spectrum, from minutes down to seconds. Today, with "conventional" FTIR instruments, the fast FTIR acquisition mode allows sub-second time resolution. Fast FTIR spectra can be obtained by reducing the spectral resolution (proportional to the movable mirror translation) and by collecting the interferograms without performing the Fourier transformation. The latter is then performed instead at the end of the experiment.[23, 135, 143, 836-840] In this case the time resolution can reach 25–50 scans per second (still producing spectra with favorable signal-to-noise ratios), this being the time scale determined by the translation of the movable mirror. In such experimental conditions FTIR spectroscopy can represent a useful tool for investigation of processes that proceed on time scales associated with kinetic effects.

The different approach of the step-scan-mode allows to reach, in principle, a time resolution limited by the readout time of the IR detectors, typically in the order of 10^{-9} s, i.e. in the ns range,[34, 839, 841-850] To perform a step-scan investigation, a single kinetics experiment must be repeated *n* times (where *n* is the number of points of the interferogram) with the movable mirror fixed in each position x_j of the Michelson interferometer at which the usual acquisition of the interferogram should have taken place. Under these conditions, the data are signals $S_{xj}(t_i)$ as a function of time t_i for each position x_j. The time-resolved interferograms are then constructed by reading the signals $S_{xj}(t_i)$ collected at the same time (in the different experiments) as a function of x_j. The method is extremely powerful; however, it can be applied only to systems that guarantee a full reproducibility at the $\Delta t = (t_{i+1} - t_i)$ level. As most important catalysts are extremely complex structurally, such a severe reproducibility constraint is only rarely achieved. Moreover, the overall time resolution of the catalytic kinetic experiments may still be limited by other factors such as the excitation source used to trigger the reaction: pressure pulses or temperature jumps may take milliseconds, defining the overall kinetic resolution.[34] For these reasons the actual time resolution of step-scan FTIR experiments performed on zeolites is, at best, of 10^{-6} s (i.e. in the few μs range). There have been only few reports on the use of step-scan FTIR to characterize homogeneous,[851] heterogeneous[852-854] catalytic systems in general and zeolites[855-862] in particular.

This section develops into five subsections: 9.1, where IR spectroscopy is the unique technique used to investigate the time evolution inside a working zeolite (*in situ* experiments); 9.2, where the catalyst performance is monitored by MS or GC in parallel with the IR spectroscopy (*operando* experiments); and 9.3 where additional spectroscopies are added to the IR *operando* set-up. Finally, Subsection 9.4 is devoted to discuss an example of CO molecules generated by the photodissociation of diphenyl cyclopropenone with a nanosecond laser pulse inside the channels of mesoporous MCM-41 silica sieve,[862] while Subsection 9.5 deals with 2D IR pressure-jump spectroscopy of adsorbed species in zeolites followed by the step-scan mode.

9.1. *In situ* IR studies on reactivity in zeolites

9.1.1. Reactivity of CO with Cp_2Cr encapsulated inside Na-Y zeolite

Interaction of CO with Cp_2Cr hosted inside non-polar polystyrene (PS) matrix system resulted in a time-stable $Cp_2Cr(CO)$ monocarbonyl complex characterized by an intense ν(CO) band at 1900 cm^{-1} (Figure 28a),[734, 863] very similar to that previously reported in literature in the case of $Cp_2Cr(CO)$ in toluene solution.[864, 865] Conversely, when the Cp_2Cr is hosted in the polar Na-Y matrix, upon CO dosage, a rapid evolution in time is observed.[866, 867] An intense ν(CO) band immediately appears at 1850 cm^{-1} (blue circle and blue curve in Figure 35a), that is due to the formation of $Cp_2Cr(CO)$ monocarbonyl complex, see reaction (38). The red-shift of ν (CO) with respect to the value found in PS and in toluene is induced by the high ionicity of the Na-Y environment showing extraframework Na^+ and framework $O^{\delta-}$ Lewis acid-base pairs, see above Sections 4.1 and 4.2.2. By waiting in time this band is progressively eroded, and simultaneously three new bands at 1893, 1773 and 1724 cm^{-1} (red triangles in Figure 35a) appear, accompanied by a weak component at ~1980 cm^{-1} (red square) growing in a similar way.

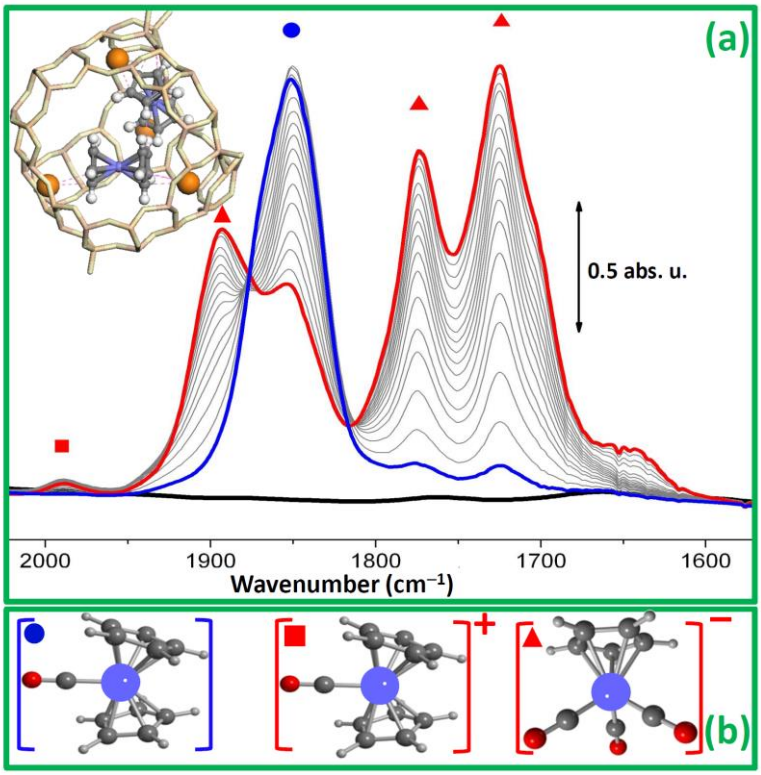

Figure 35. Part (a): time evolution of the FTIR spectra (at RT) of the Cp_2Cr/NaY systems before dosage of CO (black), immediately after (blue), and after 1h of exposure to CO (red). Gray spectra are intermediate between the blue and the red one.The left top corner inset reports two Cp_2Cr molecules encapsulated inside the supercage cavity of Na-Y zeolite represented in the stick mode (Si and Al, light orange; O, light yellow) while the Na^+ cations and the Cr, C and H atoms of the Cp_2Cr molecule are represented as orange, violet, grey and white spheres, respectively. Part (b): sticks and ball representation of the complexes responsible of the IR bands reported in part (a): neutral $Cp_2Cr(CO)$ (band labelled with a blue circle), cationic $[Cp_2Cr(CO)]^+$ complex (weak band labelled with a red square) and anionic $[CpCr(CO)_3]^-$ complex (three bands labelled with a red triangle). Previously unpublished figure reporting data from Refs.[866, 867]

$$2\ Cp_2Cr + Na^+Y^- + 2\ CO \rightarrow 2\ Cp_2Cr(CO) + Na^+\cdots Y^- \qquad (38)$$

$$2\ Cp_2Cr(CO) + Na^+\cdots Y^- + 2\ CO \rightarrow [Cp_2Cr(CO)]^+ \cdot\cdot Y^- + [CpCr(CO)_3]^- \cdot\cdot Na^+ + Cp \qquad (39)$$

The evolution of the spectra indicates that the monocarbonyl precursor (band at 1850 cm^{-1}) is transformed into a tricarbonyl charged species $[CpCr(CO)_3]^-$ (triplet at 1893, 1773 and 1724 cm^{-1})[868] through the loss of a Cp ring, while the weak component at ~1980 cm^{-1} is due to a fraction of $[Cp_2Cr(CO)]^+$ cationic species (Figure 35b).[868-870] On these basis, reaction (39) was inferred and supported by parallel Cr K-edge EXAFS analysis.[866, 867] This reaction requires the presence of two Cp_2Cr molecules inside the same supercage, see top-left inset in Figure 35a.

9.1.2. O_2-activation of H-Cu-SSZ-13 catalyst: *in situ* independent IR and XANES studies

Zeolite activation is a fundamental step in both catalysis and characterization purposes. Indeed the evacuation of water and other molecules adsorbed in the channels and cavities is necessary in catalysis to make the active sites accessible to reactants. A non-complete activation would result

in resistant water molecules that may block the activity of a fraction of the sites. The same holds when the activation is aimed to study the zeolite in presence of a specific probe molecule: the co-presence of water may prevent the probe adsorption and/or may result in misleading results because of co-adsorption on the same site.

IR spectroscopy is one of the best characterization technique to follow the progressive activation of a zeolitic framework and to verify that the completeness of the process because both the stretching ν(OH) and the bending δ(HOH) modes of the water molecule are IR active with a very high molar absorption coefficient (see Section 6.1); this makes possible to detect by IR spectroscopy very small amount of un-desorbed water molecules. This important IR check allows to prevent starting a catalytic test or a characterization study on samples that are not properly activated.

Figure 36a show the dehydration of the H-Cu-SSZ-13 zeolite in O_2 flow in the 30- 400 °C range as monitored by *in situ* FTIR spectroscopy. The desorption of adsorbed water molecules is appreciated by the disappearance of both the huge and broad absorption in the 3600-2600 cm^{-1} due to the ν(OH) mode of H-bonded water molecules (see Section 2.2) and the narrower and better defined band at 1623 cm^{-1}.[871, 872] As the spectra are not subtracted, framework contributions, *i.e.* overtones ν(T–O–T) modes, are always visible in the reported series at 1998, 1858, 1680 and 1535 cm^{-1}. The total disappearance of the 1623 cm^{-1} band at 250 °C (bold grey curve) is the indication that molecular water is almost completely desorbed at this temperature (see also the magnification in the inset of Figure 36a). The gradual appearance of 3611 and 3584 cm^{-1} bands related to ν(OH) of not H-bonded Brønsted groups is also observed together with that of free silanols located at the external surface of the zeolite (3737 cm^{-1} band) and with a component peculiar of this zeolite at 3656 cm^{-1}, assigned to $[Cu^{II}–OH]^+$ groups.[161, 363] Finally, it is interesting to note that for temperature 30 °C < T < 200°C, the band at 2420 cm^{-1} develops in intensity. Prior studies on water adsorption on protonic zeolites, deeply reviewed here in Section 2.2 (see Figure 2), demonstrated that this band is due to Fermi resonances between the perturbed zeolitic O-H stretch and O-H bending overtones of hydrogen-bonded water molecules, and that its intensity is most clearly evident at moderate water coverages in the zeolite.[136, 145, 177, 200, 873, 874]

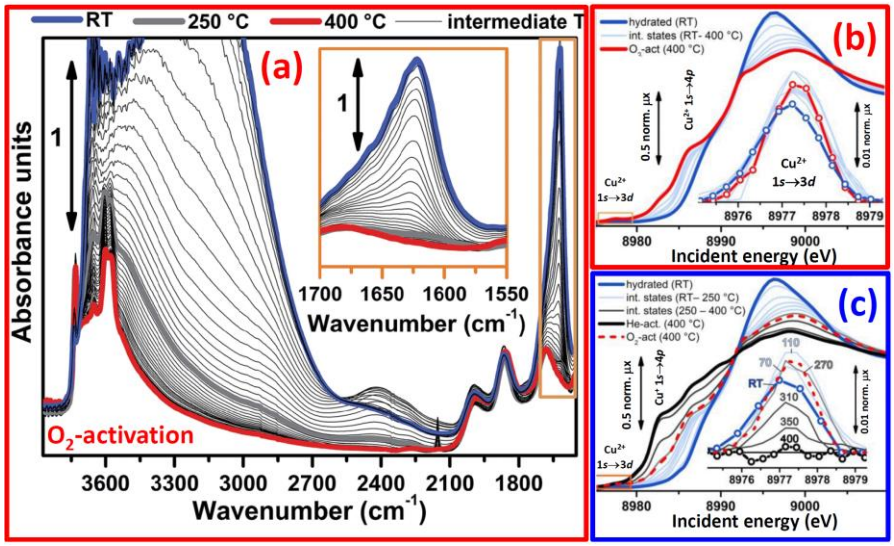

Figure 36. Part (a): Dehydration of the H-Cu-SSZ-13 zeolite in O_2 flow (30 ml min^{-1}; O_2:He = 1:1) as monitored by *in situ* FTIR spectroscopy. Spectra colors refer to different temperatures: the bold blue curve to 30 °C, bold grey curve

to 250 °C, bold red curve to 400 °C, thin black curves to intermediate temperatures. The inset shows a magnification of the signal related to the δ(HOH) bending mode of molecularly adsorbed water (spectral region highlighted by the orange box in the main panel). Part (b): *In situ* temperature-dependent XAS data collected during O_2-activation of the H-Cu-SSZ-13 in the 30-400 °C range. The main part reports the XANES spectra collected at ESRF BM23. The inset shows the magnified, background-subtracted, $1s \rightarrow 3d$ pre-edge peak typical of the d^9 Cu(II) cation, highlighted by the orange box in the main panel, for selected intermediate temperature steps. Part (c): as for parts (b) for He activation of the H-Cu-SSZ-13 catalyst. The final spectrum collected on the O_2-activated H-Cu-SSZ-13 sample at 400 °C is also reported for comparison as a red bold dashed curve. Adapted with permission from Refs.[363], copyright Royal Society of Chemistry 2015.

Borfecchia et al.[363] have supported the laboratory time resolved IR experiment reported in Figure 36a by a parallel XAS experiment preformed at the ESRF synchrotron (Figure 36b) in order to follow the evolution of the coordination and oxidation state of copper cations. The loss of water molecule coordinated to Cu^{2+} cations is monitored by the decrease of the white line (main resonance around 8995 eV). In agreement with the IR experiment this effect occurs in the 30 °C - 250 °C interval, while the XANES spectra collected in the 250 °C - 400 °C interval are almost unchanged. The presence of O_2 in the outgassing flow guarantees the maintenance of the +2 oxidation state of copper species, as testified by the $1s \rightarrow 3d$ weak (because dipole-forbidden) transition at 8977.5 eV, that is peculiar of Cu^{2+} species (d^9 cations). Activations performed in absence of O_2 (in vacuum or in flux of inert gas) follow a similar path till 250 °C, when all H_2O molecules adsorbed on Cu^{2+} are lost, while the 250 °C - 400 °C interval results in a progressive, and almost complete $Cu^{2+} \rightarrow Cu^{+}$ reduction (Figure 36c).[363] The EXAFS parts of the XAS spectrum (here not reported) reveals that in fully dehydrated conditions Cu^{+} have a lower coordination to framework oxygen atoms than Cu^{2+}.

In Section 9.3.1 we will review the same experiment performed by Kwak et al.[436] where both IR (in diffuse reflectance mode) and XANES spectra were collected simultaneously at the synchrotron (see below Figure 45). That approach has the evident advantage that the IR and XANES are collected exactly on the same sample, in the same environmental conditions allowing an almost direct one to one comparison between IR and XANES spectra collected along the temperature series; "almost" stands because the acquisition time to collect one spectrum is not the same for the two techniques. The price to pay for this important benefit is related to compromises in the experimental setup that must be taken to allow both techniques to be simultaneously operative, that differs from the ideal set-up for each single technique. This results in a lower quality of the collected spectra, that can be immediately appreciated comparing Figure 45 and Figure 36 in both their IR and XANES parts.

9.1.3. NH_3-SCR reaction followed *in situ* on Cu-SSZ-13 catalyst

The current technology of choice to reduce NOx emissions from power plants and exhausts from diesel-driven vehicles is based on the selective catalytic reduction (SCR) of nitrose oxides by ammonia (NH_3-SCR).[366-374] The best known catalysts for this reaction are V_2O_5 supported on TiO_2,[875-880] and Co-[370, 881, 882] Fe-[372, 883-887] or Cu-[162, 363, 364, 374, 430, 888-899] exchanged zeolites. Please note that the IR characterization of Cu-exchanged zeolites By N_2, CO and NO probes has been reviewd in Subsection 3.1.2.

In NH_3-SCR, NO is reduced by ammonia to N_2 and H_2O, according to the equation:

$$4\ NO + 4\ NH_3 + O_2 \rightarrow 4\ N_2 + 6\ H_2O\ . \qquad (40)$$

Among Cu-exchanged zeolites, in the last few years, large effort has been devoted to study a large variety of copper containing systems with CHA topology.[165] Most of the studies have been performed on low content Al CHA, namely SSZ-13, and SAPO-34, the homologue aluminum phosphate, varying both the copper sources and the exchange procedure. [161, 162, 363, 364, 430, 436, 890-892, 894, 895, 899-901] The reason of this interest on the CHA framework is related to its advantages with respect to other frameworks (MFI, BEA, MOR, etc…) that include a widespread thermal stability range and high activity under lean combustion e.g. in fuel-efficient diesel engines.

Despite the fact that reaction (40) has been known for many years, the precise mechanism and its rate determining step are still under discussion. Very recently, Cu-SSZ-13 has been considered as model system to propose a fully consistent catalytic cycle based on a single redox active copper center cycling through the oxidation steps +1 and +2,[364] see Figure 37a. All the species reported in the cycle have been identified by a parallel FTIR, EPR, XANES and EXAFS studies supported by DFT calculations. The proposed cycle is based on the presence of copper species and stable charge-neutral gas phase molecules only, avoiding the use of e.g. ½ O_2 or migration of charged species in order to match the stoichiometry of the reaction. Moreover, the suggested mechanism is relevant for the low end of the temperature interval relevant for the SCR reaction on these materials (250 °C - 300 °C) whereas other reactions may become important under more harsh conditions. The steps of the suggested cycle have been followed spectroscopically by the combined use of XAS (*operando*), EPR (*in situ*) and IR (*operando*), see Figure 37c-e, respectively. Cu-SSZ-13 has been characterized upon activation in diluted oxygen at 400 °C (see Section 9.1.2, Figure 36a) and then contacted by ammonia in gas phase at 100 °C. The effect of this treatment is reported in Figure 37b in difference plot. The negative bands, corresponding consumed bands are due to the ν(OH) modes of silanols (3737 cm^{-1}) and Brønsted sites (3611 and 3584 cm^{-1}) and $[Cu^{II}–OH]^+$ groups (3656 cm^{-1}), the latter species being also characterized by the perturbation mode of the framework $[TO_4]$ units at 905 cm^{-1}, not visible in the reported spectral range,[161, 162, 363] see also Section 3.3.1.

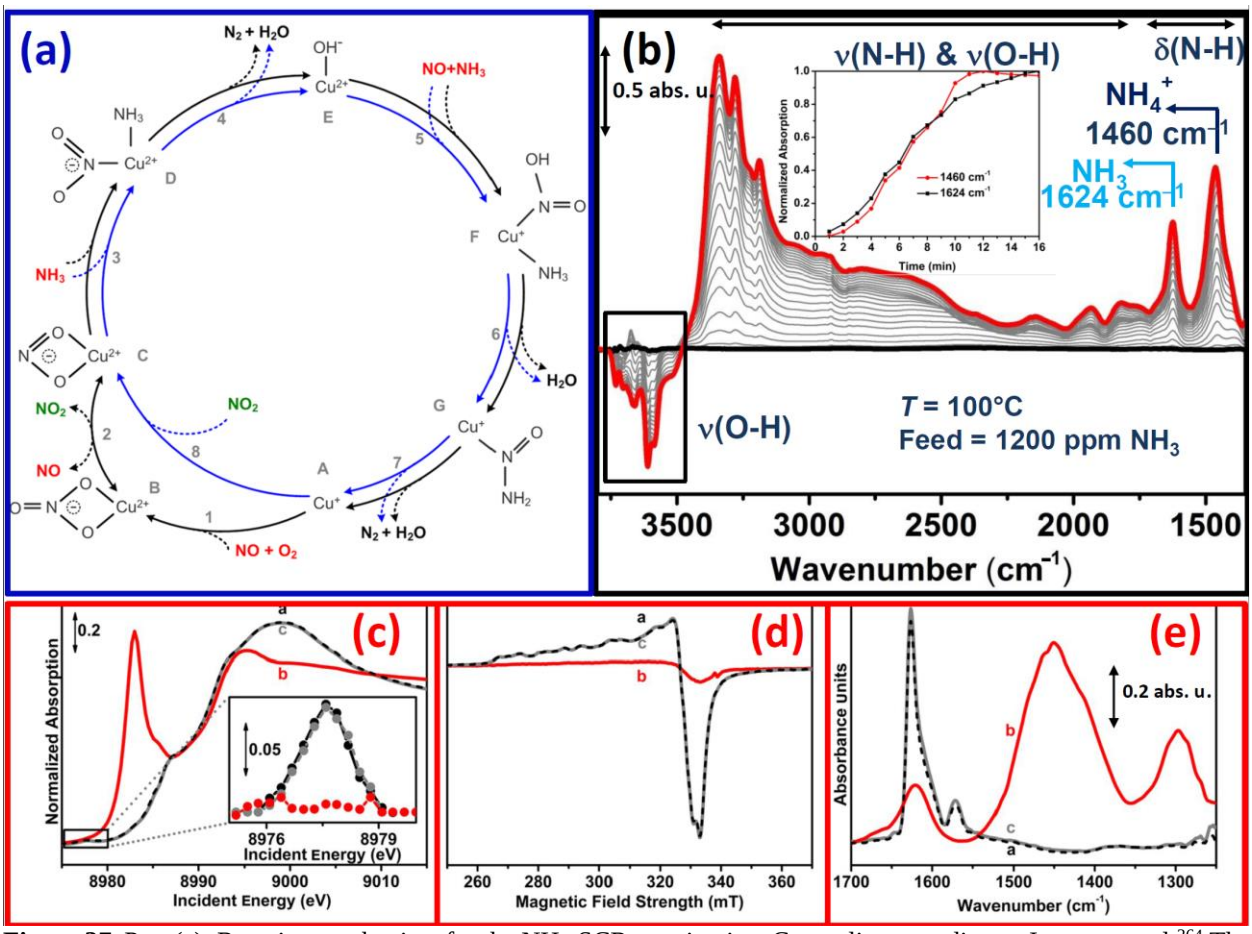

Figure 37. Part (a): Reaction mechanism for the NH_3-SCR reaction in a Cu-zeolite according to Janssens et al.[364] The fast SCR cycle is represented in blue, and the NO activation cycle is represented in black. Reactants are indicated in red, reaction products are indicated in black, and the NO_2 intermediate is indicated in green. In the standard SCR reaction, Eq. (40), the NO activation cycle, and fast SCR cycle run at equal rates; the stoichiometry of the standard SCR reaction is then found by adding these two cycles. The oxidation states of the Cu ions have been assigned according to the magnetic moment found in DFT: $M(Cu^{2+}) > 0.45$ and $M(Cu^{+}) < 0.1$. Part (b): difference FTIR dynamic spectra of NH_3 adsorption onto Cu-SSZ-13 at T = 100 °C with a flow rate of 50 ml/min (feed: 1300 ppm NH_3, He = rest). Spectrum of O_2-activated material at 400 °C (bold red spectrum in Figure 36a) has been used for subtraction. Black curve: O_2-activated material before NH_3 adsorption. Red curve: system saturated with NH_3. Grey curves: intermediate adsorption steps. The inset reports the normalized absorption of the 1460 and 1624 cm^{-1} bands as a function of exposure time to NH_3/He mixture. Part (c) *operando* XANES spectra collected during reduction and oxidation in SCR over of Cu-CHA (2.6 wt % Cu) at 200 °C in the following consecutive steps: (a) initial oxidation in 1000 ppm of NO/O_2 = 1:10 (dashed black curves); (b) reduction in 1200 ppm of NH_3/1000 ppm of NO (solid red curve); (c) re-oxidation in 1000 ppm of NO/O_2 = 1:10 (solid gray curve). Inset background-subtracted XANES Cu^{2+} $1s \rightarrow 3d$ dipole forbidden transition pre-edge peak, proportional to the amount of Cu^{2+} species. Part (d) as for part (c) for EPR spectra. Part (e) as for part (c) for IR spectra. Parts (a), (c)-(e): adapted with permission from Refs.[364], copyright American Chemistry Society 2015; part 8b) adapted with permission from Ref.[902]

Starting from low contact time of NH_3 exposure, the low frequencies region is dominated by two maxima at 1624 and 1460 cm^{-1}, which are assigned to asymmetric bending N-H vibration of molecular NH_3 adsorbed on Cu^{2+} Lewis sites and to bending N-H vibration of protonated NH_3 stabilized on Brønsted sites, respectively.[162] The multiple broad vibrational bands in the 3500-3000 cm^{-1} range are attributed to N-H stretching vibration of both NH_4^+ and molecular NH_3, while bands in the 2500-1700 cm^{-1} region are often assigned to solely NH_4^+.[162] The fact that 1624 and 1460 cm^{-1} bands develop with a similar dynamic trend as a function of the exposure time (see inset

in Figure 37b) suggests comparable acidity strength of Lewis and Brønsted adsorption sites. The 1460 cm^{-1} band intensity growth is accompanied by the consumption of the bands associated to ν(O-H) modes of Brønsted sites (negative bands observed at 3611 and 3584 cm^{-1}), due to NH_3 protonation over these specific sites with consequent formation of NH_4^+ ions. Negative bands are observed at 3737 and 3656 cm^{-1} indicating that NH_3 could also interact with less acidic silanols and CuOH sites, respectively.

In order to better investigate the difference in reactivity between NH_3 adsorbed on Cu sites and on Brønsted sites, pre-adsorbed NH_3 has been contacted with $NO+O_2$ at 200 °C as fixed temperature (Figure 38). Part (a) reports spectra collected in the first 10 minutes of contact time with $NO+O_2$: a gradual consumption of molecular NH_3 on Cu sites is observed, as evidenced by the negative bands at 1625 cm^{-1} and 1279 cm^{-1}, the latter contribution being assigned to symmetric bending N-H vibration of molecular NH_3 adsorbed on Lewis sites.[903] These two bands are completely eroded after 10 minutes. Concomitantly, negative bands of corresponding stretching vibration modes (3348, 3272 and 3182 cm^{-1}) are clearly observed. Interestingly, at these low contact times band at 1460 cm^{-1} does not decrease in intensity, but it is only slightly enhanced as a consequence of water formed *via* SCR. Only at longer contact times (see Figure 38b) maxima at 1460 cm^{-1} starts to vanish in intensity, being almost totally consumed after 50 minutes of exposure time. These results evidences that NH_3 stored on Cu sites is more reactive towards $NO+O_2$ than NH_3 stored on Brønsted sites. The fact that NH_3 stored on Brønsted sites starts to react only when Cu sites are ammonia free could be interpreted in two different ways. Assuming that SCR reaction takes place over the metal functionality of the catalyst, the migration of ammonia molecules from Brønsted sites to Cu sites is likely. According to this view, if the Brønsted sites are located close to the Cu ions in the zeolite, it is conceivable that an NO_2 molecule on a Cu ion can interact directly with a NH_3 molecule on a neighboring Brønsted site, making a reaction possible without the desorption of NO_2. Alternatively, NO_2 must be produced *in situ* and desorbed from the metal centers, allowing gas phase NO_2 to interact with NH_3 stored on a Brønsted site. This last hypothesis is reinforced by the fact that pre-adsorbed NH_3 onto H-SSZ-13, *i.e.* only NH_3 stored on Brønsted sites is present, does not show any reactivity towards $NO+O_2$, but only towards NO_2. A possible pathway for *in situ* NO_2(g) formation over Cu sites is represented by the reaction of NO with Cu-nitrates species, according to the following equilibrium:[902]

$$Cu^{2+}\cdots NO_3^- + NO(g) \leftrightarrow Cu^{2+}\cdots NO_2^- + NO_2(g) \quad . \qquad (41)$$

The formation of nitrates species stabilized on Cu^{2+} sites, *i.e.* $Cu^{2+}\cdots NO_3^-$, upon $NO+O_2$ interaction is well known.[10] In the experiment reported in Figure 38b, the formation of these species has been confirmed by the appearance of 1627 and 1570 cm^{-1} maxima at long $NO+O_2$ contact times.

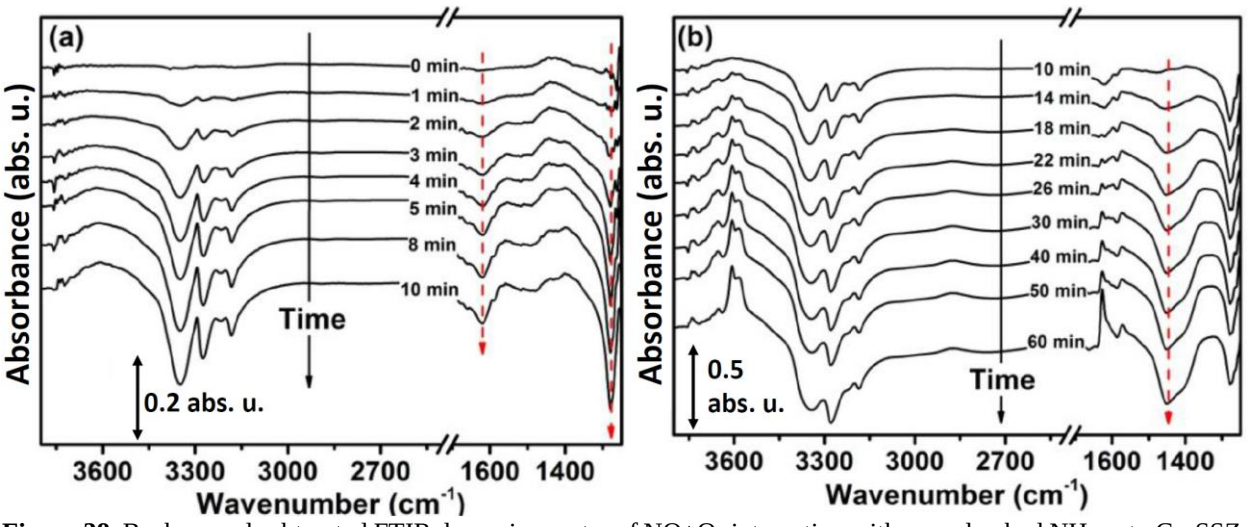

Figure 38. Background subtracted FTIR dynamic spectra of $NO+O_2$ interaction with pre-adsorbed NH_3 onto Cu-SSZ-13. Parts (a) and (b) report spectra series collected in the (0-10 min) and (10-60 min) ranges of contact time with $NO+O_2$, respectively. T = 200 °C, flow rate = 50 ml/min. Feed: NO = 1000 ppm, O_2 = 10%, He = rest. Spectrum of Cu-SSZ-13 pre-saturated with NH_3 at 200°C (bold red spectrum in Figure 37b) has been used for subtraction in both (a) and (b).Adapted with permission from Ref.[902]

9.2. *Operando* experiments on zeolite catalysts

Operando spectroscopy consists in the simultaneous spectroscopic characterization (by IR, Raman, UV-Vis, EPR, XANES, EXAFS, etc…, see below Section 9.3) of surface species and determination of catalytic activity and selectivity.[35] Here we will limit our discussion on vibrational spectroscopies. By establishing relationships between the nature and concentration of surface species on the one hand, and the catalytic activity on the other hand, it allows getting important insight in surface reaction mechanisms. At the steady state, however, the concentrations of surface intermediate species are often very low, except, in favorable cases (e.g. low temperature, or high absorption coefficient), the concentration of the not very reactive, most abundant reactive intermediate (*mari*).[904, 905] Identification by IR or Raman spectroscopy, however, can be crucial in understanding the reaction as it may, for instance, help to arbitrate between plausible reaction mechanisms proposed in the literature. Other surface species that can be abundant enough to be observable are those that accumulate on an inactive part of the catalyst and do not participate in the reaction (spectator species).[23] While such species are not generally much worth to study, their observation during the reaction can be sometimes misleading and a lot of care should be taken to distinguish them from species actually taking part in the reaction. Much more important are the species that accumulate on the active sites, leading to a decrease of the reaction rate (poison species). Such species can be naturally formed during the reaction, as a (side-)product, or added in the feed. In both cases, the study of these species (structure and location) implicitly gives important information as to the nature of the active sites they are blocking. In the following, typical examples are given, illustrating how *operando* IR spectroscopy studies can give insight on mechanisms of reactions occurring within zeolite pores.

9.2.1. *Operando* for characterizing the active Brønsted acidic sites in hydrocarbon conversion reactions

To our knowledge, the earliest *operando* study carried out on zeolite catalyzed reaction has been published by Ward, nearly 50 years ago,[906] who recorded the IR spectra of H-Y hydroxyl groups during cumene cracking. He reported a simultaneous increase of catalytic activity and decrease of free hydroxyl groups with reaction temperature, which he assigned to an increase of cumene interaction with the zeolite active sites, without, however, excluding the formation of coke species. While this interpretation is now highly disputable (the catalytic activity actually increased with temperature *despite* both a lower coverage of OH groups by cumene and coke formation), this early work clearly showed that "by studying a catalytic reaction by *in situ* [*operando*] infrared spectroscopy, new evidence concerning the centers of adsorption and catalytically active sites can be obtained"[906] and opened the way to further studies. Hence, in the early nineties, Saussey and coworkers[907] studied the transformation of cyclohexene over H-Y zeolites and have been able to establish relationships between the simultaneous decrease of the amount of zeolitic OH groups – assessed by the intensity of the ν(OH) bands (see section 2.1, above), the formation 'coke' species, evidenced by the ν(CC) bands at ca. 1600 cm^{-1}, and catalytic activity (conversion and selectivity changes). They could show in particular that the most acidic OH groups were primarily responsible and affected by coke formation.

Another strategy allowing establishing relationships between Brønsted acid sites and catalytic activity consists in selective *in-situ* poisoning the zeolite Brønsted acid sites. Such an approach has been used by Jolly et al.[908] in the case of n-hexane cracking on dealuminated zeolites: by dosing known amounts of lutidine, a probe molecule very selective for Brönsted acid sites, they could evidence the particular role of strongly acidic OH groups at 3600 cm^{-1} (see section 2.1. above) in this reaction and could exclude the participation of Lewis acid sites to the catalytic activity.

More recently, Marie et al.[909] have used *ex-situ*, Na^+-selective poisoning of the Brønsted acid sites of mordenite zeolites in order to provide experimental evidence for the catalytic role of each type of OH groups in this zeolite. A similar strategy, yet not using *operando* spectroscopy, has also been recently used by Gounder and Iglesia to determine the individual activities of mordenite OH groups for the protolytic cracking of light alkanes.[910] As already discussed in Section 5, mordenites have two very different pore systems, the 12-R main channels and the 8-MR side pockets (Figure 22). The three different acidic OH groups (already mentioned in section 5.4.1) are located in the main channels (crystallographic position O_7), in the side pockets (on the O_9), and at the interconnecting window (on the O_2). During a progressive introduction of sodium by cationic exchange of the zeolite, hydroxyls O_9H are removed preferentially (in the side pockets), followed by O_2H and O_7H are exchanged last. Using a series of progressively exchanged mordenites with increasing sodium content, the selectivity of xylene isomerization (Figure 39a) was progressively tuned to decrease disproportionation (Figure 39b), and then to increase the production of toluene while trimethyl benzene were suppressed. By comparing with the intensity of the ν(OH) for each of the three possible locations for OH groups (Figure 39c) with the simultaneously collected gas-phase chromatography data (Figure 39d), it was possible to assign the various reactions, producing each of the products, to a specific acidic OH group in a specific location in the pores. The role of sodium atoms could also be understood: Na^+ in the side pockets would favor adsorption of trimethyl-benzene at the window opening, thus changing available space in the main channels. Constrained hydroxyls in the side pockets were not accessible to the reactants under reaction conditions, but their presence lead to a global activity increase without any selectivity modification. Acid strength considerations, together with the observation of the "working hydroxyls," indicated an indirect effect of O_9H on the overall activity, probably related to a modification in the void space inside the micropores.

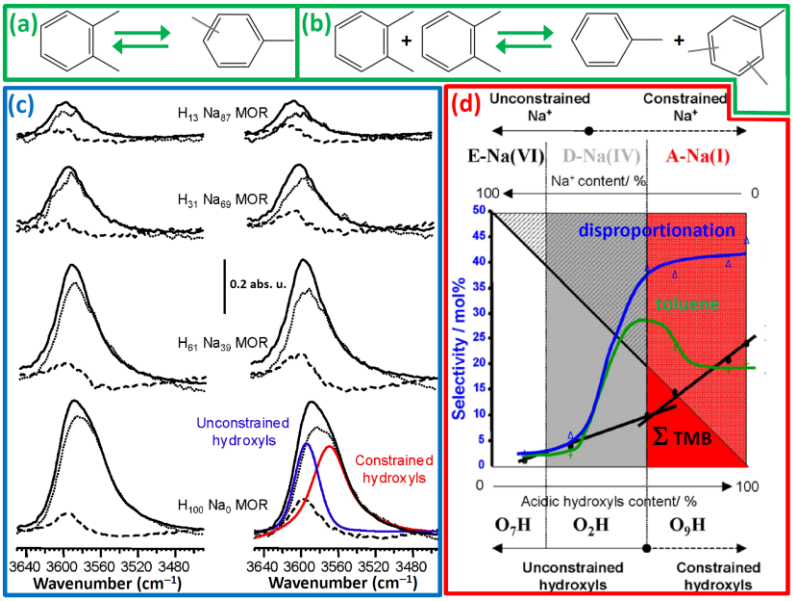

Figure 39. The two main ways for *o*-xylene conversion over acidic catalysts: Part (a) isomerization, which gives a mixture of *m*-xylene and *p*-xylene; Part (b) disproportionation which gives toluene and a mixture of trimethylbenzene isomers (1,2,3-, 1,2,4- and 1,3,5-TMB). Part (c) Left: IR spectra in the ν(OH) stretching region for selected H_xNa_{1-x} MOR samples (at different proton exchange rates: $13 \leq x \leq 100$) collected at 573 K before reaction with *o*-xylene (—) and after 1 min reaction (•••). Part (c) Right: as the left part with the (•••) spectra collected after 3 h of reaction. Spectra in dashed lines (- - -) correspond to the subtraction between (—) and (•••) and represent the hydroxyls consumed during the reaction. Spectra in the bottom right hand corner also show the expected spectra for the constrained and unconstrained OH (at high and low frequency, respectively) at 573 K before reaction. Part (d): Evolution of the selectivity in disproportionation products with the acidic hydroxyls content for isoconversion (42%) conditions obtained during the first moments of reaction at 573 K. Σ TMB is for sum of trimethylbenzene isomers. O_7H, O_2H and O_9H are for the three possible crystallographic locations of the OH groups. Reproduced from ref.[909] with permission, (copyright Elsevier, 2005).

9.2.2. *Operando* studies on ion-exchanged zeolites

By contrast with acid zeolites (see Section 2), the active sites of ion-exchanged zeolites are not detected by IR spectroscopy (see above Sections 3 and 4), and the spectroscopic observations are thus limited to the spectra of adsorbed species, from which one has to infer the nature or structure of the corresponding active site. Recent IR *operando* studies carried out over alkali exchanged zeolites will be illustrated here by the work of Groult et al.[911] who studied the conversion of methylbutynol (MBOH, 2-methyl-but-3-yn-2-ol, $(CH_3)_2C(OH)C{\equiv}CH$) over Na-X zeolite. The understanding of the transformation of methylbutinol is of interest because it has been proposed as a test reaction for acid base properties, allowing discriminating base, amphoteric and acidic catalysts on the basis of the products selectivity. Basic surfaces, in particular, lead to a decomposition of MBOH into acetone and acetylene.[912] Moreover, when carried out over a series of basic zeolites, the yield of this route generally follow the trend expected from the framework oxygen basicity (see Section 4.1, above). Generally, however, a fast deactivation generally occurs, so that the relevance of this test reaction with respect to the basic properties of the fresh catalyst may be questioned when the activity is reported at steady state.[911] In order to tackle the fast deactivation, Groult and co-workers have monitored the catalytic activity of a Na-X zeolite using a micro GC, allowing a time resolution in the order of 150 s, in parallel with the spectroscopic characterization of surface species. Examination of the stretching ν(≡C-H) band, see Figure 40a, allowed distinguishing three types of adsorbed MBOH species: species A interacting with the acid-base pairs of the zeolite through their O-H groups, leading to a nearly free ν(≡C-H) frequency at

~3325 cm^{-1}, species B, forming a π-coordination complex with the Na^+ cation characterized by $\tilde{\nu}$ (≡C-H)= 3277 cm^{-1} and species C, that is a ≡C-H ⋯ O hydrogen bonded complex with the basic oxygen centers resulting in $\tilde{\nu}$ (≡C-H) = 3215 cm^{-1}, see the corresponding schemes in the insets of Figure 40a. On the basis of mechanistic consideration, only the former species, A, with a much lower concentration than B or C, was proposed as the adsorbed intermediate leading to the observed products (acetone and acetylene), while B and C species would be spectator or reservoir species.[911] Moreover, a striking feature of these spectra (Figure 40b) is the continuous growing of intense bands at 1690-1703 cm^{-1}, characteristic of ν(C=O) stretching vibration, over the deactivation period, which the authors assigned to surface accumulation of acetone and of its dimerization product, coordinated to extra framework Na^+ cations, hence blocking the dissociation of MBOH.[911]

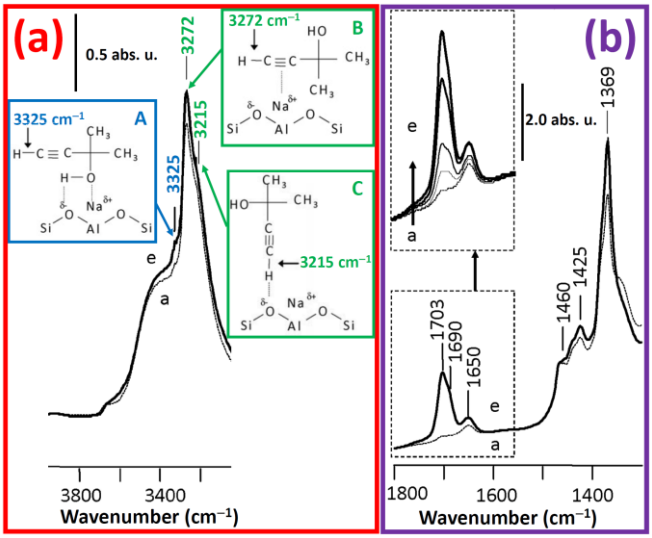

Figure 40. Evolution of the *operando* DRIFT spectra registered at 413 K during the deactivation period of MBOH transformation over Na-X. Part (a): spectra 3900–3100 cm^{-1} range at 0 min (introduction of MBOH in the carrier gas), spectrum **a** and at 20 min, when reaching the steady state, bold spectrum **e**. The complex ν(≡C-H) band shows three features assigned to reactive (MBEOH species A) and non-reactive, spectators (MBEOH species B and C). Part (b): Spectra in the 1800-1200 cm^{-1} range showing the accumulation of ketonic species during the deactivation period; same spectra as in (a). Adapted with permission from Ref.,[911] copyright Royal Society of Chemistry 2010.

9.2.3. Plasma on zeolites and *operando* IR

Plasma assisted heterogeneous catalysis is a new and quickly expanding field.[913-927] Gas phase processes are very fast under plasma conditions, and the role of the surface is hardly understood. Tracking adsorbed species by *operando* infrared spectroscopy is one of the only methods for obtaining information on the reaction mechanism. Infrared spectroscopy inside a plasma reactor showed that template removal in a zeolite was possible at very low temperature. This replacement for the calcination process maintained the small crystal size in nanoparticles of beta zeolite, and even reduced Pt inside the pores without any sintering of the metal or of the zeolite nanoparticles. The nature of the active species for hydrocarbon removal was still an open question.

Operando observation of surface species during template removal in an argon or an oxygen plasma showed that the most active species was originating in water (Figure 41).[922] The intensity of the infrared band for hydrocarbon (ν(CH) at 2900-3000 cm^{-1}, Figure 41a-c) was plotted vs time during the reaction, and compared with the intensity for adsorbed molecular water (δ(OH) at 1630 cm^{-1}). In an Ar plasma, the hydrocarbon decomposition starts quickly and nearly stops after 5 s,

when all water is removed from the surface. With an O_2 plasma, the hydrocarbon decomposition starts at the same speed, but when all residual water is removed the reaction still goes on at reduced pace (Figure 41d), probably due to the presence of ionized oxygen leading to ozone in the micropores. This ozone is the main agent for decomposition of hydrocarbons in the second stage of the reaction. These experiments were performed without external heating and the temperature in the solid remained below 150 °C. This showed that the most active species for decomposition of hydrocarbons inside the pores of a zeolite under plasma originates from the ionization of water. Radicals generated are very active species and can remove hydrocarbons and template (or even reduce Pt in that specific example) in the pores of zeolite at very moderate temperature, below 150°C, as testified by the TEM investigation (inset in Figure 41e), and the IR study of adsorbed CO performed on the Pt-β samples after cold O_2 plasma treatment (Figure 41f).

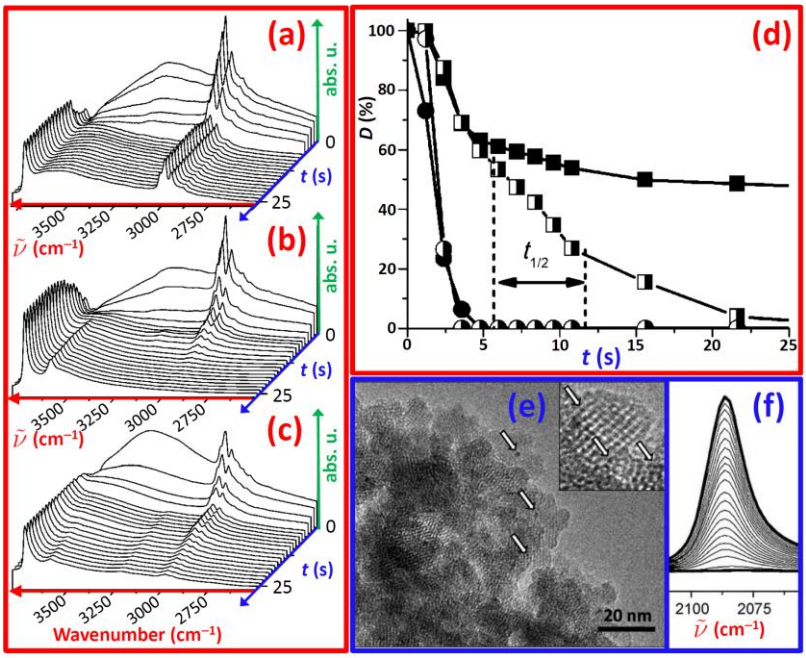

Figure 41. Part (a): time resolved (0–25 s) *operando* IR spectra of template removal of Pt-β in cold Ar plasma. t = 0 s corresponds to the plasma insertion in the cell. Platinum was introduced in H-β as Pt^{2+} via ion exchange with $[Pt(NH_3)_4(NO_3)_2]$ salt (0.75 wt% Pt). Part (b): as part (a) for Pt-β in cold O_2 plasma. Part (c): as part (a) for the parent H-β in cold O_2 plasma. Part (d) Quantification of the template degradation percentage (D) of the template (square) and desorption of the residual water (circle) for Pt-β in O_2 or Ar plasma (P = 350 Pa, half and full symbols respectively) as a function of time, measured from the intensity variations of characteristic IR bands shown in parts (a) and (b) for the template modes. Part (e): TEM image of Pt-β nanocrystals after cold O_2 plasma treatment reported in part (b). Part (f): IR spectra of C adsorbed on Pt-β nanocrystals after cold O_2 plasma treatment. Reproduced from Ref.[922] with permission, copyright Wiley-VCH, 2010.

9.2.4. *Operando* IR studies in Photocatalysis

Use of *operando* spectroscopy in photocatalysis on zeolites can be performed by adapting an *operando* reactor cell so that UV light is brought to the surface of the catalyst together with the infrared beam,[43] see Figure 42a. Mechanisms and surface species in photocatalysis are not well known, and following surface intermediates during the reaction provides very valuable information.

Using lasers as the light source, very fast transient species could be studied on metal oxides.[928] In an experiment at 10 ms time resolution following 300 ms laser pulses in an ATR cell, surface

superoxide species were shown to be kinetically competent intermediates in water photooxidation on 5 nm nanoparticles of Co_3O_4: the measured lifetime for superoxides was in the same range as the duration of the illumination pulse needed to produce O_2.

Methanol decomposition by photocatalysis on titania functionalized β zeolite (TiO_2/β) was followed at a more moderate time resolution.[43] Many key surface intermediates were detected, and the complexity of surface reactions was shown by the different time behavior of adsorbed formyl species (monodentate formates: formic acid or methyl formate) and bidentate surface formats (Figure 42b,c).

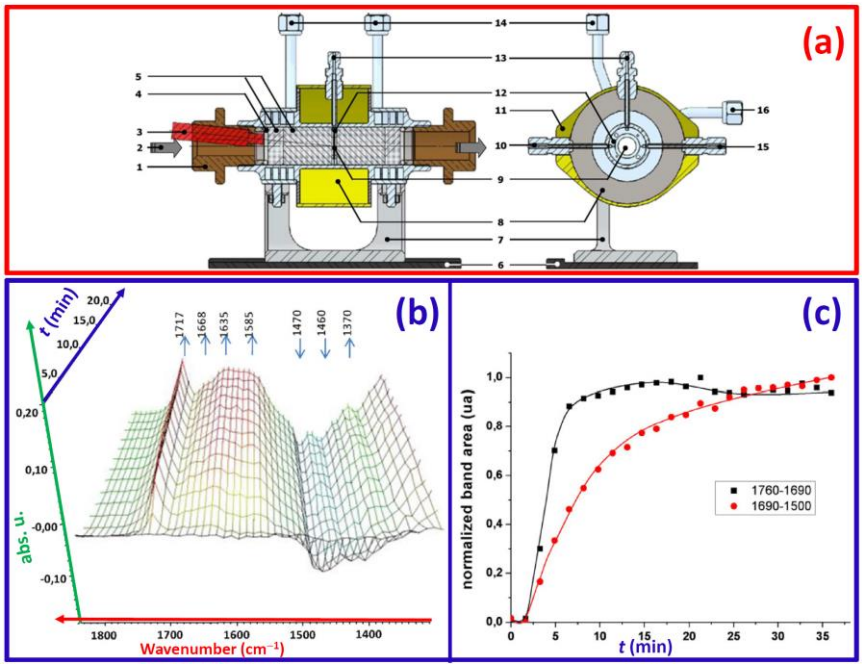

Figure 42. Part (a): Longitudinal (left) view, radial (right) schemes of the reactor-IR cell modified for UV catalysis study. (1) adjusting nut for airtightness (modified for UV-guide position), (2) IR beam, (3) UV-light guide, (4) Kalrez O-ring, (5) KBr windows, (6) spectrometer base-plate, (7) IR cell support, (8) oven location, (9) sample (wafer), (10) gas inlet, (11) external shell, (12) wafer holder, (13) thermocouple location, (14) air cooling outlet, (15) gas outlet, (16) air cooling inlet. Part (b): Evolution of IR spectra at RT during methanol photooxidation (1% of methanol in N_2 /O_2 20%/79%, vol.%, 25 cm^3 min^{-1}) vs. time of the species adsorbed on TiO_2/β during UV irradiation (subtraction result from the spectra before irradiation). Part (c): evolution of integrated band area of (CO) and formate species (OCO) during UV irradiation. t = 0 min corresponds to the time when irradiation has been established. Reproduced from Ref.[43] with permission. Copyright Elsevier, 2013.

Reaction mechanisms in photocatalysis were further studied by combining *operando* spectroscopy with SSITKA (steady state isotope transient kinetic analysis).[929] In that approach, when the reaction is running at steady state on the catalyst, the reactant is suddenly replaced by its isotopically labeled version. Surface spectroscopy shows the rate for the replacement of chemisorbed species by their labeled version, while online gas analysis shows the introduction of the labeled moiety in the final product. By comparing the two kinetic rates, linking a reaction product to surface intermediate species becomes straightforward, leading to a direct determination of reaction pathways. In the example shown in Figure 43, natural methanol is suddenly replaced in the reactant flow by ^{13}C labeled methanol. 3.5 min after the change, natural CO_2 is replaced by labeled $^{13}CO_2$ in the product flow exiting the reactor. However, on the surface of the catalyst, formate species are exchanged at a much slower rate, showing that most of the surface formate

species are not active intermediates but rather spectator species. It is only a minor fraction of surface formates that are in the direct reaction pathway.

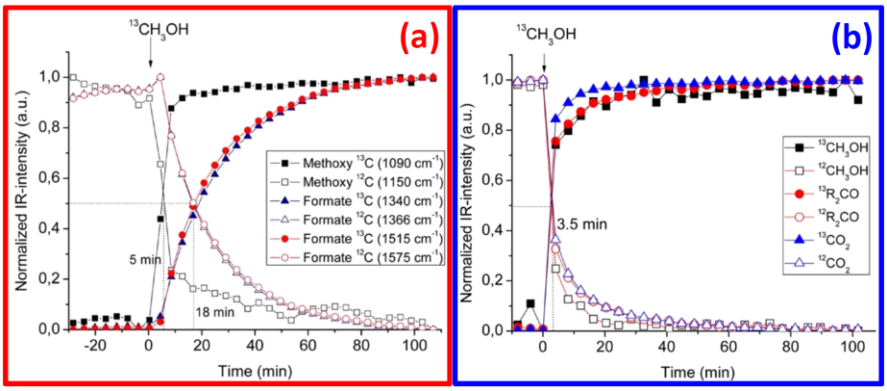

Figure 43. Part (a): evolution of the IR band intensities for adsorbed species on TiO_2-P25 and versus irradiation time. t = 0 represents the $^{12}CH_3OH$ to $^{13}CH_3OH$ isotopic exchange in the feed. Part (b): as part (a) for the (B) for final products detected in the gas phase. Reproduced from Ref.[929] with permission. Copyright American Chemical Society, 2013.

Operando IR is also already asking important questions about quantitative results in heterogeneous photocatalysis: the determination of the number of active sites is a very difficult challenge, and actual Turn Over Numbers are at present out of reach. *Operando* IR spectroscopy will probably be a key tool for their determination, and this is now an important research field.

9.2.5. MTH reaction followed by *operando* Raman

Raman spectroscopy is based on the so-called Raman effect,[930, 931] where monochromatic light interacts with matter, such that photon energy is either transferred to or from matter (inelastic scattering). The difference or shift in energy between the laser excitation and the scattered light is related to rotational, vibrational, phonon- or spin-flip processes in the sample. Due to the usually low Raman cross sections of molecules and solids, high laser powers need to be applied in order to produce a well detectable signal. One inherent problem is therefore the risk of laser-induced damages in the sample. A critical issue, in particular in the field of heterogeneous catalysis, is that laser induced heating may also lead to a significant temperature gradient between the integral catalyst bed and the sampling point.[41, 44, 932]. However, in the case of *operando* Raman spectroscopy, it is very important to know exactly the temperature at which chemical transformations occur. In both laser heating or laser damage cases, the final goal of *operando* spectroscopy, namely to establish some kind of structure–reactivity relationship, will be biased.[44]

For these reasons researchers in the field of heterogeneous catalysis have attempted to design special experimental set-ups to circumvent laser induced heating and damages, while still using high laser powers by reducing the contact time between the laser spot and the sample by either moving the solid catalyst or the laser beam in a continuous mode.[36-38, 44] In this regard, of particular interest is the new technology to homogeneously fluidize catalyst particles inside a micro-reactor and allowing to monitor with high laser power Raman spectra of heterogeneous catalytic reactions without the drawback of laser heating or damage that has been recently developed at Haldor Topsøe A/S by Beato et al.[44]

The authors modified a commercial CCR1000 catalyst cell from Linkam Scientific Instruments (Figure 44a). The reaction gas is flowing downwards from top to bottom of the reactor, passing through the sample, which is supported in a ceramic sample holder on a ceramic fiber

filter. Fluidization is achieved via a micro-device, placed downstream the reactor that provokes pressure oscillations in such a way that the flow direction is reversed in discrete pulses of about 40–100 Hz. The particles are lifted upwards by the reverse flow pulses but the net flow direction is still downwards and thereby ensures that the particles stay in the sample holder (Figure 44b).[44] Due to the particular design of the sample holder and the length and the frequency of the pulses, the particles move homogeneously in a quasi-circular mode.

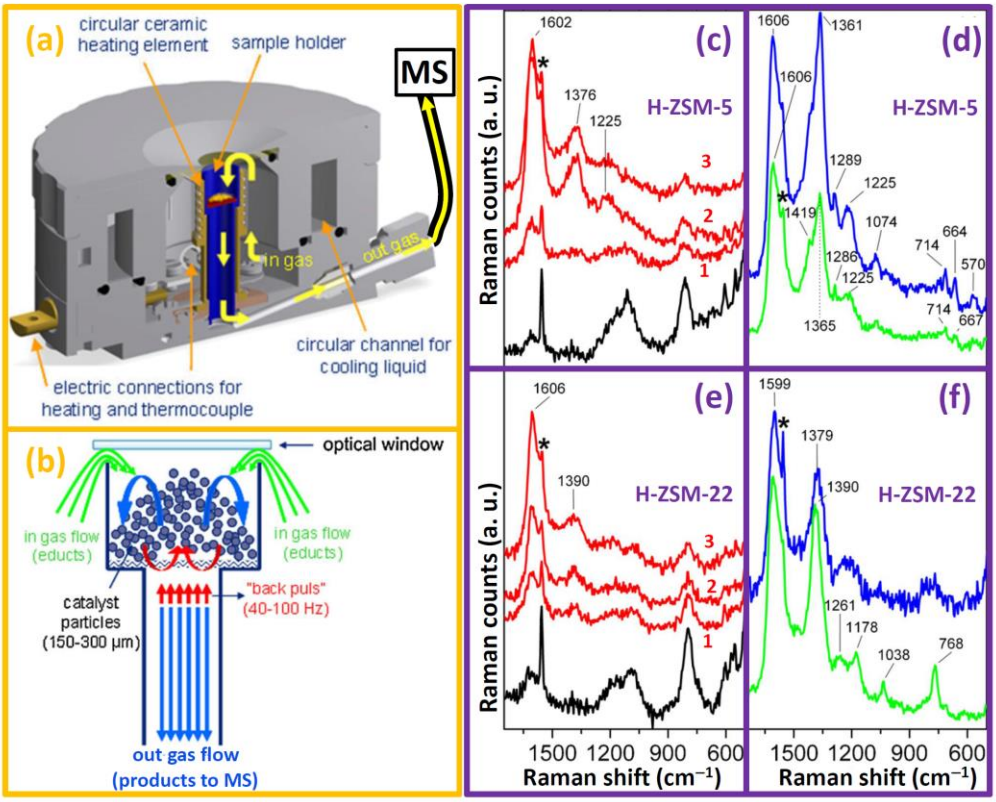

Figure 44. Part (a): detailed sketch of the Linkam CCR1000 reactor connected with a MS for product analysis. Part (b): schematic drawing of the sample holder with flow indications by arrows to illustrate the fluidization principle. Parts (c),(d): *Operando* Raman spectra of H-ZSM-5 zeolite during methanol conversion to hydrocarbons (MTH) collected using an excitation line at λ= 244 nm. Parts (e),(f): as Parts (c),(d) for H-ZSM-22 zeolite. The black spectra in part (c) and (e) are the Raman spectra after activation in air at 550 °C. The red spectra correspond to tye first, second and third successive pulses of methanol (c and e). The blue spectra in parts (d) and (f) correspond to the spectra after a long methanol pulse while the green spectra correspond to a subsequent flushing with He. Reproduced with permission from Ref.[44], Copyright Elsevier, 2013.

With the cell represented in Figure 44a,b, the authors investigated *operando* condition the methanol to hydrocarbons (MTH) reaction over H-ZSM-5 (Figure 44c,d) and H-ZSM-22 (Figure 44e,f) catalysts. This reaction is of main relevance for the modern oil industry, as liquid hydrocarbon fuels play an essential part in the global energy chain, owing to their high energy density and easy transportability.[81, 83, 88, 933] Olefins play a similar role in the production of consumer goods. In a post-oil society, fuel and olefin production will rely on alternative carbon sources, such as biomass, coal, natural gas, and CO_2. The MTH process is a key step in such routes, and can be tuned into production of gasoline-rich (methanol to gasoline; MTG) or olefin-rich (methanol to olefins; MTO)[88] The mayor problem related to the MTH, MTG and MTO reactions is the slow coke formation that take place inside the zeolite pores and catalyst activity must be

restored by controlled coke burn-off. Therefore, the industrial section consists of parallel reactors allowing for intermittent regeneration.

In the *operando* study by Beato et al.[44] CH_3OH has been introduced first gradually by means of three small pulses (red curves in Figure 44c,e) and then by a prolonged dosage (blue curves in parts (d) and (f). The reaction products were followed semi-quantitatively by online mass spectrometry (results here not reported). Finally, the methanol feed was stopped and the whole reactor flushed in a He stream (20 ml/min), in order to remove weakly adsorbed species formed upon methanol reaction (green curves in parts (d) and (f).

In the case of H-ZSM-5, right from the first pulse, a band at 1602 cm^{-1} starts to grow, while upon the second and third pulses, two more bands at 1376 and 1225 cm^{-1} start to grow (red curves in Figure 44c). At the same time the intensity of the bands related to the framework vibrations of H-ZSM-5 is strongly reduced. It is clear that during this phase the hydrocarbon molecules start to build up in the pores of the zeolite. The fact that the band at 1602 cm^{-1} starts to grow first, could indicate that some non-cyclic olefins (e.g. butadienes or pentradienes, etc.) adsorb initially and are transformed subsequently into aromatic molecules via cyclization reactions. During the long methanol pulse (blue spectrum in Figure 44d) the band at 1361 cm^{-1}, together with a should at higher frequencies is growing significantly and gets even stronger than the 1606 cm^{-1} band. In addition a number of well-defined bands of lower intensity develop (1289, 1225, 1077, 714, 664 and 570 cm^{-1}). This strong increase of the band at 1361 cm^{-1}, characteristic for the aromatic breathing mode of benzenes, together with the characteristic bands at lower frequencies indicates that at this stage the zeolite is filled up with polymethylated benzenes and naphtenes. However, most of these species are not strongly bound to the zeolite surface and are small enough to desorb again, which is demonstrated by flushing with He at reaction temperature (green spectrum in Figure 44d). The intensity of the band at 1365 cm^{-1} and the bands between 1300 and 550 cm^{-1} is halved after the flush with inert gas. At the same time the higher frequency shoulder has developed into a band at 1419 cm^{-1}, indicating that this band is related to some polycondensed aromatics, which are trapped in the zeolite pores.[44]

For H-ZSM-22 the picture looks generally similar, but some striking differences can be observed. Again, the band at 1606 cm^{-1} starts to grow first (red curves in Figure 44e), but during the subsequent pulses the band at 1390 cm^{-1} does not grow to the same extent as for H-ZSM-5, pointing to a lower content of aromatic ring molecules. This assumption is confirmed during the long methanol pulse (blue curve in Figure 44f), where the band at 1390 cm^{-1} is growing, but much less compared to H-ZSM-5. The higher frequency shoulder is absent in the case of H-ZSM-22, supporting the assumption that this band is related to larger molecules, which do not fit into the more space restricted 1D structure of ZSM-22. Conversely, for H-ZSM-22 the flushing with He at 420 °C (green curve in Figure 44f), does not decrease the band at 1390 cm^{-1}. Instead, the spectrum gets better resolved and bands below 1300 cm^{-1} are clearly recognized. For H-ZSM-22 the aromatics seem to be entrapped in the zeolite and are not able to desorb, but are transformed to thermodynamically more stable aromatic structures.[44]

Summarizing, the *operando* Raman study by Beato et al. was able to identify the first steps of the formation of aromatic molecules inside the zeolite channels that will progressively evolve into coke along the catalyst life. They succeeded in highlighting the role of the zeolite topology in this industrially relevant process. Indeed ZSM-5 framework (MFI topology, see structure in Figure 23f) exhibits a couple of interconnected 10-membered rings-pores running along [100] (5.1 Å x 5.5 Å, sinusoidal) and [010] (5.3 Å x 5.6 Å, linear) directions, while ZSM-22 framework (TON topology, see structure in Figure 23g) has a 1-dimensional set linear channels formed by 10-

membered rings with an elliptical cross section of (4.6 Å x 5.7 Å).[165] On these topological bases, the larger difficulty in desorbing aromatic products in H-ZSM-22 with respect to H-ZSM-5 is logical and fully in agreement with spectroscopic study reported in Figure 44c-f.

A further step in this direction has recently been done by Signorile et al.[65] They have characterized a pool of representative polycyclic aromatic hydrocarbons by means of UV Raman spectroscopy. The λ = 244 nm excitation wavelength was used to exploit the resonance effect and to avoid interference due to the visible fluorescence typical of these molecules. The polycyclic aromatic hydrocarbons have been analyzed in their pure form, in diluted solution, and dispersed on high surface area microporous supports. The collected data constitute a reference database to be compared with the deactivation products observed during petrolchemical reactions, such as MTH, MTG and MTO, offering the possibility to univocally identify them under Raman *operando* conditions.

9.3. Multi-technical *operando* experiments on working zeolite catalysts: combining IR and X-rays

The full investigation of complex systems, like zeolites under working conditions, requires the combined use of different vibrational (IR, Raman), structural (XRD, PDF, SAXS, EXAFS), electronic (UV-Vis, UPS, XPS, XANES, XES, XES) and magnetic (NMR, EPR) characterization techniques[162, 364, 378, 383, 494, 544, 545, 737, 934-950], possibly supported by DFT calculations.[22, 46, 202, 364, 536, 537, 553, 673, 736, 863, 949, 951-955]

Combining information from different experimental techniques is the only way to avoid the intrinsic limitation that each technique possesses, such as: (ia) the inability of XRD to determine amorphous phases; (ib) the inability of EPR to detect diamagnetic species; (ic) the inability of NMR to detect nuclei with a null spin; (id) the inability of XRD, PDF, SAXS to discriminate among different possible oxidation states; (ie) the inability of standard XRD, PDF, SAXS, IR, Raman to be element specific; the difficulty of (iia): XRD, PDF, SAXS, EXAFS to detect low Z elements and to discriminate among scattering centers with similar Z values; (iib) the difficulty of EXAFS to disentangle signals coming from different phases, (iic) the difficulty of all mentioned techniques but UPS, XPS and IR to be surface sensitive; etc… .

Possibly, the different experiments should be performed separately because this is the way to obtain the best spectrum (or pattern) for each technique. Indeed, the different techniques use photons (also electrons for UPS and XPS) which energy differ by several orders of magnitude, and consequently exhibits completely different penetration depths, implying that the ideal sample thickness for different experiments performed in transmission mode (e.g. IR, XRD, EXAFS) can be very different. This is clearly the case for spent catalysts that are no longer air sensitive and can be measured in ambient pressure, temperature and gas composition conditions and where the experiment consists in a single data collection. In such cases, the simultaneous collection of two or more spectroscopic (or scattering) data will result in worse spectra (pattern) than those collected in independent single experiments.

Conversely, the situation is more complex in the studies of a living catalyst, where particular temperatures, pressure or specific oxidative/reductive gas atmospheres or reactants flow are required. Indeed, ad-hoc conceived catalytic reactors allowing the simultaneous collection of spectroscopic or diffraction data may be different from technique to technique, so that systematic errors may be present in two independent experimental set-ups operating formally under the same

conditions. Analogous problem in the comparison of results coming from separated experiments may arise when the goal of the experiment is to follow the sample characteristic as a function of an external parameter such as temperature, pressure, reactants feed etc… . Indeed, in such cases it may be very important to guarantee that the spectra (patterns) collected by the different instruments can be really compared i.e. that the external parameter that is tuned along the experiment is really the same in the data collection of the different techniques. If this key point cannot be verified then misleading results may be obtained in the comparison of the datasets collected by the different techniques. In these cases, an approach where the different datasets are collected simultaneously on the same sample in the same cell, under exactly the same environmental conditions, may be a winning approach, even if it will be unavoidably affected by a degradation of the S/N quality of the spectra (patterns).

In such cases, important compromises must be reached. Hard X-rays, used for XRD, EXAFS and XANES, represent a penetrating radiation, while IR and UV-Vis are not. Optimizing the sample thickness for an X-ray experiment in transmission mode will imply that the volume probed by X-rays will be much larger than that probed by IR, UV-Vis or Raman spectroscopies. The limitation is however alleviated in the case of using dispersive XAS (or when using microfocus in other XAS detection modalities) as the size of the X-ray beam in two dimensions can be tuned, as desired, in the range of 1 to 100 microns, sampling thus a volume of the same order of magnitude than IR or UV-vis. For IR measurement this implies that the diffuse-reflectance mode (DRIFT) should be used instead of the optimal transmission one. Such a choice is the best one if the investigated process is supposed to modify uniformly the sample in all its volume (like zeolite crystallization experiments or pressure/temperature-induced solid state transformation). If this is not the case, such as for an oxidation/reduction process that evolves from the surface through the bulk, then much thinner samples must be used, with the unavoidable drawback of having XAS spectra characterized by a low edge-jump ($\Delta\mu x$) and a consequent poorer S/N ratio, and limited counts of the elastically scattered photons in the XRD detector.

9.3.1. O_2-activation of H-Cu-SSZ-13 catalyst: an *operando* IR/XANES and XRPD study.

The relevance of Cu-exchanged zeolites in general and of SSZ-13 zeolite in particular in the selective catalytic reduction (SCR) of NO by NH_3 has already been underlined above in Sections 9.1.3 will not be repeated here.

It has been shown that the state of the catalyst depends on the procedure adopted along its activation procedure,[363, 436] see Section 9.1.2 and Figure 36. Kwak et al. have been able to follow the activation of H-Cu-SSZ-13 catalyst in the 25 to 400 °C interval under a 20:80 O_2:He gas stream heating at 10 °C/min heating by simultaneously collecting DRIFT (Figure 45a-c) and XANES (Figure 45g,h) spectra and XRPD patterns (Figure 45d-f). IR spectroscopy allowed them to follow the whole dehydration process, showing the consumption of the broad band in the 3600-2600 cm^{-1} region, due to the ν(O-H) stretching of confined H_2O molecules in mutual H-bonding inside the CHA framework (Figure 45a), see Section 2, and the parallel disappearance of water bending mode at 1630 cm^{-1} (Figure 45a). framework ν(T-O-T) region where, between the broad $\nu_{sym}(TO_4)$ and $\nu_{asym}(TO_4)$ modes of the framework [TO_4] units, see Section 8. In this region Cu^{2+} cations are able to perturb the $\nu_{sym}(TO_4)$ and $\nu_{asym}(TO_4)$ modes and this perturbation depends on the hydration form of the cation, resulting in a band around 950 cm^{-1} in the hydrated form of H-Cu-ZZS-13, that

progressively moves around 900 cm^{-1} along dehydration (Figure 45a). The XANES data reported in (Figure 45g) confirm the dehydration observed by IR (decrease in intensity and blue shift of the white line resonance around 8995 eV) and indicates that the oxidation state of coper cations after an activation process in O_2 flux up to 400 °C is +2. The results of Kwak et al.[436] (Figure 45a,b,g)are in full agreement with those of Borfecchia et al.[363] (Figure 36) with the additional plus value that they have been collected simultaneously on the same sample in the same temperature/flux/history conditions.

Finally, the time/temperature-dependent XRPD study reported in the same study (Figure 45d-f) allows the authors to follow the evolution of the lattice parameters $a \equiv b$ and c along the dehydration process. Interestingly, while the unit cell parameters $a \equiv b$ decrease by about 0.2 Å as the sample is dehydrated, unit cell parameter c increases by about 0.6 Å. The authors have interpreted these variations in terms of a movement of Cu^{2+} ions from the large zeolite cages into cation positions that allows a stronger interaction with the oxygen ions of the framework.

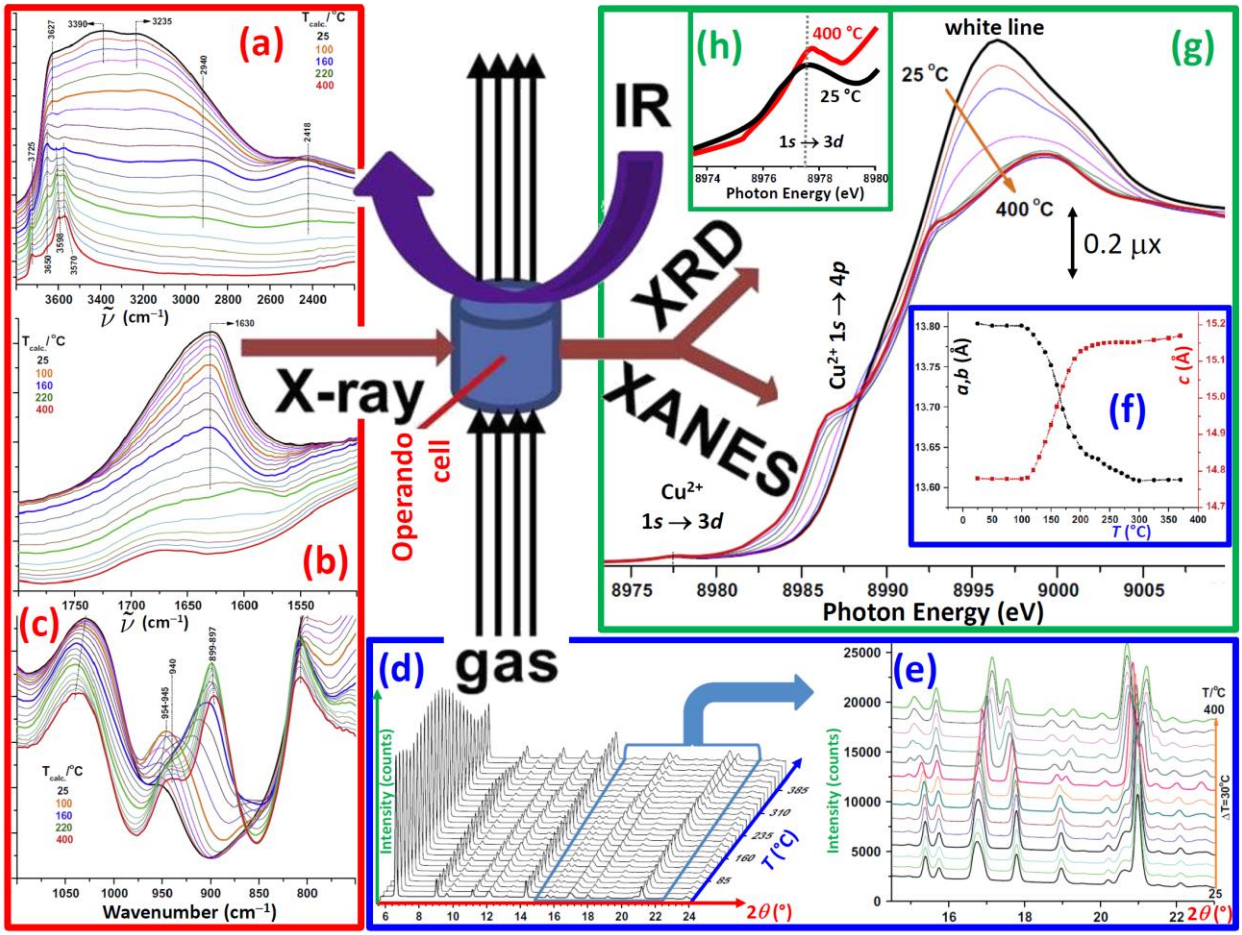

Figure 45. O_2-activation of H-Cu-SSZ-13 catalyst, in the 25-400 °C range, followed by *operando* DRIFT parts (a)-(c), XRD parts (d)-(f) and XANES part (g),(h) techniques. Heating rate: 10 °C/min; total flow rate: 10 cm^3/min.] Part (a): ν(OH) stretching region. Part (b): δ(H_2O) bending region. Part (c): framework ν(Si-O) stretching region. Part (d) 3D view of the XRPD patterns. Part (e) Selection of XRPD patterns reported in a 2D view in the 15.5–23.0 ° 2θ region. Part (f): Evolution of the $a \equiv b$ and c lattice parameters of the CHA framework (space group $R\bar{3}m$) long the thermal activation, as refined from the XRPD data reported in parts (d), (e). Part (g): normalized XANES spectra collected along the thermal activation. Part (h) zoom on the weak, dipole forbidden, 1s→3d transition for the first (25 °C) and the last (400 °C) spectrum of the series shown in part (g). The drown in the centrum schematize the

experimental set-up available at the X18A beamline of the National Synchrotron Light Source at Brookhaven National Laboratory. Reproduced from Ref.[436] with permission, copyright Elsevier, 2014.

9.4. Photo-induced reactions monitored by the FTIR step-scan mode

μs time-resolved step-scan FTIR absorption spectroscopy has been used by the group of Frei in Berkeley to catch the IR spectrum of triplet excited duroquinone occluded in zeolite Na-Y zeolite.[855] To the best of our knowledge this result represented the first time-resolved IR spectrum of a transient molecule in a zeolite. Authors used the ^{18}O isotope labeling to assign the strong absorption observed a 1542 cm^{-1} to the ν(CO) stretching mode of the excited state. The observed $\Delta\tilde{\nu}$ (CO) = −100 cm^{-1} of this band, relative to the ν(CO) of the ground state, establishes the ππ* character of the lowest triplet state of duroquinone, as espected due to the highly polar environment of the zeolite Na-Y cage. The lifetime of the excited triplet state was found to be 20 μs at −50 degrees °C.[855] Successively, the same group used the step-scan FTIR method to monitor short-lived radicals (formyl, acetyl radical) in zeolites[857, 858, 860] and Fe-AlPOs[859] molecular sieves.

Successively Andersen and Frei used time-resolved FTIR spectroscopy to follow the formation of CO molecules in the channels of mesoporous MCM-41 silica sieve generated by photodissociation of diphenyl cyclopropenone (DPCP) obtained with a nanosecond laser pulse,[862] according to the scheme reported in Figure 46a. The precursor was selected based on the ultrafast dissociation time and a quantum yield close to unity.[956] They monitored the process by using both the step-scan (Figure 46b,d) and rapid-scan (Figure 46c,e) methods. The experimental set-up relies on the generation of the species of interest (CO molecule in this case) from a photolabile precursor with a nanosecond laser pulse. The temporal resolution of the step-scan method covers the continuous range from a few ns to some ms. The slower part of the processes can be monitored by the rapid-scan FTIR method covering the range from 15 ms to s. The wide time span of the combined techniques is likely to encompass the time it takes for CO molecules to escape from the mesopores of MCM-41 particles. Andersen and Frei monitored the diffusion of CO generated inside the mesopores of MCM-41 at room temperature using these techniques. Transient CO was generated by photodissociation of diphenyl cyclopropenone (DPCP) present inside the solvent-free mesopores of MCM-41 using a nanosecond UV laser pulse.

The time resolved spectra showed a very broad absorption of CO in the 2200-2080 cm^{-1} region that decays in a biphasic mode (Figure 46b,c). Two-thirds of the band intensity decays on the hundreds of μs scale, with a lifetime of $\tau = 344 \pm 70$ μs. The process represents the escape of the CO molecules through the mesopores into the surrounding gas phase, and a diffusion constant of 1.5 x 10^{-9} m^2s^{-1} was derived (assuming control by intra-MCM-41 particle diffusion). The broad profile of the absorption is attributed to contact of the random hopping CO with siloxane and silanol groups of the pore surface. Measurements using MCM-41 with the silanols partially capped by trimethyl silyl groups (data not reported in this review, see the original work[862]) gave further insight into the nature of the IR band profile. The residual carbon monoxide remains much longer in the pores and features distinct peaks at 2167 and 2105 cm^{-1} characteristic for CO adsorbed on SiOH groups C-end on and O-end on, respectively (see the discussion on the linkage isomerism of simple molecules at subsections 3.1.1 and 7.2.3). The bands decrease with time constants of 113 ± 3 ms (2167 cm^{-1}) and 155 ± 15 ms (2105 cm^{-1}) suggesting that CO in these sites is additionally trapped by surrounding diphenyl acetylene coproduct and/or precursor molecules.[862]

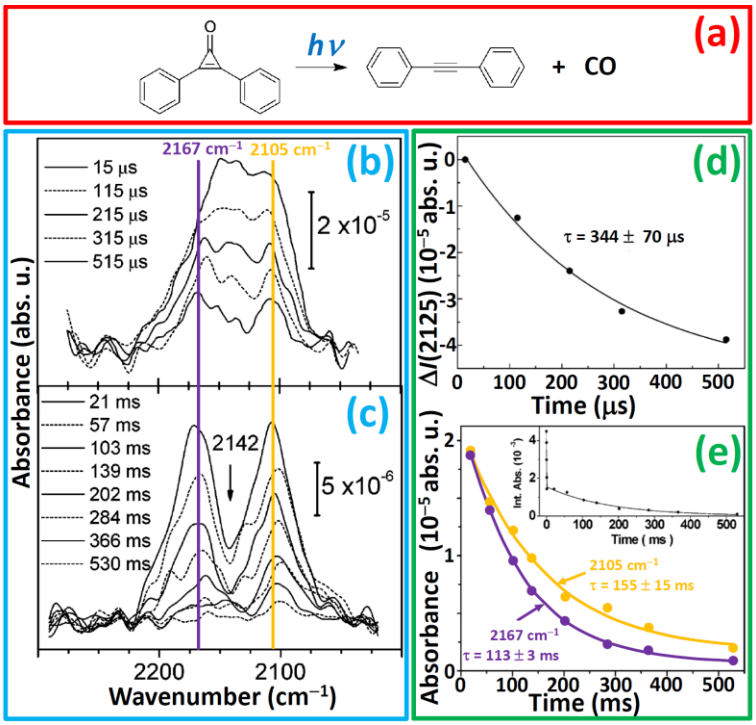

Figure 46. Part (a): reaction scheme representing the generation of transient CO molecules by the photodissociation DPCP present inside the solvent-free mesopores of MCM-41 using a nanosecond UV laser pulse. Parts (b,c): time-resolved FTIR absorption spectra of CO formed inside MCM-41 recorded upon laser-induced photolysis of DPCP, collected in stepscan mode (average of 21 experiments) and rapid-scan mode (average of 12 experiments), parts ((b) and (c), respectively. The rapid-scan spectra were normalized so that the spectra in parts (b) and (c) correspond to the same amount of DPCP depleted (and CO produced) per laser pulse. Note that the absorbance scale of the millisecond spectra is enlarged. Part (d): Single-exponential fit of the absorbance difference at 2125 cm^{-1} (obtaind plotting the spectra in part b in difference mode) yielding a decay time of 344 ± 70 µs (once corrected by the detector response). Part (e): single-exponential fits of the absorbance decay at 2105 and 2167 cm^{-1} (part c) yielding decay times τ of 155 ± 15 ms and 113 ± 3 ms, respectively. The insert shows the decay of the full CO profile (integrated from 2220 to 2060 cm^{-1}) in both the step-scan data and the rapid-scan data. Reproduced from Ref.[862] with permission, copyright American Chemical Society, 2006.

Andersen and Frei[862] concluded their study by underlining the relevance of their findings to understand the mechanistic understanding of CO_2 photoreduction in nanoporous transition metal silica hosts like Ti-MCM-41.[957] The finding that CO escapes from the mesopores at room temperature in less than a millisecond shows that the nanoporous silica environment of MCM-41 will not limit photocatalytic turnover rates and is favorable in terms of preventing back reaction.[958]

9.5. 2D IR Pressure-Jump Spectroscopy of Adsorbed Species in Zeolites followed by the step-scan mode

As discussed above, step-scan Fourier transform interferometers can easily reach the µs timescale if the observation can be repeated with sufficient reproducibility. At this timescale, adsorbed molecules in a zeolite each have their eigen-response frequency to a pressure perturbation or modulation. Using pressure and temperature measurements, Grenier and co-workers[959] and Rees and co-workers[960-962] have explored the pressure modulation frequencies, indicated the frequencies for given adsorbates on given zeolites, and extracted diffusion kinetic parameters from their results. Chenevarin and Thibault-Starzyk[963] showed that it is possible to use these eigen

frequencies to extract IR spectral information for complex mixtures on surfaces. Thus, several adsorption sites, or several adsorbed molecules in a mixture, would each lead to a specific eigen-response frequency to a pressure modulation, that will result in the spectral signature for each individual species on each individual adsorption site. The technique is named two-dimensional pressure-jump IR spectroscopy of adsorbed species (2D-PJAS-IR).[861, 963]

2D-PJAS-IR is based on ms time-resolved spectroscopy and sudden pressure changes in the IR cell containing the solid sample and the gas probe molecule. The pressure jump leads to a relaxation process by diffusion and adsorption, which is monitored by IR spectroscopy. The 2D spectrum is obtained by two Fourier transforms in the IR wavelength domain and in the time domain. The potential of the technique was shown by studying probe molecule (acetonitrile) adsorption on mordenite. 2D-PJAS-IR allowed the first direct detection of three distinct OH vibration bands in the IR spectrum of mordenite, and revealed three different interactions with acetonitrile, which depend on the adsorption site.[963] Protonation of acetonitrile at high temperature was shown to take place only in the side pockets. Summarizing, they used the high time resolution of the technique to reach dynamic adsorption parameters on the μs timescale. These dynamic properties were used to distinguish the various adsorption sites of acetonitrile probe in mordenite. In Ref.[861] they analyzed the collected spectra in the frame of the two-dimensional correlation spectroscopy (2D-COS).[408-417]

Successively, 2D-PJAS-IR technique was applied by Rivallan et al.[964] to CO adsorption on Pt-ZSM-5 catalyst. Three different methods were used for dispersing Pt in ZSM-5: (i) wet impregnation resulting in two classes of Pt nanoparticles differing in size hosted in the zeolite channels (smaller ones) and in the mesopores and the external surfaces (larger class > 2.5 nm); colloidal impregnation, showing no Pt nanoparticle inside the channels owing to the too large size of the used colloid; and ion exchange, showing long, thin and cylindrical Pt particles shaped by the zeolite channels.

Also in this case the technique was able of discriminating the adsorption sites (Pt nanoparticle located inside the ZSM-5 channels and on its external surface, see the cartoon reported in Figure 47a) by Fourier analysis of the evolution of the IR spectrum after a sudden change in the CO pressure. In the corresponding 2D maps (Figure 47b), two different frequency regions appear for the IR bands of both CO gas (2140–2120 cm^{-1}) and adsorbed CO on Pt nanoparticles (2100–2000 cm^{-1}). One resonance is at high frequency (HF) at 130 Hz or 250 Hz, depending on the Si/Al ratio and textural properties, and a second one is at low frequency (LF; below 50 Hz). The ion-exchanged sample, which contains platinum only in the channels, exhibits essentially one single response at 130 Hz, that is, higher than on colloidal impregnated sample (<50 Hz). This latter frequency was addressed to the CO adsorption–desorption oscillation process occurring on the external surface. The difference in frequency observed between the two resonances can be explained in terms of the mean free path, which is shorter in the channels than on the outer surface. The wet impregnated sample leads to oscillations at HF and LF (Figure 47b), which confirms the presence of both Pt particles in the mesopores and on the external surface. In the same study, two different Pt nanoparticle sintering mechanisms were observed in the mesopores and on the external surface of the ZSM-5 support.[964]

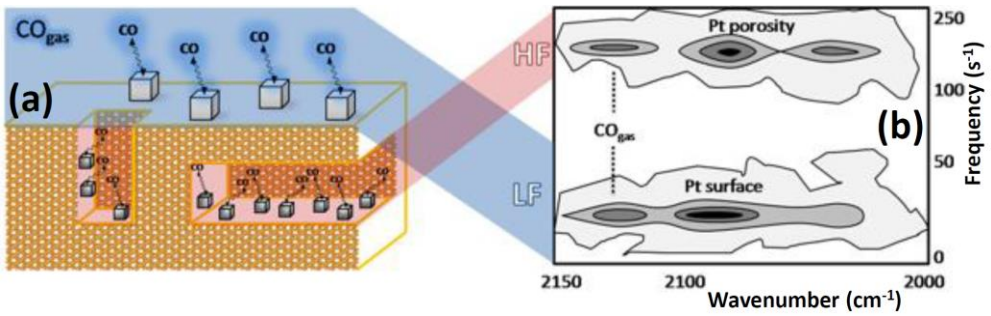

Figure 47. Part (a): cartoon showing CO molecules adsorbed on Pt nanoparticle located both inside the wet impregnated ZSM-5 channels and on the zeolite external surface. Part (b): 2D-PJAS-IR maps (at 573 K) of CO adsorbed on WI Pt/ZSM-5. (ion exchanged ZSM-5 at LF and colloidal impregnated at HF do not lead to any signal (HF=high frequency; LF=low frequency). Adapted from Ref.[964] with permission, copyright Wiley VCH, 2010.

10. Conclusions and perspectives

IR spectroscopy has been a major tool for characterising zeolites since the 50's, and several major authors summarized the achievements of the technique in their time.[1-34] Some very important aspects of zeolite science made considerable progress during the last ten years: knowledge of the structure of the Brønsted acid site, its interaction with Lewis sites, new preparation methods with increased accessibility… all these needed a careful look back and a rational presentation (Sections 2 and 3). At the same time, new experimental approaches appeared, and new information can now be brought by these already ancient spectrometers.

We first presented here a *vista* on more than 30 years of studying acidity in zeolites. It seems that a coherent and comprehensive understanding of acidity in zeolites is now possible. Even the frontiers of superacidity (Subsection 2.3) are better understood, and scales of acid strength were established, covering the whole range of our materials. This is not however a simple topic and accessibility of the acid site for reactants, adsorbates and probe molecules lead to important perturbation in the measurements. These perturbations are now well understood and described. IR has shown itself as a reliable tool for a quantitative description of such parameters.

Our understanding of zeolite basicity also progressed significantly (Section 4). New probe molecules appeared, and modelling confirmed the proposed relationships between probe molecules and the solid.

In the last decade, hierarchical pore systems progressively became one of the most important methods for increasing applicability of zeolites in oil refining, for dealing with heavier products. Mesopores are very efficient for optimising transport in the catalyst. Infrared established itself quickly as a major characterization tool for describing improved accessibility (subsection 5.). Playing with the size of the probe molecule is now standard for the infrared spectroscopist who is given a new sample to describe. The accessibility index, applied with many different probe molecules, provided a scale for comparing different solids and different methods for improving diffusion limitations. The location of the various sites in zeolites can now be determined: silanols, Brønsted sites, Lewis sites or metals. New experimental tools such as time resolved perturbations (Section 9), or microscopy (Section 8), are employed successfully and give new information on these questions.

It is probably in quantitative measurements that the most important advances were made. High precision gravimetry can be combined with *in situ* spectroscopy and finally solve the question of the quantitative aspect of infrared spectroscopy (Section 6). The amount of adsorbed species or the amount of OH groups on the surface can be determined with great accuracy. That approach started

providing reliable molar absorption coefficients for some common probes, and it will in the close future give every experimentalist the tools for always getting reliable quantitative measurements for all adsorbed species (tables for ε values, and clear experimental guidelines). The determination of thermodynamic values is also a quantitative measurement that became standard in the last years. Adsorption enthalpies can now be measured and adsorption modes described in great depth. New data treatment methods can extract a great wealth of information, identify individual adsorption states and their corresponding spectrum and energy (Section 7).

Vibrational spectroscopy has long been limited in space and time resolution. New methods for Raman spectroscopy increased its sensitivity enough for using it in microscopy (Subsection 8.3), and spectroscopic mapping of catalytic crystals can be done at 0.5 µm (Subsection 8.2). Infrared now established itself as one of the fastest characterisation method (Section 9), reaching potentially the nanosecond. Very short-lived intermediates can be identified, and the dynamic of adsorption can be explored. This is of course only the tip of the now so important *operando* spectroscopy (Subsection 9.2). *Operando* spectroscopy is the study of the working catalyst, the system being under real reaction conditions. *Operando* obviously means time resolved, but most often at the scale of the second. That is far enough for describing most of the reaction mechanisms and for identification of the intermediates, sometimes using kinetic tools such as isotope transients for determining the kinetic parameters of the reaction. Vibrational spectroscopy is the ideal tool for *operando* studies: it is easy, fast and versatile. It has been applied to most catalytic applications, even in the field of photochemistry or plasma assisted catalysis.

All these new tools are only leaving the characterisation laboratory. They still need to be spread and widely used by the application scientists. This will lead to new advances in zeolite science, and we can hope for further progress with these spectroscopic methods.

After this global tour, it is clear that the field is still progressing quickly. The new tools obtained in the last years will be applied for many other problems, and some unexpected applications will be possible. Tuneable lasers will change the way we do spectroscopy. Stimulated Raman Scattering has been used for microscopy, but it will also be applied in the "simple" Raman characterisation of zeolite samples, which was up to now limited by fluorescence and low sensitivity. Tuneable lasers will also be used to perform Raman enhanced experiments (Subsection 3.3.2) and to replace Fourier Transform spectroscopy, and their availability in the mid-infrared will lead to completely new infrared spectrometers, with unexpected time resolution and ease of use. This will surely change the whole domain of vibrational spectroscopy of zeolites in the next ten years.

Acknowledgements

We thank Prof. Jean-Claude Lavalley, Prof. Jacques Saussey and Prof. Adriano Zecchina for their inspirational guidance in the field of *in situ* and *operando* IR spectroscopy of zeolites. The figure of the TOC has been kindly created by Dr. Elisa Borfecchia (University of Turin). C.L. acknowledges the Mega-grant of the Russian Federation Government to support scientific research at Southern Federal University, No. 14.Y26.31.0001.

Appendix 1: abbreviations

2D-COS	two-dimensional correlation spectroscopy
2D-PJASIR	two-dimensional pressure-jump IR spectroscopy of adsorbed species
ACI	accessibility Index

AGIR	analysis by combined gravimetry and IR
ATR	attenuated total reflectance (spectroscopy)
BHW	Bellamy-Hallam-Williams (plot or relation)
CARS	coherent anti-Stokes Raman scattering
Coll	2,4,6-trimethylpyridine (collidine)
Cp_2Cr	cromocene
DFT	density functional theory
DPCP	diphenyl cyclopropenone
DRIFT	diffuse reflectance infrared Fourier transform
DTBPy	di-tert-butylpyridine
EXAFS	extended X-ray absorption fine structure
FTIR	Fourier transform infrared
FWHM	full width at half maximum
GC	gas chromatography
HF	high frequency (band in FAU and MOR frameworks)
H-USY	protonic form of USY zeolite
INS	inelastic neutron scattering
IR	infrared
LF	low frequency (band in FAU and MOR frameworks)
LMCT	ligand to metal charge transfer
LP-MOR	large-port mordenite
Lu	2,6-dimethylpyridine (lutidine)
mari	most abundant reactive intermediate
MBOH	methylbutynol
MC	main channel (in MOR framework)
MS	mass spectrometer (spectrometry)
MTG	methanol to gasoline
MTH	methanol to hydrocarbons
MTO	methanol to olefins
NIR	near-IR
NMR	nuclear magnetic resonance
PA	proton affinity
PhCN	benzonitrile
P_{CO}	CO equilibrium pressures
P_{NO}	NO equilibrium pressures
PS	polystyrene
Py	pyridine
SERS	surface-enhanced Raman spectroscopy
SCR	selective catalytic reduction
SRS	stimulated Raman scattering
SSITKA	steady state isotope transient kinetic analysis
SP	side pocket (in MOR framework)
SP-MOR	small-port mordenite
TERS	tip-enhanced Raman spectroscopy
THF	tetrahydrofuran
TMB	1,3,5-trimethylbenzene
TPD	temperature programmed desorption

TS-1	titanosilicate with MFI topology
UC	unit cell
USY	ultra-stable Y zeolites (dealuminated form)
UV-Vis	ultraviolet-visible
VTIR	variable temperature IR
XANES	X-ray absorption near edge structure
XAS	X-ray absorption spectroscopy

References

1. A. Janin, J. C. Lavalley, A. Macedo and F. Raatz, *Zeolites*, 1988, **368**, 117.
2. G. A. Ozin and S. Ozkar, *Chem. Mat.*, 1992, **4**, 511.
3. A. Zecchina and C. O. Arean, *Catal. Rev.-Sci. Eng.*, 1993, **35**, 261.
4. J. C. Lavalley, *Catal. Today*, 1996, **27**, 377.
5. J. A. Lercher, C. Grundling and G. EderMirth, *Catal. Today*, 1996, **27**, 353.
6. A. Zecchina and C. O. Arean, *Chem. Soc. Rev.*, 1996, **25**, 187.
7. P. P. KnopsGerrits, D. E. DeVos, E. J. P. Feijen and P. A. Jacobs, *Microporous Mater.*, 1997, **8**, 3.
8. L. M. Kustov, *Top. Catal.*, 1997, **4**, 131.
9. H. Knözinger and S. Huber, *J. Chem. Soc.-Faraday Trans.*, 1998, **94**, 2047.
10. K. I. Hadjiivanov, *Catal. Rev.-Sci. Eng.*, 2000, **42**, 71.
11. C. O. Arean, *Comments Inorg. Chem.*, 2000, **22**, 241.
12. P. C. Stair, *Curr. Opin. Solid State Mat. Sci.*, 2001, **5**, 365.
13. M. Hunger and J. Weitkamp, *Angew. Chem.-Int. Edit.*, 2001, **40**, 2954.
14. J. Ryczkowski, *Catal. Today*, 2001, **68**, 263.
15. K. I. Hadjiivanov and G. N. Vayssilov, *Adv. Catal.*, 2002, **47**, 307.
16. J. Guzman and B. C. Gates, *Dalton Trans.*, 2003, 3303.
17. E. Garrone and C. Otero Arean, *Chem. Soc. Rev.*, 2005, **34**, 846.
18. A. Zecchina, G. Spoto and S. Bordiga, *Phys. Chem. Chem. Phys.*, 2005, **7**, 1627.
19. J. C. Fierro-Gonzalez, S. Kuba, Y. L. Hao and B. C. Gates, *J. Phys. Chem. B*, 2006, **110**, 13326.
20. P. C. Stair, *Adv. Catal.*, 2007, **51**, 75.
21. A. Zecchina, M. Rivallan, G. Berlier, C. Lamberti and G. Ricchiardi, *Phys. Chem. Chem. Phys.*, 2007, **9**, 3483.
22. S. Bordiga, F. Bonino, A. Damin and C. Lamberti, *Phys. Chem. Chem. Phys.*, 2007, **9**, 4854.
23. C. Lamberti, E. Groppo, G. Spoto, S. Bordiga and A. Zecchina, *Adv. Catal.*, 2007, **51**, 1.
24. B. M. Weckhuysen, *Angew. Chem.-Int. Edit.*, 2009, **48**, 4910.
25. A. Aerts, C. E. A. Kirschhock and J. A. Martens, *Chem. Soc. Rev.*, 2010, **39**, 4626.
26. E. Stavitski and B. M. Weckhuysen, *Chem. Soc. Rev.*, 2010, **39**, 4615.
27. I. E. Wachs and C. A. Roberts, *Chem. Soc. Rev.*, 2010, **39**, 5002.
28. A. Vimont, F. Thibault-Starzyk and M. Daturi, *Chem. Soc. Rev.*, 2010, **39**, 4928.
29. C. Lamberti, E. Groppo, A. Zecchina and S. Bordiga, *Chem. Soc. Rev.*, 2010, **39**, 4951.
30. F. T. Fan, Z. C. Feng and C. Li, *Chem. Soc. Rev.*, 2010, **39**, 4794.
31. F. T. Fan, Z. C. Feng and C. Li, *Accounts Chem. Res.*, 2010, **43**, 378.
32. E. G. Derouane, J. C. Vedrine, R. R. Pinto, P. M. Borges, L. Costa, M. Lemos, F. Lemos and F. R. Ribeiro, *Catal. Rev.-Sci. Eng.*, 2013, **55**, 454.
33. P. Serna and B. C. Gates, *Accounts Chem. Res.*, 2014, **47**, 2612.
34. F. Zaera, *Chem. Soc. Rev.*, 2014, **43**, 7624.
35. M. A. Banares, *Catal. Today*, 2005, **100**, 71.
36. W. Kiefer and H. J. Bernstein, *Appl. Spectrosc.*, 1971, **25**, 609.
37. A. Muller and T. Weber, *Appl. Catal.*, 1991, **77**, 243.
38. Y. T. Chua and P. C. Stair, *J. Catal.*, 2000, **196**, 66.
39. G. Spoto, E. N. Gribov, G. Ricchiardi, A. Damin, D. Scarano, S. Bordiga, C. Lamberti and A. Zecchina, *Prog. Surf. Sci.*, 2004, **76**, 71.
40. E. Stavitski, M. H. F. Kox, I. Swart, F. M. F. de Groot and B. M. Weckhuysen, *Angew. Chem.-Int. Edit.*, 2008, **47**, 3543.
41. F. C. Meunier, *Chem. Soc. Rev.*, 2010, **39**, 4602.
42. P. Bazin, A. Alenda and F. Thibault-Starzyk, *Dalton Trans.*, 2010, **39**, 8432.

43. M. El-Roz, P. Bazin and F. Thibault-Starzyk, *Catal. Today*, 2013, **205**, 111.
44. P. Beato, E. Schachtl, K. Barbera, F. Bonino and S. Bordiga, *Catal. Today*, 2013, **205**, 128.
45. C. Li, G. Xiong, Q. Xin, J. Liu, P. Ying, Z. Feng, J. Li, W. Yang, Y. Wang, G. Wang, X. Liu, M. Lin, X. Wang and E. Min, *Angew. Chem. Int. Ed.*, 1999, **38**, 2220.
46. G. Ricchiardi, A. Damin, S. Bordiga, C. Lamberti, G. Spanò, F. Rivetti and A. Zecchina, *J. Am. Chem. Soc.*, 2001, **123**, 11409.
47. S. Bordiga, A. Damin, F. Bonino, G. Ricchiardi, C. Lamberti and A. Zecchina, *Angew. Chem.-Int. Edit.*, 2002, **41**, 4734.
48. S. Bordiga, A. Damin, F. Bonino, G. Ricchiardi, A. Zecchina, R. Tagliapietra and C. Lamberti, *Phys. Chem. Chem. Phys.*, 2003, **5**, 4390.
49. H. Kim, K. M. Kosuda, R. P. Van Duyne and P. C. Stair, *Chem. Soc. Rev.*, 2010, **39**, 4820.
50. P. K. Dutta and D. Robins, *Langmuir*, 1991, **7**, 2004.
51. W. F. Yan, L. L. Bao, S. M. Mahurin and S. Dai, *Appl. Spectrosc.*, 2004, **58**, 18.
52. N. Liu, M. Z. Gong, P. Zhang, L. X. Li, W. B. Li and R. Lee, *J. Mater. Sci.*, 2011, **46**, 3162.
53. M. Severance and P. K. Dutta, *J. Phys. Chem. C*, 2014, **118**, 28580.
54. M. Fleischmann, P. J. Hendra and A. J. McQuillan, *Chem. Phys. Lett.*, 1974, **26**, 163.
55. J. A. Dieringer, A. D. McFarland, N. C. Shah, D. A. Stuart, A. V. Whitney, C. R. Yonzon, M. A. Young, X. Y. Zhang and R. P. Van Duyne, *Faraday Discuss.*, 2006, **132**, 9.
56. S. M. Nie and S. R. Emery, *Science*, 1997, **275**, 1102.
57. C. W. Freudiger, W. Min, B. G. Saar, S. Lu, G. R. Holtom, C. W. He, J. C. Tsai, J. X. Kang and X. S. Xie, *Science*, 2008, **322**, 1857.
58. P. Nandakumar, A. Kovalev and A. Volkmer, *New J. Phys.*, 2009, **11**, 9.
59. W. Min, C. W. Freudiger, S. J. Lu and X. S. Xie, *Annu. Rev. Phys. Chem.*, 2011, **62**, 507.
60. Y. Ozeki, F. Dake, S. Kajiyama, K. Fukui and K. Itoh, *Opt. Express*, 2009, **17**, 3651.
61. D. Fu, F. K. Lu, X. Zhang, C. Freudiger, D. R. Pernik, G. Holtom and X. S. Xie, *J. Am. Chem. Soc.*, 2012, **134**, 3623.
62. C. W. Freudiger, W. L. Yang, G. R. Holtom, N. Peyghambarian, X. S. Xie and K. Q. Kieu, *Nat. Photonics*, 2014, **8**, 153.
63. B. Pettinger, B. Ren, G. Picardi, R. Schuster and G. Ertl, *Phys. Rev. Lett.*, 2004, **92**, 4.
64. J. F. Li, Y. F. Huang, Y. Ding, Z. L. Yang, S. B. Li, X. S. Zhou, F. R. Fan, W. Zhang, Z. Y. Zhou, D. Y. Wu, B. Ren, Z. L. Wang and Z. Q. Tian, *Nature*, 2010, **464**, 392.
65. M. Signorile, F. Bonino, A. Damin and S. Bordiga, *J. Phys. Chem. C*, 2015, **119**, 11694.
66. V. Van Speybroeck, K. Hemelsoet, L. Joos, M. Waroquier, R. G. Bell and C. R. A. Catlow, *Chem. Soc. Rev.*, 2015.
67. W. Holderich, M. Hesse and F. Naumann, *Angew. Chem.-Int. Edit. Engl.*, 1988, **27**, 226.
68. A. Corma, *Chem. Rev.*, 1995, **95**, 559.
69. A. Corma and A. Martinez, *Adv. Mater.*, 1995, **7**, 137.
70. A. Corma, V. Fornes, J. B. Monton and A. V. Orchilles, *J. Catal.*, 1987, **107**, 288.
71. S. M. Babitz, B. A. Williams, J. T. Miller, R. Q. Snurr, W. O. Haag and H. H. Kung, *Appl. Catal. A-Gen.*, 1999, **179**, 71.
72. B. A. Williams, S. M. Babitz, J. T. Miller, R. Q. Snurr and H. H. Kung, *Appl. Catal. A-Gen.*, 1999, **177**, 161.
73. N. Rahimi and R. Karimzadeh, *Appl. Catal. A-Gen.*, 2011, **398**, 1.
74. G. Bellussi, G. Pazzuconi, C. Perego, G. Girotti and G. Terzoni, *J. Catal.*, 1995, **157**, 227.
75. T. Matsuda, T. Urata and E. Kikuchi, *Appl. Catal. A-Gen.*, 1995, **123**, 205.
76. P. G. Smirniotis and E. Ruckenstein, *Ind. Eng. Chem. Res.*, 1995, **34**, 1517.
77. S. Gopal and P. G. Smirniotis, *J. Catal.*, 2004, **225**, 278.
78. J. F. Denayer, G. V. Baron, G. Vanbutsele, P. A. Jacobs and J. A. Martens, *J. Catal.*, 2000, **190**, 469.
79. C. Woltz, A. Jentys and J. A. Lercher, *J. Catal.*, 2006, **237**, 337.
80. A. Martins, J. M. Silva and M. F. Ribeiro, *Appl. Catal. A-Gen.*, 2013, **466**, 293.
81. M. Stocker, *Microporous Mesoporous Mat.*, 1999, **29**, 3.
82. M. Bjorgen, U. Olsbye and S. Kolboe, *J. Catal.*, 2003, **215**, 30.
83. J. F. Haw, W. G. Song, D. M. Marcus and J. B. Nicholas, *Accounts Chem. Res.*, 2003, **36**, 317.
84. M. Bjorgen, U. Olsbye, D. Petersen and S. Kolboe, *J. Catal.*, 2004, **221**, 1.
85. U. Olsbye, M. Bjorgen, S. Svelle, K. P. Lillerud and S. Kolboe, *Catal. Today*, 2005, **106**, 108.
86. M. Bjorgen, S. Svelle, F. Joensen, J. Nerlov, S. Kolboe, F. Bonino, L. Palumbo, S. Bordiga and U. Olsbye, *J. Catal.*, 2007, **249**, 195.

87. F. Bleken, W. Skistad, K. Barbera, M. Kustova, S. Bordiga, P. Beato, K. P. Lillerud, S. Svelle and U. Olsbye, *Phys. Chem. Chem. Phys.*, 2011, **13**, 2539.
88. U. Olsbye, S. Svelle, M. Bjorgen, P. Beato, T. V. W. Janssens, F. Joensen, S. Bordiga and K. P. Lillerud, *Angew. Chem.-Int. Edit.*, 2012, **51**, 5810.
89. F. L. Bleken, K. Barbera, F. Bonino, U. Olsbye, K. P. Lillerud, S. Bordiga, P. Beato, T. V. W. Janssens and S. Svelle, *J. Catal.*, 2013, **307**, 62.
90. F. Schmidt, C. Hoffmann, F. Giordanino, S. Bordiga, P. Simon, W. Carrillo-Cabrera and S. Kaskel, *J. Catal.*, 2013, **307**, 238.
91. M. Milina, S. Mitchell, P. Crivelli, D. Cooke and J. Perez-Ramirez, *Nat. Commun.*, 2014, **5**, 10.
92. J. F. Haw, J. B. Nicholas, W. G. Song, F. Deng, Z. K. Wang, T. Xu and C. S. Heneghan, *J. Am. Chem. Soc.*, 2000, **122**, 4763.
93. W. G. Song, H. Fu and J. F. Haw, *J. Am. Chem. Soc.*, 2001, **123**, 4749.
94. W. Wang and M. Hunger, *Accounts Chem. Res.*, 2008, **41**, 895.
95. F. Bleken, M. Bjorgen, L. Palumbo, S. Bordiga, S. Svelle, K. P. Lillerud and U. Olsbye, *Top. Catal.*, 2009, **52**, 218.
96. B. P. C. Hereijgers, F. Bleken, M. H. Nilsen, S. Svelle, K. P. Lillerud, M. Bjorgen, B. M. Weckhuysen and U. Olsbye, *J. Catal.*, 2009, **264**, 77.
97. S. Lopez-Orozco, A. Inayat, A. Schwab, T. Selvam and W. Schwieger, *Adv. Mater.*, 2011, **23**, 2602.
98. M. Bjorgen, F. Joensen, M. S. Holm, U. Olsbye, K. P. Lillerud and S. Svelle, *Appl. Catal. A-Gen.*, 2008, **345**, 43.
99. M. S. Holm, S. Svelle, F. Joensen, P. Beato, C. H. Christensen, S. Bordiga and M. Bjorgen, *Appl. Catal. A-Gen.*, 2009, **356**, 23.
100. G. J. Hutchings, P. Johnston, D. F. Lee, A. Warwick, C. D. Williams and M. Wilkinson, *J. Catal.*, 1994, **147**, 177.
101. G. J. Kramer, R. A. van Santen, C. A. Emeis and A. K. Nowak, *Nature*, 1993, **363**, 529.
102. A. G. Pelmenschikov and R. A. Vansanten, *J. Phys. Chem.*, 1993, **97**, 10678.
103. U. Fleischer, W. Kutzelnigg, A. Bleiber and J. Sauer, *J. Am. Chem. Soc.*, 1993, **115**, 7833.
104. J. Sauer, *Stud. Surf. Sci. Catal.*, 1994, **84**, 2039.
105. S. Scheiner, *Hydrogen Bonding, A Theoretical Perspective*, Oxford University Press, New York Oxford, 1997.
106. R. A. van Santen, *Catal. Today*, 1997, **38**, 377.
107. T. Xu, N. Kob, R. S. Drago, J. B. Nicholas and J. F. Haw, *J. Am. Chem. Soc.*, 1997, **119**, 12231.
108. U. Eichler, M. Brandle and J. Sauer, *J. Phys. Chem. B*, 1997, **101**, 10035.
109. R. Duchateau, R. J. Harmsen, H. C. L. Abbenhuis, R. A. van Santen, A. Meetsma, S. K. H. Thiele and M. Kranenburg, *Chem.-Eur. J.*, 1999, **5**, 3130.
110. J. F. Haw, J. H. Zhang, K. Shimizu, T. N. Venkatraman, D. P. Luigi, W. G. Song, D. H. Barich and J. B. Nicholas, *J. Am. Chem. Soc.*, 2000, **122**, 12561.
111. A. Simperler, R. G. Bell and M. W. Anderson, *J. Phys. Chem. B*, 2004, **108**, 7142.
112. A. Simperler, R. G. Bell, M. D. Foster, A. E. Gray, D. W. Lewis and M. W. Anderson, *J. Phys. Chem. B*, 2004, **108**, 7152.
113. S. H. Li, A. M. Zheng, Y. C. Su, H. L. Zhang, L. Chen, J. Yang, C. H. Ye and F. Deng, *J. Am. Chem. Soc.*, 2007, **129**, 11161.
114. W. F. Kladnig, *J. Phys. Chem.*, 1979, **83**, 765.
115. A. K. Ghosh and G. Curthoys, *J. Chem. Soc. Faraday Trans. 1*, 1983, **79**, 147.
116. M. W. Anderson and J. Klinowski, *Zeolites*, 1986, **6**, 150.
117. D. Freude, M. Hunger, H. Pfeifer and W. Schwieger, *Chem. Phys. Lett.*, 1986, **128**, 62.
118. D. J. Parrillo and R. J. Gorte, *J. Phys. Chem.*, 1993, **97**, 8786.
119. D. J. Parrillo, R. J. Gorte and W. E. Farneth, *J. Am. Chem. Soc.*, 1993, **115**, 12441.
120. H. Sato, *Catal. Rev.-Sci. Eng.*, 1997, **39**, 395.
121. C. Jia, P. Massiani and D. Barthomeuf, *J. Chem. Soc.-Faraday Trans.*, 1993, **89**, 3659.
122. J. F. Haw, M. B. Hall, A. E. Alvarado-Swaisgood, E. J. Munson, Z. Lin, L. W. Beck and T. Howard, *J. Am. Chem. Soc.*, 1994, **116**, 7308.
123. W. E. Farneth and R. J. Gorte, *Chem. Rev.*, 1995, **95**, 615.
124. M. Hunger, *Solid State Nucl. Magn. Reson.*, 1996, **6**, 1.
125. M. Hunger, U. Schenk, M. Breuninger, R. Glaser and J. Weitkamp, *Microporous Mesoporous Mat.*, 1999, **27**, 261.
126. C. Pazé, A. Zecchina, S. Spera, G. Spano and F. Rivetti, *Phys. Chem. Chem. Phys.*, 2000, **2**, 5756.

127. G. Busca, *Chem. Rev.*, 2007, **107**, 5366.
128. B. Gil, S. I. Zones, S. J. Hwang, M. Bejblova and J. Cejka, *J. Phys. Chem. C*, 2008, **112**, 2997.
129. W. P. Zhang, S. T. Xu, X. W. Han and X. H. Bao, *Chem. Soc. Rev.*, 2012, **41**, 192.
130. L. M. Peng, Y. Liu, N. J. Kim, J. E. Readman and C. P. Grey, *Nat. Mater.*, 2005, **4**, 216.
131. L. Peng, H. Huo, Y. Liu and C. P. Grey, *J. Am. Chem. Soc.*, 2007, **129**, 335.
132. V. L. Zholobenko, L. M. Kustov, V. Y. Borovkov and V. B. Kazansky, *Zeolites*, 1988, **8**, 175.
133. A. Zecchina, S. Bordiga, G. Spoto, D. Scarano, G. Petrini, G. Leofanti, M. Padovan and C. O. Arean, *J. Chem. Soc.-Faraday Trans.*, 1992, **88**, 2959.
134. A. G. Pelmenschikov, G. Morosi, A. Gamba, A. Zecchina, S. Bordiga and E. A. Paukshtis, *J. Phys. Chem.*, 1993, **97**, 11979.
135. G. Spoto, S. Bordiga, G. Ricchiardi, D. Scarano, A. Zecchina and E. Borello, *J. Chem. Soc.-Faraday Trans.*, 1994, **90**, 2827.
136. R. Buzzoni, S. Bordiga, G. Ricchiardi, G. Spoto and A. Zecchina, *J. Phys. Chem.*, 1995, **99**, 11937.
137. A. Zecchina, R. Buzzoni, S. Bordiga, F. Geobaldo, D. Scarano, G. Ricchiardi and G. Spoto, *Stud. Surf. Sci. Catal.*, 1995, **97**, 213.
138. R. Buzzoni, S. Bordiga, G. Ricchiardi, C. Lamberti, A. Zecchina and G. Bellussi, *Langmuir*, 1996, **12**, 930.
139. A. Zecchina, S. Bordiga, G. Spoto, D. Scarano, G. Spano and F. Geobaldo, *J. Chem. Soc.-Faraday Trans.*, 1996, **92**, 4863.
140. A. Zecchina, F. Geobaldo, C. Lamberti, S. Bordiga, G. T. Palomino and C. O. Arean, *Catal. Lett.*, 1996, **42**, 25.
141. F. Wakabayashi, J. N. Kondo, K. Domen and C. Hirose, *J. Phys. Chem.*, 1996, **100**, 1442.
142. S. Bordiga, B. Civalleri, G. Spoto, C. Paze, C. Lamberti, P. Ugliengo and A. Zecchina, *J. Chem. Soc.-Faraday Trans.*, 1997, **93**, 3893.
143. F. Geobaldo, G. Spoto, S. Bordiga, C. Lamberti and A. Zecchina, *J. Chem. Soc.-Faraday Trans.*, 1997, **93**, 1243.
144. A. Zecchina, L. Marchese, S. Bordiga, C. Paze and E. Gianotti, *J. Phys. Chem. B*, 1997, **101**, 10128.
145. C. Pazé, S. Bordiga, C. Lamberti, M. Salvalaggio, A. Zecchina and G. Bellussi, *J. Phys. Chem. B*, 1997, **101**, 4740.
146. C. Pazé, S. Bordiga, G. Spoto, C. Lamberti and A. Zecchina, *J. Chem. Soc.-Faraday Trans.*, 1998, **94**, 309.
147. C. Pazé, B. Civalleri, S. Bordiga and A. Zecchina, *J. Phys. Chem. B*, 1998, **102**, 10753.
148. A. Zecchina, C. Lamberti and S. Bordiga, *Catal. Today*, 1998, **41**, 169.
149. G. Spoto, F. Geobaldo, S. Bordiga, C. Lamberti, D. Scarano and A. Zecchina, *Top. Catal.*, 1999, **8**, 279.
150. A. Zecchina, F. Xamena, C. Paze, G. T. Palomino, S. Bordiga and C. O. Arean, *Phys. Chem. Chem. Phys.*, 2001, **3**, 1228.
151. A. Zecchina, G. Spoto, G. Ricchiardi, S. Bordiga, F. Bonino, C. Prestipino and C. Lamberti, *Stud. Surf. Sci. Catal.*, 2002, **142**, 3.
152. S. Bordiga, L. Regli, D. Cocina, C. Lamberti, M. Bjorgen and K. P. Lillerud, *J. Phys. Chem. B*, 2005, **109**, 2779.
153. L. Regli, A. Zecchina, J. G. Vitillo, D. Cocina, G. Spoto, C. Lamberti, K. P. Lillerud, U. Olsbye and S. Bordiga, *Phys. Chem. Chem. Phys.*, 2005, **7**, 3197.
154. E. N. Gribov, D. Cocina, G. Spoto, S. Bordiga, G. Ricchiardi and A. Zecchina, *Phys. Chem. Chem. Phys.*, 2006, **8**, 1186.
155. M. Bregolato, V. Bolis, C. Busco, P. Ugliengo, S. Bordiga, F. Cavani, N. Ballarini, L. Maselli, S. Passeri, I. Rossetti and L. Forni, *J. Catal.*, 2007, **245**, 285.
156. L. Regli, S. Bordiga, C. Lamberti, K. P. Lillerud, S. I. Zones and A. Zecchina, *J. Phys. Chem. C*, 2007, **111**, 2992.
157. P. Sazama, J. Dedecek, V. Gabova, B. Wichterlova, G. Spoto and S. Bordiga, *J. Catal.*, 2008, **254**, 180.
158. K. Barbera, F. Bonino, S. Bordiga, T. V. W. Janssens and P. Beato, *J. Catal.*, 2011, **280**, 196.
159. R. Skorpa, S. Bordiga, F. Bleken, U. Olsbye, B. Arstad, J. Tolchard, K. Mathisen, S. Svelle and M. Bjorgen, *Microporous Mesoporous Mat.*, 2011, **141**, 146.
160. B. T. L. Bleken, L. Mino, F. Giordanino, P. Beato, S. Svelle, K. P. Lillerud and S. Bordiga, *Phys. Chem. Chem. Phys.*, 2013, **15**, 13363.
161. F. Giordanino, P. N. R. Vennestrom, L. F. Lundegaard, F. N. Stappen, S. Mossin, P. Beato, S. Bordiga and C. Lamberti, *Dalton Trans.*, 2013, **42**, 12741.
162. F. Giordanino, E. Borfecchia, K. A. Lomachenko, A. Lazzarini, G. Agostini, E. Gallo, A. V. Soldatov, P. Beato, S. Bordiga and C. Lamberti, *J. Phys. Chem. Lett.*, 2014, **5**, 1552.

163. W. Skistad, S. Teketel, F. L. Bleken, P. Beato, S. Bordiga, M. H. Nilsen, U. Olsbye, S. Svelle and K. P. Lillerud, *Top. Catal.*, 2014, **57**, 143.
164. R. M. Szostak, *Molecular Sieves*, Van Nostrand Reinhold, New York, 1989.
165. C. Baerlocher, W. M. Meier and D. H. Olson, *Atlas of Zeolite Frameworks Types*, Elsevier, Amsterdam, 2001.
166. G. P. Heitmann, G. Dahlhoff and W. F. Holderich, *J. Catal.*, 1999, **186**, 12.
167. G. P. Heitmann, G. Dahlhoff, J. P. M. Niederer and W. F. Holderich, *J. Catal.*, 2000, **194**, 122.
168. S. Bordiga, I. Roggero, P. Ugliengo, A. Zecchina, V. Bolis, G. Artioli, R. Buzzoni, G. Marra, F. Rivetti, G. Spano and C. Lamberti, *J. Chem. Soc.-Dalton Trans.*, 2000, 3921.
169. S. Bordiga, P. Ugliengo, A. Damin, C. Lamberti, G. Spoto, A. Zecchina, G. Spano, R. Buzzoni, L. Dalloro and F. Rivetti, *Top. Catal.*, 2001, **15**, 43.
170. V. Bolis, C. Busco, S. Bordiga, P. Ugliengo, C. Lamberti and A. Zecchina, *Appl. Surf. Sci.*, 2002, **196**, 56.
171. A. B. Fernandez, A. Marinas, T. Blasco, V. Fornes and A. Corma, *J. Catal.*, 2006, **243**, 270.
172. K. Nakamoto, M. Margoshes and R. E. Rundle, *J. Am. Chem. Soc.*, 1955, **77**, 6480.
173. G. C. Pimentel and A. L. McClellan, in *The Hydrogen bond*, Freeman, San Francisco, 1960.
174. L. Kubelkova, S. Beran and J. A. Lercher, *Zeolites*, 1989, **9**, 539.
175. A. V. Kiselev, *Surf. Sci.*, 1965, **3**, 292.
176. G. A. Galkin, A. V. Kiselev and V. I. Lygin, *Trans. Faraday Soc.* , 1964, **60**, 431.
177. A. Zecchina, F. Geobaldo, G. Spoto, S. Bordiga, G. Ricchiardi, R. Buzzoni and G. Petrini, *J. Phys. Chem.*, 1996, **100**, 16584.
178. U. Bohner and G. Zundel, *J. Phys. Chem.*, 1986, **90**, 964.
179. S. Bratos, *J. Chem. Phys.*, 1975, **63**, 3499.
180. G. Herzberg, *Molecular Spectra Molecular Structure. Vol. II Infrared Raman Spectra Polyatomic Molecules*, Van Nostrand, New York, 1996.
181. K. Nakamoto, *Infrared and Raman Spectra of Inorganic and Coordination Compounds. Part A: Theory and Applications in Inorganic Chemistry (6th Ed.)*, John Wiley & Sons, Hoboken, New Jersey, 2009.
182. P. Kondratyuk, *Spectroc. Acta Pt. A-Molec. Biomolec. Spectr.*, 2005, **61**, 589.
183. G. Herzberg, *Molecular Spectra and Molecular Structure. Vol.II: Infrared and Raman Spectra of Polyatomic Molecules*, Van Nostrand Company, Inc., New York, 1945.
184. S. E. Odinokov and A. V. Iogansen, *Spectrochim. Acta A*, 1972, **28**, 2343.
185. U. Böhner and G. Zundel, *J. Phys. Chem.*, 1986, **90**, 964.
186. A. G. Pelmenschikov, J. Vanwolput, J. Janchen and R. A. van Santen, *J. Phys. Chem.*, 1995, **99**, 3612.
187. F. Wakabayashi, J. N. Kondo, K. Domen and C. Hirose, *J. Phys. Chem.*, 1995, **99**, 10573.
188. D. Hadzi and S. Bratos, in *The Hydrogen Bond*, eds. P. Shuster, G. Zundel and C. Sandorfy, North Holland, Amsterdam, 1976, vol. 2, p. 565.
189. L. J. Bellamy, H. E. Hallam and R. L. Williams, *Trans. Faraday Soc.*, 1958, **54**, 1120.
190. L. J. Bellamy and R. L. Williams, *Trans. Faraday Soc.*, 1959, **55**, 14.
191. L. J. Bellamy and H. E. Hallam, *Trans. Faraday Soc.*, 1959, **55**, 220.
192. L. J. Bellamy, C. P. Conduit, R. J. Pace and R. L. Williams, *Trans. Faraday Soc.*, 1959, **55**, 1677.
193. L. J. Bellamy, R. L. Williams and G. L. Caldow, *Proc. Roy. Soc. A*, 1960, **255**, 22.
194. J. G. David and H. E. Hallam, *Trans. Faraday Soc.*, 1964, **60**, 2013.
195. L. J. Bellamy and R. J. Pace, *Spectrochim. Acta A*, 1969, **25**, 319.
196. P. G. Rouxhet and R. E. Sempels, *J. Chem. Soc. Faraday Trans. 1*, 1974, **70**, 2021.
197. G. Busca, in *Metal Oxides: Chemistry and Applications*, ed. J. L. C. Fierro, CRC Press, Boca Raton FL, 2006, pp. 248.
198. A. G. Pelmenschikov, R. A. van Santen, J. Janchen and E. Meijer, *J. Phys. Chem.*, 1993, **97**, 11071.
199. L. Kubelkova, J. Kotrla and J. Florian, *J. Phys. Chem.*, 1995, **99**, 10285.
200. R. Buzzoni, S. Bordiga, G. Spoto, D. Scarano, G. Ricchiardi, C. Lamberti and A. Zecchina, *Stud. Surf. Sci. Catal.*, 1995, **98**, 104.
201. C. Pazé, A. Zecchina, S. Spera, A. Cosma, E. Merlo, G. Spano and G. Girotti, *Phys. Chem. Chem. Phys.*, 1999, **1**, 2627.
202. F. Bonino, A. Damin, S. Bordiga, C. Lamberti and A. Zecchina, *Langmuir*, 2003, **19**, 2155.
203. S. Bordiga, G. Ricchiardi, G. Spoto, D. Scarano, L. Carnelli, A. Zecchina and C. O. Arean, *J. Chem. Soc.-Faraday Trans.*, 1993, **89**, 1843.
204. F. Geobaldo, C. Lamberti, G. Ricchiardi, S. Bordiga, A. Zecchina, G. T. Palomino and C. O. Arean, *J. Phys. Chem.*, 1995, **99**, 11167.
205. L. Andrews and G. L. Johnson, *J. Chem. Phys.*, 1983, **79**, 3670.

206. G. L. Johnson and L. Andrews, *J. Phys. Chem.*, 1983, **87**, 1852.
207. L. Andrews, *J. Mol. Struct.*, 1983, **100**, 281.
208. L. Andrews, *J. Phys. Chem.*, 1984, **88**, 2940.
209. L. Andrews and S. R. Davis, *J. Chem. Phys.*, 1985, **83**, 4983.
210. L. Andrews, R. B. Bohn, R. T. Arlinghaus and R. D. Hunt, *Chem. Phys. Lett.*, 1989, **158**, 564.
211. B. Onida, B. Bonelli, L. Borello, S. Fiorilli, F. Geobaldo and E. Garrone, *J. Phys. Chem. B*, 2002, **106**, 10518.
212. R. Anquetil, J. Saussey and J. C. Lavalley, *Phys. Chem. Chem. Phys.*, 1999, **1**, 555.
213. C. Morterra, G. Cerrato, F. Pinna, M. Signoretto and G. Strukul, *J. Catal.*, 1994, **149**, 181.
214. C. Morterra, G. Cerrato and M. Signoretto, *Catal. Lett.*, 1996, **41**, 101.
215. C. Morterra, G. Cerrato, V. Bolis, S. DiCiero and M. Signoretto, *J. Chem. Soc.-Faraday Trans.*, 1997, **93**, 1179.
216. X. M. Song and A. Sayari, *Catal. Rev.-Sci. Eng.*, 1996, **38**, 329.
217. I. Palinko, B. Torok, G. K. S. Prakash and G. A. Olah, *Appl. Catal. A-Gen.*, 1998, **174**, 147.
218. B. Torok, I. Kiricsi, A. Molnar and G. A. Olah, *J. Catal.*, 2000, **193**, 132.
219. H. Jobic, A. Tuel, M. Krossner and J. Sauer, *J. Phys. Chem.*, 1996, **100**, 19545.
220. V. F. Sears, *Neutron News*, 1992, **3/3**, 26.
221. H. Jobic, eds. B. Imelik and J. C. Védrine, Plenum, New York, 1994, p. 347.
222. B. Cadioli, E. Gallinella, C. Coulombeau, H. Jobic and G. Berthier, *J. Phys. Chem.*, 1993, **97**, 7844.
223. M. Krossner and J. Sauer, *J. Phys. Chem.*, 1996, **100**, 6199.
224. W. J. Mortier, *J. Catal.*, 1978, **55**, 138.
225. W. J. Mortier, *Compilation of extraframework sites in zeolites*, Butterworth & Co., Guildfoed (UK), 1982.
226. S. Bordiga, E. E. Platero, C. O. Arean, C. Lamberti and A. Zecchina, *J. Catal.*, 1992, **137**, 179.
227. S. Bordiga, D. Scarano, G. Spoto, A. Zecchina, C. Lamberti and C. O. Arean, *Vib. Spectrosc.*, 1993, **5**, 69.
228. A. Zecchina, S. Bordiga, C. Lamberti, G. Spoto, L. Carnelli and C. O. Arean, *J. Phys. Chem.*, 1994, **98**, 9577.
229. S. Bordiga, C. Lamberti, F. Geobaldo, A. Zecchina, G. T. Palomino and C. O. Arean, *Langmuir*, 1995, **11**, 527.
230. C. Lamberti, S. Bordiga, F. Geobaldo, A. Zecchina and C. O. Arean, *J. Chem. Phys.*, 1995, **103**, 3158.
231. S. Bordiga, E. Garrone, C. Lamberti, A. Zecchina, C. O. Arean, V. B. Kazansky and L. M. Kustov, *J. Chem. Soc.-Faraday Trans.*, 1994, **90**, 3367.
232. J. Sanz, V. Fornes and A. Corma, 1988, **84**, 3113.
233. A. Corma, V. Fornes and F. Rey, 1990, **59**, 267.
234. Q. L. Wang, G. Giannetto and M. Guisnet, *J. Catal.*, 1991, **130**, 471.
235. P. J. Kunkeler, B. J. Zuurdeeg, J. C. van der Waal, J. A. van Bokhoven, D. C. Koningsberger and H. van Bekkum, *J. Catal.*, 1998, **180**, 234.
236. K. S. Triantafyllidis, A. G. Vlessidis and N. P. Evmiridis, *Ind. Eng. Chem. Res.*, 2000, **39**, 307.
237. C. J. A. Mota, D. L. Bhering and N. Rosenbach, *Angew. Chem.-Int. Edit.*, 2004, **43**, 3050.
238. M. J. Nash, A. M. Shough, D. W. Fickel, D. J. Doren and R. F. Lobo, *J. Am. Chem. Soc.*, 2008, **130**, 2460.
239. Y. Garcia-Basabe, I. Rodriguez-Iznaga, L. C. de Menorval, P. Llewellyn, G. Maurin, D. W. Lewis, R. Binions, M. Autie and A. R. Ruiz-Salvador, *Microporous Mesoporous Mat.*, 2010, **135**, 187.
240. G. Agostini, C. Lamberti, L. Palin, M. Milanesio, N. Danilina, B. Xu, M. Janousch and J. A. van Bokhoven, *J. Am. Chem. Soc.*, 2010, **132**, 667.
241. S. M. T. Almutairi, B. Mezari, G. A. Filonenko, P. Magusin, M. S. Rigutto, E. A. Pidko and E. J. M. Hensen, *ChemCatChem*, 2013, **5**, 452.
242. L. F. Isernia, *Mater. Res.-Ibero-am. J. Mater.*, 2013, **16**, 792.
243. Z. C. Wang, L. Z. Wang, Y. J. Jiang, M. Hunger and J. Huang, *ACS Catal.*, 2014, **4**, 1144.
244. T. Ennaert, J. Geboers, E. Gobechiya, C. M. Courtin, M. Kurttepeli, K. Houthoofd, C. E. A. Kirschhock, P. Magusin, S. Bals, P. A. Jacobs and B. F. Sels, *ACS Catal.*, 2015, **5**, 754.
245. S. Bordiga, F. Boscherini, S. Coluccia, F. Genoni, C. Lamberti, G. Leofanti, L. Marchese, G. Petrini, G. Vlaic and A. Zecchina, *Catal. Lett.*, 1994, **26**, 195.
246. S. Bordiga, S. Coluccia, C. Lamberti, L. Marchese, A. Zecchina, F. Boscherini, F. Buffa, F. Genoni, G. Leofanti, G. Petrini and G. Vlaic, *J. Phys. Chem.*, 1994, **98**, 4125.
247. B. Notari, in *Advances in Catalysis, Vol 41*, eds. D. D. Eley, W. O. Haag and B. Gates, Elsevier Academic Press Inc, San Diego, 1996, vol. 41, pp. 253.
248. T. Armaroli, F. Milella, B. Notari, R. J. Willey and G. Busca, *Top. Catal.*, 2001, **15**, 63.
249. G. Berlier, G. Spoto, S. Bordiga, G. Ricchiardi, P. Fisicaro, A. Zecchina, I. Rossetti, E. Selli, L. Forni, E. Giamello and C. Lamberti, *J. Catal.*, 2002, **208**, 64.
250. A. M. Ferretti, C. Oliva, L. Forni, G. Berlier, A. Zecchina and C. Lamberti, *J. Catal.*, 2002, **208**, 83.

251. G. Berlier, A. Zecchina, G. Spoto, G. Ricchiardi, S. Bordiga and C. Lamberti, *J. Catal.*, 2003, **215**, 264.
252. M. Moliner, Y. Roman-Leshkov and M. E. Davis, *Proc. Natl. Acad. Sci. U. S. A.*, 2010, **107**, 6164.
253. M. Moliner, J. Gonzalez, M. T. Portilla, T. Willhammar, F. Rey, F. J. Llopis, X. D. Zou and A. Corma, *J. Am. Chem. Soc.*, 2011, **133**, 9497.
254. E. Nikolla, Y. Roman-Leshkov, M. Moliner and M. E. Davis, *ACS Catal.*, 2011, **1**, 408.
255. R. Bermejo-Deval, R. S. Assary, E. Nikolla, M. Moliner, Y. Roman-Leshkov, S. J. Hwang, A. Palsdottir, D. Silverman, R. F. Lobo, L. A. Curtiss and M. E. Davis, *Proc. Natl. Acad. Sci. U. S. A.*, 2012, **109**, 9727.
256. M. Moliner, *Dalton Trans.*, 2014, **43**, 4197.
257. J. A. van Bokhoven and C. Lamberti, *Coord. Chem. Rev.*, 2014, **277**, 275.
258. G. L. Marra, A. N. Fitch, A. Zecchina, G. Ricchiardi, M. Salvalaggio, S. Bordiga and C. Lamberti, *J. Phys. Chem. B*, 1997, **101**, 10653.
259. A. V. Larin, L. Leherte and D. P. Vercauteren, *Phys. Chem. Chem. Phys.*, 2002, **4**, 2416.
260. A. V. Larin, D. P. Vercauteren, C. Lamberti, S. Bordiga and A. Zecchina, *Phys. Chem. Chem. Phys.*, 2002, **4**, 2424.
261. G. E. Ewing, *J. Chem. Phys.*, 1962, **37**, 2250.
262. H. Willner and F. Aubke, *Angew. Chem.-Int. Edit. Engl.*, 1997, **36**, 2403.
263. M. F. Zhou, L. Andrews and C. W. Bauschlicher, *Chem. Rev.*, 2001, **101**, 1931.
264. A. J. Lupinetti, S. H. Strauss and G. Frenking, *Prog. Inorg. Chem.*, 2001, **49**, 1.
265. S. H. Strauss, *J. Chem. Soc.-Dalton Trans.*, 2000, 1.
266. V. Bolis, A. Barbaglia, S. Bordiga, C. Lamberti and A. Zecchina, *J. Phys. Chem. B*, 2004, **108**, 9970.
267. C. Lamberti, C. Morterra, S. Bordiga, G. Cerrato and D. Scarano, *Vib. Spectrosc.*, 1993, **4**, 273.
268. C. Lamberti, S. Bordiga, G. Cerrato, C. Morterra, D. Scarano, G. Spoto and A. Zecchina, *Comput. Phys. Commun.*, 1993, **74**, 119.
269. R. Shannon, *Acta Cryst. A*, 1976, **32**, 751.
270. G. E. Leoni, G. E. Ewing and G. C. Pimentel, *J. Chem. Phys.*, 1964, **40**, 2298.
271. R. H. Hauge, S. E. Gransden and J. L. Margrave, *J. Chem. Soc. Dalton Trans.*, 1979, 745.
272. A. M. Ferrari, P. Ugliengo and E. Garrone, *J. Chem. Phys.*, 1996, **105**, 4129.
273. A. M. Ferrari, K. M. Neymann and N. Rösch, *J. Phys. Chem.*, 1997, **101**, 9292.
274. C. O. Arean, G. T. Palomino, E. Garrone, D. Nachtigallova and P. Nachtigall, *J. Phys. Chem. B*, 2006, **110**, 395.
275. C. O. Arean, D. Nachtigallova, P. Nachtigall, E. Garrone and M. R. Delgado, *Phys. Chem. Chem. Phys.*, 2007, **9**, 1421.
276. C. O. Arean, M. R. Delgado, K. Frolich, R. Bulanek, A. Pulido, G. F. Bibiloni and P. Nachtigall, *J. Phys. Chem. C*, 2008, **112**, 4658.
277. E. Garrone, R. Bulanek, K. Frolich, C. O. Arean, M. R. Delgado, G. T. Palomino, D. Nachtigallova and P. Nachtigall, *J. Phys. Chem. B*, 2006, **110**, 22542.
278. P. Nachtigall, M. R. Delgado, K. Frolich, R. Bulanek, G. T. Palomino, C. L. Bauca and C. O. Arean, *Microporous Mesoporous Mat.*, 2007, **106**, 162.
279. P. Nachtigall, O. Bludsky, L. Grajciar, D. Nachtigallova, M. R. Delgado and C. O. Arean, *Phys. Chem. Chem. Phys.*, 2009, **11**, 791.
280. D. Nachtigallova, O. Bludsky, C. O. Arean, R. Bulanek and P. Nachtigall, *Phys. Chem. Chem. Phys.*, 2006, **8**, 4849.
281. A. Pulido, P. Nachtigall, M. R. Delgado and C. O. Arean, *ChemPhysChem*, 2009, **10**, 1058.
282. G. Pacchioni, G. Cogliandro and P. S. Bagus, *Int. J. Quantum Chem.*, 1992, **42**, 1115.
283. E. Garrone, B. Bonelli, A. A. Tsyganenko, M. R. Dalgado, G. T. Palomino, O. V. Manoilova and C. O. Arean, *J. Phys. Chem. B*, 2003, **107**, 2537.
284. A. A. Tsyganenko, P. Y. Storozhev and C. O. Arean, *Kinet. Catal.*, 2004, **45**, 530.
285. R. Bulanek and E. Koudelkova, *Microporous Mesoporous Mat.*, 2012, **151**, 149.
286. C. Bisio, P. Massiani, K. Fajerwerg, L. Sordelli, L. Stievano, E. R. Silva, S. Coluccia and G. Martra, *Microporous Mesoporous Mat.*, 2006, **90**, 175.
287. C. O. Arean, G. T. Palomino, A. A. Tsyganenko and E. Garrone, *Int. J. Mol. Sci.*, 2002, **3**, 764.
288. C. O. Arean, A. A. Tsyganenko, E. E. Platero, E. Garrone and A. Zecchina, *Angew. Chem.-Int. Edit.*, 1998, **37**, 3161.
289. W. Mozgawa, *J. Mol. Struct.*, 2000, **555**, 299.
290. P. P. KnopsGerrits, D. E. DeVos and P. A. Jacobs, *J. Mol. Catal. A-Chem.*, 1997, **117**, 57.
291. M. C. Campa, D. Pietrogiacomi, S. Tuti, G. Ferraris and V. Indovina, *Appl. Catal. B-Environ.*, 1998, **18**, 151.
292. S. P. Varkey, C. Ratnasamy and P. Ratnasamy, *J. Mol. Catal. A-Chem.*, 1998, **135**, 295.

293. M. Salavati-Niasari, M. Shaterian, M. R. Ganjali and P. Norouzi, *J. Mol. Catal. A-Chem.*, 2007, **261**, 147.
294. H. Y. Chen and W. M. H. Sachtler, *Catal. Today*, 1998, **42**, 73.
295. L. J. Lobree, I. C. Hwang, J. A. Reimer and A. T. Bell, *J. Catal.*, 1999, **186**, 242.
296. E. M. El-Malki, R. A. van Santen and W. M. H. Sachtler, *J. Catal.*, 2000, **196**, 212.
297. P. Marturano, L. Drozdova, A. Kogelbauer and R. Prins, *J. Catal.*, 2000, **192**, 236.
298. G. Berlier, G. Spoto, P. Fisicaro, S. Bordiga, A. Zecchina, E. Giamello and C. Lamberti, *Microchem J.*, 2002, **71**, 101.
299. G. Berlier, G. Spoto, G. Ricchiardi, S. Bordiga, C. Lamberti and A. Zecchina, *J. Mol. Catal. A-Chem.*, 2002, **182**, 359.
300. G. Berlier, F. Bonino, A. Zecchina, S. Bordiga and C. Lamberti, *ChemPhysChem*, 2003, **4**, 1073.
301. D. Meloni, R. Monaci, V. Solinas, G. Berlier, S. Bordiga, I. Rossetti, C. Oliva and L. Forni, *J. Catal.*, 2003, **214**, 169.
302. G. Berlier, M. Pourny, S. Bordiga, G. Spoto, A. Zecchina and C. Lamberti, *J. Catal.*, 2005, **229**, 45.
303. G. Berlier, C. Prestipino, M. Rivallan, S. Bordiga, C. Lamberti and A. Zecchina, *J. Phys. Chem. B*, 2005, **109**, 22377.
304. G. Berlier, E. Gribov, D. Cocina, G. Spoto and A. Zecchina, *J. Catal.*, 2006, **238**, 243.
305. G. Berlier, C. Lamberti, M. Rivallan and G. Mul, *Phys. Chem. Chem. Phys.*, 2010, **12**, 358.
306. Y. J. Li and J. N. Armor, *J. Catal.*, 1994, **150**, 376.
307. Y. J. Li, T. L. Slager and J. N. Armor, *J. Catal.*, 1994, **150**, 388.
308. M. C. Campa, S. DeRossi, G. Ferraris and V. Indovina, *Appl. Catal. B-Environ.*, 1996, **8**, 315.
309. R. S. da Cruz, A. J. S. Mascarenhas and H. M. C. Andrade, *Appl. Catal. B-Environ.*, 1998, **18**, 223.
310. E. Ivanova, K. Hadjiivanov, D. Klissurski, M. Bevilacqua, T. Armaroli and G. Busca, *Microporous Mesoporous Mat.*, 2001, **46**, 299.
311. C. Resini, T. Montanari, L. Nappi, G. Bagnasco, M. Turco, G. Busca, F. Bregani, M. Notaro and G. Rocchini, *J. Catal.*, 2003, **214**, 179.
312. S. Dzwigaj and M. Che, *J. Phys. Chem. B*, 2006, **110**, 12490.
313. A. Mihaylova, K. Hadjiivanov, S. Dzwigaj and M. Che, *J. Phys. Chem. B*, 2006, **110**, 19530.
314. L. Daza, B. Pawelec, J. A. Anderson and J. L. G. Fierro, *Appl. Catal. A-Gen.*, 1992, **87**, 145.
315. D. K. Murray, T. Howard, P. W. Goguen, T. R. Krawietz and J. F. Haw, *J. Am. Chem. Soc.*, 1994, **116**, 6354.
316. H. Berndt, G. Lietz, B. Lucke and J. Volter, *Appl. Catal. A-Gen.*, 1996, **146**, 351.
317. E. M. El-Malki, R. A. van Santen and W. M. H. Sachtler, *J. Phys. Chem. B*, 1999, **103**, 4611.
318. V. B. Kazansky, V. Y. Borovkov, A. I. Serikh, R. A. van Santen and B. G. Anderson, *Catal. Lett.*, 2000, **66**, 39.
319. V. B. Kazansky, A. I. Serykh and E. A. Pidko, *J. Catal.*, 2004, **225**, 369.
320. V. B. Kazansky and E. A. Pidko, *J. Phys. Chem. B*, 2005, **109**, 2103.
321. A. N. Subbotin, G. M. Zhidomirov, I. R. Subbotina and V. B. Kazansky, *Kinet. Catal.*, 2013, **54**, 744.
322. J. Penzien, A. Abraham, J. A. van Bokhoven, A. Jentys, T. E. Muller, C. Sievers and J. A. Lercher, *J. Phys. Chem. B*, 2004, **108**, 4116.
323. Y. G. Kolyagin, V. V. Ordomsky, Y. Z. Khimyak, A. I. Rebrov, F. Fajula and Ivanova, II, *J. Catal.*, 2006, **238**, 122.
324. D. J. Wang, J. H. Lunsford and M. P. Rosynek, *J. Catal.*, 1997, **169**, 347.
325. W. Liu and Y. D. Xu, *J. Catal.*, 1999, **185**, 386.
326. L. L. Sheu, H. Knozinger and W. M. H. Sachtler, 1989, **57**, 61.
327. D. Tessier, A. Rakai and F. Bozonverduraz, *J. Chem. Soc.-Faraday Trans.*, 1992, **88**, 741.
328. C. Descorme, P. Gelin, M. Primet and C. Lecuyer, *Catal. Lett.*, 1996, **41**, 133.
329. K. Shimizu, F. Okada, Y. Nakamura, A. Satsuma and T. Hattori, *J. Catal.*, 2000, **195**, 151.
330. X. Wang, H. Y. Chen and W. M. H. Sachtler, *J. Catal.*, 2001, **197**, 281.
331. D. Scarano, S. Bordiga, C. Lamberti, G. Ricchiardi, S. Bertarione and G. Spoto, *Appl. Catal. A-Gen.*, 2006, **307**, 3.
332. K. Hadjiivanov and H. Knozinger, *J. Phys. Chem. B*, 1998, **102**, 10936.
333. K. I. Hadjiivanov, *Microporous Mesoporous Mat.*, 1998, **24**, 41.
334. S. Bordiga, G. T. Palomino, D. Arduino, C. Lamberti, A. Zecchina and C. O. Arean, *J. Mol. Catal. A-Chem.*, 1999, **146**, 97.
335. S. Bordiga, C. Lamberti, G. T. Palomino, F. Geobaldo, D. Arduino and A. Zecchina, *Microporous Mesoporous Mater.*, 1999, **30**, 129.
336. V. Bolis, S. Bordiga, G. T. Palomino, A. Zecchina and C. Lamberti, *Thermochim. Acta*, 2001, **379**, 131.

337. Y. Kuroda, H. Onishi, T. Mori, Y. Yoshikawa, R. Kumashiro, M. Nagao and H. Kobayashi, *J. Phys. Chem. B*, 2002, **106**, 8976.
338. W. S. Ju, M. Matsuoka, K. Iino, H. Yamashita and M. Anpo, *J. Phys. Chem. B*, 2004, **108**, 2128.
339. G. Agostini, S. Usseglio, E. Groppo, M. J. Uddin, C. Prestipino, S. Bordiga, A. Zecchina, P. L. Solari and C. Lamberti, *Chem. Mat.*, 2009, **21**, 1343.
340. A. Uzun, V. A. Bhirud, P. W. Kletnieks, J. F. Haw and B. C. Gates, *J. Phys. Chem. C*, 2007, **111**, 15064.
341. L. M. Kustov, D. Ostgard and W. M. H. Sachtler, *Catal. Lett.*, 1991, **9**, 121.
342. G. J. Li, T. Fujimoto, A. Fukuoka and M. Ichikawa, *Catal. Lett.*, 1992, **12**, 171.
343. V. L. Zholobenko, G. D. Lei, B. T. Carvill, B. A. Lerner and W. M. H. Sachtler, *J. Chem. Soc.-Faraday Trans.*, 1994, **90**, 233.
344. S. L. Qiu, R. Ohnishi and M. Ichikawa, *J. Phys. Chem.*, 1994, **98**, 2719.
345. T. M. Salama, T. Shido, H. Minagawa and M. Ichikawa, *J. Catal.*, 1995, **152**, 322.
346. T. M. Salama, R. Ohnishi, T. Shido and M. Ichikawa, *J. Catal.*, 1996, **162**, 169.
347. D. Guillemot, V. Y. Borovkov, V. B. Kazansky, M. PolissetThfoin and J. Fraissard, *J. Chem. Soc.-Faraday Trans.*, 1997, **93**, 3587.
348. Z. X. Gao, Q. Sun, H. Y. Chen, X. Wang and W. M. H. Sachtler, *Catal. Lett.*, 2001, **72**, 1.
349. M. M. Mohamed, T. M. Salama, R. Ohnishi and M. Ichikawa, *Langmuir*, 2001, **17**, 5678.
350. J. C. Fierro-Gonzalez, B. G. Anderson, K. Ramesh, C. P. Vinod, J. W. Niemantsverdriet and B. C. Gates, *Catal. Lett.*, 2005, **101**, 265.
351. M. Y. Mihaylov, J. C. Fierro-Gonzalez, H. Knozinger, B. C. Gates and K. I. Hadjiivanov, *J. Phys. Chem. B*, 2006, **110**, 7695.
352. R. A. Schoonheydt, *Catal. Rev.-Sci. Eng.*, 1993, **35**, 129.
353. G. Centi and S. Perathoner, *Appl. Catal. A-Gen.*, 1995, **132**, 179.
354. J. Sauer and M. Sierka, *J. Comput. Chem.*, 2000, **21**, 1470.
355. H. Yahiro and M. Iwamoto, *Appl. Catal. A-Gen.*, 2001, **222**, 163.
356. A. Delabie, K. Pierloot, M. H. Groothaert, R. A. Schoonheydt and L. G. Vanquickenborne, *Eur. J. Inorg. Chem.*, 2002, 515.
357. G. Calzaferri, C. Leiggener, S. Glaus, D. Schurch and K. Kuge, *Chem. Soc. Rev.*, 2003, **32**, 29.
358. M. Matsuoka and M. Anpo, *Curr. Opin. Solid State Mat. Sci.*, 2003, **7**, 451.
359. P. Sherwood, A. H. de Vries, M. F. Guest, G. Schreckenbach, C. R. A. Catlow, S. A. French, A. A. Sokol, S. T. Bromley, W. Thiel, A. J. Turner, S. Billeter, F. Terstegen, S. Thiel, J. Kendrick, S. C. Rogers, J. Casci, M. Watson, F. King, E. Karlsen, M. Sjovoll, A. Fahmi, A. Schafer and C. Lennartz, *Theochem-J. Mol. Struct.*, 2003, **632**, 1.
360. Y. Kuroda and M. Iwamoto, *Top. Catal.*, 2004, **28**, 111.
361. D. Berthomieu and G. Delahay, *Catal. Rev.-Sci. Eng.*, 2006, **48**, 269.
362. P. Vanelderen, J. Vancauwenbergh, B. F. Sels and R. A. Schoonheydt, *Coord. Chem. Rev.*, 2013, **257**, 483.
363. E. Borfecchia, K. A. Lomachenko, F. Giordanino, H. Falsig, P. Beato, A. V. Soldatov, S. Bordiga and C. Lamberti, *Chem. Sci.*, 2015, **6**, 548.
364. T. V. W. Janssens, H. Falsig, L. F. Lundegaard, P. N. R. Vennestrøm, S. B. Rasmussen, P. G. Moses, F. Giordanino, E. Borfecchia, K. A. Lomachenko, C. Lamberti, S. Bordiga, A. Godiksen, S. Mossin and P. Beato, *ACS Catal.*, 2015, **5**, 2832.
365. T. Gunter, H. W. P. Carvalho, D. E. Doronkin, T. Sheppard, P. Glatzel, A. J. Atkins, J. Rudolph, C. R. Jacob, M. Casapu and J.-D. Grunwaldt, *Chem. Commun.*, 2015, **51**, 9227.
366. J. N. Armor, *Appl. Catal. B-Environ.*, 1992, **1**, 221.
367. F. Kapteijn, J. RodriguezMirasol and J. A. Moulijn, *Appl. Catal. B-Environ.*, 1996, **9**, 25.
368. A. Fritz and V. Pitchon, *Appl. Catal. B-Environ.*, 1997, **13**, 1.
369. M. Shelef, *Chem. Rev.*, 1995, **95**, 209.
370. G. Busca, M. A. Larrubia, L. Arrighi and G. Ramis, *Catal. Today*, 2005, **107-08**, 139.
371. K. Rahkamaa-Tolonen, T. Maunula, M. Lomma, M. Huuhtanen and R. L. Keiski, *Catal. Today*, 2005, **100**, 217.
372. S. Brandenberger, O. Krocher, A. Tissler and R. Althoff, *Catal. Rev.-Sci. Eng.*, 2008, **50**, 492.
373. J. H. Li, H. Z. Chang, L. Ma, J. M. Hao and R. T. Yang, *Catal. Today*, 2011, **175**, 147.
374. A. M. Beale, F. Gao, I. Lezcano-Gonzalez, C. H. F. Peden and J. Szanyi, *Chem. Soc. Rev.*, 2015, **44**, doi: 10.1039/C5CS00108K.
375. G. Spoto, S. Bordiga, D. Scarano and A. Zecchina, *Catal. Lett.*, 1992, **13**, 39.
376. G. Spoto, A. Zecchina, S. Bordiga, G. Ricchiardi, G. Martra, G. Leofanti and G. Petrini, *Appl Catal B-Environ*, 1994, **3**, 151.

377. G. Spoto, S. Bordiga, G. Ricchiardi, D. Scarano, A. Zecchina and F. Geobaldo, *J. Chem. Soc. Faraday Trans.*, 1995, **91**, 3285.
378. C. Lamberti, S. Bordiga, M. Salvalaggio, G. Spoto, A. Zecchina, F. Geobaldo, G. Vlaic and M. Bellatreccia, *J. Phys. Chem. B*, 1997, **101**, 344.
379. C. Lamberti, S. Bordiga, A. Zecchina, M. Salvalaggio, F. Geobaldo and C. O. Arean, *J. Chem. Soc.-Faraday Trans.*, 1998, **94**, 1519.
380. A. Zecchina, S. Bordiga, M. Salvalaggio, G. Spoto, D. Scarano and C. Lamberti, *J. Catal.*, 1998, **173**, 540.
381. A. Zecchina, S. Bordiga, G. T. Palomino, D. Scarano, C. Lamberti and M. Salvalaggio, *J. Phys. Chem. B*, 1999, **103**, 3833.
382. A. Zecchina, C. O. Arean, G. T. Palomino, F. Geobaldo, C. Lamberti, G. Spoto and S. Bordiga, *Phys. Chem. Chem. Phys.*, 1999, **1**, 1649.
383. G. Turnes Palomino, P. Fisicaro, S. Bordiga, A. Zecchina, E. Giamello and C. Lamberti, *J. Phys. Chem. B*, 2000, **104**, 4064.
384. G. Turnes Palomino, S. Bordiga, A. Zecchina, G. L. Marra and C. Lamberti, *J. Phys. Chem. B*, 2000, **104**, 8641.
385. C. Prestipino, G. Berlier, F. Xamena, G. Spoto, S. Bordiga, A. Zecchina, G. T. Palomino, T. Yamamoto and C. Lamberti, *Chem. Phys. Lett.*, 2002, **363**, 389.
386. F. X. L. I. Xamena, P. Fisicaro, G. Berlier, A. Zecchina, G. T. Palomino, C. Prestipino, S. Bordiga, E. Giamello and C. Lamberti, *J. Phys. Chem. B*, 2003, **107**, 7036.
387. Q. Xu, *Coord. Chem. Rev.* , 2002, **231**, 83.
388. K. I. Hadjiivanov, M. M. Kantcheva and D. G. Klissurski, *J. Chem. Soc.-Faraday Trans.*, 1996, **92**, 4595.
389. D. Nachtigallova, P. Nachtigall, M. Sierka and J. Sauer, *Phys. Chem. Chem. Phys.*, 1999, **1**, 2019.
390. D. Nachtigallova, P. Nachtigall and J. Sauer, *Phys. Chem. Chem. Phys.*, 2001, **3**, 1552.
391. Y. Kuroda, A. Kotani, H. Maeda, H. Moriwaki, T. Morimato and M. Nagao, *J. Chem. Soc. Faraday Trans.*, 1992, **88**, 1583.
392. Y. Kuroda, R. Kumashiro, A. Itadani, M. Nagao and H. Kobayashi, *Phys. Chem. Chem. Phys.*, 2001, **3**, 1383.
393. M. Iwamoto, H. Furukawa, Y. Mine, F. Uemura, S. I. Mikuriya and S. Kagawa, *J. Chem. Soc.-Chem. Commun.*, 1986, 1272.
394. M. Iwamoto, H. Yahiro, Y. Mine and S. Kagawa, *Chem. Lett.*, 1989, 213.
395. M. Iwamoto and H. Hamada, *Catal. Today*, 1991, **10**, 57.
396. M. Iwamoto, H. Yahiro, K. Tanda, N. Mizuno, Y. Mine and S. Kagawa, *J. Phys. Chem.*, 1991, **95**, 3727.
397. M. Iwamoto, H. Yahiro, S. Shundo, Y. Yoshihiro and N. Mizuno, *Appl. Catal.*, 1991, **69**, L15.
398. M. Iwamoto, H. Yahiro, N. Mizuno, W. X. Zhang, Y. Mine, H. Furukawa and S. Kagawa, *J. Phys. Chem.*, 1992, **96**, 9360.
399. M. Iwamoto and H. Yahiro, *Catal. Today*, 1994, **22**, 5.
400. S. Sato, Y. Yoshihiro, H. Yahiro, N. Mizuno and M. Iwamoto, *Appl. Catal.*, 1991, **70**, L1.
401. M. H. Groothaert, K. Lievens, H. Leeman, B. M. Weckhuysen and R. A. Schoonheydt, *J. Catal.*, 2003, **220**, 500.
402. F. Amano, T. Tanaka and T. Funabiki, *J. Mol. Catal. A-Chem.*, 2004, **221**, 89.
403. M. Richter, M. J. G. Fait, R. Eckelt, E. Schreier, M. Schneider, M. M. Pohl and R. Fricke, *Appl. Catal. B-Environ.*, 2007, **73**, 269.
404. C. Lamberti, G. T. Palomino, S. Bordiga, G. Berlier, F. D'Acapito and A. Zecchina, *Angew. Chem. Int. Edit.*, 2000, **39**, 2138.
405. V. Bolis, S. Maggiorini, L. Meda, F. D'Acapito, G. T. Palomino, S. Bordiga and C. Lamberti, *J. Chem. Phys.*, 2000, **113**, 9248.
406. M. Iwamoto and Y. Hoshino, *Inorg. Chem.*, 1996, **35**, 6918.
407. C. Prestipino, L. Capello, F. D'Acapito and C. Lamberti, *Phys. Chem. Chem. Phys.*, 2005, **7**, 1743.
408. I. Noda, *Appl. Spectrosc.*, 1990, **44**, 550.
409. I. Noda, *Appl. Spectrosc.*, 1993, **47**, 1329.
410. I. Noda, A. E. Dowrey and C. Marcott, *Appl. Spectrosc.*, 1993, **47**, 1317.
411. S. Ekgasit and H. Ishida, *Appl. Spectrosc.*, 1995, **49**, 1243.
412. I. Noda, A. E. Dowrey, C. Marcott, G. M. Story and Y. Ozaki, *Appl. Spectrosc.*, 2000, **54**, 236A.
413. F. Thibault-Starzyk, A. Vimont, C. Fernandez and J. P. Gilson, *Chem. Commun.*, 2000, 1003.
414. F. Thibault-Starzyk, A. Vimont and J. P. Gilson, *Catal. Today*, 2001, **70**, 227.
415. N. T. Hunt, *Chem. Soc. Rev.*, 2009, **38**, 1837.
416. S. Garrett-Roe and P. Hamm, *Accounts Chem. Res.*, 2009, **42**, 1412.
417. C. R. Baiz, P. L. McRobbie, J. M. Anna, E. Geva and K. J. Kubarych, *Accounts Chem. Res.*, 2009, **42**, 1395.

418. J. J. Rack, J. D. Webb and S. H. Strauss, *Inorg. Chem.*, 1996, **35**, 277.
419. D. Costa, G. Martra, M. Che, L. Manceron and M. Kermarec, *J. Am. Chem. Soc.*, 2002, **124**, 7210.
420. G. Martra, S. Coluccia, M. Che, L. Manceron, M. Kermarec and D. Costa, *J. Phys. Chem. B*, 2003, **107**, 6096.
421. D. Gianolio, E. Groppo, J. G. Vitillo, A. Damin, S. Bordiga, A. Zecchina and C. Lamberti, *Chem. Commun.*, 2010, **46**, 976.
422. D. Scarano, S. Bordiga, C. Lamberti, G. Spoto, G. Ricchiardi, A. Zecchina and C. O. Arean, *Surf. Sci.*, 1998, **411**, 272.
423. S. Bordiga, C. Pazé, G. Berlier, D. Scarano, G. Spoto, A. Zecchina and C. Lamberti, *Catal. Today*, 2001, **70**, 91.
424. G. T. Palomino, E. Giamello, P. Fisicaro, S. Bordiga, C. Lamberti and A. Zecchina, *Stud. Surf. Sci. Catal.*, 2000, **130**, 2915.
425. J. Szanyi, J. H. Kwak, H. Zhu and C. H. F. Peden, *Phys. Chem. Chem. Phys.*, 2013, **15**, 2368.
426. G. T. Palomino, S. Bordiga, C. Lamberti, A. Zecchina and C. O. Arean, *Stud. Surf. Sci. Catal.*, 2002, **142**, 199.
427. A. Zecchina, D. Scarano, G. Spoto, S. Bordiga, C. Lamberti and G. Bellussi, *Stud. Surf. Sci. Catal.*, 1998, **117**, 343.
428. Y. Kuroda, Y. Yoshikawa, S. Konno, H. Hamano, H. Maeda, R. Kumashiro and M. Nagao, *J. Phys. Chem.*, 1995, **99**, 10621.
429. J. Dedecek, B. Wichterlova and P. Kubat, *Microporous Mesoporous Mater.*, 1999, **32**, 63.
430. F. Gao, E. D. Walter, E. M. Karp, J. Y. Luo, R. G. Tonkyn, J. H. Kwak, J. Szanyi and C. H. F. Peden, *J. Catal.*, 2013, **300**, 20.
431. G. Leofanti, A. Marsella, B. Cremaschi, M. Garilli, A. Zecchina, G. Spoto, S. Bordiga, P. Fisicaro, G. Berlier, C. Prestipino, G. Casali and C. Lamberti, *J. Catal.*, 2001, **202**, 279.
432. A. Corma, V. Fornés and E. Palomares, *Appl. Catal. B-Environ.*, 1997, **11**, 233.
433. J. Dedecek, Z. Sobalik, Z. Tvaruzkova, D. Kaucky and B. Wichterlova, *J. Phys. Chem.*, 1995, **99**, 16327.
434. A. A. Davydov and A. A. Budneva, *React. Kinet. Catal. Lett.*, 1983, **25**, 121.
435. K. Hadjiivanov, D. Klissurski, G. Ramis and G. Busca, *Appl. Catal. B-Environ.*, 1996, **7**, 251.
436. J. H. Kwak, T. Varga, C. H. F. Peden, F. Gao, J. C. Hanson and J. Szanyi, *J. Catal.*, 2014, **314**, 83.
437. I. Mirsojew, S. Ernst, J. Weitkamp and H. Knozinger, *Catal. Lett.*, 1994, **24**, 235.
438. C. O. Arean, G. T. Palomino, F. Geobaldo and A. Zecchina, *J. Phys. Chem.*, 1996, **100**, 6678.
439. J. Halasz, Z. Konya, A. Fudala and I. Kiricsi, *Catal. Today*, 1996, **31**, 293.
440. E. Kikuchi, M. Ogura, I. Terasaki and Y. Goto, *J. Catal.*, 1996, **161**, 465.
441. M. Sigl, S. Ernst, J. Weitkamp and H. Knozinger, *Catal. Lett.*, 1997, **45**, 27.
442. H. Kosslick, G. Lischke, H. Landmesser, B. Parlitz, W. Storek and R. Fricke, *J. Catal.*, 1998, **176**, 102.
443. G. Mul, J. Perez-Ramirez, F. Kapteijn and J. A. Moulijn, *Catal. Lett.*, 2002, **80**, 129.
444. M. Garcia-Sanchez, P. Magusin, E. J. M. Hensen, P. C. Thune, X. Rozanska and R. A. van Santen, *J. Catal.*, 2003, **219**, 352.
445. G. T. Palomino, J. J. C. Pascual, M. R. Delgado, J. B. Parra and C. O. Arean, *Mater. Chem. Phys.*, 2004, **85**, 145.
446. S. Endud and K. L. Wong, *Microporous Mesoporous Mat.*, 2007, **101**, 256.
447. B. Tang, W. L. Dai, G. J. Wu, N. J. Guan, L. D. Li and M. Hunger, *ACS Catal.*, 2014, **4**, 2801.
448. M. Weihe, M. Hunger, M. Breuninger, H. G. Karge and J. Whitkamp, *J. Catal.*, 2001, **198**, 256.
449. X. N. Wang, Z. Zhao, C. M. Xu, A. J. Duan, L. Zhang and G. Y. Jiang, *J. Rare Earths*, 2007, **25**, 321.
450. Q. Shu, B. L. Yang, H. Yuan, S. Qing and G. L. Zhu, *Catal. Commun.*, 2007, **8**, 2159.
451. W. C. Zhan, Y. L. Guo, Y. Q. Wang, X. H. Liu, Y. Guo, Y. S. Wang, Z. G. Zhang and G. Z. Lu, *J. Phys. Chem. B*, 2007, **111**, 12103.
452. T. Noda, K. Suzuki, N. Katada and M. Niwa, *J. Catal.*, 2008, **259**, 203.
453. L. Gutierrez and E. A. Lombardo, *Appl. Catal. A-Gen.*, 2009, **360**, 107.
454. M. Xue, R. Chitrakar, K. Sakane, T. Hirotsu, K. Ooi, Y. Yoshimura, M. Toba and Q. Feng, *J. Colloid Interface Sci.*, 2006, **298**, 535.
455. M. Alvaro, V. Fornes, S. Garcia, H. Garcia and J. C. Scaiano, *J. Phys. Chem. B*, 1998, **102**, 8744.
456. J. Rocha and L. D. Carlos, *Curr. Opin. Solid State Mat. Sci.*, 2003, **7**, 199.
457. Y. Hasegawa, Y. Wada and S. Yanagida, *J. Photochem. Photobiol. C-Photochem. Rev.*, 2004, **5**, 183.
458. Y. G. Wang, H. R. Li, L. J. Gu, Q. Y. Gan, Y. N. Li and G. Calzaferri, *Microporous Mesoporous Mat.*, 2009, **121**, 1.

459. Y. Wang, H. R. Li, Y. Feng, H. J. Zhang, G. Calzaferri and T. Z. Ren, *Angew. Chem.-Int. Edit.*, 2010, **49**, 1434.
460. P. P. Cao, Y. G. Wang, H. R. Li and X. Y. Yu, *J. Mater. Chem.*, 2011, **21**, 2709.
461. L. Chen and B. Yan, *Dalton Trans.*, 2014, **43**, 14123.
462. J. N. Hao and B. Yan, *Dalton Trans.*, 2014, **43**, 2810.
463. P. Li, D. Y. Wang, D. Liang, L. Zhang, S. M. Zhang and Y. G. Wang, *Mater. Res. Bull.*, 2014, **55**, 216.
464. Y. Wang and H. R. Li, *Crystengcomm*, 2014, **16**, 9764.
465. S. E. Spiridonov, K. S. U. Nasukhanov, O. V. Kryukov, E. B. Podyacheva and S. N. Khadzhiev, *Kinet. Catal.*, 1992, **33**, 317.
466. P. Tynjala and T. T. Pakkanen, *J. Mol. Catal. A-Chem.*, 1996, **110**, 153.
467. E. F. Sousa-Aguiar, V. L. D. Camorim, F. M. Z. Zotin and R. L. C. dos Santos, *Microporous Mesoporous Mat.*, 1998, **25**, 25.
468. D. Li, F. Li, J. Ren and Y. H. Sun, *Appl. Catal. A-Gen.*, 2003, **241**, 15.
469. S. E. Siporin, B. C. McClaine and R. J. Davis, *Langmuir*, 2003, **19**, 4707.
470. A. Martins, J. M. Silva, C. Henriques, F. R. Ribeiro and M. F. Ribeiro, *Catal. Today*, 2005, **107-08**, 663.
471. F. P. Tian, W. C. Wu, Z. X. Jiang, C. H. Liang, Y. X. Yang, P. L. Ying, X. P. Sun, T. X. Cai and C. Li, *J. Colloid Interface Sci.*, 2006, **301**, 395.
472. D. F. Jin, B. Zhu, Z. Y. Hou, J. H. Fel, H. Lou and X. M. Zheng, *Fuel*, 2007, **86**, 2707.
473. E. Ito, Y. J. Mergler, B. E. Nieuwenhuys, H. Vanbekkum and C. M. Vandenbleek, *Microporous Mater.*, 1995, **4**, 455.
474. E. Ito, Y. J. Mergler, B. E. Nieuwenhuys, H. P. A. Calis, H. vanBekkum and C. M. vandenBleek, *J. Chem. Soc.-Faraday Trans.*, 1996, **92**, 1799.
475. V. I. Parvulescu, P. Grange and B. Delmon, *J. Phys. Chem. B*, 1997, **101**, 6933.
476. A. M. G. Pedrosa, M. J. B. Souza, A. O. S. Silva, D. M. A. Melo and A. S. Araujo, *J. Therm. Anal. Calorim.*, 2006, **84**, 503.
477. H. G. Wang, L. J. Song, H. Jiang, J. Xu, L. L. Jin, X. T. Zhang and Z. L. Sun, *Fuel Process. Technol.*, 2009, **90**, 835.
478. A. Goldbach, L. Iton, M. Grimsditch and M. L. Saboungi, *J. Am. Chem. Soc.*, 1996, **118**, 2004.
479. V. I. Parvulescu, P. Oelker, P. Grange and B. Delmon, *Appl. Catal. B-Environ.*, 1998, **16**, 1.
480. T. Baba, S. Hikita, Y. Ono, T. Yoshida, T. Tanaka and S. Yoshida, *J. Mol. Catal. A-Chem.*, 1995, **98**, 49.
481. C. Kladis, S. K. Bhargava, K. Foger and D. B. Akolekar, *Catal. Today*, 2000, **63**, 297.
482. H. R. Li, H. H. Zhang, L. Y. Wang, D. Mu, S. T. Qi, X. J. Hu, L. Zhang and J. S. Yuan, *J. Mater. Chem.*, 2012, **22**, 9338.
483. Z. Q. Qin, H. S. Li and Y. G. Wang, *Opt. Mater.*, 2014, **37**, 483.
484. L. Chen and B. Yan, *Spectroc. Acta Pt. A-Molec. Biomolec. Spectr.*, 2014, **131**, 1.
485. C. Tiseanu, B. Gagea, V. I. Parvulescu, V. Lorenz-Fonfria, A. Gessner and M. U. Kumke, *Langmuir*, 2007, **23**, 6781.
486. J. P. Rainho, M. Pillinger, L. D. Carlos, S. J. L. Ribeiro, R. M. Almeida and J. Rocha, *J. Mater. Chem.*, 2002, **12**, 1162.
487. T. Baba, S. Hikita, R. Koide, Y. Ono, T. Hanada, T. Tanaka and S. Yoshida, *J. Chem. Soc.-Faraday Trans.*, 1993, **89**, 3177.
488. E. Groppo, C. Lamberti, S. Bordiga, G. Spoto and A. Zecchina, *Chem. Rev.*, 2005, **105**, 115.
489. E. Groppo, C. Lamberti, S. Bordiga, G. Spoto and A. Zecchina, *J. Phys. Chem. B*, 2005, **109**, 15024.
490. S. Bordiga, G. T. Palomino, C. Paze and A. Zecchina, *Microporous Mesoporous Mater.*, 2000, **34**, 67.
491. M. Mihaylov, K. Chakarova and K. Hadjiivanov, *J. Catal.*, 2004, **228**, 273.
492. A. Zecchina, D. Scarano, S. Bordiga, G. Spoto and C. Lamberti, *Adv. Catal.*, 2001, **46**, 265.
493. E. Escalona Platero, D. Scarano, G. Spoto and A. Zecchina, *Faraday Discuss. Chem. Soc.*, 1985, **80**, 183.
494. F. Bonino, S. Chavan, J. G. Vitillo, E. Groppo, G. Agostini, C. Lamberti, P. D. C. Dietzel, C. Prestipino and S. Bordiga, *Chem. Mater.*, 2008, **20**, 4957.
495. S. Chavan, J. G. Vitillo, E. Groppo, F. Bonino, C. Lamberti, P. D. C. Dietzel and S. Bordiga, *J. Phys. Chem. C*, 2009, **113**, 3292.
496. M. Guisnet, P. Ayrault, C. Coutanceau, M. F. Alvarez and J. Datka, *J. Chem. Soc.-Faraday Trans.*, 1997, **93**, 1661.
497. J. P. Marques, I. Gener, P. Ayrault, J. C. Bordado, J. M. Lopes, F. R. Ribeiro and M. Guisnet, *Microporous Mesoporous Mat.*, 2003, **60**, 251.
498. J. C. Groen, L. A. A. Peffer, J. A. Moulijn and J. Perez-Ramirez, *Chem.-Eur. J.*, 2005, **11**, 4983.
499. J. A. Martens, R. Parton, L. Uytterhoeven, P. A. Jacobs and G. F. Froment, *Appl. Catal.*, 1991, **76**, 95.

500. J. Wang, J. N. Park, Y. K. Park and C. W. Lee, *J. Catal.*, 2003, **220**, 265.
501. B. Xu, S. Bordiga, R. Prins and J. A. van Bokhoven, *Appl. Catal. A-Gen.*, 2007, **333**, 245.
502. L. M. Kustov, V. B. Kazansky, S. Beran, L. Kubelkova and P. Jiru, *J. Phys. Chem.*, 1987, **91**, 5247.
503. E. Loeffler, U. Lohse, C. Peuker, G. Oehlmann, L. M. Kustov, V. L. Zholobenko and V. B. Kazansky, *Zeolites*, 1990, **10**, 266.
504. S. Khabtou, T. Chevreau and J. C. Lavalley, *Microporous Mater.*, 1994, **3**, 133.
505. P. Wu, T. Komatsu and T. Yashima, *J. Chem. Soc.-Faraday Trans.*, 1996, **92**, 861.
506. J. Datka, B. Sulikowski and B. Gil, *J. Phys. Chem.*, 1996, **100**, 11242.
507. I. Ahmad, J. A. Anderson, T. J. Dines and C. H. Rochester, *J. Colloid Interface Sci.*, 1998, **207**, 371.
508. M. L. Occelli, S. Biz, A. Auroux and G. J. Ray, *Microporous Mesoporous Mat.*, 1998, **26**, 193.
509. J. Datka, B. Gil, J. Zlamaniec, P. Batamack, J. Fraissard and P. Massiani, *Pol. J. Chem.*, 1999, **73**, 1535.
510. Y. Fan, X. J. Bao, X. Y. Lin, G. Shi and H. Y. Liu, *J. Phys. Chem. B*, 2006, **110**, 15411.
511. V. Machado, J. Rocha, A. P. Carvalho and A. Martins, *Appl. Catal. A-Gen.*, 2012, **445**, 329.
512. P. Ratnasamy and R. Kumar, *Catal. Today*, 1991, **9**, 329.
513. H. Kosslick, V. A. Tuan, R. Fricke, C. Peuker, W. Pilz and W. Storek, *J. Phys. Chem.*, 1993, **97**, 5678.
514. C. Peuker, *J. Mol. Struct.*, 1995, **349**, 317.
515. N. K. Mal, A. Bhaumik, R. Kumar and A. V. Ramaswamy, *Catal. Lett.*, 1995, **33**, 387.
516. B. Sulikowski, *Heterogeneous Chem. Rev.*, 1996, **3**, 203.
517. I. Arends, R. A. Sheldon, M. Wallau and U. Schuchardt, *Angew. Chem.-Int. Edit.*, 1997, **36**, 1144.
518. R. J. Francis and D. O'Hare, *J. Chem. Soc.-Dalton Trans.*, 1998, 3133.
519. Z. Gabelica and S. Valange, *Microporous Mesoporous Mater.*, 1999, **30**, 57.
520. R. Millini, G. Perego and G. Bellussi, *Top. Catal.*, 1999, **9**, 13.
521. G. M. Johnson, P. J. Mead and M. T. Weller, *Microporous Mesoporous Mat.*, 2000, **38**, 445.
522. Y. Ma, W. Tong, H. Zhou and S. L. Suib, *Microporous Mesoporous Mater.*, 2000, **37**, 243.
523. M. Renz, T. Blasco, A. Corma, V. Fornes, R. Jensen and L. Nemeth, *Chem.-Eur. J.*, 2002, **8**, 4708.
524. A. Corma, M. E. Domine and S. Valencia, *J. Catal.*, 2003, **215**, 294.
525. L. G. A. van de Water, M. A. Zwijnenburg, W. G. Sloof, J. C. van der Waal, J. C. Jansen and T. Maschmeyer, *ChemPhysChem*, 2004, **5**, 1328.
526. M. Boronat, P. Concepcion, A. Corma, M. Renz and S. Valencia, *J. Catal.*, 2005, **234**, 111.
527. L. Shi, K. E. Christensen, K. Jansson, J. Sun and X. Zou, *Chem. Mat.*, 2007, **19**, 5973.
528. M. G. Clerici, in *Metal Oxide Catalysis*, eds. S. D. Jackson and J. S. J. Hargreaves, Wiley-VCH Verlag GmbH & Co. KGaA, Weinheim, 2009, pp. 705.
529. M. El-Roz, L. Lakiss, A. Vicente, K. N. Bozhilov, F. Thibault-Starzyk and V. Valtchev, *Chem. Sci.*, 2014, **5**, 68.
530. W. N. P. van der Graaff, G. N. Li, B. Mezari, E. A. Pidko and E. J. M. Hensen, *ChemCatChem*, 2015, **7**, 1152.
531. L. P. Li, X. J. Cui, S. T. Xu, J. F. Li, Z. F. Qin and J. G. Wang, *Mater. Express*, 2015, **5**, 73.
532. L. Regli, S. Bordiga, C. Busco, C. Prestipino, P. Ugliengo, A. Zecchina and C. Lamberti, *J. Am. Chem. Soc.*, 2007, **129**, 12131.
533. L. Regli, C. Lamberti, C. Busco, A. Zecchina, C. Prestipino, K. P. Lillerud, S. I. Zones and S. Bordiga, *Stud. Surf. Sci. Catal.*, 2007, **170**, 585.
534. E. M. Flanigen, H. Khatami and H. A. Szymanski, in *Molecular Sieve Zeolites-I*, eds. F. E. M. and L. B. Sand, American Chemical Society, Washinton DC, 1974, vol. I, ch. 16, pp. 201.
535. A. J. M. De Man, B. W. H. Van Beest, M. Leslie and R. A. Van Santen, *J. Phys. Chem.*, 1990, **94**, 2524.
536. A. Damin, F. Bonino, G. Ricchiardi, S. Bordiga, A. Zecchina and C. Lamberti, *J. Phys. Chem. B*, 2002, **106**, 7524.
537. S. Bordiga, A. Damin, F. Bonino, A. Zecchina, G. Spanò, F. Rivetti, V. Bolis and C. Lamberti, *J. Phys. Chem. B*, 2002, **106**, 9892.
538. M. R. Boccuti, K. M. Rao, A. Zecchina, G. Leofanti and G. Petrini, *Stud. Surf. Sci. Catal.*, 1989, **48**, 133.
539. D. Scarano, A. Zecchina, S. Bordiga, F. Geobaldo, G. Spoto, G. Petrini, G. Leofanti, M. Padovan and G. Tozzola, *J. Chem. Soc.-Faraday Trans.*, 1993, **89**, 4123.
540. M. A. Camblor, A. Corma and J. Perezpariente, *J. Chem. Soc.-Chem. Commun.*, 1993, 557.
541. E. Astorino, J. B. Peri, R. J. Willey and G. Busca, *J. Catal.*, 1995, **157**, 482.
542. T. Blasco, A. Corma, M. T. Navarro and J. P. Pariente, *J. Catal.*, 1995, **156**, 65.
543. T. Blasco, M. A. Camblor, A. Corma, P. Esteve, J. M. Guil, A. Martinez, J. A. Perdigon-Melon and S. Valencia, *J. Phys. Chem. B*, 1998, **102**, 75.

544. E. A. Eilertsen, S. Bordiga, C. Lamberti, A. Damin, F. Bonino, B. Arstad, S. Svelle, U. Olsbye and K. P. Lillerud, *ChemCatChem*, 2011, **3**, 1869.
545. E. A. Eilertsen, F. Giordanino, C. Lamberti, S. Bordiga, A. Damin, F. Bonino, U. Olsbye and K. P. Lillerud, *Chem. Commun.*, 2011, **47**, 11867.
546. C. Li, S.-F. Fu, H. Zhang and Q. Xin, *J. Chem. Soc. Chem. Commun.*, 1994, 17.
547. J. F. Bengoa, N. G. Gallegos, S. G. Marchetti, A. M. Alvarez, M. V. Cagnoli and A. A. Yeramian, *Microporous Mesoporous Mat.*, 1998, **24**, 163.
548. C. Perego, A. Carati, P. Ingallina, M. A. Mantegazza and G. Bellussi, *Appl. Catal. A-Gen.*, 2001, **221**, 63.
549. A. Corma and H. Garcia, *Chem. Rev.*, 2002, **102**, 3837.
550. L. Dal Pozzo, G. Fornasari and T. Monti, *Catal. Commun.*, 2002, **3**, 369.
551. G. Tozzola, M. A. Mantegazza, G. Ranghino, G. Petrini, S. Bordiga, G. Ricchiardi, C. Lamberti, R. Zulian and A. Zecchina, *J. Catal.*, 1998, **179**, 64.
552. C. Prestipino, F. Bonino, S. Usseglio, A. Damin, A. Tasso, M. G. Clerici, S. Bordiga, F. D'Acapito, A. Zecchina and C. Lamberti, *ChemPhysChem*, 2004, **5**, 1799.
553. F. Bonino, A. Damin, G. Ricchiardi, Ricci M, Spanò G, D'Aloisio R, Zecchina A, Lamberti C, Prestipino C and S. Bordiga, *J. Phys. Chem. B*, 2004, **108**, 3573.
554. K. Tanabe and W. F. Holderich, *Appl. Catal. A-Gen.*, 1999, **181**, 399.
555. R. J. Davis, *J. Catal.*, 2003, **216**, 396.
556. C. P. Nicholas, in *Zeolites in Industrial Separation and Catalysis*, Wiley-VCH Verlag GmbH & Co. KGaA, Weinheim, 2010, pp. 355.
557. S. Kulprathipanja and R. B. James, in *Zeolites in Industrial Separation and Catalysis*, Wiley-VCH Verlag GmbH & Co. KGaA, Weinheim, 2010, pp. 173.
558. S. Kulprathipanja, in *Zeolites in Industrial Separation and Catalysis*, Wiley-VCH Verlag GmbH & Co. KGaA, Weinheim, 2010, pp. 203.
559. D. Barthomeuf, *Catal. Rev. Sci.-Engin.*, 1996, **38**, 521.
560. J. Weitkamp, M. Hunger and U. Rymsa, *Microporous Mesoporous Mater.*, 2001, **48**, 255.
561. J. Weitkamp and M. Hunger, 2007, **168**, 787.
562. M. Sánchez-Sánchez and T. Blasco, *Catal. Today*, 2009, **143**, 293.
563. H. Hattori, *Chem. Rev.*, 1995, **95**, 537.
564. T. Frising and P. Leflaive, *Microporous Mesoporous Mat.*, 2008, **114**, 27.
565. R. T. Sanderson, *Science*, 1951, **114**, 670.
566. R. T. Sanderson, *Chemical Bonds and Bond Energy*, Academic Press, New York, 1976.
567. S. E. Siporin, B. C. McClaine and R. J. Davis, *Langmuir*, 2003, **19**, 4707.
568. T. Belin, Mve Mfoumou, C. , S. Mignard and Y. Pouilloux, *Microporous Mesoporous Mater.*, 2013, **182**, 109.
569. S. Ernst, M. Hartmann, S. Sauerbeck and T. Bongers, 2000, **200**, 117.
570. C. Mirodatos, P. Pichat and D. Barthomeuf, *J. Phys. Chem.*
, 1976, **80**, 1335.
571. M. Srasra, P. Rouxhet, E. M. Gaigneaux and S. Delsarte, *J. Phys. Chem. C*, 2006, **114**.
572. X. Chen, J. Guo, Z. Fu, H. He and Y. Lon, *J. Porous Mater.*, 2013, **20**, 1271.
573. T. Steiner, *Angew. Chem.-Int. Edit.*, 2002, **41**, 48.
574. P. O. Scokart and P. G. Rouxhet, *Bull. Soc. Chim. Belges*, 1981, **90**, 983.
575. D. Barthomeuf, *J. Phys. Chem.*, 1984, **88**, 42.
576. M. M. Huang and S. Kaliaguine, *J. Chem. Soc.-Faraday Trans.*, 1992, **88**, 751.
577. M. Huang and S. Kaliaguine, 1992, **88**, 751.
578. D. Barthomeuf, *J. Phys. Chem.*, 1984, **88**, 42.
579. D. Murphy, P. Massiani, R. Franck and D. Barthomeuf, *J. Phys. Chem.*, 1996, **100**, 6731.
580. M. Sánchez-Sánchez and T. Blasco, *J. Am. Chem. Soc.*, 2002, **124**, 3443.
581. J. Kučera, P. Nachtigall, J. Kotrla, G. Košová and J. Čejka, *J. Phys. Chem. B*, 2004, **108**, 16012.
582. M. A. Sanchez-Castillo, N. Agarwal, C. Miller, R. D. Cortright, R. J. Madon and J. A. Dumesic, *J. Catal.*, 2002, **205**, 67.
583. M. Sánchez-Sánchez and T. Blasco, *J. Am. Chem. Soc.*, 2002, **124**, 3443.
584. H. Forster, H. Fuess, E. Geidel, B. Hunger, H. Jobic, C. Kirschhock, O. Klepel and K. Krause, *Phys. Chem. Chem. Phys.*, 1999, **1**, 593.
585. R. J. Corrêa, *Tetrahedron Lett.*, 2003, **44**, 7299.
586. *http://webbook.nist.gov*.
587. J. Xie, M. Huang and S. Kaliaguine, *React. Kinet. Catal. Lett.*, 1996, **58**, 217.

588. E. Bosch, S. Huber, J. Weitkamp and H. Knözinger, *Phys. Chem. Chem. Phys.*, 1999, **1**, 579.
589. A. A. Tsyganenko, *Top. Catal.*, 2013, **56**, 905.
590. A. A. Tsyganenko, N. V. Zakharov and P. D. Murzin, *Catal. Today*, 2014, **226**, 73.
591. P. Hobza and Z. Havlas, *Chem. Rev.*, 2000, **100**, 4253.
592. K. Hermansson, *J. Phys. Chem. A*, 2002, **106**, 4695.
593. S. Scheiner and T. Kar, *J. Phys. Chem. A*, 2002, **106**, 1784.
594. A. J. Barnes, *J. Mol. Struct.*, 2004, **704**, 3.
595. M. Sanchez-Sanchez, T. Blasco and A. Corma, *J. Phys. Chem. C*, 2008, **112**, 16961.
596. S. N. Delanoye, W. A. Herrebout and B. J. van der Veken, *J. Am. Chem. Soc.*, 2002, **124**, 7490.
597. E. B. Uvarova, L. M. Kustov and V. B. Kazansky, *Stud. Surf. Sci. Catal.*, 1995, **94**, 254.
598. A. V. Ivanov, A. E. Koklin, E. B. Uvarova and L. M. Kustov, *Phys. Chem. Chem. Phys.*, 2003, **5**, 4718.
599. J. C. Lavalley, J. Lamotte, A. Travert, J. Czyzniewska and M. Ziolek, *J. Chem. Soc.-Faraday Trans.*, 1998, **94**, 331.
600. B. Bonelli, B. Civalleri, B. Fubini, P. Ugliengo, C. O. Arean and E. Garrone, *J. Phys. Chem. B*, 2000, **104**, 10978.
601. E. Garrone, B. Bonelli, C. Lamberti, B. Civalleri, M. Rocchia, P. Roy and C. O. Arean, *J. Chem. Phys.*, 2002, **117**, 10274.
602. G. D. Pirngruber, P. Raybaud, Y. Belmabkhout, J. Cejka and A. Zukal, *Phys. Chem. Chem. Phys.*, 2010, **12**, 13534.
603. C. Bisio, G. Martra, S. Coluccia and P. Massiani, *J. Phys. Chem. C*, 2008, **112**, 10520.
604. P. A. Jacobs, F. M. Van Cauwelaert and E. F. Vansant, *J. Chem. Soc. Farad. Trans. 1*, 1973, **69**, 2130.
605. A. Vimont, F. Thibault-Starzyk and J. C. Lavalley, *J. Phys. Chem. B*, 2000, **104**, 286.
606. J. Liu, P. L. Ying, Q. Xin and C. Li, *Zeolites*, 1997, **19**, 197.
607. F. Thibault-Starzyk, O. Marie, N. Malicki, A. Vos, R. Schoonheydt, P. Geerlings, C. Henriques, C. Pommier and P. Massiani, *Stud. Surf. Sci. Catal.*, 2005, **158**, 663.
608. O. Marie, N. Malicki, C. Pommier, P. Massiani, A. Vos, R. Schoonheydt, P. Geerlings, C. Henriques and F. Thibault-Starzyk, *Chem. Commun.*, 2005, 1049.
609. E. A. Pidko, P. Mignon, P. Geerlings, R. A. Schoonheydt and R. A. van Santen, *J. Phys. Chem. C*, 2008, **112**, 5510.
610. E. A. Pidko and R. A. Van Santen, *Int. J. Quantum Chem.*, 2010, **110**, 210.
611. G. L. Woolery, L. B. Alemany, R. M. Dessau and A. W. Chester, *Zeolites*, 1986, **6**, 14.
612. R. M. Dessau, K. D. Schmitt, G. T. Kerr, G. L. Woolery and L. B. Alemany, *J. Catal.*, 1987, **104**, 484.
613. B. Kraushaar, J. W. De Haan and J. H. C. Van Hooff, *J. Catal.*, 1988, **109**, 470.
614. R. W. Weber, J. C. Q. Fletcher, K. P. Moller and C. T. Oconnor, *Microporous Mater.*, 1996, **7**, 15.
615. A. Corma, V. Fornés, L. Forni, F. Márquez, J. Martínez-Triguero and D. Moscotti, *J. Catal.*, 1998, **179**, 451.
616. T. Armaroli, M. Trombetta, A. G. Alejandre, J. R. Solis and G. Busca, *Phys. Chem. Chem. Phys.*, 2000, **2**, 3341.
617. K. H. Rhodes, S. A. Davis, F. Caruso, B. J. Zhang and S. Mann, *Chem. Mat.*, 2000, **12**, 2832.
618. M. W. Anderson, S. M. Holmes, N. Hanif and C. S. Cundy, *Angew. Chem.-Int. Edit.*, 2000, **39**, 2707.
619. S. van Donk, A. H. Janssen, J. H. Bitter and K. P. de Jong, *Catal. Rev.*, 2003, **45**, 297.
620. M. Hartmann, *Angew. Chem.-Int. Edit.*, 2004, **43**, 5880.
621. L. Tosheva and V. P. Valtchev, *Chem. Mat.*, 2005, **17**, 2494.
622. J. C. Groen, J. A. Moulijn and J. Perez-Ramirez, *J. Mater. Chem.*, 2006, **16**, 2121.
623. F. S. Xiao, L. F. Wang, C. Y. Yin, K. F. Lin, Y. Di, J. X. Li, R. R. Xu, D. S. Su, R. Schlogl, T. Yokoi and T. Tatsumi, *Angew. Chem.-Int. Edit.*, 2006, **45**, 3090.
624. M. A. Snyder and M. Tsapatsis, *Angew. Chem.-Int. Edit.*, 2007, **46**, 7560.
625. K. Egeblad, C. H. Christensen, M. Kustova and C. H. Christensen, *Chem. Mat.*, 2008, **20**, 946.
626. W. Fan, M. A. Snyder, S. Kumar, P. S. Lee, W. C. Yoo, A. V. McCormick, R. L. Penn, A. Stein and M. Tsapatsis, *Nat. Mater.*, 2008, **7**, 984.
627. J. Perez-Ramirez, C. H. Christensen, K. Egeblad, C. H. Christensen and J. C. Groen, *Chem. Soc. Rev.*, 2008, **37**, 2530.
628. J. Perez-Ramirez, D. Verboekend, A. Bonilla and S. Abello, *Adv. Funct. Mater.*, 2009, **19**, 3972.
629. A. Bonilla, D. Baudouin and J. Perez-Ramirez, *J. Catal.*, 2009, **265**, 170.
630. F. Thibault-Starzyk, I. Stan, S. Abelló, A. Bonilla, K. Thomas, C. Fernandez, J.-P. Gilson and J. Pérez-Ramírez, *J. Catal.*, 2009, **264**, 11.
631. C. Fernandez, I. Stan, J. P. Gilson, K. Thomas, A. Vicente, A. Bonilla and J. Perez-Ramirez, *Chem.-Eur. J.*, 2010, **16**, 6224.

632. D. Verboekend, L. A. Villaescusa, K. Thomas, I. Stan and J. Perez-Ramirez, *Catal. Today*, 2010, **152**, 11.
633. Y. P. Khitev, Y. G. Kolyagin, Ivanova, II, O. A. Ponomareva, F. Thibault-Starzyk, J. P. Gilson, C. Fernandez and F. Fajula, *Microporous Mesoporous Mat.*, 2011, **146**, 201.
634. D. Verboekend, A. M. Chabaneix, K. Thomas, J. P. Gilson and J. Perez-Ramirez, *Crystengcomm*, 2011, **13**, 3408.
635. A. Inayat, B. Reinhardt, H. Uhlig, W. D. Einicke and D. Enke, *Chem. Soc. Rev.*, 2013, **42**, 3753.
636. D. Tzoulaki, A. Jentys, J. Perez-Ramirez, K. Egeblad and J. A. Lercher, *Catal. Today*, 2012, **198**, 3.
637. Z. Xue, T. Zhang, J. Ma, H. Miao, W. Fan, Y. Zhang and R. Li, *Microporous Mesoporous Mater.*, 2012, **151**, 271.
638. D. Verboekend, G. Vile and J. Perez-Ramirez, *Adv. Funct. Mater.*, 2012, **22**, 916.
639. P. Sazama, Z. Sobalik, J. Dedecek, I. Jakubec, V. Parvulescu, Z. Bastl, J. Rathousky and H. Jirglova, *Angew. Chem.-Int. Edit.*, 2013, **52**, 2038.
640. D. P. Serrano, J. M. Escola and P. Pizarro, *Chem. Soc. Rev.*, 2013, **42**, 4004.
641. K. Sadowska, K. Góra-Marek and J. Datka, *J. Phys. Chem. C*, 2013, **117**, 9237.
642. W. Chaikittisilp, Y. Suzuki, R. R. Mukti, T. Suzuki, K. Sugita, K. Itabashi, A. Shimojima and T. Okubo, *Angew. Chem.-Int. Edit.*, 2013, **52**, 3355.
643. Ivanova, II and E. E. Knyazeva, *Chem. Soc. Rev.*, 2013, **42**, 3671.
644. K. Moller and T. Bein, *Chem. Soc. Rev.*, 2013, **42**, 3689.
645. C. M. A. Parlett, K. Wilson and A. F. Lee, *Chem. Soc. Rev.*, 2013, **42**, 3876.
646. L. Gueudre, M. Milina, S. Mitchell and J. Perez-Ramirez, *Adv. Funct. Mater.*, 2014, **24**, 209.
647. P. A. Jacobs, M. Dusselier and B. F. Sels, *Angew. Chem.-Int. Edit.*, 2014, **53**, 8621.
648. D. D. Xu, Y. H. Ma, Z. F. Jing, L. Han, B. Singh, J. Feng, X. F. Shen, F. L. Cao, P. Oleynikov, H. Sun, O. Terasaki and S. N. Che, *Nat. Commun.*, 2014, **5**, 9.
649. T. C. Keller, S. Isabettini, D. Verboekend, E. G. Rodrigues and J. Perez-Ramirez, *Chem. Sci.*, 2014, **5**, 677.
650. M. Khaleel, A. J. Wagner, K. A. Mkhoyan and M. Tsapatsis, *Angew. Chem.-Int. Edit.*, 2014, **53**, 9456.
651. B. Li, Z. J. Hu, B. Kong, J. X. Wang, W. Li, Z. K. Sun, X. F. Qian, Y. S. Yang, W. Shen, H. L. Xu and D. Y. Zhao, *Chem. Sci.*, 2014, **5**, 1565.
652. K. Góra-Marek, K. Tarach and M. Choi, *J. Phys. Chem. C*, 2014, **118**, 12266.
653. K. Mlekodaj, K. Tarach, J. Datka, K. Gora-Marek and W. Makowski, *Microporous Mesoporous Mater.*, 2014, **183**, 54.
654. M. Milina, S. Mitchell, D. Cooke, P. Crivelli and J. Perez-Ramirez, *Angew. Chem.-Int. Edit.*, 2015, **54**, 1591.
655. K. L. Liu, A. V. Kubarev, J. Van Loon, H. Uji-i, D. E. De Vos, J. Hofkens and M. B. J. Roeffaers, *ACS Nano*, 2014, **8**, 12650.
656. R. A. Beyerlein, C. ChoiFeng, J. B. Hall, B. J. Huggins and G. J. Ray, *Top. Catal.*, 1997, **4**, 27.
657. M. A. Kuehne, H. H. Kung and J. T. Miller, *J. Catal.*, 1997, **171**, 293.
658. M. A. Kuehne, S. M. Babitz, H. H. Kung and J. T. Miller, *Appl. Catal. A-Gen.*, 1998, **166**, 293.
659. A. Corma, G. W. Huber, L. Sauvanaud and P. O'Connor, *J. Catal.*, 2007, **247**, 307.
660. H. S. Cerqueira, G. Caeiro, L. Costa and F. R. Ribeiro, *J. Mol. Catal. A-Chem.*, 2008, **292**, 1.
661. P. Kortunov, S. Vasenkov, J. Karger, R. Valiullin, P. Gottschalk, M. F. Elia, M. Perez, M. Stocker, B. Drescher, G. McElhiney, C. Berger, R. Glaser and J. Weitkamp, *J. Am. Chem. Soc.*, 2005, **127**, 13055.
662. N. Malicki, P. Beccat, P. Bourges, C. Fernandez, A.-A. Quoineaud, L. J. Simon and F. Thibault-Starzyk, *Stud. Surf. Sci. Catal.*, 2007, **170**, 762.
663. M. Connolly, *J. Appl. Cryst.*, 1983, **16**, 548.
664. O. Marie, P. Massiani and F. Thibault-Starzyk, *J. Phys. Chem. B*, 2004, **108**, 5073.
665. F. Wakabayashi, J. Kondo, A. Wada, K. Domen and C. Hirose, *J. Phys. Chem.*, 1993, **97**, 10761.
666. V. L. Zholobenko, M. A. Makarova and J. Dwyer, *J. Phys. Chem.*, 1993, **97**, 5962.
667. M. Maache, A. Janin, J. C. Lavalley and E. Benazzi, *Zeolites*, 1995, **15**, 507.
668. Z. Tvaruzkova, K. Habersberger and P. Jiru, *React. Kinet. Catal. Lett.*, 1991, **44**, 361.
669. S. Jolly, J. Saussey and J. C. Lavalley, *Catal. Lett.*, 1994, **24**, 141.
670. B. Wichterlova, Z. Tvaruzkova, Z. Sobalik and P. Sarv, *Microporous Mesoporous Mater.*, 1998, **24**, 223.
671. M. Trombetta, G. Busca, S. Rossini, V. Piccoli, U. Cornaro, A. Guercio, R. Catani and R. J. Willey, *J. Catal.*, 1998, **179**, 581.
672. P. Kubanek, B. Wichterlova and Z. Sobalik, *J. Catal.*, 2002, **211**, 109.
673. A. Damin, S. Bordiga, A. Zecchina, K. Doll and C. Lamberti, *J. Chem. Phys.*, 2003, **118**, 10183.
674. O. Marie, F. Thibault-Starzyk and J. C. Lavalley, *Phys. Chem. Chem. Phys.*, 2000, **2**, 5341.
675. M. Bevilacqua and G. Busca, *Catal. Commun.*, 2002, **3**, 497.

676. M. Bevilacqua, A. G. Alejandre, C. Resini, M. Casagrande, J. Ramirez and G. Busca, *Phys. Chem. Chem. Phys.*, 2002, **4**, 4575.
677. T. Montanari, M. Bevilacqua and G. Busca, *Appl. Catal. A-Gen.*, 2006, **307**, 21.
678. B. Onida, F. Geobaldo, F. Testa, F. Crea and E. Garrone, *Microporous Mesoporous Mat.*, 1999, **30**, 119.
679. N. S. Nesterenko, F. Thibault-Starzyk, V. Montouillout, V. V. Yuschenko, C. Fernandez, J. P. Gilson, F. Fajula and Ivanova, II, *Microporous Mesoporous Mater.*, 2004, **71**, 157.
680. N. S. Nesterenko, F. Thibault-Starzyk, V. Montouillout, V. V. Yushchenko, C. Fernandez, J. P. Gilson, F. Fajula and I. I. Ivanova, *Kin. Catal.*, 2006, **47**, 40.
681. T. Onfroy, G. Clet and M. Houalla, *Microporous Mesoporous Mater.*, 2005, **82**, 99.
682. D. F. Swinehart, *J. Chem. Educ.*, 1962, **39**, 333.
683. A. Rodger, in *Encyclopedia of Biophysics*, ed. G. K. Roberts, Springer Berlin Heidelberg, 2013, ch. 783, pp. 184.
684. J. Datka, A. M. Turek, J. M. Jehng and I. E. Wachs, *J. Catal.*, 1992, **135**, 186.
685. M. Crocker, R. H. M. Herold, M. H. W. Sonnemans, C. A. Emeis, A. E. Wilson and J. N. Vandermoolen, *J. Phys. Chem.*, 1993, **97**, 432.
686. C. A. Emeis, *J. Catal.*, 1993, **141**, 347.
687. V. Bolis, G. Magnacca, G. Cerrato and C. Morterra, *Thermochim. Acta*, 2001, **379**, 147.
688. C. Morterra, G. Magnacca and V. Bolis, *Catal. Today*, 2001, **70**, 43.
689. F. Thibault-Starzyk, B. Gil, S. Aiello, T. Chevreau and J. P. Gilson, *Microporous Mesoporous Mater.*, 2004, **67**, 107.
690. A. Popov, E. Kondratieva, J. M. Goupil, L. Mariey, P. Bazin, J. P. Gilson, A. Travert and F. Mauge, *J. Phys. Chem. C*, 2010, **114**, 15661.
691. A. A. Tsyganenko, E. E. Platero, C. O. Arean, E. Garrone and A. Zecchina, *Catal. Lett.*, 1999, **61**, 187.
692. C. O. Arean, A. A. Tsyganenko, O. V. Manoilova, G. T. Palomino, M. P. Mentruit and E. Garrone, *Chem. Commun.*, 2001, 455.
693. C. O. Arean, O. V. Manoilova, A. A. Tsyganenko, G. T. Palomino, M. P. Mentruit, F. Geobaldo and E. Garrone, *Eur. J. Inorg. Chem.*, 2001, 1739.
694. O. V. Manoilova, M. P. Mentruit, G. T. Palomino, A. A. Tsyganenko and C. O. Arean, *Vib. Spectrosc.*, 2001, **26**, 107.
695. C. O. Arean, O. V. Manoilova, M. R. Delgado, A. A. Tsyganenko and E. Garrone, *Phys. Chem. Chem. Phys.*, 2001, **3**, 4187.
696. C. O. Arean, M. R. Delgado, O. V. Manoilova, G. T. Palomino, A. A. Tsyganenko and E. Garrone, *Chem. Phys. Lett.*, 2002, **362**, 109.
697. C. O. Arean, O. V. Manoilova, G. T. Palomino, M. R. Delgado, A. A. Tsyganenko, B. Bonelli and E. Garrone, *Phys. Chem. Chem. Phys.*, 2002, **4**, 5713.
698. C. P. Arean, M. P. Mentruit, M. R. Delgado, G. T. Palomino, O. V. Manoilova, A. A. Tsyganenko and E. Garrone, *Stud. Surf. Sci. Catal.*, 2002, **142**, 207.
699. C. O. Arean, O. V. Manoilova, B. Bonelli, M. R. Delgado, G. T. Palomino and E. Garrone, *Chem. Phys. Lett.*, 2003, **370**, 631.
700. P. Y. Storozhev, C. O. Arean, E. Garrone, P. Ugliengo, V. A. Ermoshin and A. A. Tsyganenko, *Chem. Phys. Lett.*, 2003, **374**, 439.
701. A. V. Rudakova, R. F. Lobo and K. M. Bulanin, *J. Phys. Chem. B*, 2003, **107**, 5212.
702. G. Spoto, E. Gribov, S. Bordiga, C. Lamberti, G. Ricchiardi, D. Scarano and A. Zecchina, *Chem. Commun.*, 2004, 2768.
703. C. O. Arean, M. R. Delgado, G. T. Palomino, M. T. Rubio, N. M. Tsyganenko, A. A. Tsyganenko and E. Garrone, *Microporous Mesoporous Mat.*, 2005, **80**, 247.
704. P. Nachtigall, E. Garrone, G. T. Palomino, M. R. Delgado, D. Nachtigallova and C. O. Arean, *Phys. Chem. Chem. Phys.*, 2006, **8**, 2286.
705. A. A. Tsyganenko, E. V. Kondratieva, V. S. Yanko and P. Y. Storozhev, *J. Mater. Chem.*, 2006, **16**, 2358.
706. C. O. Arean, G. T. Palomino and M. R. L. Carayol, *Appl. Surf. Sci.*, 2007, **253**, 5701.
707. M. R. Delgado and C. O. Area, *Appl. Surf. Sci.*, 2007, **253**, 5705.
708. C. O. Arean, *J. Mol. Struct.*, 2008, **880**, 31.
709. B. Bonelli, C. O. Arean, M. Armandi, M. R. Delgado and E. Garrone, *ChemPhysChem*, 2008, **9**, 1747.
710. G. T. Palomino, M. R. L. Carayol and C. O. Arean, *Catal. Today*, 2008, **138**, 249.
711. M. Armandi, E. Garrone, C. O. Arean and B. Bonelli, *ChemPhysChem*, 2009, **10**, 3316.
712. G. T. Palomino, B. Bonelli, C. O. Arean, J. B. Parra, M. R. L. Carayol, M. Armandi, C. O. Ania and E. Garrone, *Int. J. Hydrog. Energy*, 2009, **34**, 4371.

713. C. O. Arean and M. R. Delgado, *Appl. Surf. Sci.*, 2010, **256**, 5259.
714. M. Armandi, B. Bonelli, I. Bottero, C. O. Arean and E. Garrone, *J. Phys. Chem. C*, 2010, **114**, 6658.
715. M. R. Delgado and C. O. Arean, *Energy*, 2011, **36**, 5286.
716. C. O. Arean, M. R. Delgado, G. F. Bibiloni, O. Bludsky and P. Nachtigall, *ChemPhysChem*, 2011, **12**, 1435.
717. A. Zukal, C. O. Arean, M. R. Delgado, P. Nachtigall, A. Pulido, J. Mayerova and J. Cejka, *Microporous Mesoporous Mat.*, 2011, **146**, 97.
718. O. Zavorotynska, J. G. Vitillo, G. Spoto and A. Zecchina, *Int. J. Hydrog. Energy*, 2011, **36**, 7944.
719. P. Nachtigall, M. R. Delgado, D. Nachtigallova and C. O. Arean, *Phys. Chem. Chem. Phys.*, 2012, **14**, 1552.
720. R. Bulanek and E. Koudelkova, *J. Therm. Anal. Calorim.*, 2013, **113**, 97.
721. M. R. Delgado, R. Bulanek, P. Chlubna and C. O. Arean, *Catal. Today*, 2014, **227**, 45.
722. F. Rouquerol, J. Rouquerol and K. Sing, *Adsorption by Powders and Porous Solids Principles, Methodology and Applications*, Academic Press, London, 1999.
723. J. Pires, M. B. Decarvalho, F. R. Ribeiro and E. G. Derouane, 1993, **85**, 295.
724. T. Yamazaki, M. Katoh, S. Ozawa and Y. Ogino, *Mol. Phys.*, 1993, **80**, 313.
725. S. K. Wirawan and D. Creaser, *Microporous Mesoporous Mat.*, 2006, **91**, 196.
726. J. A. Dunne, R. Mariwals, M. Rao, S. Sircar, R. J. Gorte and A. L. Myers, *Langmuir*, 1996, **12**, 5888.
727. J. A. Dunne, M. Rao, S. Sircar, R. J. Gorte and A. L. Myers, *Langmuir*, 1996, **12**, 5896.
728. S. Savitz, A. L. Myers and R. J. Gorte, *J. Phys. Chem. B*, 1999, **103**, 3687.
729. V. Bolis, S. Bordiga, C. Lamberti, A. Zecchina, A. Carati, F. Rivetti, G. Spano and G. Petrini, *Langmuir*, 1999, **15**, 5753.
730. V. Bolis, S. Bordiga, C. Lamberti, A. Zecchina, A. Carati, F. Rivetti, G. Spano and G. Petrini, *Microporous Mesoporous Mater.*, 1999, **30**, 67.
731. B. Bonelli, E. Garrone, B. Fubini, B. Onida, M. R. Delgado and C. O. Arean, *Phys. Chem. Chem. Phys.*, 2003, **5**, 2900.
732. A. Pulido, P. Nachtigall, A. Zukal, I. Dominguez and J. Cejka, *J. Phys. Chem. C*, 2009, **113**, 2928.
733. A. Zukal, A. Pulido, B. Gil, P. Nachtigall, O. Bludsky, M. Rubes and J. Cejka, *Phys. Chem. Chem. Phys.*, 2010, **12**, 6413.
734. J. Estephane, E. Groppo, J. G. Vitillo, A. Damin, C. Lamberti, S. Bordiga and A. Zecchina, *Phys. Chem. Chem. Phys.*, 2009, **11**, 2218.
735. G. Turnes Palomino, C. Palomino Cabello and C. Otero Arean, *Eur. J. Inorg. Chem.*, 2011, 1703.
736. S. M. Chavan, O. Zavorotynska, C. Lamberti and S. Bordiga, *Dalton Trans.*, 2013, **42**, 12586.
737. F. Bonino, C. Lamberti, S. Chavan, J. G. Vitillo and S. Bordiga, in *Metal-Organic Frameworks in heterogeneous catalysis*, eds. F. X. Llabrés i Xamena and J. Gascón, RSC, Cambridge, 2013, pp. 76.
738. G. T. Palomino, C. O. Arean and M. R. L. Carayol, *Appl. Surf. Sci.*, 2010, **256**, 5281.
739. C. O. Arean, G. T. Palomino, M. R. L. Carayol, A. Pulido, M. Rubes, O. Bludsky and P. Nachtigall, *Chem. Phys. Lett.*, 2009, **477**, 139.
740. P. J. E. Harlick and F. H. Tezel, *Microporous Mesoporous Mat.*, 2004, **76**, 71.
741. A. Pulido, M. R. Delgado, O. Bludsky, M. Rubes, P. Nachtigall and C. O. Arean, *Energy Environ. Sci.*, 2009, **2**, 1187.
742. E. Garrone, B. Bonelli and C. Otero Arean, *Chem. Phys. Lett.*, 2008, **456**, 68.
743. M. S. Westwell, M. S. Searle, J. Klein and D. H. Williams, *J. Phys. Chem.*, 1996, **100**, 16000.
744. A. A. Stolov, W. A. Herrebout and B. J. van der Veken, *J. Am. Chem. Soc.*, 1998, **120**, 7310.
745. G. Sugihara, D. S. Shigematsu, S. Nagadome, S. Lee, Y. Sasaki and H. Igimi, *Langmuir*, 2000, **16**, 1825.
746. D. H. Williams, E. Stephens, D. P. O'Brien and M. Zhou, *Angew. Chem.-Int. Edit.*, 2004, **43**, 6596.
747. A. A. Tsyganenko, *High Energy Chem.*, 2008, **42**, 610.
748. A. A. Tsyganenko, A. M. Chizhik and A. I. Chizhik, *Phys. Chem. Chem. Phys.*, 2010, **12**, 6387.
749. T. W. Hansen, J. B. Wagner, P. L. Hansen, S. Dahl, H. Topsoe and C. J. H. Jacobsen, *Science*, 2001, **294**, 1508.
750. P. L. Gai, *Microsc. microanal.*, 2002, **8**, 21.
751. P. L. Hansen, J. B. Wagner, S. Helveg, J. R. Rostrup-Nielsen, B. S. Clausen and H. Topsoe, *Science*, 2002, **295**, 2053.
752. S. Helveg, C. Lopez-Cartes, J. Sehested, P. L. Hansen, B. S. Clausen, J. R. Rostrup-Nielsen, F. Abild-Pedersen and J. K. Norskov, *Nature*, 2004, **427**, 426.
753. R. Sharma, *J. Mater. Res.*, 2005, **20**, 1695.
754. J. F. Creemer, S. Helveg, G. H. Hoveling, S. Ullmann, A. M. Molenbroek, P. M. Sarro and H. W. Zandbergen, *Ultramicroscopy*, 2008, **108**, 993.
755. P. A. Crozier, R. G. Wang and R. Sharma, *Ultramicroscopy*, 2008, **108**, 1432.

756. S. B. Simonsen, S. Dahl, E. Johnson and S. Helveg, *J. Catal.*, 2008, **255**, 1.
757. A. D. Gamalski, J. Tersoff, R. Sharma, C. Ducati and S. Hofmann, *Nano Lett.*, 2010, **10**, 2972.
758. G. A. Somorjai, S. K. Beaumont and S. Alayoglu, *Angew. Chem.-Int. Edit.*, 2011, **50**, 10116.
759. T. Fujita, P. F. Guan, K. McKenna, X. Y. Lang, A. Hirata, L. Zhang, T. Tokunaga, S. Arai, Y. Yamamoto, N. Tanaka, Y. Ishikawa, N. Asao, Y. Yamamoto, J. Erlebacher and M. W. Chen, *Nat. Mater.*, 2012, **11**, 775.
760. J. R. Jinschek and S. Helveg, *Micron*, 2012, **43**, 1156.
761. H. L. Xin, E. A. Pach, R. E. Diaz, E. A. Stach, M. Salmeron and H. M. Zheng, *ACS Nano*, 2012, **6**, 4241.
762. Y. Kuwauchi, S. Takeda, H. Yoshida, K. Sun, M. Haruta and H. Kohno, *Nano Lett.*, 2013, **13**, 3073.
763. E. Sayah, D. Brouri and P. Massiani, *Catal. Today*, 2013, **218**, 10.
764. S. R. Zhang, L. Nguyen, Y. Zhu, S. H. Zhan, C. K. Tsung and F. Tao, *Accounts Chem. Res.*, 2013, **46**, 1731.
765. S. R. Zhang, J. J. Shan, Y. Zhu, A. I. Frenkel, A. Patlolla, W. X. Huang, S. J. Yoon, L. Wang, H. Yoshida, S. Takeda and F. Tao, *J. Am. Chem. Soc.*, 2013, **135**, 8283.
766. H. L. L. Xin, S. Alayoglu, R. Z. Tao, A. Genc, C. M. Wang, L. Kovarik, E. A. Stach, L. W. Wang, M. Salmeron, G. A. Somorjai and H. M. Zheng, *Nano Lett.*, 2014, **14**, 3203.
767. Z. Ristanovic, J. P. Hofmann, U. Deka, T. U. Schulli, M. Rohnke, A. M. Beale and B. M. Weckhuysen, *Angew. Chem.-Int. Edit.*, 2013, **52**, 13382.
768. J. D. Grunwaldt, *J. Phys.: Conf. Series*, 2009, **190**, Art. n. 012151.
769. J. D. Grunwaldt and C. G. Schroer, *Chem. Soc. Rev.*, 2010, **39**, 4741.
770. A. M. Beale, S. D. M. Jacques and B. M. Weckhuysen, *Chem. Soc. Rev.*, 2010, **39**, 4656.
771. I. L. C. Buurmans and B. M. Weckhuysen, *Nat. Chem.*, 2012, **4**, 873.
772. S. Bordiga, E. Groppo, G. Agostini, J. A. van Bokhoven and C. Lamberti, *Chem. Rev.*, 2013, **113**, 1736.
773. J. D. Grunwaldt, J. B. Wagner and R. E. Dunin-Borkowski, *ChemCatChem*, 2013, **5**, 62.
774. L. Mino, G. Agostini, E. Borfecchia, D. Gianolio, A. Piovano, E. Gallo and C. Lamberti, *J. Phys. D-Appl. Phys.*, 2013, **46**, Art. N. 423001.
775. C. Garino, E. Borfecchia, R. Gobetto, J. A. van Bokhoven and C. Lamberti, *Coord. Chem. Rev.*, 2014, **277**, 130.
776. S. Megelski, A. Lieb, M. Pauchard, A. Drechsler, S. Glaus, C. Debus, A. J. Meixner and G. Calzaferri, *J. Phys. Chem. B*, 2001, **105**, 25.
777. L. Karwacki, E. Stavitski, M. H. F. Kox, J. Kornatowski and B. M. Weckhuysen, *Angew. Chem.-Int. Edit.*, 2007, **46**, 7228.
778. M. B. J. Roeffaers, B. F. Sels, H. Uji-i, B. Blanpain, P. L'Hoest, P. A. Jacobs, F. C. De Schryver, J. Hofkens and D. E. De Vos, *Angew. Chem.-Int. Edit.*, 2007, **46**, 1706.
779. E. Stavitski, M. H. F. Kox and B. M. Weckhuysen, *Chem.-Eur. J.*, 2007, **13**, 7057.
780. M. H. F. Kox, E. Stavitski and B. M. Weckhuysen, *Angew. Chem.-Int. Edit.*, 2007, **46**, 3652.
781. G. De Cremer, Y. Antoku, M. B. J. Roeffaers, M. Sliwa, J. Van Noyen, S. Smout, J. Hofkens, D. E. De Vos, B. F. Sels and T. Vosch, *Angew. Chem.-Int. Edit.*, 2008, **47**, 2813.
782. M. H. F. Kox, E. Stavitski, J. C. Groen, J. Perez-Ramirez, F. Kapteijn and B. M. Weckhuysen, *Chem.-Eur. J.*, 2008, **14**, 1718.
783. D. Mores, E. Stavitski, M. H. F. Kox, J. Kornatowski, U. Olsbye and B. M. Weckhuysen, *Chem.-Eur. J.*, 2008, **14**, 11320.
784. M. B. J. Roeffaers, R. Ameloot, M. Baruah, H. Uji-i, M. Bulut, G. De Cremer, U. Muller, P. A. Jacobs, J. Hofkens, B. F. Sels and D. E. De Vos, *J. Am. Chem. Soc.*, 2008, **130**, 5763.
785. M. B. J. Roeffaers, R. Ameloot, A. J. Bons, W. Mortier, G. De Cremer, R. de Kloe, J. Hofkens, D. E. De Vos and B. F. Sels, *J. Am. Chem. Soc.*, 2008, **130**, 13516.
786. L. Karwacki, M. H. F. Kox, D. A. M. de Winter, M. R. Drury, J. D. Meeldijk, E. Stavitski, W. Schmidt, M. Mertens, P. Cubillas, N. John, A. Chan, N. Kahn, S. R. Bare, M. Anderson, J. Kornatowski and B. M. Weckhuysen, *Nat. Mater.*, 2009, **8**, 959.
787. M. B. J. Roeffaers, G. De Cremer, J. Libeert, R. Ameloot, P. Dedecker, A. J. Bons, M. Buckins, J. A. Martens, B. F. Sels, D. E. De Vos and J. Hofkens, *Angew. Chem.-Int. Edit.*, 2009, **48**, 9285.
788. G. De Cremer, B. F. Sels, D. E. De Vos, J. Hofkens and M. B. J. Roeffaers, *Chem. Soc. Rev.*, 2010, **39**, 4703.
789. A. N. Parvulescu, D. Mores, E. Stavitski, C. M. Teodorescu, P. C. A. Bruijnincx, R. Gebbink and B. M. Weckhuysen, *J. Am. Chem. Soc.*, 2010, **132**, 10429.
790. C. Chmelik and J. Karger, *Chem. Soc. Rev.*, 2010, **39**, 4864.
791. M. A. van der Veen, B. F. Sels, D. E. De Vos and T. Verbiest, *J. Am. Chem. Soc.*, 2010, **132**, 6630.
792. I. L. C. Buurmans, J. Ruiz-Martinez, W. V. Knowles, D. van der Beek, J. A. Bergwerff, E. T. C. Vogt and B. M. Weckhuysen, *Nat. Chem.*, 2011, **3**, 862.

793. M. A. Karreman, I. L. C. Buurmans, J. W. Geus, A. V. Agronskaia, J. Ruiz-Martinez, H. C. Gerritsen and B. M. Weckhuysen, *Angew. Chem.-Int. Edit.*, 2012, **51**, 1428.
794. R. Ameloot, F. Vermoortele, J. Hofkens, F. C. De Schryver, D. E. De Vos and M. B. J. Roeffaers, *Angew. Chem.-Int. Edit.*, 2013, **52**, 401.
795. B. Ruhle, M. Davies, T. Bein and C. Brauchle, *Z.Naturforsch.(B)*, 2013, **68**, 423.
796. D. P. Yan, Y. Q. Tang, H. Y. Lin and D. Wang, *Sci Rep*, 2014, **4**, 7.
797. C. Sprung and B. M. Weckhuysen, *J. Am. Chem. Soc.*, 2015, **137**, 1916.
798. R. A. Schoonheydt, *Chem. Soc. Rev.*, 2010, **39**, 5051.
799. K. T. Jackson and R. F. Howe, *Stud. Surf. Sci. Catal.*, 1994, **83**, 187.
800. R. L. Frost, M. Weier and W. N. Martens, *Spectroc. Acta Pt. A-Molec. Biomolec. Spectr.*, 2006, **63**, 685.
801. S. N. Azizi and S. E. Tilami, *J. Solid State Chem.*, 2013, **198**, 138.
802. M. Nowotny, J. A. Lercher and H. Kessler, *Zeolites*, 1991, **11**, 454.
803. F. Schuth, *J. Phys. Chem.*, 1992, **96**, 7493.
804. U. Roland, R. Salzer and S. Stolle, *Stud. Surf. Sci. Catal.*, 1994, **84**, 1231.
805. G. Muller, J. Bodis and J. Kornatowski, *Microporous Mesoporous Mat.*, 2004, **69**, 1.
806. J. Karger, R. Valiullin and S. Vasenkov, *New J. Phys.*, 2005, **7**, 15.
807. P. Kortunov, C. Chmelik, J. Karger, R. A. Rakoczy, D. M. Ruthven, Y. Traa, S. Vasenkov and J. Weitkamp, *Adsorpt.-J. Int. Adsorpt. Soc.*, 2005, **11**, 235.
808. C. Chmelik, P. Kortunov, S. Vasenkov and J. Karger, *Adsorpt.-J. Int. Adsorpt. Soc.*, 2005, **11**, 455.
809. C. Chmelik, E. Lehmann, S. Vasenkov, B. Staudte and J. Karger, *Application of interference and IR microscopy for studies of intracrystalline molecular transport in AFI type zeolites*, Springer, Dordrecht, 2006.
810. L. Heinke, C. Chmelik, P. Kortunov, D. M. Ruthven, D. B. Shah, S. Vasenkov and J. Karger, *Chem. Eng. Technol.*, 2007, **30**, 995.
811. L. Heinke, C. Chmelik, P. Kortunov, D. B. Shah, S. Brandani, D. M. Ruthven and J. Karger, *Microporous Mesoporous Mat.*, 2007, **104**, 18.
812. L. Heinke, C. Chmelik, P. Kortunov, S. Vasenkov, D. M. Ruthven, D. B. Shah and J. Karger, *Chem. Ing. Tech.*, 2007, **79**, 1195.
813. R. A. Schoonheydt, *Angew. Chem.-Int. Edit.*, 2008, **47**, 9188.
814. C. Chmelik, L. Heinke, J. M. van Baten and R. Krishna, *Microporous Mesoporous Mat.*, 2009, **125**, 11.
815. J. Karger, J. Caro, P. Cool, M. O. Coppens, D. Jones, F. Kapteijn, F. Rodriguez-Reinoso, M. Stocker, D. Theodorou, E. F. Vansant and J. Weitkamp, *Chem. Eng. Technol.*, 2009, **32**, 1494.
816. C. Chmelik, L. Heinke, R. Valiullin and J. Karger, *Chem. Ing. Tech.*, 2010, **82**, 779.
817. C. Chmelik and J. Karger, *Adsorpt.-J. Int. Adsorpt. Soc.*, 2010, **16**, 515.
818. V. R. R. Marthala, M. Hunger, F. Kettner, H. Krautscheid, C. Chmelik, J. Karger and J. Weitkamp, *Chem. Mat.*, 2011, **23**, 2521.
819. J. Karger, *ChemPhysChem*, 2015, **16**, 24.
820. G. D. Price, J. J. Pluth, J. V. Smith, J. M. Bennett and R. L. Patton, *J. Am. Chem. Soc.*, 1982, **104**, 5971.
821. D. G. Hay, H. Jaeger and K. G. Wilshier, *Zeolites*, 1990, **10**, 571.
822. C. Weidenthaler, R. X. Fischer, R. D. Shannon and O. Medenbach, *J. Phys. Chem.*, 1994, **98**, 12687.
823. B. G. Saar, Y. N. Zeng, C. W. Freudiger, Y. S. Liu, M. E. Himmel, X. S. Xie and S. Y. Ding, *Angew. Chem.-Int. Edit.*, 2010, **49**, 5476.
824. Y. Ozeki, W. Umemura, Y. Otsuka, S. Satoh, H. Hashimoto, K. Sumimura, N. Nishizawa, K. Fukui and K. Itoh, *Nat. Photonics*, 2012, **6**, 844.
825. P. Wang, J. J. Li, P. Wang, C. R. Hu, D. L. Zhang, M. Sturek and J. X. Cheng, *Angew. Chem.-Int. Edit.*, 2013, **52**, 13042.
826. L. Wei, Y. Yu, Y. H. Shen, M. C. Wang and W. Min, *Proc. Natl. Acad. Sci. U. S. A.*, 2013, **110**, 11226.
827. Z. X. Chen, D. W. Paley, L. Wei, A. L. Weisman, R. A. Friesner, C. Nuckolls and W. Min, *J. Am. Chem. Soc.*, 2014, **136**, 8027.
828. D. Fu, Y. Yu, A. Folick, E. Currie, R. V. Farese, T. H. Tsai, X. S. Xie and M. C. Wang, *J. Am. Chem. Soc.*, 2014, **136**, 8820.
829. Y. H. Shen, F. Xu, L. Wei, F. H. Hu and W. Min, *Angew. Chem.-Int. Edit.*, 2014, **53**, 5596.
830. D. L. Zhang, P. Wang, M. N. Slipchenko and J. X. Cheng, *Accounts Chem. Res.*, 2014, **47**, 2282.
831. W. S. Chiu, N. A. Belsey, N. L. Garrett, J. Moger, M. B. Delgado-Charro and R. H. Guy, *Proc. Natl. Acad. Sci. U. S. A.*, 2015, **112**, 7725.
832. F. Raatz, E. Freund and C. Marcilly, *J. Chem. Soc. Faraday Trans. 1*, 1983, **79**, 2299.
833. F. Raatz, C. Marcilly and E. Freund, *Zeolites*, 1985, **5**, 329.

834. P. C. Van Geem, K. F. M. G. J. Scholle, G. P. M. Van der Velden and W. S. Veeman, *J. Phys. Chem.*, 1988, **92**, 1585.
835. R. Fricke, H. Kosslick, G. Lischke and M. Richter, *Chem. Rev.*, 2000, **100**, 2303.
836. C. O. Arean, E. Escalona Platero, G. Spoto and A. Zecchina, *J. Mol. Catal.*, 1989, **56**, 211.
837. E. Escalona Platero, C. Otero Arean, D. Scarano, G. Spoto and A. Zecchina, *Mater. Chem. Phys.*, 1991, **29**, 347.
838. A. Zecchina, G. Spoto, G. Ghiotti and E. Garrone, *J Mol Catal*, 1994, **86**, 423.
839. G. D. Smith and R. A. Palmer, in *Handbook of vibrational spectroscopy*, eds. J. M. Chalmers and P. R. Griffiths, John Wiley & Sons, Chichester, 2002, vol. 1, pp. 625.
840. J. Saussey and F. Thibault-Starzyk, in *In-situ spectroscopy of catalysts*, ed. B. M. Weckhuysen, American Scientific Publisher, Stevenson Ranch (California), 2004.
841. P. R. Griffiths and J. A. de Haseth, *Fourier Transform Infrared Spectrometry*, John Wiley & Sons, New York, 1986.
842. V. G. Gregoriou, J. L. Chao, H. Toriumi and R. A. Palmer, *Chem. Phys. Lett.*, 1991, **179**, 491.
843. W. Uhmann, A. Becker, C. Taran and F. Siebert, *Appl. Spectrosc.*, 1991, **45**, 390.
844. T. J. Johnson, A. Simon, J. M. Weil and G. W. Harris, *Appl. Spectrosc.*, 1993, **47**, 1376.
845. T. Nakano, T. Yokoyama and H. Toriumi, *Appl. Spectrosc.*, 1993, **47**, 1354.
846. R. A. Palmer, J. L. Chao, R. M. Dittmar, V. G. Gregoriou and S. E. Plunkett, *Appl. Spectrosc.*, 1993, **47**, 1297.
847. S. V. Shilov, S. Okretic, H. W. Siesler and M. A. Czarnecki, *Appl. Spectrosc. Rev.*, 1996, **31**, 125.
848. C. Zscherp, R. Schlesinger, J. Tittor, D. Oesterhelt and J. Heberle, *Proc. Natl. Acad. Sci. U. S. A.*, 1999, **96**, 5498.
849. R. Brudler, R. Rammelsberg, T. T. Woo, E. D. Getzoff and K. Gerwert, *Nat. Struct. Biol.*, 2001, **8**, 265.
850. I. Yeom, Y.-H and H. Frei, in *In-situ spectroscopy of catalysts*, ed. B. M. Weckhuysen, American Scientific Publisher, Stevenson Ranch (California), 2004.
851. S. M. Massick, J. G. Rabor, S. Elbers, J. Marhenke, S. Bernhard, J. R. Schoonover and P. C. Ford, *Inorg. Chem.*, 2000, **39**, 3098.
852. B. O. Budevska and P. R. Griffiths, *Anal. Chem.*, 1993, **65**, 2963.
853. A. Wille and E. Fridell, *Appl. Catal. B-Environ.*, 2007, **70**, 294.
854. F. Thibault-Starzyk, E. Seguin, S. Thomas, M. Daturi, H. Arnolds and D. A. King, *Science*, 2009, **324**, 1048.
855. H. Sun and H. Frei, *J. Phys. Chem. B*, 1997, **101**, 205.
856. H. Frei, *AIP Conf. Proc.*, 1998, **430**, 28.
857. S. Vasenkov and H. Frei, *J. Am. Chem. Soc.*, 1998, **120**, 4031.
858. S. Vasenkov and H. Frei, *J. Phys. Chem. A*, 2000, **104**, 4327.
859. Y. H. Yeom and H. Frei, *J. Phys. Chem. A*, 2002, **106**, 3350.
860. Y. H. Yeom and H. Frei, *J. Phys. Chem. B*, 2003, **107**, 6286.
861. F. Thibault-Starzyk, S. Chenevarin and C. Fernandez, *Stud. Surf. Sci. Catal.*, 2004, **154**, 1730.
862. L. K. Andersen and H. Frei, *J. Phys. Chem. B*, 2006, **110**, 22601.
863. J. Estephane, E. Groppo, J. G. Vitillo, A. Damin, D. Gianolio, C. Lamberti, S. Bordiga, E. A. Quadrelli, J. M. Basset, G. Kervern, L. Emsley, G. Pintacuda and A. Zecchina, *J. Phys. Chem. C*, 2010, **114**, 4451.
864. K. L. Tang Wong and H. H. Brintzinger, *J. Am. Chem. Soc.*, 1975, **97**, 5143.
865. H. H. Brintzinger, D. Fischer, R. Mulhaupt, B. Rieger and R. M. Waymouth, *Angew Chem Int Edit*, 1995, **34**, 1143.
866. J. Estephane, E. Groppo, A. Damin, J. G. Vitillo, D. Gianolio, C. Lamberti, S. Bordiga, C. Prestipino, S. Nikitenko, E. A. Quadrelli, M. Taoufik, J. M. Basset and A. Zecchina, *J. Phys. Chem. C*, 2009, **113**, 7305.
867. D. Gianolio, E. Groppo, J. Estephane, C. Prestipino, S. Nikitenko, A. Zecchina, S. Bordiga, M. Taoufik, E. A. Quadrelli, J. M. Basset and C. Lamberti, *J. Phys.: Conf. Ser.*, 2009, **190**, 012140.
868. K. A. E. O'Callaghan, S. J. Brown, J. A. Page, M. C. Baird, T. C. Richards and W. E. Geiger, *Organometallics*, 1991, **10**, 3119.
869. M. Y. Darensbourg, P. Jimenez, J. R. Sackett, J. M. Hanckel and R. L. Kump, *J. Am. Chem. Soc.*, 1982, **104**, 1521.
870. B. Longato, B. D. Martin, J. R. Norton and O. P. Anderson, 1985, **24**, 1389.
871. S. Bordiga, L. Regli, C. Lamberti, A. Zecchina, M. Bjorgen and K. P. Lillerud, *J. Phys. Chem. B*, 2005, **109**, 7724.
872. K. Hadjiivanov, J. Saussey, J. L. Freysz and J. C. Lavalley, *Catal. Lett.*, 1998, **52**, 103.
873. F. Haase and J. Sauer, *J. Am. Chem. Soc.*, 1995, **117**, 3780.

874. J. Kotrla, D. Nachtigallova, L. Kubelkova, L. Heeribout, C. Doremieux-Morin and J. Fraissard, *J. Phys. Chem. B*, 1998, **102**, 2454.
875. H. Schneider, S. Tschudin, M. Schneider, A. Wokaun and A. Baiker, *J. Catal.*, 1994, **147**, 5.
876. G. Busca, L. Lietti, G. Ramis and F. Berti, *Appl. Catal. B-Environ.*, 1998, **18**, 1.
877. I. Nova, C. Ciardelli, E. Tronconi, D. Chatterjee and B. Bandl-Konrad, *Aiche J.*, 2006, **52**, 3222.
878. C. Ciardelli, I. Nova, E. Tronconi, D. Chatterjee, B. Bandl-Konrad, M. Weibel and B. Krutzsch, *Appl. Catal. B-Environ.*, 2007, **70**, 80.
879. E. Tronconi, I. Nova, C. Ciardelli, D. Chatterjee and M. Weibel, *J. Catal.*, 2007, **245**, 1.
880. H. H. Phil, M. P. Reddy, P. A. Kumar, L. K. Ju and J. S. Hyo, *Appl. Catal. B-Environ.*, 2008, **78**, 301.
881. N. W. Cant and I. O. Y. Liu, *Catal. Today*, 2000, **63**, 133.
882. Z. Sobalik, P. Sazama, J. Dedecek and B. Wichterlova, *Appl. Catal. A-Gen.*, 2014, **474**, 178.
883. M. Schwidder, M. S. Kumar, K. Klementiev, M. M. Pohl, A. Bruckner and W. Grunert, *J. Catal.*, 2005, **231**, 314.
884. M. Schwidder, M. S. Kumar, U. Bentrup, J. Perez-Ramirez, A. Bruckner and W. Grunert, *Microporous Mesoporous Mat.*, 2008, **111**, 124.
885. A. Grossale, I. Nova and E. Tronconi, *Catal. Today*, 2008, **136**, 18.
886. A. Grossale, I. Nova and E. Tronconi, *J. Catal.*, 2009, **265**, 141.
887. I. Malpartida, O. Marie, P. Bazin, M. Daturi and X. Jeandel, *Appl. Catal. B-Environ.*, 2012, **113**, 52.
888. L. Olsson, H. Sjovall and R. J. Blint, *Appl. Catal. B-Environ.*, 2008, **81**, 203.
889. H. Sjovall, R. J. Blint and L. Olsson, *Appl. Catal. B-Environ.*, 2009, **92**, 138.
890. L. M. Ren, L. F. Zhu, C. G. Yang, Y. M. Chen, Q. Sun, H. Y. Zhang, C. J. Li, F. Nawaz, X. J. Meng and F. S. Xiao, *Chem. Commun.*, 2011, **47**, 9789.
891. U. Deka, A. Juhin, E. A. Eilertsen, H. Emerich, M. A. Green, S. T. Korhonen, B. M. Weckhuysen and A. M. Beale, *J. Phys. Chem. C*, 2012, **116**, 4809.
892. J. H. Kwak, D. Tran, S. D. Burton, J. Szanyi, J. H. Lee and C. H. F. Peden, *J. Catal.*, 2012, **287**, 203.
893. L. Wang, W. Li, G. S. Qi and D. Weng, *J. Catal.*, 2012, **289**, 21.
894. U. Deka, I. Lezcano-Gonzalez, B. M. Weckhuysen and A. M. Beale, *ACS Catal.*, 2013, **3**, 413.
895. F. Gao, E. D. Walter, N. M. Washton, J. Szanyi and C. H. F. Peden, *ACS Catal.*, 2013, **3**, 2083.
896. P. N. R. Vennestrom, A. Katerinopoulou, R. R. Tiruvalam, A. Kustov, P. G. Moses, P. Concepcion and A. Corma, *ACS Catal.*, 2013, **3**, 2158.
897. P. N. R. Vennestrom, T. V. W. Janssens, A. Kustov, M. Grill, A. Puig-Molina, L. F. Lundegaard, R. R. Tiruvalam, P. Concepcion and A. Corma, *J. Catal.*, 2014, **309**, 477.
898. J. J. Xue, X. Q. Wang, G. S. Qi, J. Wang, M. Q. Shen and W. Li, *J. Catal.*, 2013, **297**, 56.
899. S. Shwan, M. Skoglundh, L. F. Lundegaard, R. R. Tiruvalam, T. V. W. Janssens, A. Carlsson and P. N. R. Vennestrom, *ACS Catal.*, 2015, **5**, 16.
900. R. Martinez-Franco, M. Moliner, J. R. Thogersen and A. Corma, *ChemCatChem*, 2013, **5**, 3316.
901. M. Moreno-Gonzalez, B. Hueso, M. Boronat, T. Blasco and A. Corma, *J. Phys. Chem. Lett.*, 2015, **6**, 1011.
902. F. Giordanino, *Towards a consistent NH_3-SCR mechanism over Cu sites in zeolites: Cu-SSZ-13 as model and outperforming catalyst, PhD in chemical and materials sciences, Department of chemistry, University of Turin*, 2014.
903. I. Lezcano-Gonzalez, U. Deka, B. Arstad, A. Van Yperen-De Deyne, K. Hemelsoet, M. Waroquier, V. Van Speybroeck, B. M. Weckhuysen and A. M. Beale, *Phys. Chem. Chem. Phys.*, 2014, **16**, 1639.
904. M. Boudart and G. Djega-Mariadassou, *Kinetics of Heterogeneous Catalytic Reactions*, Princeton University Press, Princeton, New Jersey (USA), 1984.
905. G. Djega-Mariadassou and M. Boudart, *J. Catal.*, 2003, **216**, 89.
906. J. W. Ward, *J. Catal.*, 1968, **11**, 259.
907. J. F. Joly, N. Zanierszydlowski, S. Colin, F. Raatz, J. Saussey and J. C. Lavalley, *Catal. Today*, 1991, **9**, 31.
908. S. Jolly, J. Saussey, J. C. Lavalley, N. Zanier, E. Benazzi and J. F. Joly, *Ber. Bunsen-Ges. Phys. Chem. Chem. Phys.*, 1993, **97**, 313.
909. O. Marie, F. Thibault-Starzyk and P. Massiani, *J. Catal.*, 2005, **230**, 28.
910. R. Gounder and E. Iglesia, *J. Am. Chem. Soc.*, 2009, **131**, 1958.
911. J. F. Groust, G. Costentin, J. M. Krafft and P. Massiani, *Phys. Chem. Chem. Phys.*, 2010, **12**, 937.
912. H. Lauron-Pernot, *Catal. Rev.-Sci. Eng.*, 2006, **48**, 315.
913. M. Magureanu, N. B. Mandache, P. Eloy, E. M. Gaigneaux and V. I. Parvulescu, *Appl. Catal. B-Environ.*, 2005, **61**, 12.
914. C. Subrahmanyam, A. Magureanu, A. Renken and L. Kiwi-Minsker, *Appl. Catal. B-Environ.*, 2006, **65**, 150.
915. C. Subrahmanyam, A. Renken and L. Kiwi-Minsker, *Appl. Catal. B-Environ.*, 2006, **65**, 157.

916. M. Magureanu, N. B. Mandache, J. C. Hu, R. Richards, M. Florea and V. I. Parvulescu, *Appl. Catal. B-Environ.*, 2007, **76**, 275.
917. C. Subrahmanyarn, A. Renken and L. Kiwi-Minsker, *Plasma Chem. Plasma Process.*, 2007, **27**, 13.
918. A. E. Wallis, J. C. Whitehead and K. Zhang, *Appl. Catal. B-Environ.*, 2007, **74**, 111.
919. A. E. Wallis, J. C. Whitehead and K. Zhang, *Catal. Lett.*, 2007, **113**, 29.
920. Y. Chao, C. T. Huang, H. M. Lee and M. B. Chang, *Int. J. Hydrog. Energy*, 2008, **33**, 664.
921. W. Chu, L. N. Wang, P. A. Chernavskii and A. Y. Khodakov, *Angew. Chem.-Int. Edit.*, 2008, **47**, 5052.
922. M. Rivallan, I. Yordanov, S. Thomas, C. Lancelot, S. Mintova and F. Thibault-Starzyk, *ChemCatChem*, 2010, **2**, 1074.
923. H. B. Huang, D. Q. Ye, D. Y. C. Leung, F. D. Feng and X. J. Guan, *J. Mol. Catal. A-Chem.*, 2011, **336**, 87.
924. T. Liu, Q. Q. Yu, H. Wang, X. Y. Jiang and X. M. Zheng, *Chin. J. Catal.*, 2011, **32**, 1502.
925. T. Witvrouwen, S. Paulussen and B. Sels, *Plasma Process. Polym.*, 2012, **9**, 750.
926. A. Gomez-Ramirez, V. J. Rico, J. Cotrino, A. Gonzalez-Elipe and R. M. Lambert, *ACS Catal.*, 2014, **4**, 402.
927. K. Abedi, F. Ghorbani-Shahna, B. Jaleh, A. Bahrami, R. Yarahmadi, R. Haddadi and M. Gandomi, *J. Electrost.*, 2015, **73**, 80.
928. M. Zhang and H. Frei, *Catal. Lett.*, 2015, **145**, 420.
929. M. El-Roz, P. Bazin, M. Daturi and F. Thibault-Starzyk, *ACS Catal.*, 2013, **3**, 2790.
930. C. V. Raman, *Indian J. Phys.*, 1928, **2**, 387.
931. G. Landsberg and L. Mandelstam, *Naturwissenschaften*, 1928, **16**, 557.
932. S. J. Tinnemans, M. H. F. Kox, M. W. Sletering, T. A. X. Nijhuis, T. Visser and B. M. Weckhuysen, *Phys. Chem. Chem. Phys.*, 2006, **8**, 2413.
933. F. J. Keil, *Microporous Mesoporous Mat.*, 1999, **29**, 49.
934. A. Bruckner, *Catal. Rev.-Sci. Eng.*, 2003, **45**, 97.
935. C. Prestipino, L. Regli, J. G. Vitillo, F. Bonino, A. Damin, C. Lamberti, A. Zecchina, P. L. Solari, K. O. Kongshaug and S. Bordiga, *Chem. Mater.*, 2006, **18**, 1337.
936. E. Groppo, M. J. Uddin, S. Bordiga, A. Zecchina and C. Lamberti, *Angew. Chem.-Int. Edit.*, 2008, **47**, 9269.
937. M. A. Newton, *Chem. Soc. Rev.*, 2008, **37**, 2644.
938. S. Nikitenko, A. M. Beale, A. M. J. van der Eerden, S. D. M. Jacques, O. Leynaud, M. G. O'Brien, D. Detollenaere, R. Kaptein, B. M. Weckhuysen and W. Bras, *J. Synchrotron Radiat.*, 2008, **15**, 632.
939. G. Agostini, R. Pellegrini, G. Leofanti, L. Bertinetti, S. Bertarione, E. Groppo, A. Zecchina and C. Lamberti, *J. Phys. Chem. C*, 2009, **113**, 10485.
940. M. A. Newton and W. van Beek, *Chem. Soc. Rev.*, 2010, **39**, 4845.
941. M. G. O'Brien, A. M. Beale and B. M. Weckhuysen, *Chem. Soc. Rev.*, 2010, **39**, 4767.
942. U. Bentrup, *Chem. Soc. Rev.*, 2010, **39**, 4718.
943. E. Borfecchia, S. Maurelli, D. Gianolio, E. Groppo, M. Chiesa, F. Bonino and C. Lamberti, *J. Phys. Chem. C*, 2012, **116**, 19839.
944. A. Kubacka, A. Iglesias-Juez, A. Martínez-Arias, M. Di Michiel, M. A. Newton and M. Fernández-García, *ChemCatChem*, 2012, **4**, 725.
945. M. A. Newton and M. Fernández-García, in *In-situ Characterization of Heterogeneous Catalysts*, eds. J. A. Rodriguez, J. C. Hanson and P. J. Chupas, John Wiley & Sons, 2013.
946. E. Borfecchia, D. Gianolio, G. Agostini, S. Bordiga and C. Lamberti, in *Metal Organic Frameworks as Heterogeneous Catalysts*, eds. F. X. Llabrés i Xamena and J. Gascón, The Royal Society of Chemistry, Cambridge, 2013, pp. 143.
947. G. Agostini, C. Lamberti, R. Pellegrini, G. Leofanti, F. Giannici, A. Longo and E. Groppo, *ACS Catal.*, 2014, **4**, 187.
948. E. Groppo, G. Agostini, E. Borfecchia, L. Wei, F. Giannici, G. Portale, A. Longo and C. Lamberti, *J. Phys. Chem. C*, 2014, **118**, 8406.
949. E. Groppo, E. Gallo, K. Seenivasan, K. A. Lomachenko, A. Sommazzi, S. Bordiga, P. Glatzel, R. van Silfhout, A. Kachatkou, W. Bras and C. Lamberti, *ChemCatChem*, 2015, **7**, DOI: 10.1002/cctc.201402989.
950. C. Lamberti, E. Borfecchia, J. A. van Bokhoven and M. Fernández García, in *XAS and XES; Theory and Applications*, eds. J. A. van Bokhoven and C. Lamberti, Wiley, New York, 2015.
951. F. Bonino, A. Damin, S. Bordiga, M. Selva, P. Tundo and A. Zecchina, *Angew. Chem.-Int. Edit.*, 2005, **44**, 4774.
952. L. Valenzano, B. Civalleri, S. Bordiga, M. H. Nilsen, S. Jakobsen, K.-P. Lillerud and C. Lamberti, *Chem. Mater.*, 2011, **23**, 1700.
953. L. Valenzano, J. G. Vitillo, S. Chavan, B. Civalleri, F. Bonino, S. Bordiga and C. Lamberti, *Catal. Today*, 2012, **182**, 67.

954. K. Seenivasan, E. Gallo, A. Piovano, J. G. Vitillo, A. Sommazzi, S. Bordiga, C. Lamberti, P. Glatzel and E. Groppo, *Dalton Trans.*, 2013, **42**, 12706.
955. A. L. Bugaev, A. A. Guda, K. A. Lomachenko, V. V. Srabionyan, L. A. Bugaev, A. V. Soldatov, C. Lamberti, V. P. Dmitriev and J. A. van Bokhoven, *J. Phys. Chem. C*, 2014, **118**, 10416.
956. S. Takeuchi and T. Tahara, *J. Chem. Phys.*, 2004, **120**, 4768.
957. N. Ulagappan and H. Frei, *J. Phys. Chem. A*, 2000, **104**, 7834.
958. W. Y. Lin, H. X. Han and H. Frei, *J. Phys. Chem. B*, 2004, **108**, 18269.
959. V. Bourdin, P. Grenier, F. Meunier and L. M. Sun, *Aiche J.*, 1996, **42**, 700.
960. J. Valyon, G. Onyestyak and L. V. C. Rees, *J. Phys. Chem. B*, 1998, **102**, 8994.
961. G. Onyestyak, J. Valyon and L. V. C. Rees, *Phys. Chem. Chem. Phys.*, 2000, **2**, 3077.
962. J. Valyon, G. Onyestyak and L. V. C. Rees, *Langmuir*, 2000, **16**, 1331.
963. S. Chenevarin and F. Thibault-Starzyk, *Angew. Chem.-Int. Edit.*, 2004, **43**, 1155.
964. M. Rivallan, E. Seguin, S. Thomas, M. Lepage, N. Takagi, H. Hirata and F. Thibault-Starzyk, *Angew. Chem.-Int. Edit.*, 2010, **49**, 785.